DISSERTATION | DOCTORAL THESIS

Titel | Title

Novel insights into the biological activity of ruthenium-based prodrug systems

verfasst von | submitted by

Mag.rer.nat. Beatrix Schönhacker-Alte

angestrebter akademischer Grad | in partial fulfilment of the requirements for the degree of

Doktorin der Naturwissenschaften (Dr.rer.nat.)

Wien | Vienna, 2025

Studienkennzahl lt. Studienblatt | Degree programme code as it appears on the student record sheet:	UA 796 605 419
Dissertationsgebiet lt. Studienblatt | Field of study as it appears on the student record sheet:	Chemie
Betreut von | Supervisor:	emer. o. Univ.-Prof. Dr. Dr. Bernhard Keppler ao. Univ.-Prof. Mag. Dr. Walter Berger

Declaration

This cumulative doctoral thesis comprises three co-authored peer-reviewed manuscripts all of which are enclosed in the chapter “Results”. Each of these manuscripts was realized in collaboration with colleagues from our working group or from other institutions. My contribution to the research papers is stated in the prologues and interludes before each manuscript PDF, respectively. All other parts of this thesis were written by myself and revised by my supervisors Prof. Dr. Bernhard Keppler and Prof. Dr. Walter Berger.

The main part of the research work performed by myself was carried out under the supervision of Prof. Dr. Walter Berger and Prof. Dr. Petra Heffeter at the Center for Cancer Research, Medical University Vienna, Austria. I was mainly funded by the University of Vienna and the Medical University on Vienna.

Animal care and *in vivo* drug applications were performed by the technicians Gerhard Zeitler and Sushilla van Schonhoven, who were employees of the Center for Cancer Research, when I was conducting the research comprised in this thesis. Synthesis and chemical characterization of organometallic complexes used during this thesis were conducted at the Institute of Inorganic Chemistry, University of Vienna under the supervision of Dr. Wolfgang Kandioller in the group of Prof. Dr. Bernhard Keppler.

All *in vivo* experiments performed during this thesis have been approved by the ethics committee of the Medical University of Vienna and the Austrian Ministry for Science and Technology (Bundesministerium für Wissenschaft und Forschung) RefII/10b (Gentechnik und Tierversuche;) under the reference BMWF-66.009/0084-II/3b/2013.

Parts of the results generated during this thesis were presented by me at several international and national conferences:

- Poster Presentation at the AACR Annual Meeting 2015, Philadelphia, USA
- Poster Presentation at the YSA PhD Symposium 2015, Vienna, Austria
- Poster Presentation at the 13th European Biological Inorganic Chemistry (EuroBIC 13) 2016, Budapest, Hungary
- Oral Presentation at 6th Metallomics Conference 2017, Vienna, Austria

Danksagung

Wer mich kennt, weiß, dass ich keine Scheu habe, nachzudenken, mich anzustrengen und tief in ein Thema einzutauchen. Das durfte ich über mehrere Jahre im faszinierenden Thema der präklinischen Wirkstoffentwicklung ausleben und unter Beweis stellen. Durch einige Begebenheiten schreibe ich diese Dissertation nicht wie ursprünglich geplant am Ende meiner Forschungstätigkeit, sondern mit einigen Jahren Abstand zu dieser ereignisreichen und unvergleichlichen Zeit. Nach wie vor denke ich gerne daran zurück, wie spannend, lustig, teilweise auch tragisch es war, gemeinsam Zellen zu pflegen, an Methoden zu feilen und zu versuchen, all die kleinen Puzzleteile von Ergebnissen zu einem großen Ganzen zusammenzufügen. All das gelingt nur, wenn man als Team arbeitet. Mein herzlicher Dank gilt an dieser Stelle meinen ehemaligen Kolleginnen und Kollegen sowie den Gruppenleiter:innen Walter Berger und Petra Heffeter. Ohne euch wäre dies nicht zustande gekommen und die Zeit in der Forschung nicht in positiver Erinnerung. Ebenso möchte ich mich bei Prof. Bernhard Keppler bedanken, der mit seinem Engagement für die interdisziplinäre Zusammenarbeit und der Bereitstellung der Finanzierung diese, meine Arbeit ermöglicht hat.

Dieser Dissertation ging eine lange Reise voraus – wissenschaftlich wie auch persönlich. Ich bin froh, auf all diesen Ebenen gut angekommen zu sein, nicht zuletzt dank der Menschen, die diesen Weg mit mir gegangen sind. Einen besonderen Dank schulde ich diesbezüglich meinem Mann, der mich durch die Höhen und Tiefen der Laborarbeit wie auch des Schreibens meiner wissenschaftlichen Arbeiten begleitet hat. Ebenso danke ich meiner Familie, die sich meine Erzählungen über Zellen, Ergebnisse und Theorien immer wieder mit Interesse angehört hat.

List of Figures

Figure 1: Global Cancer Data on the Incidence and Mortality of Cancer in the year 2022 3
Figure 2: Cancer development regarding accumulation of genetic changes 5
Figure 3: Hallmarks of cancer 6
Figure 4: Outline of cell cycle control. 7
Figure 5: An overview of mechanisms of apoptosis. 9
Figure 6: Illustration of the stages of apoptotic programmed cell death 10
Figure 7: Use of central carbon metabolism 12
Figure 8: Overview of selected milestones in cancer therapy 14
Figure 9: Examples of active compounds in chemotherapy Cisplatin, Doxorubicin and Paclitaxel 17
Figure 10: From Prescription to Patient Health A multitude of factors may affect the outcome of a treatment. 18
Figure 11: Classification of most commonly used nanocarriers for drug delivery. 20
Figure 12: Schematic representation of a polymeric drug delivery system described by H. Ringsdorf 21
Figure 13: human serum albumin binding sites for drugs (left) and fatty acids (right) 22
Figure 14: Simplified preparation methods of two different approaches to albumin-based drug delivery systems 23
Figure 15: Overview on the (pre)clinically developed albumin-targeted anticancer drugs 23
Figure 16: Naturally occurring coordination complexes relevant for biological processes 25
Figure 17: Summary of the Mechanism of Action of Metal-Based Drugs 26
Figure 18: Cisplatin and its derivatives oxaliplatin, carboplatin and nedaplatin 27
Figure 19: Examples of ruthenium coordination complexes which are or have been in clinical development 29
Figure 20: Ru(III) complexes KP418, NAMI-A, KP1019 and BOLD-100 30
Figure 21: Schematic representation of targets of KP1019 and BOLD-100 32
Figure 22: Full dose response curves in sensitive and resistant cell lines 131
Figure 23: Western Blot of selected proteins relevant for ER homeostasis and apoptosis induction 131
Figure 24: Xenograft growth curves of Capan-1 compared to CapanR (a) and HCT116 compared to HCTR (b) 132
Figure 25: Comparative genomic hybridisation of HCT116, HCTR, Capan-1 and CapanR 133
Figure 26: Cytotoxicity of KP1339, TRAIL and the combination in sensitive and resistant cell lines 134
Figure 27: full range cytotoxicity assays on BOLD-100 with two concentrations of TRAIL 134

List of Tables

Table 1: results of cytotoxicity test to establish a cross-resistance pattern 133
Table 2: Detailed Information about cell lines used for generation of additional data 140
Table 3: used antibodies 141

Zusammenfassung

Durch die Entwicklung neuer und die Verbesserung bestehender Krebstherapien trägt die naturwissenschaftliche Forschung dazu bei, mehr Krebspatient:innen zu heilen oder zumindest lebensverlängernde Behandlungen bei gleichzeitig hoher Lebensqualität zu ermöglichen. Um dieses Ziel zu unterstützen, wurden in dieser Arbeit die folgenden Ziele verfolgt: präklinische Entwicklung neuartiger Metall-Aren-Komplexe als potenzielle Wirkstoffe in der Krebstherapie sowie detaillierte Untersuchung von Faktoren, die die Sensitivität bzw. Resistenz gegenüber dem in klinischer Entwicklung befindlichen Rutheniumkomplex BOLD-100 beeinflussen.

Hinsichtlich des ersten formulierten Ziels wählten wir Organoruthenium- und -rhodiumkomplexe aus, deren In-Vivo-Aktivitätsprofil durch die Entwicklung einer Prodrug-Formulierung verbessert werden sollte. Dazu wurden die Komplexe an ein abbaubares Poly(organo)phosphazen-Polymer gekoppelt, dessen Design auf erhöhte Wasserlöslichkeit und gezielte Aktivierung des Wirkstoffs bei Aufnahme in den Tumor ausgelegt wurde. Die im Anschluss an die Synthese und chemische Charakterisierung durchgeführten In-Vivo-Experimente bestätigten den Erfolg des Designs.

Hinsichtlich des zweiten Ziels wurden zunächst 23 Krebszelllinien auf ihre Sensitivität gegenüber Behandlung mit BOLD-100 untersucht, um basierend auf den Ergebnissen ein Panel von fünf Zelllinien für die weitergehende Evaluierung auszuwählen. Anschließend an den Nachweis, dass die Sensitivität gegenüber BOLD-100 weder mit erhöhter Rutheniumaufnahme noch mit Sensitivität gegenüber oxidativem Stress oder den Bestandteilen von BOLD-100 korreliert, wurden Unterschiede in der Reaktion der ausgewählten Zelllinien mithilfe biochemischer Studien, einschließlich genomweiter Genexpressionsarrays, identifiziert: Nach Behandlung mit BOLD-100 stoppten intrinsisch resistente Zelllinien ihren Zellzyklus in der G2-Phase. Im Gegensatz dazu führten sensitive Zelllinien den Zelltod durch Aktivierung von Caspase 8 aus. Als auslösendes Ereignis wurde ein einzigartiger Verlust wichtiger zellulärer Chaperone, einschließlich GRP78, in Kombination mit verstärkter Proteinschädigung identifiziert.

Ergänzend zu diesen Ergebnissen sollte das Verständnis der Mechanismen von BOLD-100-Sensitivität und -Resistenz vertieft werden. Hierfür wurden beide sensitiven Zelllinien des Panels immer höheren Konzentrationen von BOLD-100 ausgesetzt und als resistente Sublinien CapanR und HCTR etabliert. Die Ergebnisse der vergleichenden Untersuchungen zwischen diesen und den ursprünglichen Zelllinien bestätigten, dass die Resistenz nicht durch verringerte Rutheniumaufnahme verursacht wird. Auch zeigte ein Sensitivitätsscreen mit acht anderen Wirkstoffen keinerlei auffällige Kreuzresistenz. Unabhängig davon verhielten sich die neuen Sublinien ähnlich den intrinsisch resistenten Zelllinien hinsichtlich der Kombinationstherapie mit dem TNF-related apoptosis-inducing Liganden (TRAIL). Zusammengefasst deutete dies erneut auf einen einzigartigen Mechanismus der Wirkung von BOLD-100 und damit auch der Resistenz hin, der in nachfolgenden Studien insbesondere von D. Baier und T. Mendrina eingehend untersucht und entschlüsselt werden konnte.

Abschließend konnten die für die vorliegende Doktorarbeit definierten Ziele erreicht und somit ein wichtiger Beitrag zum Verständnis der biologischen Aktivität von Rutheniumkomplexen geleistet werden.

Abstract

Scientific research is helping to cure more cancer patients or at least to provide life-prolonging treatments while maintaining a high quality of life through developing new and improving existing cancer therapies. To support this goal, this work aimed to facilitate the preclinical development of novel metal-arene complexes as potential active ingredients in cancer therapy. In addition, factors that influence sensitivity or resistance to the ruthenium complex BOLD-100, which is currently in clinical development, were investigated extensively.

Regarding the first aim, we selected organoruthenium and -rhodium complexes whose *in vivo* activity profile should be improved by developing a prodrug formulation. To achieve this, the complexes were coupled to a degradable poly(organo)phosphazene polymer designed to increase water solubility and targeted activation of the drug upon uptake into the tumor. Following synthesis and chemical characterization, *in vivo* experiments confirmed the success of the design.

Regarding the second aim, 23 cell lines were initially screened for their sensitivity to BOLD-100 treatment and, based on the results, a panel of five cell lines was selected for further evaluation. Following the demonstration that sensitivity to BOLD-100 does not correlate with increased ruthenium uptake, with sensitivity to oxidative stress or the constituents of BOLD-100, differences in the response of the selected cell lines were identified using whole genome expression arrays and further biochemical studies. Upon exposure to BOLD-100, intrinsically resistant cell lines arrested their cell cycle in G2 phase. In contrast, sensitive cell lines executed cell death *via* activation of caspase 8. A unique depletion of key cellular chaperones including GRP78 in combination with enhanced protein damage was identified as a triggering event.

In addition to these results, the understanding of the underlying mechanisms of sensitivity and resistance was expanded. For this purpose, both sensitive cell lines of the panel were exposed to increasing concentrations of BOLD-100 and established as resistant sublines CapanR and HCTR. The results of the comparative studies between the resistant sublines and the original cell lines confirmed that the resistance is not caused by reduced ruthenium uptake. A sensitivity screen with eight other active substances showed no noticeable cross-resistance. Still, the new sublines behaved similarly to the intrinsically resistant cell lines in a combination therapy with the TNF-related apoptosis-inducing ligand *(*TRAIL). These results are a further indicator for a unique mode of action of BOLD-100 and thus also for the resistance which were investigated and deciphered in detail in subsequent studies especially by D. Baier and T. Mendrina.

In summary, the aims defined for this thesis were achieved and thus an important contribution to the understanding of the biological activity of ruthenium complexes was made.

Table of Contents

Declaration ... ii

Danksagung ... iii

List of Figures ... iv

List of Tables ... iv

Zusammenfassung ... v

Abstract ... vii

INTRODUCTION ... 1

Cancer – spreading sideways and clinging onto surrounding structures ... 1

Cancer classification ... 1

Cancer statistics ... 2

From healthy cells to cancerous growth ... 4

Hallmarks of cancer ... 5

Anticancer therapy ... 14

Historical aspects of anticancer therapy ... 14

Current standard in anticancer therapy ... 15

Reduction of toxicity and increased tumor targeting by usage of nanocarrier systems ... 18

Coordination complexes as anticancer agents ... 25

Choosing the weapon ... 26

Rational design of ruthenium complexes ... 28

Aims of this thesis ... 33

RESULTS ... 34

Prologue: First peer-reviewed paper ... 34

Synthesis and in vivo anticancer evaluation of poly(organo)phosphazene-based metallodrug conjugates ... 35

Supplementary information ... 46

Interlude: Second peer-reviewed paper 65

Sensitivity towards the GRP78 inhibitor KP1339/IT-139 is characterized by apoptosis induction via caspase 8 upon disruption of ER homeostasis 66

Supporting figures 76

Supporting information 87

Interlude: Third peer reviewed paper 96

The Anticancer Ruthenium Compound BOLD-100 Targets Glycolysis and Generates a Metabolic Vulnerability towards Glucose Deprivation 97

Supplementary Materials 126

Additional data 131

DISCUSSION 135

General discussion 135

Summary and outlook 138

MATERIAL AND METHODS 140

ABBREVIATIONS 142

REFERENCES 144

Introduction

Cancer – spreading sideways and clinging onto surrounding structures

Malignancies as a form of illness have affected humans since the very beginning of our species more than one million years ago. The term “cancer” was first used by Hippocrates (460 –375 BC) because the spreading of cancerous lesions seemed reminiscent of the way a crab walks [1]. According to his notes, those growing tumors were mostly observed in adults and could be distinguishing into *carcinos* (a tumor), *carcinoma* (a malignant tumor), and *cancer* (a non-healing malignant ulcer) [2]. This new terminus was further developed by Celsus (25 BC – AD 50) and Galen (131 – 200 AD), who both compared cancer to “a crab that adheres to surrounding structures with his claws” [2]. This is most likely referring to the invasive growth of some tumors, which can already been witnessed without further magnification.

Cancer classification

Since ancient times, tumors have been classified with reference to the organ or body part of origin (breast, lung, etc.), the texture (hard, soft) and the possible presence of an ulceration [1]. This changed profoundly around 1500, when Jean Fernel pointed out that diseases will lead to alterations in the normal physiology and induce specific pathological changes [3]. His texts are the first systemic treatises on physiology and pathology and thereby revolutionized the thinking of every physician [3]. Subsequently, several important developments in the understanding of anatomy have been made. A milestone was reached around 1650, when the increasing use of microscopes allowed visualizing of delicate structures, such as single cells, which were too small to be identified by the naked eye. This enabled scientists to understand the physiology and pathology at another level [3].

The classification of tumors according to tissue of origin, the primary site, is still in use today. However, classification based on the histological type (tissue of origin) is more accurate since the primary sites usually consist of several different cell types, which can be the origin of a cancerous de-differentiation. In more detail, the international standard for the classification and nomenclature of histologies is the International Classification of Diseases for Oncology, Third Edition (ICD-O-3) [4]. Based on their histologies, cancers are grouped into six major categories:

- Carcinomas are malignancies of epithelial origin which are divided into two major subtypes: adenocarcinoma, which develops in an organ or gland, and squamous cell carcinoma, which originates in the squamous epithelium [5].
- Sarcoma refers to cancer that originates in supportive and connective tissues such as bones, tendons, cartilage, muscle, and fat [5].
- Myeloma is cancer that originates in the plasma cells of bone marrow.
- Leukemias are cancers of the bone marrow and are also often called "liquid cancers" or "blood cancers" [5].

- Lymphomas develop in the glands or nodes of the lymphatic system, a network of vessels, nodes, and organs (specifically the spleen, tonsils, and thymus) that purify bodily fluids and produce infection-fighting white blood cells, or lymphocytes. These lymphomas are referred to as extranodal lymphomas. The lymphomas are subclassified into Hodgkin lymphoma and Non-Hodgkin lymphoma, which are distinguished by the presence or absence of Reed-Sternberg cells [5].
- Mixed types

Besides the major categories, numerous subcategories can be named. Some examples of those are germ cell tumors, neuroendocrine tumors and tumors originating from brain and spinal cord [6, 7].

Cancer statistics

While centuries have passed, the term “cancer” is still in use today. Due to the refined diagnostic methods in combination with a drastically increased expectancy of life, these cases of disease are on an all-time high. Worldwide, an estimated 19.3 million new cancer cases and almost 10.0 million disease-associated deaths occurred in 2020 [8]. Female breast cancer has surpassed lung cancer as the most commonly diagnosed malignancy, with an estimated 2.3 million new cases (11.7%), followed by lung (11.4%), colorectal (10.0%), prostate (7.3%), and stomach (5.6%) cancers [8]. Lung carcinoma remained the leading cause of cancer death, with an estimated 1.8 million deaths (18%), followed by colorectal (9.4%), liver (8.3%), stomach (7.7%), and female breast (6.9%) cancers [8]. For 2022, cancer incidence and mortality for women and men are shown in Figure 1.

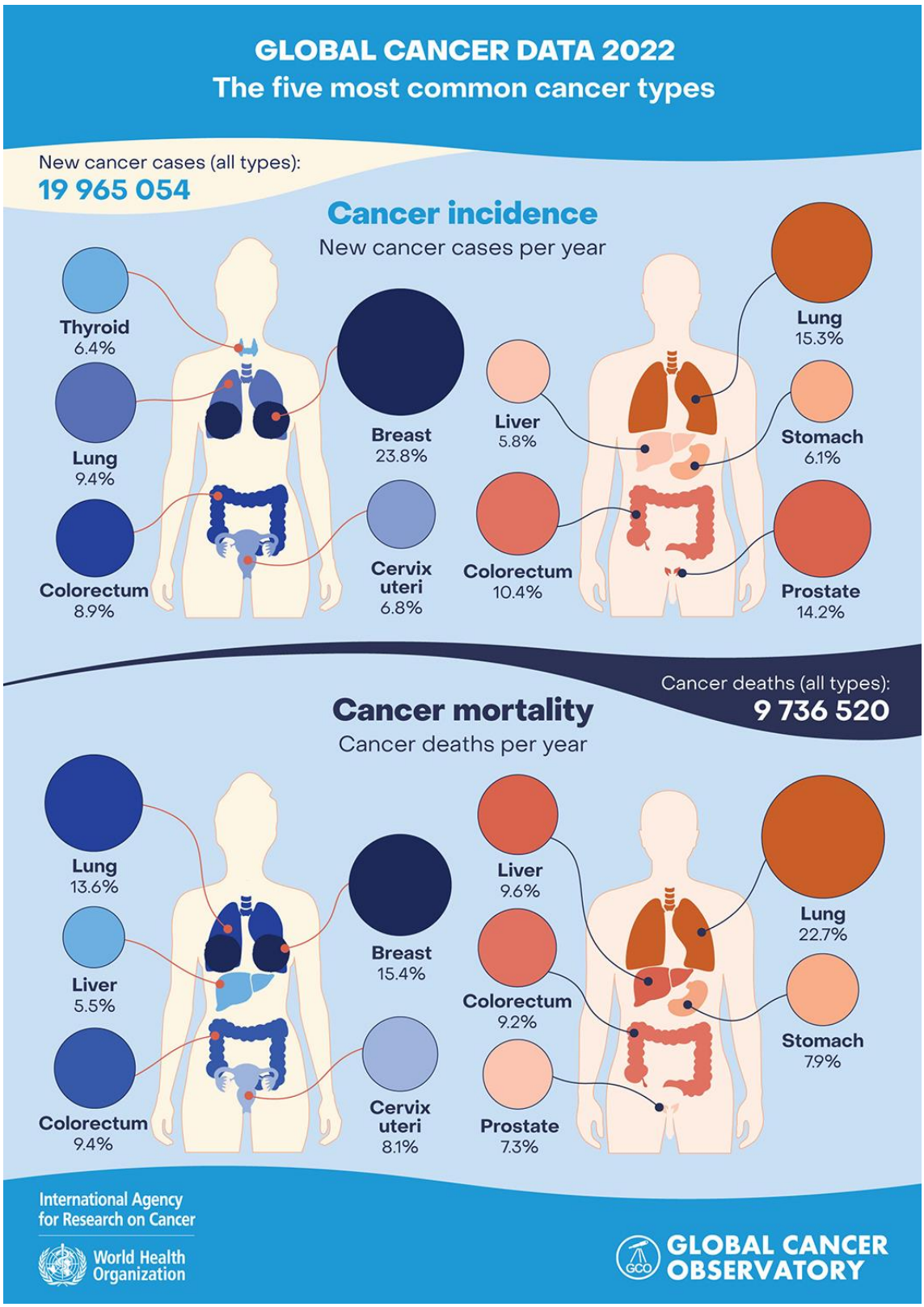

Figure 1: Global Cancer Data on the Incidence and Mortality of Cancer in the year 2022
Figure from https://gco.iarc.who.int/en;

The global cancer burden is expected to be 28.4 million cases in 2040, a 47% rise from 2020, with a larger increase in transitioning (64% to 95%) versus transitioned (32% to 56%) countries due to demographic changes [8]. This may be further exacerbated by increasing risk factors associated with globalization and a growing economy [8].

From healthy cells to cancerous growth

For healthy cells, their fate and actions are tightly controlled. This is not the case for cancer cells. The transition from the healthy but controlled state into cancerous chaos is called “carcinogenesis” and is considered as a multistep process. The concept is divided into four steps: tumor initiation, tumor promotion, malignant conversion, and tumor progression [9].

To initiate a tumor, mutations have to accumulate which is only possible, if they arise in cells that proliferate and survive for a longer time span. Notably, this initial event might be caused by a chemical carcinogen, a virus or even just an replication error [9]. Once cells have been altered by an initiating event, further promotion is necessary to result in a (benign) tumor. Hence, this step of tumor development is called “tumor promotion”. It is facilitated by compounds which promote the proliferation of the affected cells and give rise to a larger population of cells that are at risk of further genetic changes and malignant conversion [9]. If the cell population had not been affected by an initiating event before being in contact with the promotor, it will not result in tumor formation [10]. If a compound exhibits potential as both an initiator and a promoter, tumor development is possible without the application of another agent; such compounds are referred to as a ”'complete carcinogens” [11].

As time passes and contact with one or more promoting agents is repeated, further genetic changes accumulate (Figure 2). The more of these changes accumulate, the higher the probability is that a subset of cells will obtain a malignant phenotype, a process called “malignant conversion” [9]. Although the probability for malignant conversion is quite low, an increasing number of cells (for example: in a benign tumor) as well as exposure to DNA-damaging agents may increase it substantially [12]. From a causal perspective, this step may rely on the activation of protooncogenes and inactivation of tumor suppressor genes [9].

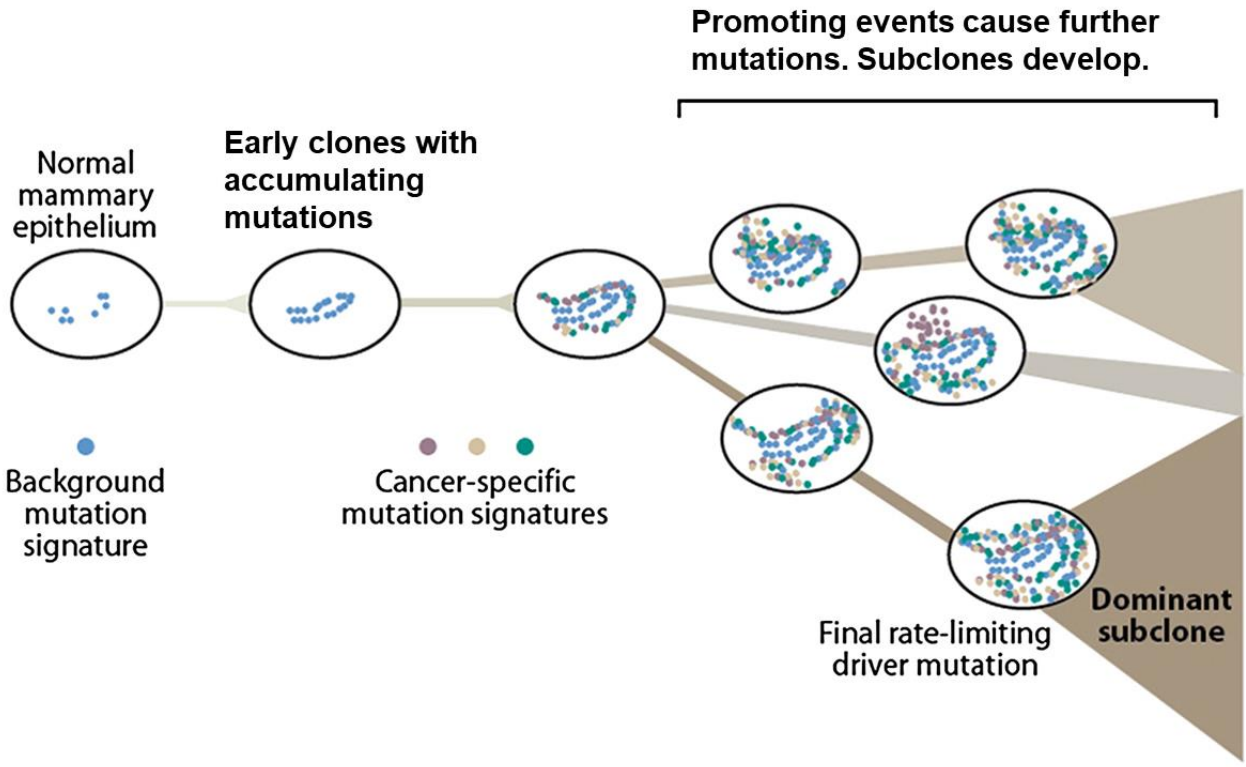

Figure 2: Cancer development regarding accumulation of genetic changes
Graphical abstract from [13], Labels modified, timeline removed, Licenced by https://creativecommons.org/licenses/by/3.0/

Finally, the process of malignant cells acquiring more aggressive traits over time is called “tumor progression” and associated with genomic instability and karyotypic aberrations [9, 10, 14]. The latter result in further genetic and epigenetic changes as well as phenotypically in an increased growth rate, invasiveness and biochemical alterations [14]. For these reasons, each tumor has a unique pattern of genetic changes that must be understood in terms of diagnostics and therapy.

Hallmarks of cancer

At the end of the 20th century, major innovations in research techniques have simultaneously increased two aspects of cancer research: the depth of the molecular mechanisms underlying cancerous growth and the complexity of the collected information. On the one hand, the identification of oncogenes and tumor suppressors supported the understanding of carcinogenesis and offered new approaches in cancer treatment. On the other hand, the number of identified oncogenes and tumor suppressors grew nearly exponentially, leaving researchers with increasing uncertainty about the relevance of their findings and the selection of research priorities [15].

In order to deal with this problem, new approaches were required that made it possible to classify the seemingly infinite amount of information. This new mindset was provided by Douglas Hanahan and Robert A. Weinberg in the groundbreaking review “The hallmarks of cancer”: “*We suggest that the vast catalog of cancer cell genotypes is a manifestation of six essential alterations in cell physiology that collectively dictate malignant growth […]: self-sufficiency in growth signals,*

insensitivity to growth-inhibitory (antigrowth) signals, evasion of programmed cell death (apoptosis), limitless replicative potential, sustained angiogenesis, and tissue invasion and metastasis [15]". Their suggestion was well received and adopted by researchers all around the world. Since then, the understanding of these traits which distinguish normal cell from cancerous ones has grown immensely. The original concept has since been expanded to include new and emerging hallmark capabilities, such as reprogramming of energy metabolism, evading immune destruction, unlocking phenotypic plasticity and senescent cells [16, 17]. Additionally, genome instability and mutation, tumor promoting inflammation, non-mutational epigenetic reprogramming and polymorphic microbiomes were identified as enabling characteristics (Figure 3) [16, 17].

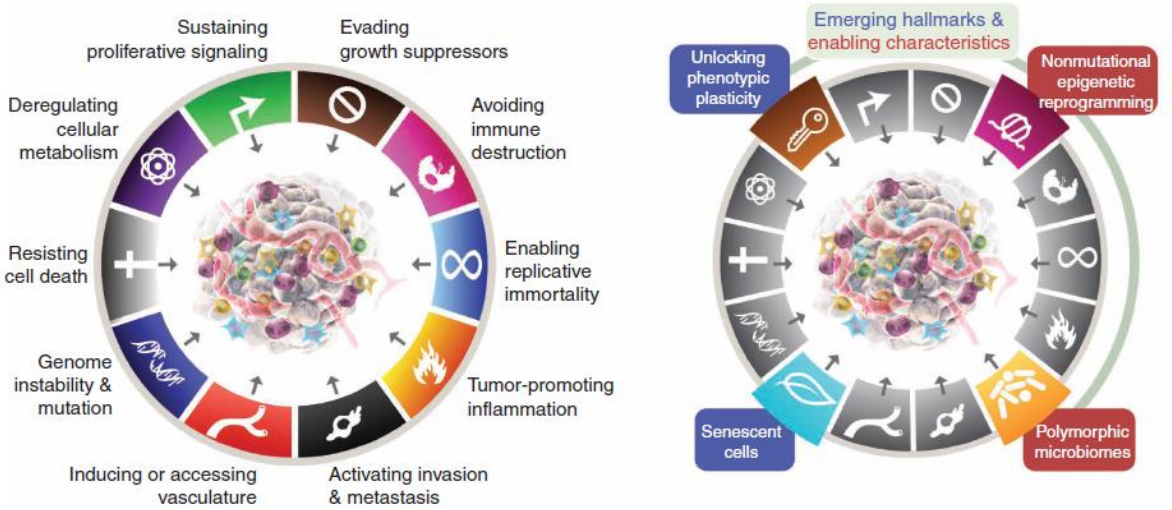

Figure 3: Hallmarks of cancer
Left, the Hallmarks of Cancer currently embody eight hallmark capabilities and two enabling characteristics. Right, additional proposed emerging hallmarks and enabling characteristics involving "unlocking phenotypic plasticity," "nonmutational epigenetic reprogramming," "polymorphic microbiomes," and "senescent cells" are incorporated. Reprinted from [15] ©2021 with permission from American Association for Cancer Research

In the following sections, several of the currently known hallmarks of cancer are presented in their basic features. Due to the importance for the research presented in the results, special attention will be given to evasion of programmed cell death and derangement of metabolism.

Unlimited growth and replication

Healthy cells should only replicate if this action is beneficial for tissue and organism. This behavior is often interpreted as "altruistic". Contrary to this rather romantic interpretation, compliance is ensured by multiple mechanisms and signaling circuits, which comprise growth and antigrowth signals (Figure 4). Therefore, incipient cancer cells must ensure self-sufficiency in growth signals and evasion of antiproliferative signals in order to thrive. During G1 phase, cells congregate information from major cellular signaling pathways to decide whether or not progression into S phase is feasible [18]. This integration results in an appropriate level of cyclin dependent kinases (CDK) activity in large part *via* changes in the levels of cyclins and cyclin dependent kinase inhibitors (CKIs). The changes in CKI levels are achieved through the regulation of both

transcription and protein stability [18]. Since several of those mitogenic signals are generated externally, they first need to be transmitted across the cell membrane to trigger proliferation. This is achieved by transmembrane receptors that bind distinctive classes of signaling molecules [15]. Prominent examples of such mitogens and their respective receptors are epidermal growth factor (EGF) and EGF receptor (EGFR), or fibroblast growth factor (FGF) and FGF receptor (FGFR). In addition, some growth factors may even interact with more than one receptor [19].

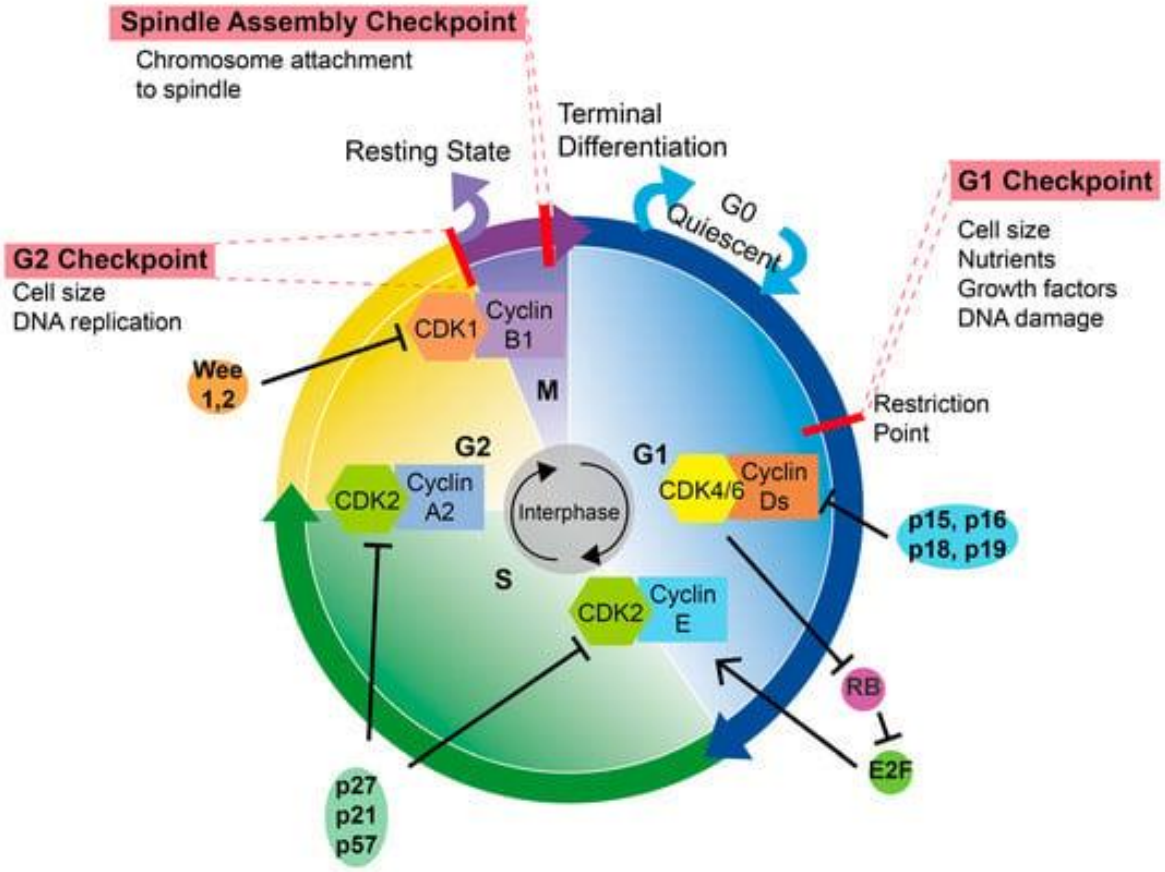

Figure 4: Outline of cell cycle control.
The cell cycle is positively controlled by cyclin-dependent kinases (CDKs) and cyclins' interactions and negatively controlled by cyclin-dependent protein kinase inhibitors (CKIs). S, DNA synthesis; M, mitosis; G1 and G2, index transition phase; G0, index quiescent status. Black lines end with arrow meaning promotion, black lines end with bar meaning inhibition, colorful arrows meaning cell cycle progression.
Figure 1 from [20], license under https://creativecommons.org/licenses/by/4.0/

There are three strategies how independence from external growth signals can be achieved in cancer: 1) by alteration of extracellular growth signals, 2) mutation/overexpression of transcellular signal transducers, or 3) deregulation of intracellular circuits that translate those signals into action [15]. In autocrine stimulation, cancer cells generate a signaling loop where the synthesized growth factors are used to stimulate growth in the same cells they originated from [21]. This strategy is often applied by glioblastoma and sarcoma cells which produce for example platelet-derived growth factor (PDGF) and tumor growth factor alpha (TGFα) [21]. Regarding transmembrane receptors, it is important to mention that in most cases their intracellular domain comprises a tyrosine kinase. Tyrosine kinase activation and binding to its substrate often involves dimerization

and cross phosphorylation in order to start the intracellular signaling cascade. In healthy cells, the proximity which enables dimerization is induced by ligand binding. In cancer cells, vast overexpression of certain receptors has been reported to either cause hyperactivation or even ligand-independent dimerization [21]. A prominent example for changed intracellular signaling mechanisms in cancer is the SOS-Ras-Raf-MAPK cascade, as activating Ras mutations have been identified in about 30% of human cancers [22].

While proliferative signals are sustained, amplified or generated by cancer cells, growth-inhibitors signal may put the expansion and further development of the tumor at risk. Like their counterpart, anti-proliferative signals often involve extracellular messengers [15]. Those may only affect the fate of cells if their signal is transduced to the inside of the cell by transmembrane receptors [15]. General strategies resulting in insensitivity are the opposite of those described before: alteration of the receptor to disable signal transduction and disruption of the downstream signaling cascade. Since the majority of antiproliferative signals are integrated in the Rb-pathway, alterations are observed frequently [23]. Within this pathway, impairment often affects the retinoblastoma protein (Rb) and the related proteins p107 and p130 [23, 24].

Remarkably, the combination of the acquired capabilities “growth signal autonomy” and “insensitivity to antigrowth signals” does not suffice to ensure expansive tumor growth. Behind this is an intrinsic, cell autonomous program that limits the number of divisions a cell may undergo [15]. This mechanism has been identified as telomeres which constitute the ends of the chromosomes and erode progressively with each cell cycle [25]. When eroded thoroughly, the telomeres no longer execute their original function to protect the chromosomes which yields karyotypic disarray and finally cell death [15, 25]. To avoid this, cells have to find a way to ensure that their telomeres are restored. Two mechanisms have been described in cancer: 1) upregulation of the telomerase enzyme which mechanism is the addition of nucleotides and 2) alternative lengthening of telomeres which includes interchromosomal exchanges based on recombination [26, 27].

Evasion of programmed cell death

While the unlimited proliferation and replication contributes significantly to the growth of cancerous tissue, the evasion of programmed cell death represents another crucial trait. In fact, the death of healthy cells is regulated to a similar extent as has already been described for their origination. Compliance is ensured by multiple mechanisms and signaling circuits which integrate various information from inside and outside the cell [28]. This includes damage sensors for DNA, such as the tumor suppressor protein p53, death signals from other cells such as Fas ligand (FasL) to activate the Fas receptor, and the loss of signals received from the extracellular matrix (Figure 5) [29, 30].

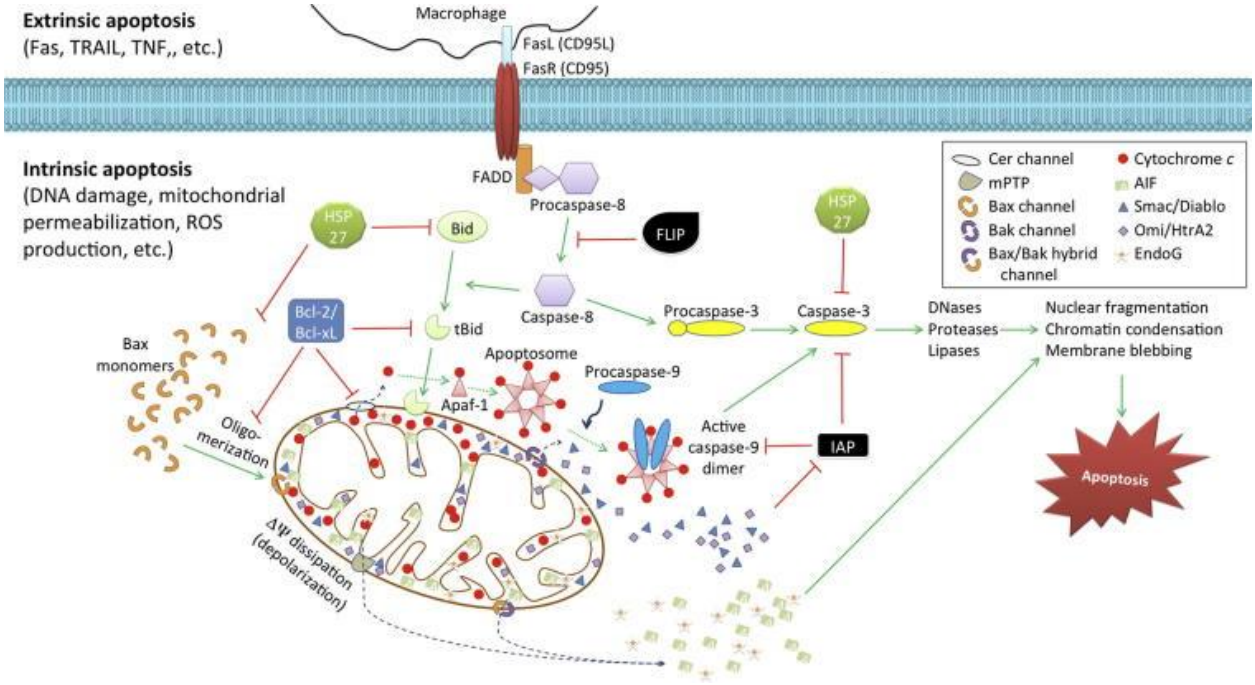

Figure 5: An overview of mechanisms of apoptosis.
Figure 3 from [31], licenced under https://creativecommons.org/licenses/by-nc-nd/4.0/

Once it is decided that a cell should die, it strives to execute its death to the greater good of the organism. Depending on the triggering events, the resulting form of programmed cell death may either yield the recycling of material or the generation of molecular patterns that attract further defense mechanism, mainly the immune system [28, 32]. The former is called “apoptosis” and was already described in the 1980ies as regulated breakdown of cells, here depicted in Figure 6 [33, 34]. The latter has been known as necrosis for a similar time span and was regarded as a non-regulated, passive and disheveled process for many decades [29, 32, 35]. In recent years, evidence has accumulated that non-apoptotic forms of cell death are also tightly controlled and have evolved to detect pathogens and promote tissue repair [28]. Accordingly, recent literature refers to these forms of cell death as “pyroptosis” and “necroptosis” [28, 32, 36].

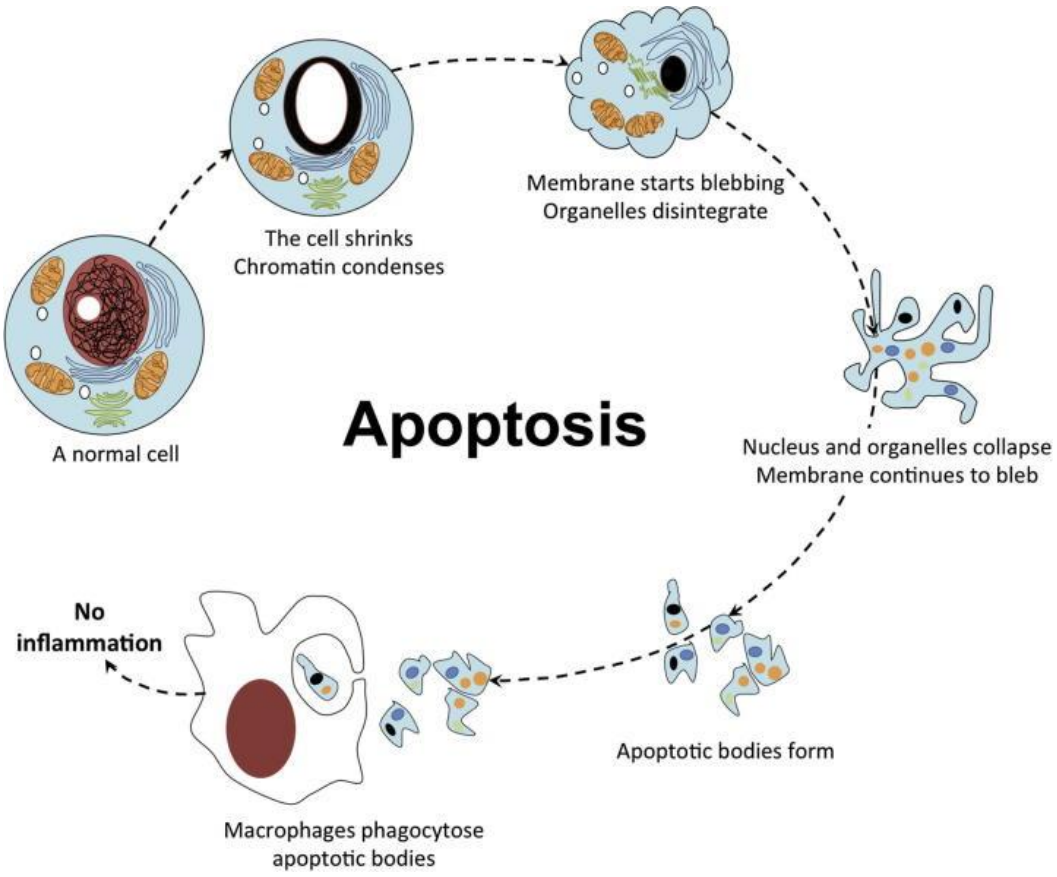

Figure 6: Illustration of the stages of apoptotic programmed cell death
The different stages of apoptotic cell death start by cellular shrinkage and chromatin condensation, concomitant with formation of membrane blebs. Organelles and nucleus fragment and the blebs begin formation of apoptotic bodies which are eventually engulfed by macrophages or neighbouring cells by endocytosis/phagocytosis. Figure 4 from [31], licenced under https://creativecommons.org/licenses/by-nc-nd/4.0/

In cancer cells several strategies to evade programmed cell death have been documented: 1) production of survival factors, 2) alteration of the transmembrane signal transducers or ligands to disable signal transduction, 3) loss of proapoptotic regulators, and 4) deregulation of intracellular circuits that translate cell death signals into action [15].

As an example for the first strategy, Insulin-like growth factor I receptor signaling plays a key role in the transformation process as a crucial antiapoptotic effector [37]. In more detail, IGF-2 signaling triggers the PI3-kinase-AKT pathway which results in antiapoptotic survival signals and mitigation of apoptosis [38].

Alteration of incoming death signals transmitted by ligands may occur by competitive binding. In this way, inhibition of FasL-induced apoptosis can be achieved by secretion of the soluble decoy receptor 3 (DcR3). [39]. When secreted, DcR3 captures FasL which may no longer interact with its transmembrane receptor Fas and the signal to undergo apoptosis is diminished or even extinguished.

The most prominent example for the loss of proapoptotic regulators is the already mentioned p53. More than 50% of human cancers display p53 mutations which result in functional inactivation of

the p53 protein [40]. This means not only the loss of a key component of the DNA damage recognition, but also that once inactivated, p53 is no longer able to induce apoptosis upon other initiators such as hypoxia and oncogene hyperexpression [41].

The last of the strategies comprises various individual adjustments in order to evade programmed cell death. One way or another, those adjustments deregulate the intracellular circuits that translate cell death signals into action. Often, this deregulation involves an overexpression of Bcl-2 or the related Bcl-XL protein which exert antiapoptotic functions [42, 43]. Together with other members of the Bcl-2 protein family like the proapoptotic Bax, these signals decide whether or not mitochondrial death signaling through the release of cytochrome C is triggered [44]. Finally, mitochondrial death signaling results in the activation of caspases to execute programmed cell death [44].

Derangement of metabolism

Due to the uncontrolled proliferation of cancer cells inside a tumor, sooner or later the demand of oxygen and nutrients will exceed the supply [45]. The same holds true for the removal of waste products. Cancerous tissue may limit this disproportion by sustained activation of angiogenesis. While angiogenesis in general represents a physiological response, its sustained or even constant activation is classified as a hallmark of cancer. This strategy alone is still not sufficient to cater to the developing tumors needs. Therefore, cancer cells make use of all mechanisms available in their genetic program to meet their needs for energy and building blocks for the composition of diverse macromolecules [46]. In mammalian cells, glucose and glutamine are two principal nutrients whose catabolism charges reservoirs of diverse intermediates which serve as the building blocks mentioned before [47]. Consistently, tumors excelling the glucose consumption of of non-proliferating normal tissues was first described nearly a century ago [48] and is since known as “Warburg effect”. This is of relevance, because the influx of glucose into healthy cells is considered to be driven by extracellular signaling rather than the immediate bioenergetic requirements of a cell [47]. For instance, despite the abundance of glucose in the culture medium, hematopoietic and neuronal cells cease to take up sufficient amounts of glucose when deprived of growth signals [49, 50].

Although abundance of soluble protein is present in plasma and interstitial fluid of tissues, it is usually not used as a source of amino acids by healthy cells. This again distinguishes the metabolism of cancerous cells from their untransformed counterparts, as some cancer cells resort to the engulfment and catabolism of extracellular macromolecules [51]. For example, the engulfment of extracellular macromolecules may be executed through the unselective uptake of extracellular fluid into giant vesicles which is called “macropinocytosis” [52]. Subsequent to the uptake, the vesicles will fuse with lysosomes in order to recover free amino acids through the proteolytic degradation [52]. Notably, this process is stimulated by actin cytoskeleton remodeling, which is increased in cells with mutant Ras and c-Src alleles [53]. In a similar way, KRASG12D-

transformed mouse embryonic fibroblasts (MEF) are able to proliferate in culture medium lacking the essential amino acid leucine but supplemented with physiological levels of serum albumin [54]. This effect is limited to certain signaling pathways. Even though PI3-kinase-AKT-signaling stimulates the uptake of low-molecular weight nutrients, it does not promote cellular utilization of extracellular protein [54].

While the uptake and digestion of macromolecules represents a crucial survival strategy in times of need, it is not sufficient to satisfy all cellular needs. Indeed, the majority of biomass is produced *via* intermediates of the tricarboxylic acid (TCA) cycle as depicted in Figure 7 [51]. Usually perceived as catabolic process, it also may facilitate the production of macromolecules by remodeling the available sources for carbon and energy into precursors and intermediates [51]. Simultaneously, it allows to produce citrate for production of fatty acids to renew cell membranes, to provide oxalacetate for the synthesis of aspartate and subsequently pyrimidine bases and asparagine as well as to support amino acid generation with the precursor *α*-ketoglutarate [55, 56].

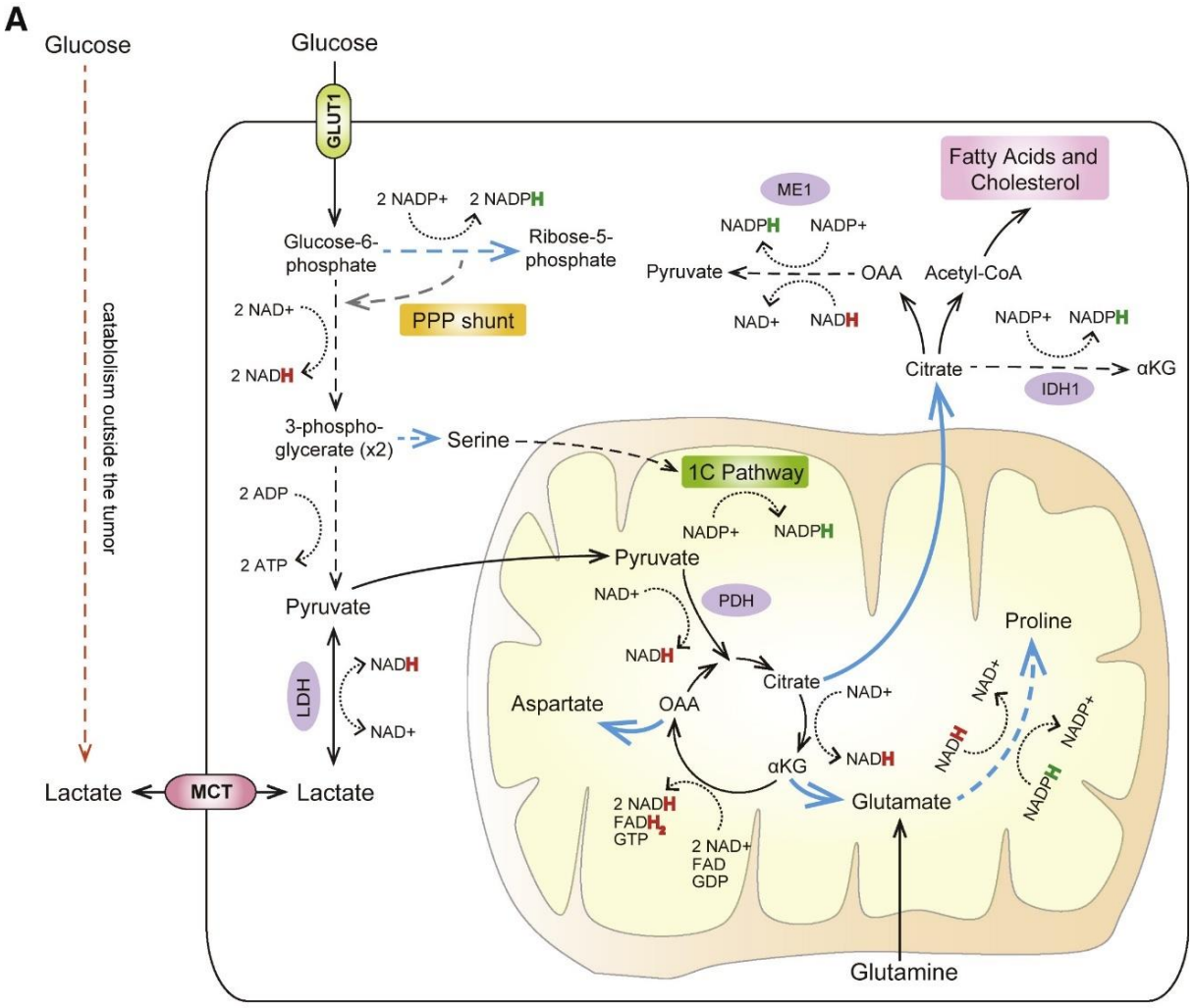

Figure 7: Use of central carbon metabolism
A) Multiple central carbon metabolism intermediates serve as structural building blocks and/or donors of reducing power to support the deregulated biomass production by transformed cells.
Reprinted from [51] ©2022 with permission from Elsevier Inc.

Furthermore, reduced nitrogen-containing nutrients may by depleted in cancerous tissue which some types of transformed cells have managed to overcome [51]. Since nitrogen is an essential component for the generation of proteins as well as nucleic acids, such a capability is crucial for proliferating cells. Scavenging of free ammonium from their environment was reported among the manifold strategies as well as remodeling their metabolism to prioritize the use of nitrogen donors for nucleotide and non-essential amino acid synthesis [51].

Anticancer therapy

Historical aspects of anticancer therapy

Attempts to cure cancer go back several thousand years (Figure 8). The Egyptians treated tumors and cancers with a variety of options of which two were cautery and knives, which can be regarded as an early form of surgical treatment [1]. Likewise, aggressive surgical removal of early stage tumors was recommended by Galen before 50 BC [1]. In addition, Galen warned that “even after excision, and when a well-healed scar is formed, breast carcinomas may recur with swelling in the armpit and cause death by spreading into the body” [1]. Thereby, he already vaguely described advanced metastatic disease. While Galen could only emphasize for early removal to prevent an unfortunate course, technological advances enabled modern surgeons to improve the outcome in patients. Modern time observations similar to Galen’s led to the development of sentinel lymph node biopsies as standard method for staging the axilla in early-stage breast cancer [57, 58]. Remarkably, also the aggressive surgical removal of early stage tumors survived the test of time and is still in use, albeit in a much more refined version and with steadily increasing technological support.

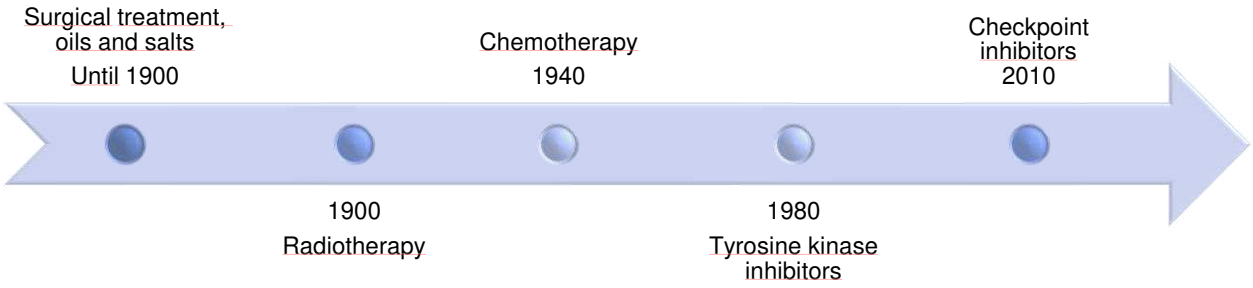

Figure 8: Overview of selected milestones in cancer therapy

Besides the treatment with early forms of surgery, the predecessors of modern chemotherapy can also be traced back to the Egyptians who used salts and introduced arsenic paste that remained in use as ‘‘Egyptian ointment’’ until the 19th century [1]. During the same era herbal treatments like tea, fruit juices, figs, and boiled cabbage were used by Sumerians, Chinese, Indians, Persians, and Hebrews [1]. But in advanced cases, they did not hesitate to resort to solutions and pastes of iron, copper, sulfur, and mercury [59]. Despite these early examples, the use of metals in cancer therapy was interrupted for several centuries. Meanwhile, Hippocrates as well as his successor Galen suggested that cancer was caused by an accumulation of “bad bile” and, therefore, prescribed simple and compound natural herbal remedies to purge it from the body [60]. It was not until in the Middle Ages, when first minerals and then metals were again added again to the “Materia Medica” [60]. Again, several hundred years passed until in the 1800’s chemical compounds were (re)introduced [60].

Unfortunately, the history of anticancer therapy as described above had been a story of very limited success for centuries. This was caused, at least partially, by the limited knowledge and insight about the underlying principles and the causes of the illness, which was sought to be cured. The crucial steps to our modern understanding of cancer where taken between 1940 and the early 1960's, when scientists discovered that the cellular information was transmitted by DNA not proteins, how DNA was structured and finally how the comprised information was coded [61]. These ground-breaking findings facilitated new, science-based explanations of the effectiveness of old and new agents in cancer treatment. They sparked the search for genetic markers to understand the development of cancer and to predict the effectiveness of a treatment.

Current standard in anticancer therapy

Nowadays, oncology is an extremely broad field comprising highly specialized sub-disciplines which are reminiscent of the modern classification of tumors described previously. There are many types of cancer treatment with the major types being surgery and radiation therapy for local diseases and systemic cancer therapy for systemic diseases. The size, type, location as well as the stage of the tumor will be assessed to identify appropriate treatment options including combinations thereof. For example, for head and neck, laryngeal, or uterine cancer radiation therapy is often combined with surgery while for sarcomas or breast, esophageal, lung, or rectal cancers the combination of chemotherapy and surgery has improved the results [5, 7].

Once the tumor reaches an advanced stage, where it has spread across the body and formed metastases, systemic therapy is the only suitable treatment. Since this form of therapy is also the most relevant for the results to be discussed in the respective section, it will be discussed in more detail here. As a first brief overview, systemic therapy can be subdivided into conventional cytotoxic therapy, hormonal therapy, immune therapy including monoclonal antibodies and tumor vaccines, therapy using differentiating drugs and therapy using targeted drugs. Each of these modalities features its own set of advantages and disadvantages. For instance, (oncogene)-targeted drugs like imatinib are able to selectively inhibit cancer cells with the BCR-Abl gene variant, which is a major advantage for patients with a corresponding tumor [62]. However, this specific mutation occurs only in chronic myelogenous leukemia (CML) which accounts for only a very small proportion of the total number of cancer cases worldwide [62]. In contrast to this, immune therapy may be applied in a variety of tumor types as it employs the patient's own immune system to attack and destroy cancerous cells. While evolving from healthy to malignant cells, the capability to evade destruction by the immune system is frequently acquired [16] which is sought to be reversed by this type of therapy using for example immune checkpoint inhibitors (ICIs) [63]. Targeted against specific regulatory immune receptors on the surface of immune cells like cytotoxic T-cells, ICIs abolish signals that attenuate the immune response towards tumor cells [63]. In recent years, the clinical management of tumor types with exceptional mutation rates and thus immunogenicity has turned around completely. Especially treatment option for melanoma,

lung and bladder cancer were revolutionised [64]. Despite this success, this type of treatment has often been declared “a double-edged sword” because of its capability to cause life-threatening side effects, mainly by overstimulation of the immune system [64]. Another strategy to employ the body’s resident defense resources are cancer vaccines. Like commonly known vaccines, these aim to “teach” the immune system to recognise the tumor cells *via* cancer-specific antigens. However, solid tumors present different hurdles than infectious diseases, which is why many questions still need to be answered before this strategy can gain a foothold in clinical routine [65]. AS an example for routinely applied treatments, hormonal therapy represents a suitable option for several variants of breast cancer and prostate cancer as their growth is often dependent on hormones. It has to be noted that this approach is rarely curative as it mostly limits the growth of the existing tumor thereby prolonging the life of the patient. This is different for the classical cytotoxic agents, also often called “chemotherapeutics”. This term comprises several groups of agents, the most important of which are alkylating agents, antimetabolites, inhibitors of topoisomerases, anthracyclines, tubulin poisons and metal containing agents. Their approach aims for or at least includes the chance of healing, although the therapy itself represents a balancing act: cytotoxic agents will affect both healthy and cancerous cells, although the latter are hit much harder. Therefore, these treatment options frequently have strong adverse effects which result in distinctly reduced quality of life for these patients.

Examples of chemotherapeutic agents including their potential and disadvantages

In the late 1970s, cisplatin was developed as antineoplastic agent to be used against a variety of malignancies (Figure 9). Today, it is used as a single-agent or in combination therapy for induction and neoadjuvant therapy against a broad spectrum of human tumors which include early-stage ovarian, non-small cell lung (typically diagnosed in smokers), head and neck, as well as advanced bladder cancer. [66, 67]. Its activity is attributed mainly to formation of DNA cross-links and adducts as well as, to a lesser amount, to the generation of superoxide radicals [66]. The treatment with cisplatin is often successful at first. However, this drug is a well-known example of the problems often caused by chemotherapeutics: adverse effects such as toxicities and resistance development. For cisplatin, the list of toxicities is long, comprising nephrotoxicity, gastrointestinal toxicity, myelosuppression, ototoxicity and neurotoxicity [66]. Although extensive research was performed to help reduce those effects, only very limited options are available such as saline diuresis to prevent nephrotoxicity. So far, protection against all these toxicities could not be provided by a single agent [66].

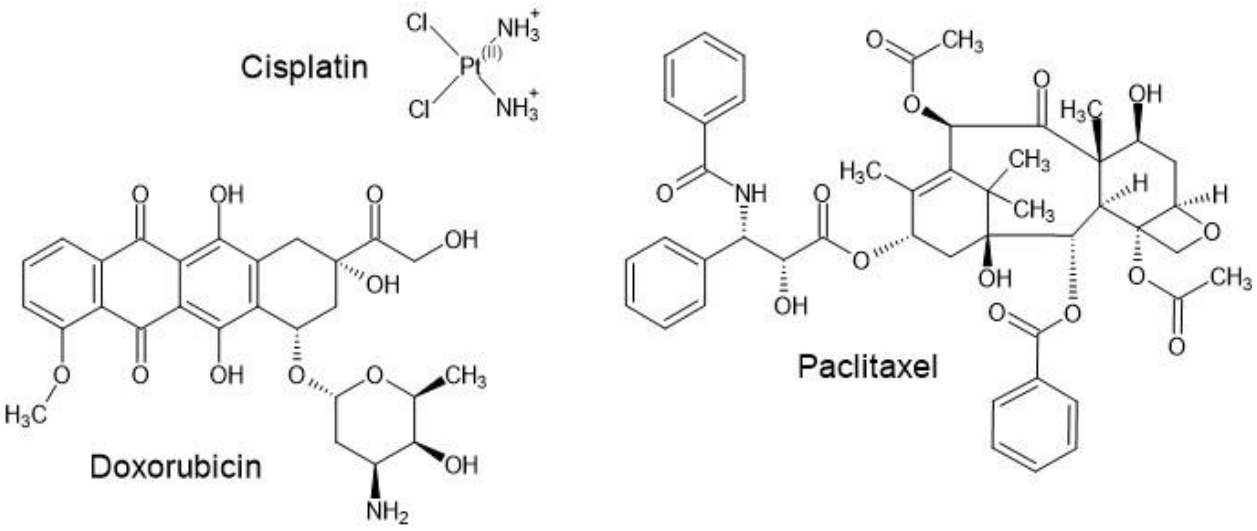

Figure 9: Examples of active compounds in chemotherapy Cisplatin, Doxorubicin and Paclitaxel

Anthracyclines have been the key components of many cytotoxic regimens since their introduction in the 1960's [68]. The most prominent examples are doxorubicin (Figure 9) and daunorubicin. Despite the long-lasting success, the precise mechanism of doxorubicins anticancer activity is not fully understood. So far, investigations have reported contribution to DNA damage and the production of reactive oxygen species (ROS) production [69]. Further documentation also comprises the induction of programmed cell death as well as involvement in immunomodulation [69]. Moving forward to the 21st century, beneficial results regarding long-term survival (e.g. greater than 70% for breast cancer in Europe [70]) are the reason, these agents are still used for the treatment of e.g. breast cancer, sarcoma, or lymphoma [68]. However, this class of agents frequently has cardiotoxic effects, which can cause increased morbidity and mortality among patients [71]. Despite extensive research, only very few methods are available to minimize the impact of anthracycline cardiotoxicity. The best-known example is Doxil®, a formulation where doxorubicin is packaged into pegylated-liposomes, which was able to minimize cardiotoxicity. However, this formulation has high affinity for the skin and a very long circulation time. Consequently, a major adverse effect is dose-limiting hand-foot-syndrome, which has the formal name “palmar-plantar erythrodysesthesia” [72].

Paclitaxel, which is better known as Taxol®, was the first member of the taxane family to be used in cancer chemotherapy (Figure 9). Contrary to cisplatin and doxorubicin, its cytotoxic effect does not interfere with the DNA but stabilizes the microtubule during mitosis, thereby causing a cell cycle arrest that results in apoptosis [73]. In addition, angiogenesis is inhibited by paclitaxel already at low concentrations [74]. As a chemotherapeutic agent paclitaxel is used to treat a variety of solid tumors such as ovarian, breast and non-small cell lung cancers as well as malignant brain tumors [73]. Unfortunately, significant toxicities, such as peripheral neuropathy, limit the effectiveness of paclitaxel-based treatment regimens. Since this adverse effect had already been reported together with dose-limiting neutropenia, hypersensitivity reactions, and cardiac arrhythmias during clinical development [75], this limitation did not come as a surprise.

However, Paclitaxel is still successfully used as treatment option for cancer patients whose tumor relapsed after initially responding to cisplatin or doxorubicin [76]. In order to improve its tolerability, the albumin-based nanoformulation Abraxane® has been developed [77], which is described in more detail below.

Reduction of toxicity and increased tumor targeting by usage of nanocarrier systems

Adverse effects represent a major limitation regarding treatment options and the resulting quality of life for the person affected by disseminated cancer. For the same reason, clinical trials of novel drug candidates also face premature discontinuation [78, 79]. Therefore, enormous efforts to understand the underlying processes lead to the description of two kinds of effect: 1) While the term “on-target effect” refers to exaggerated and adverse pharmacologic effects at the target of interest, 2) “off-target effect” refers to adverse effects as a result of modulation of other targets [80]. Although the specific mode of action is different for those kinds of effects, in theory, both could be omitted, if the therapeutic agent could be designed to exclusively target the tumor tissue. This goal seems almost unattainable even more so for systemic therapy of advanced cancers, which should reach even distant metastasis. Yet, the ADME-scheme as a basic principle of pharmacologic toxicology has been applied to achieve remarkable advancements [81]. The acronym ADME stands for absorption, distribution, metabolism and excretion which can be viewed in a general way as entering the body (A), moving about the body (D), changing within the body (M) and leaving the body (E) (Figure 10, in more detail) [81].

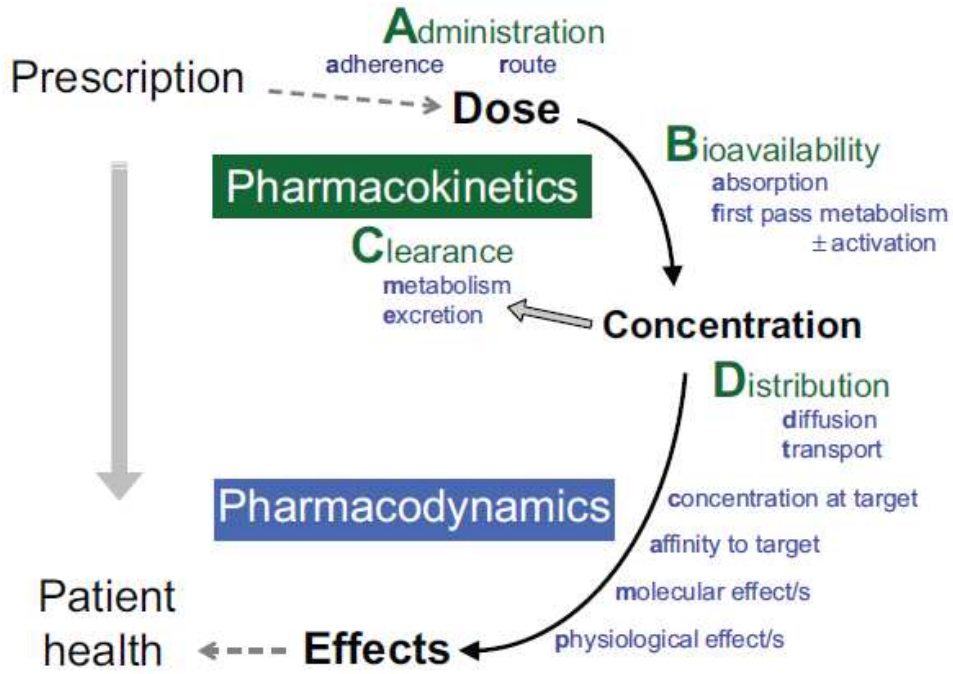

Figure 10: From Prescription to Patient Health
A multitude of factors may affect the outcome of a treatment. This involved general aspects like administered dose and administration route, but also individual factors which may not be influenced (for example: metabolism, excretion)
Figure 1 from [81] © Authors Doogue and Polasek, 2012

Since distribution over the whole body is a prerequisite for success of systemic cancer therapies, altering the distribution of the compound inside the body is important. On one hand, it is a delicate task yet not impossible as local accumulation might be increased. On the other hand, the change of the compound within the body allows the active substance to be absorbed and distributed while reversibly being inactivated by chemical alteration or packaging. This inactive derivative is referred to as “prodrug” [82].

Among the various packaging techniques used to create a prodrug, nanomaterials represent an opportunity to achieve sophisticated targeting while ensuring usability of a wide range of functions [83]. The power of this approach has convincingly been demonstrated by the success of Doxil® and Abraxane®. In general, nanoparticles are not only designed to control the release (site) of the active substance but also to prolong the plasma half-life of a (pro-) drug and specifically enhance accumulation in the tissue of interest [84].

Depending on the chosen strategy, targeting of the tumor may be *via* covalently binding to ligand on the nanoparticle surface which will interact with its counterpart on the surface of the target cell (active targeting) or accumulation in the malignant tissue by the enhanced permeability and retention (EPR) effect (passive targeting) [85]. The latter is based on a specific characteristic of the solid tissue, where the architecture of the vasculature is defective which increases its permeability for macromolecular drugs [86]. Additionally, lymphatic drainage of tumor tissues is impaired. As a consequence, macromolecules are deposited in the tumor interstitium and retained for days to weeks [87].

To exploit this effect for the treatment of patients, nano-sized drug carriers can be used with an ideal size between 10–100 nm - although the upper limit is not well defined [88]. Recently, advances in bio-pharmacology were achieved due to the evolution of adjacent disciplines such as the biology of diseases, the physico-chemistry of colloids and the assembling of materials at the nanoscale [89].

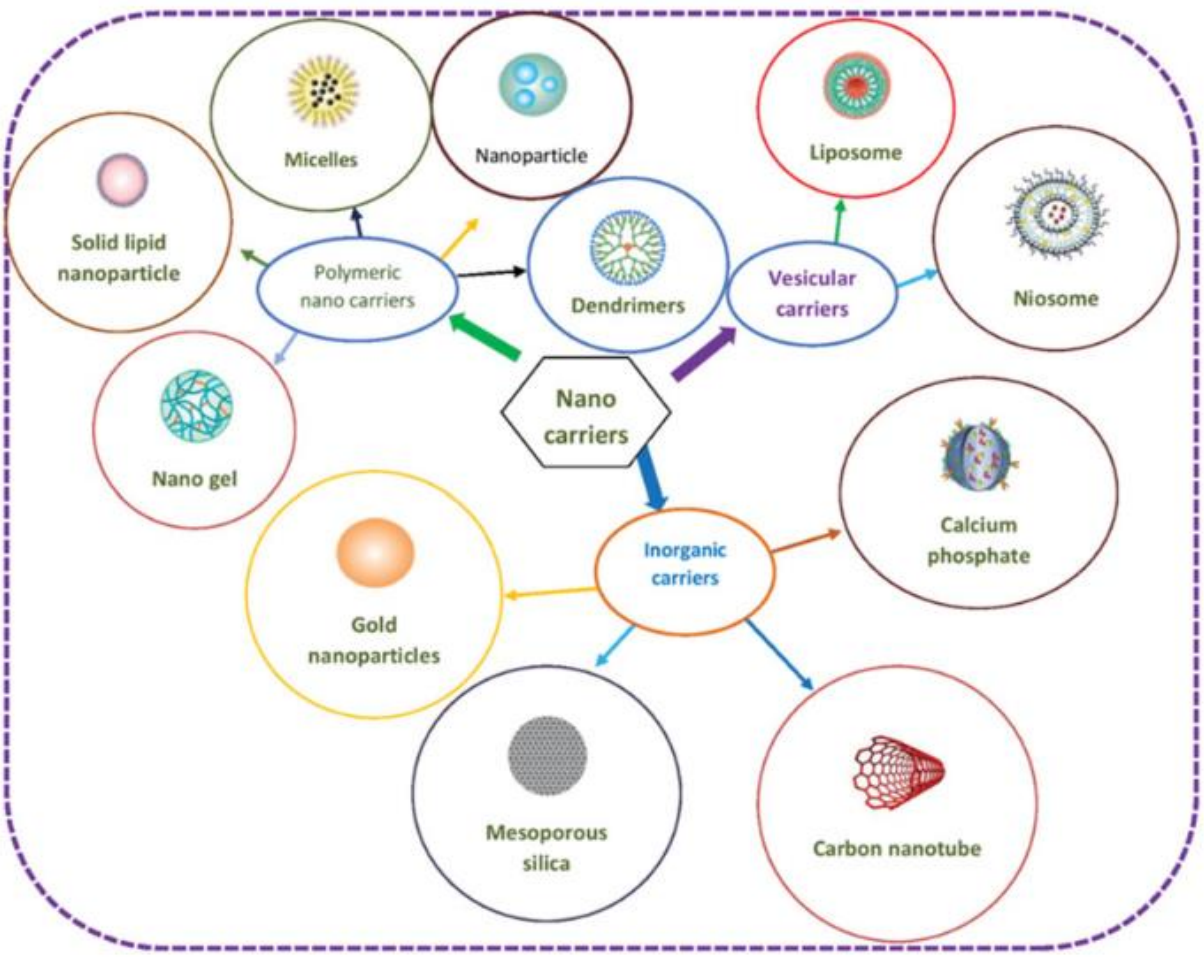

Figure 11: Classification of most commonly used nanocarriers for drug delivery.
Figure 1 from [90], Licensed under https://creativecommons.org/licenses/by/4.0/

Those nanocarriers are usually based on organic, inorganic, lipid, or glycan structures as well as on synthetic polymers (Figure 11) and have already been utilized for the development and improvement of diverse cancer therapeutics [83]. Since polymers and the natural carrier protein albumin are the most relevant for the results of this thesis, those will be discussed in more detail in the following chapter.

Polymers

In 2003, the term “polymer therapeutics” was coined by Ruth Duncan to encompass several designs of water-soluble polymers: polymeric drugs, polymer-drug conjugates, polymer-protein conjugates as well as polymeric micelles and multi-component polyplexes [91]. Of these, the polymer-drug conjugates, which have been described by H. Ringsdorf in a ground-breaking publication in 1975 [92], are of specific interest for this thesis. A polymer backbone serves as anchoring structure for the solubilizer (ensures solubility in water), a targeting moiety (allows active targeting of receptors etc.) and the cleavable linker which binds the actual drug (Figure 12).

Nowadays, the chemical engineering of polymers offers various options to improve drug loading and release rate through the control of hydrophilicity/lipophilicity, pharmacokinetics, etc. In addition, modification of the parts of the polymer which build the surface with ligands enables recognition of cell-specific receptors [93]. Thereby, cellular specificity and superior intracellular delivery may be achieved [93]. These features led to the characterization of polymers as interesting systems to deliver drugs with specifically adjusted pharmacokinetics, biocompatibility, and biodegradability [94].

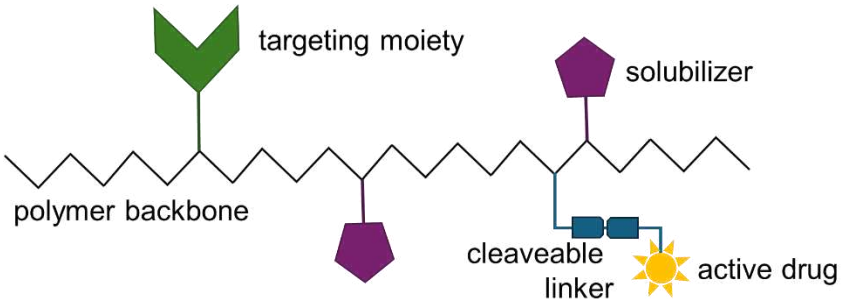

Figure 12: Schematic representation of a polymeric drug delivery system described by H. Ringsdorf

Generally, polymers used in therapy of patients have to meet some requirements, such as being non-toxic and non-immunogenic [95]. The molecular weight of such conjugates should be high enough to ensure long circulation, but the optimum is different for non-biodegradable (< 40 kDa, allows renal clearance) and biodegradable polymeric carriers (30 - 100 kDa, mostly above renal clearance threshold) [95]. Besides the criterium of the weight, the particle surface needs to be considered because the characteristics thereof – especially the charge – influences the mobility of the polymer [96]. When comparing the mobility of particles in an hydrogel mimicking the extracellular matrix, highly charged particles were observed to migrate significantly less than uncharged particles of the same size [96]. Notably, this effect was observed similarly for negatively and positively charged particles. In order to avoid inefficient delivery of drug-loaded particles due to decreased mobility, their surface charge may be shielded by addition of surfactant, such as polyethylene glycol (PEG) [96]. This concept was successfully applied in a unique formulation of doxorubicin: Doxil®, doxorubicin-containing liposomes which are covered with a PEG layer [72]. Consequently, the plasma half-life of the liposomes more than doubles and allows the drug to remain encapsulated until it reaches the tumor site [72].

Albumin as a natural carrier

In drug delivery for systemic treatment, human serum albumin is of utmost importance. Acounting for 60% of total plasma protein content, it serves a multitude of functions. Besides being responsible for colloid osmotic blood pressure, human serum albumin acts as an extremely versatile carrier that may solubilize and transport fatty acids, metabolic products, metal ions and even diverse drugs (Figure 13) [97, 98]. This is achieved mostly by non-covalent interactions such as hydrophobic, electrostatic, Van der Waals forces as well as hydrogen bonding [99]. Moreover, its interactions with specific receptors (e.g. the neonatal Fc receptor) which shields it from degradation in lysosomes, resulting in an unusual plasma half-life of 19 days [99, 100].

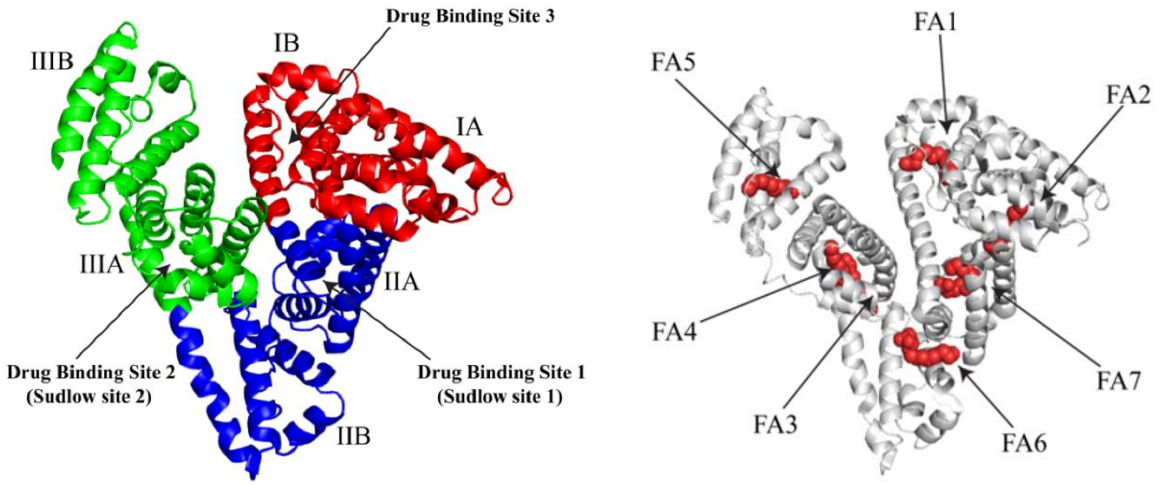

Figure 13: human serum albumin binding sites for drugs (left) and fatty acids (right) (Figures 1 and 3 from [97]) Licensed under https://creativecommons.org/licenses/by/4.0/

Besides accumulation of albumin in the solid tumor due to the defective blood vessel system in the malignant tissue causing the EPR effect, there is increasing evidence that cancer cells have a very high albumin uptake to cover their enhanced need for nutrients and amino acids [51, 52]. These different nutrient acquisition strategies from healthy tissues makes albumin a promising tool for the specific delivery of anticancer drugs to the cancer cell. Consequently, albumin is an appealing carrier in nanomedicine. Moreover, its natural origin, high biocompatibility, biodegradability and non-immunogenicity are immanent features that also ensure safety for its clinical application [100]. Recently, drug delivery systems have utilized albumin in various ways, including albumin fusion proteins, prodrugs and serum albumin nanoparticles (Figure 14). Several of them are in advanced clinical trials or approved for therapy [101]. The most prominent example of these is Abraxane®, a formulation of paclitaxel packed into three-dimensional, water-soluble albumin-based nanoparticles (Figure 14, right) [100]. These nanoparticles exhibit a size of approximately 130 nm and encapsulate paclitaxel through non-covalent interaction of its hydrophobic regions with hydrophobic pockets in human serum albumin without using solvents or surfactants [99, 100]. In clinical studies, higher response rates in combination with decreased adverse effects were observed. Similarly, in vivo experiments with tumor-bearing mice the albumin-based formulation achieved significantly higher intratumoral paclitaxel concentration [100]. Abraxane is currently approved for multiple tumor types including advanced metastatic breast cancer, metastatic pancreatic carcinoma as well as advanced non-small-cell lung carcinoma.

In addition to Abraxane®, in 2021 Fyarro® (sirolimus-releasing albumin particles using the Abraxane technology) has been approved for treatment of perivascular epithelioid cell tumors [102].

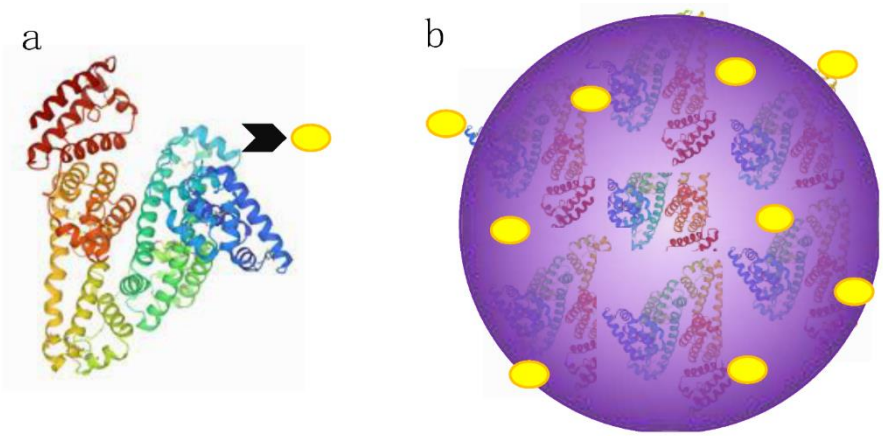

*Figure 14: Simplified preparation methods of two different approaches to albumin-based drug delivery systems: (**a**) drug-conjugated albumin and (**b**) drug-containing NPs (Figure 2 from [101])*

Another prominent example is Aldoxorubicin®. In this formulation, a small-molecular derivative of doxorubicin was designed in a prodrug concept. In more detail, a cleavable linker (an acid-sensitive hydrazine moiety) containing a albumin-targeting moiety (6-maleimidocaproic acid hydrazide) was attached to doxorubicin [103]. Once applied into the bloodstream, the maleimide moiety immediately forms a covalent bond with serum albumin forming a natural nanoformulation. Subsequently, the now albumin-bound doxorubicin accumulates in the tumor due to the EPR-effect. In the acidic environment at the tumor site, the linker moiety is cleaved releasing the active doxorubicin in a highly tumor-specific manner [104]. Aldoxorubicin has been tested in a clinical phase III trial against soft-tissue sarcoma [105]. Besides Aldoxorubicin, also some platinum prodrugs (KP2156, Albuplatin, BTP114) using maleimide for albumin-targeting have been developed during the last years [106, 107]. An overview on the clinical development status of diverse albumin-targeted drugs is given in Figure 15.

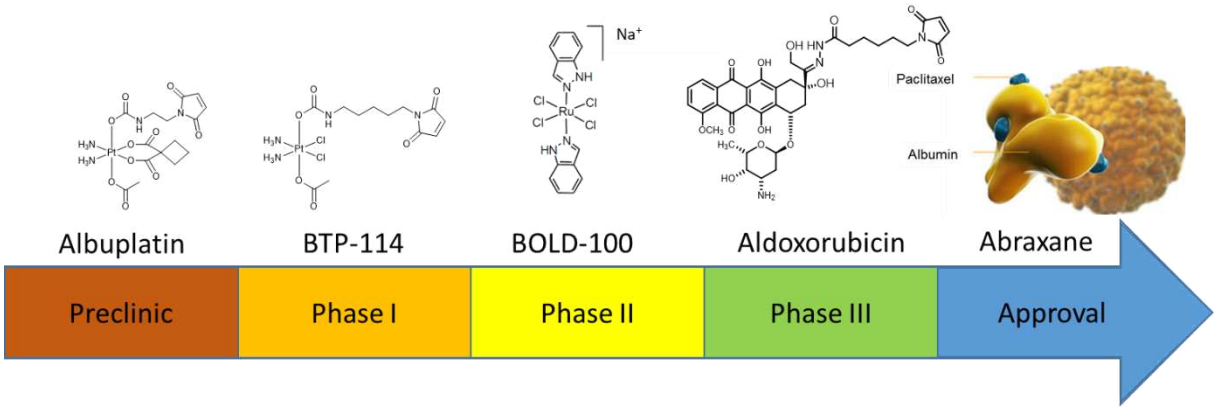

Figure 15: Overview on the (pre)clinically developed albumin-targeted anticancer drugs

Although serum albumin is the most abundant transport protein, several other blood components such as lipoproteins and immunoglobulins are able to bind substances including proteins, nutrients and active compounds. For this reason, the role of plasma proteins concerning the pharmacological profile of a drug has already been discussed controversially over several years

[100, 101, 108]. Originally, only the unbound drug was regarded as the therapeutically active fraction. As a consequence, the interaction of the active compound with plasma proteins is regularly assessed, often in vitro as a cell-free assay [108]. Since this setup differs a lot from the dynamics and kinetics of a dynamic system like a body, the results of the protein-binding capacity of a drug measured with this method often do not correlate with other pharmacokinetic parameters such as plasma half-life or clearance [108]. Although the compound may remain inactive while bound to proteins, this interaction still exerts a beneficial effect on the compounds overall clinical performance: it protects the drug from renal clearance and metabolism [100].

Coordination complexes as anticancer agents

In the previous parts of this introduction, the principles, challenges and approaches of anticancer therapy were described. The aim was to provide a comprehensive picture of the multiple and interconnected aspects to be considered for the development and application of substances to be used as remedies against cancer. In this part, a specific subgroup of agents used in systemic therapy will be the center of attention: coordination complexes. The common denominator of this class of agents is the central metal atom surrounded by non-metal atoms that may or may not be connected to larger structures like molecules or proteins [109]. The surrounding atoms or structures are chemically bound to the central metal ion and are called ligands. Several examples of coordination complexes are essential for biological processes, such as chlorophyll, hemoglobin and vitamin B12 (Figure 16) [109].

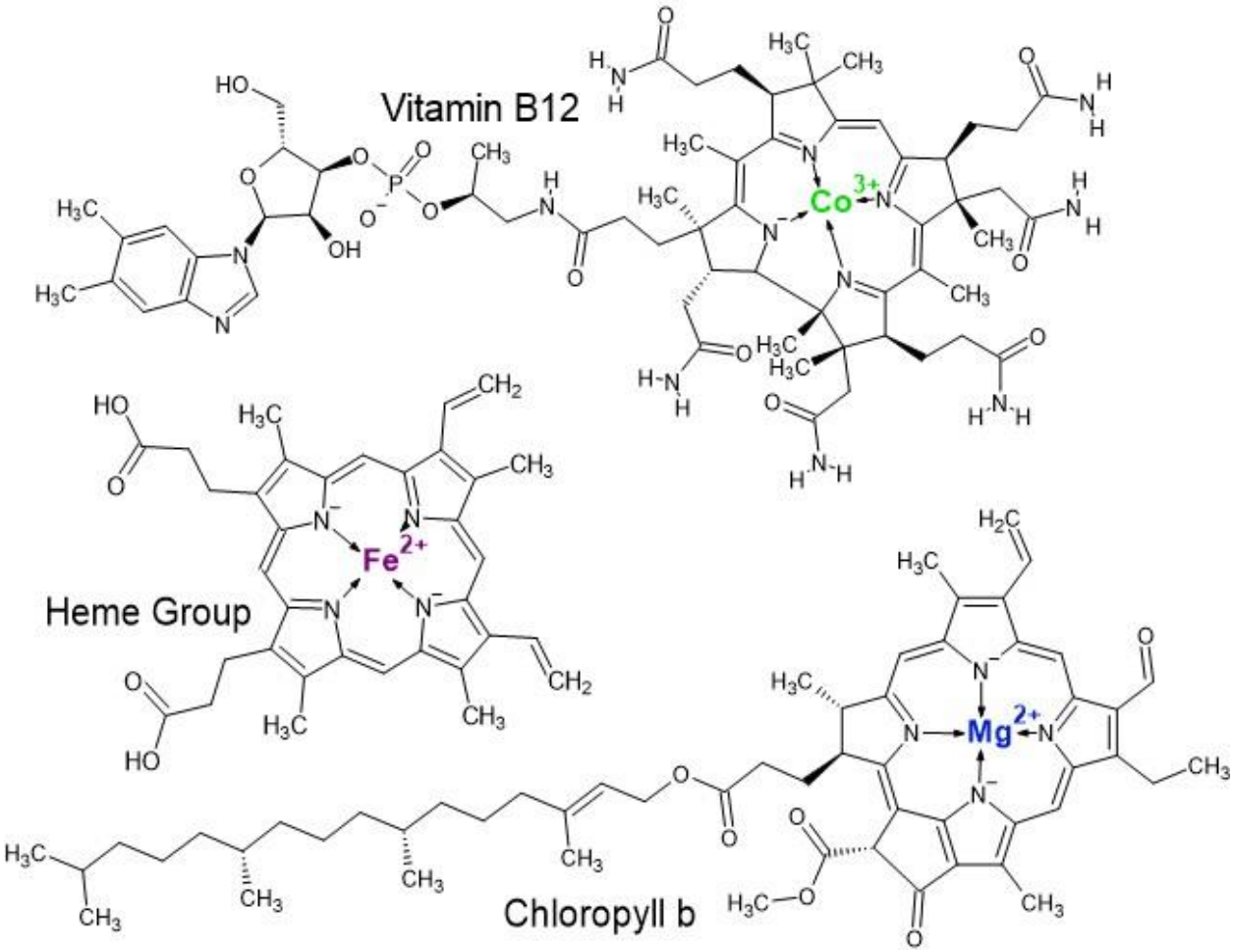

Figure 16: Naturally occurring coordination complexes relevant for biological processes

Within a coordination complex, the central atom as well as the ligands contribute to the characteristics and capacity of the whole structure. Being the component that mainly interacts with the surrounding area, ligands are decisive for the overall solubility, stability and the ability to interact with biological targets [110]. The chemical and physical properties of the central metal ion will strongly influence or even enable the underlying biological modes of action [110]. Coordination

complexes often constitute the active center embedded in biomacromolecules such as heme groups within hemoglobin. In biology, biochemistry and medicinal chemistry, a wide spectrum of functions has been described which includes but is not limited to acid-base/redox catalysis, structural functions, signaling and electron transport [111]. This versatility in combination with the potential of modern bio-inorganic chemistry has drawn the attention of researchers and physicians alike in order to address the challenges of cancer therapy.

Choosing the weapon

When treating late stage cancer and ensuring an adequate quality of life for the patient, it is important to consider the multiple significant changes cancerous cells have accumulated during their transformation. These multiple changes, which often makes treatment challenging, are frequently seen in cancer cells at the advanced stage of the disease. With this regard, metal drugs offer a broad spectrum of modes of action that scientists may utilize, advance, improve and combine. At first, it should be distinguished which role the metal fulfills in the compound as several distinctly different ones have been reported. These roles include functional, structural, transportational, catalytical and photo-sensitizing functions (Figure 17) [112, 113].

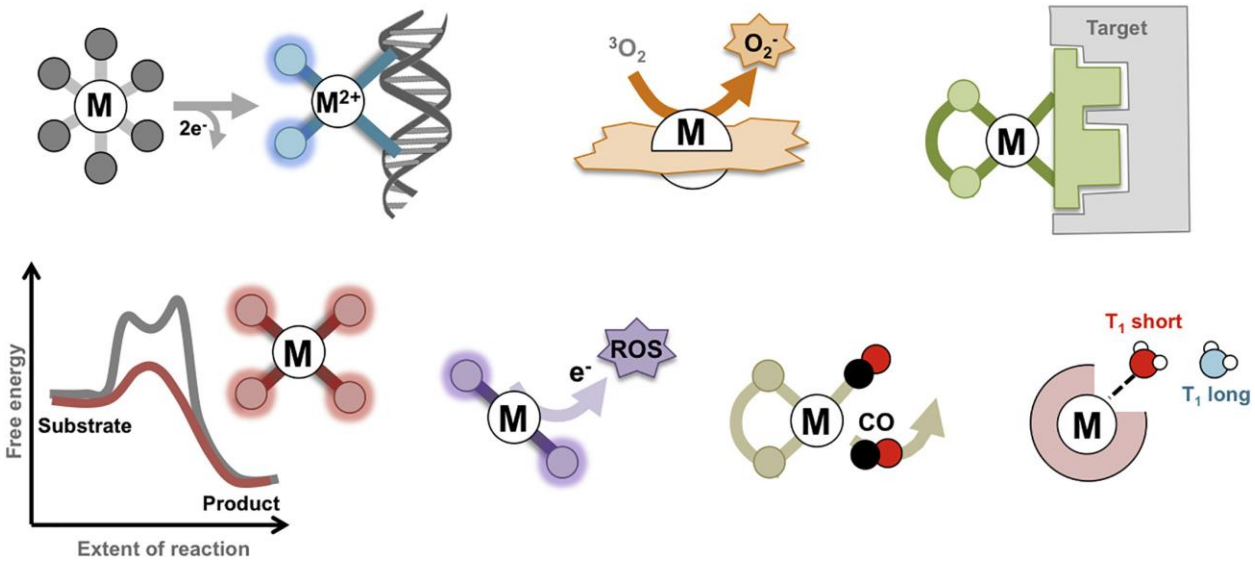

Figure 17: Summary of the Mechanism of Action of Metal-Based Drugs
The depicted Mechanisms in the upper row are (left to right): functional (metal adducts of DNA, generation of reactive oxygen species as part of an enzyme) and structural. In the lower row, the mechanisms depicted are catalytical, photosensitizing and transportational.
Reprinted from [113], © 2019 with permission of Elsevier Inc.

Structural as well as transportational functions imply that although the action of the metal is crucial for the overall impact of the drug, it is not the final active component. Instead and dependent on the actual design, it will be the vehicle delivering a bioactive molecule to the target cell/ tissue, where it is released [113]. As structural components, the metal ion provides the basic framework for the construction of three-dimensional structural mimics for selective enzyme inhibition by blocking its substrate-binding site(s) [114]. When executing a catalytical or photo-sensitizing function, the metal center of the compound is actively involved in the actual effect on the target.

Since the compound is not consumed in the process, even very small amounts of the compound may exert a crucial effect. Examples of this strategy are the production of reactive oxygen species or the mimicking of relevant enzymes such as SOD [113]. The most complex role concerns the metal as a functional unit of the active compound and thus may be further subdivided into redox-active and covalent-binding drugs [113]. While the former refers to the activation of a prodrug by either oxidation or reduction caused by the characteristics of the target environment, the latter comprises metal ions covalently bound to essential biomolecules, e.g., DNA, proteins, enzymes, etc. Thereby, their function is inhibited ultimately causing cell death [113]. A prominent example for this mode of action is cisplatin, which once inside a cell forms activated platinum(II) species that bind to nuclear DNA producing mainly intra-strand crosslinks. In addition, direct interaction of proteins with cisplatin, auranofin as well as several metal compounds with a ruthenium core have been documented [112, 113, 115]. Remarkably, there are even effects of metal drugs which have not yet been fully understood. Possibly the most important of these is the interplay with a patient's immune system [116]. Long-lasting anticancer immune responses were reported upon metal drug treatment, suggesting altered visibility and susceptibility of cancer cells toward innate and adaptive immunity [117]. This might offer innovative treatment schemes for future generations of patients, especially if the combination with other classes of therapeutics such as immune checkpoint inhibitors [116].

As of today, cisplatin is the most prominent example of a coordination complex successfully used in anticancer therapy [118, 119]. Following its application in clinics and first drawbacks regarding adverse effects and resistance development, research aimed to improve the situation by substitution of the ligands, still holding onto platinum(II) as a center [119, 120]. Therefore, these second-generation platinum drugs are mostly considered cisplatin derivatives. Examples from this era of research are carboplatin, oxaliplatin and nedaplatin (Figure 18) [120].

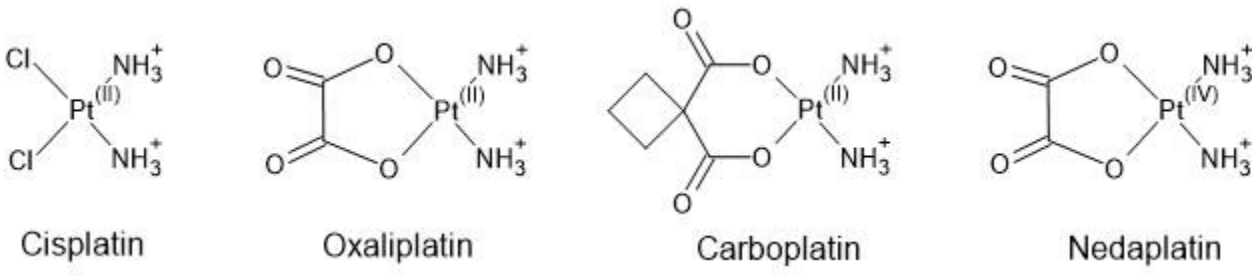

Figure 18: Cisplatin and its derivatives oxaliplatin, carboplatin and nedaplatin

Both carbo- and oxaliplatin exhibited more favorable toxicity profiles compared to their predecessor, which enabled higher doses to be applied for treatment. This was important, when directly compared to the efficacy of cisplatin, because their therapeutic results were slightly inferior [120]. The same general characteristics apply to nedaplatin, the most recently developed cisplatin derivative already mentioned. However, in contrast to carbo- and oxaliplatin, nedaplatin

did not receive international approval but was approved regionally in Japan, Korea, and China [110].

Despite the improvements the cisplatin derivatives achieved, it became evident that this approach would not suffice to meet the complex challenges of successful cancer treatment. Therefore, several transition metals were examined for their potential as therapeutic coordination compounds because of their distinct physicochemical characteristics [121]. Within this group, special focus was laid on metals, which on the one hand would offer variable valency caused by their ability to easily accept electrons from donors and on the other hand would not be toxic on their own [121]. In particular, ruthenium(III), iridium(III), palladium(II), gold(I), titanium(II), copper(II), and iron(II) emerged as promising candidates, which as expected and aimed for result in completely different modes of action and antiproliferative activity [119].

Notably, half of those candidates belong to the platinum metal group (ruthenium, palladium, platinum, osmium, iridium, rhodium) [122]. Within the platinum metal group, ruthenium occupies a special position, as it also shares chemical similarity with iron. This was considered especially important, since it allows redox reactions and was thought to be exploited like a trojan horse, where cancer cells would accumulate ruthenium compounds mistaking them for an iron source [115, 120]. Inspired by these opportunities, the development of ruthenium coordination complexes flourished.

Rational design of ruthenium complexes

Ruthenium may occupy oxidation states ranging from −2 to +8, of which Ru(II) and Ru(III) are the most relevant in the biological environment. Complexes of ruthenium(III) exhibit higher thermodynamic stability than ruthenium(II) complexes which allows for a prodrug design. The change from one oxidation state into another can be initiated by diverse influences such as acidic pH, hypoxia or high levels of glutathione [115]. However, the exact coordination sphere tightly controls the capability of the cellular redox systems to interact with the ruthenium complex by oxidation or reduction [123]. Additionally, the oxidation state affects the number of ligands and the coordination geometry. Although tetrahedral, square-pyramidal and octahedral are known for ruthenium compounds, with respect to those developed for anticancer therapy, only two major classes are relevant so far: octahedral ruthenium(III) complexes and piano-stool ruthenium(II) compounds [123]. The latter possesses an arene ligand as top part of the compound, which stabilizes the oxidation state thereby preventing redox activity of the central ruthenium atom. In contrast, ruthenium(III) coordination compounds that feature the classical octahedral conformation may engage in reduction and oxidation of the ruthenium core in the cellular environment [123].

Ruthenium(II) complexes in (pre)clinical development

With respect to ruthenium(II), RAPTA-C (Figure 19, left) is mentioned as the most prominent member of its family [124, 125]. Notably, the family name “RAPTA” reflects the structural features:

in their piano-stool confirmation, the ruthenium center (R) is η^6-coordinated with an arene ligand (A) and an amphiphilic, monodentate 1,3,5-triaza-7-phosphaadamantane (PTA), while the two remaining coordination sites are occupied by relatively labile chlorido ligands but might be substituted differently in derivatives to modulate the overall reactivity of the complex [126]. In RAPTA-C, cymene serves as the arene ligand [126]. Following promising results *in vitro* and *in vivo*, RAPTA-C was clinically tested where it exhibited anti-metastatic, anti-angiogenic and anti-tumoral activities [125]. To identify the mechanism underlying these actions, RAPTA compounds were immobilized and incubated with whole cell extracts followed by mass spectrometry of the bound fraction. The results indicated the formation of specific protein - ruthenium interactions as well as histone - deoxyribonucleic acid alterations rather than direct interaction with the DNA, implying protein-binding may be a major factor in the activity of these compounds [125, 127].

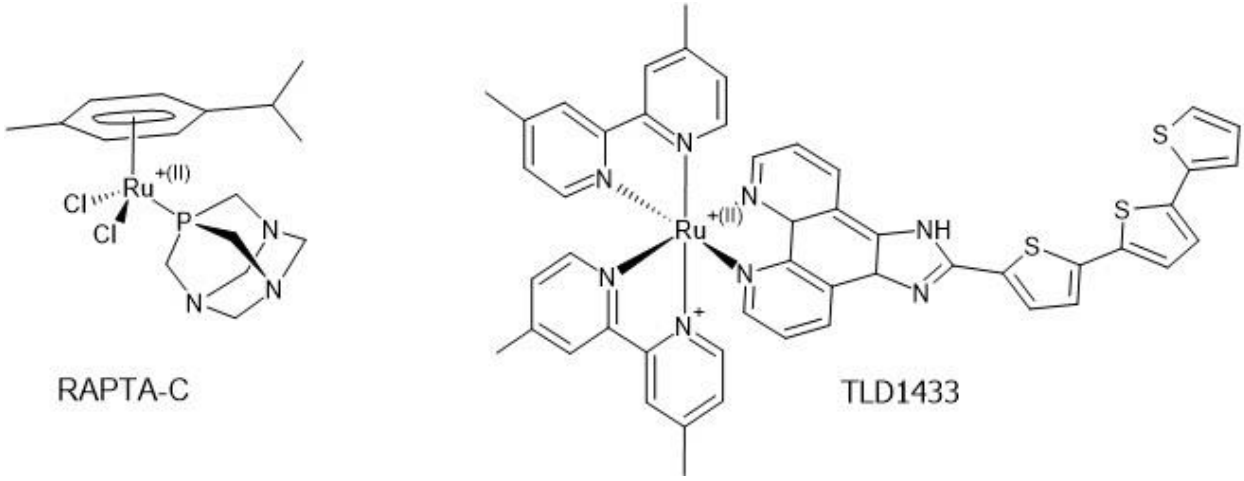

Figure 19: Examples of ruthenium coordination complexes which are or have been in clinical development

A relatively new candidate utilizing ruthenium(II) is $[Ru(bpy)(IP\text{-}TT)]^{2+}$, whereby IP-TT stands for "2-(2′,2″:5″,2‴-terthiophene)imidazo[4,5*f*]1,10-phenanthroline", better known as TLD1433 (Figure 19, right). In this design, the photochemical and photophysical properties are arranged to combine the features of photosensitizers in photodynamic therapy (PDT) and photochemotherapy (PCT) in one compound. [128]. Both aspects are based on the photodynamic effect which refers to "damage or destruction of living tissue by visible light in the presence of a photosensitizer and oxygen" [129]. This is achieved by energy transfer from the photosensitizer to either oxygen or water, yielding several reactive oxygen species like singlet oxygen, superoxide and hydroperoxyl radicals [128]. However, its intracellular distribution, interaction partners as well as its particular mode of action are to be elucidated. In a clinical phase 1b trial as a topical treatment for non-muscle-invasive bladder cancer, the drug achieved promising results for all six patients [128]. Currently, a multicenter clinical phase II trial (NCT03945162) is being conducted and is enrolling the same patient group. Results from this trial in which the applied formulation of TLD1433 is called "Ruvidar®" are expected late 2025 or early 2026 [130].

Ruthenium(III) complexes in clinical development

At present, there are two ruthenium(III) complexes, which have entered clinical development: NAMI-A and KP1019/BOLD-100 (Figure 20). Both originate from the search for novel anticancer compounds following the discovery of adverse effects of and resistance development against cisplatin treatment. Despite obvious structural similarities, striking differences in their chemical and biological effects were uncovered [131]. While NAMI-A kept its original name throughout the years, the name of BOLD-100 changed several times because its development has been pursued by different enterprises. Therefore, literature for this particular complex can be found under the names KP1339, NKP1339, IT-139 and BOLD-100 [132]. In this introduction, the name “BOLD-100” will be used.

In the 1980s, a series of first-in-class coordination complexes featuring ruthenium(III) as central atom was designed, synthesized and evaluated for their anticancer efficacy *in vitro* by B.K. Keppler and his group [133]. The compound panel also included trans-[$RuCl_4$(1H-imidazole)$_2$] (KP418), depicted in on the left side of Figure 20.

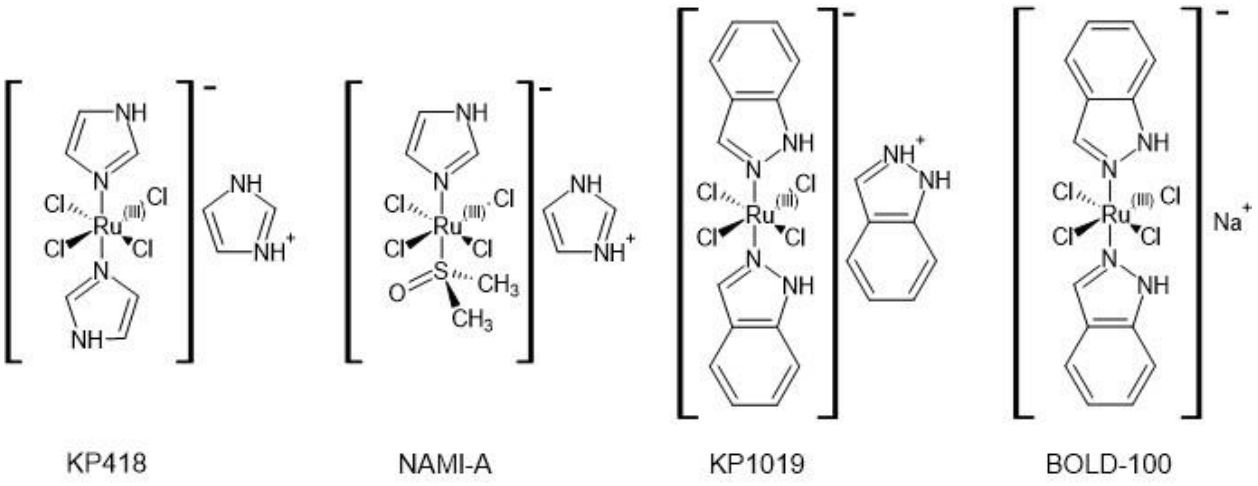

Figure 20: Ru(III) complexes KP418, NAMI-A, KP1019 and BOLD-100

Already in the first investigations, KP418 manifested a high efficacy against an autochthonous model of colorectal cancer, even exceeding the effect of the reference substances [131]. Subsequent efforts to optimize the ratio between efficacy and potential adverse effects triggered the development of NAMI-A in which one of the axial imidazole ligands was replaced with dimethylsulfoxide (DMSO) and the indazolium analogue (KP1019/BOLD-100) of the initial complex [131, 132, 134].

From a chemical perspective, NAMI-A is stable in the solid state but undergoes an hydrolysis in aqueous solution in a pH-dependent manner. Accordingly, the original complex disappears from the solution within a few minutes at physiological pH [135]. This was confirmed in binding studies using serum protein, where ruthenium was bound to albumin as a naked metal ion following the exchange of all ligands. Thus, the complex was considered as prodrug [131]. Remarkably, NAMI-

A exerted a strong anti-metastatic effect, while demonstrating only very mild cytotoxicity in cell culture. Although this finding was reported very early in the development by Sava *et al*. [136], the underlying mechanisms were only unravelled later. On one hand, NAMI-A scavenges nitric oxide through displacement of the DMSO ligand, which ultimately inhibits angiogenesis, because nitric oxide normally stimulates cell migration and angiogenesis as downstream effectors of the nitric oxide synthetase pathway as well as of several VEGF-activated enzymes [137]. On the other hand, collagens of the extracellular matrix and cell-surface integrins seem to be affected by NAMI-A, causing increased adhesion and therefore reduced invasiveness of cancer cells [137]. The latter mechanism coincides with the limited cellular uptake of ruthenium upon NAMI-A treatment as well as with its low cytotoxicity in cell culture [131]. Despite performing successfully in a phase I clinical study, a phase I/II trial of NAMI-A in combination with gemcitabine for the treatment of non-small cell lung cancer was terminated early due to low efficacy and occurrence of adverse effects [138].

With regard to KP1019, this drug was investigated as the indazolium analogue of KP418 for its anticancer activity, selectivity, mode of action and clinical application. These results demonstrated that KP1019 had similar anticancer efficacy as KP418 against an autochthonous rat colon cancer model but caused less adverse effects [139]. Subsequently, the drug entered a phase I clinical trial which is a dose escalation study. However, while KP1019 obtained promising results including stable disease in 5 out of 6 patients, practical problems arose: its exceptional tolerability combined with the limited solubility required impractically large injection volumes. Consequently, the further development focused on the 35-fold better soluble sodium salt of KP1019, BOLD-100. [133]. As BOLD-100 is administered intravenously, its stability and hydrolysis behaviour as well as its interaction with serum proteins are crucial to understand. Notably, BOLD-100 was reported to rapidly interact with plasma proteins such as serum albumin and transferrin [133]. In accordance with these findings, the plasma half-life of BOLD-100 was determined to be exceptionally long, ranging from 69 h to more than 200 h [140]. This is in accordance with recent investigations on radioactively labelled BOLD-100 using the isotopes ^{103}Ru and ^{97}Ru, which detected increasing concentrations of ruthenium in the tumor over the course of 24 h [141]. Thus, the findings suggest that BOLD-100 accumulates in the tumor following the EPR effect [51, 139]. Subsequently to the breakdown of macromolecules to satisfy the need of cancer cells for nutrients and followed by the suggested activation by reduction, the effects of the activated drugs become apparent [133, 139].

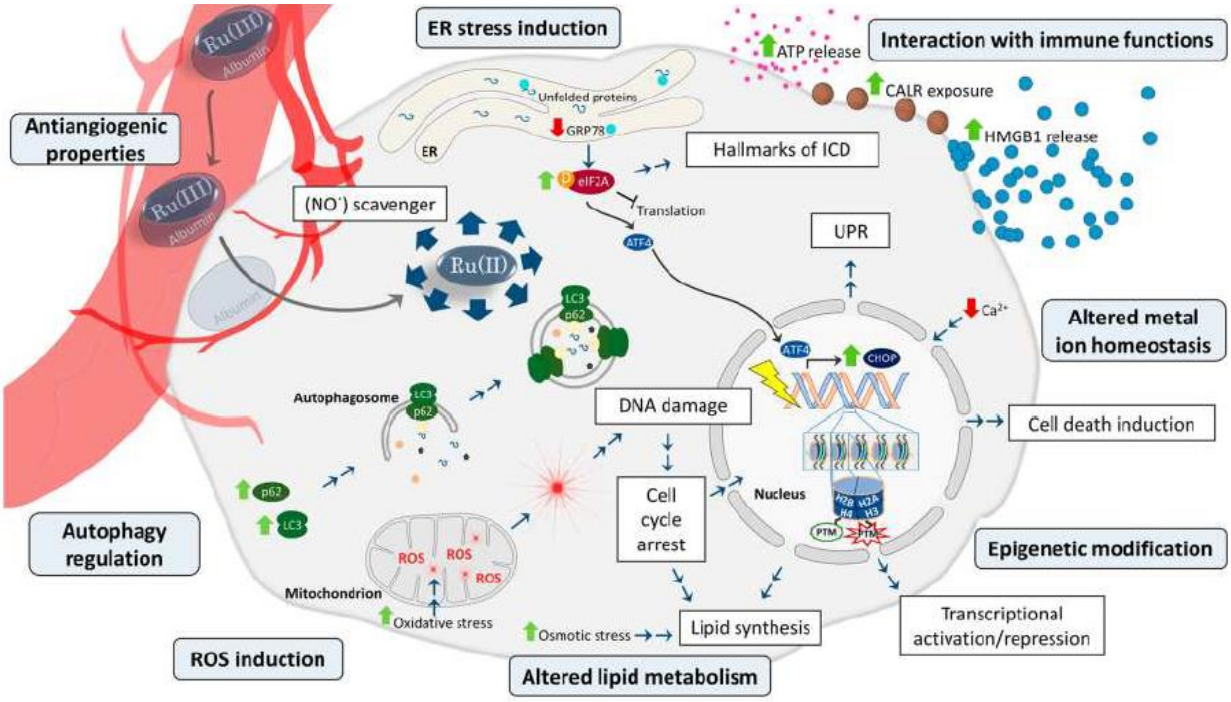

Figure 21: Schematic representation of targets of KP1019 and BOLD-100
Used with permission of Royal Society of Chemistry; from [142]; permission conveyed through Copyright Clearance Center,

The mode of action of BOLD-100, as far as is has been elucidated, is unique and multimodal (Figure 21). It comprises the increase of intracellular ROS and upregulation of the pro-apoptotic p38 MAPK pathway, but also affects the homeostasis of the endoplasmic reticulum [139, 143-145]. The unfolded protein response (UPR) including the levels of glucose related protein 78 (GRP78) was strongly influenced by BOLD-100 treatment [145]. Moreover, distinct changes have been identified recently in metabolism of lipids and sugars upon BOLD-100 treatment [146, 147].

Currently, a phase Ib/IIa dose-escalation study aims to compare the performance of BOLD-100 in combination with FOLFOX for chemotherapy in patients with advanced solid tumors (NCT04421820) [148]. FOLFOX is the combination therapy regime of folinic acid, fluorouracil and oxaliplatin, which is frequently applied for colon carcinoma [148]. Since this trial is estimated to be completed by September 2024, results from this trial are expected late 2024 or early 2025 [148]. Due to previous and preliminary results, BOLD-100 was awarded with Orphan Drug Designation for pancreatic and gastric cancer [132].

Aims of this thesis

Ensuring appropriate quality of life for cancer patients, while offering improved therapy with satisfying efficacy, is an ongoing and urgent need in modern medicine that life sciences are struggling to fulfill. In this regard, novel delivery systems of active anticancer agents as well as prodrug systems are of high interest. Consequently, this thesis aims to investigate the impact of polymer conjugation on the anticancer activity of ruthenium arene drugs and to further elucidate the molecular mechanisms underlying the anti-cancer activity of the clinically developed prodrug BOLD-100. This is important as even a promising candidate like BOLD-100 will not be effective against the all cancer types and subtypes. Therefore, predictive markers are needed in order to select patients, who will most likely benefit from this therapeutic approach. At the same time, this information is crucial for enrollment of patients in further clinical trials.

This work has been performed in close collaboration with synthetic chemists from the Institute of Polymer Chemistry Johannes Kepler, University Linz (group of Ian Teasdale) and from the Institute of Inorganic Chemistry, University of Vienna (group of Bernhard Keppler), who performed all chemical synthesis and characterizations of the used compounds.

In more detail, the specific aims of this thesis were:

1. *In vivo* characterization of the pharmacology and anticancer activity of novel ruthenium and rhodium arene-coupled poly(organo)phosphazene-based nanocarriers
2. Characterization of differences between intrinsically BOLD-100-sensitive and -resistant cell lines to find novel markers indicative for either sensitivity or resistance
3. Further elucidation of the mode of action of BOLD-100 with a focus on its impact on cell cycle distribution and cell cycle regulation
4. Establishment of novel BOLD-100-resistant sublines and characterization of their modes of drug resistance

Results

Prologue: First peer-reviewed paper

Synthesis and in vivo anticancer evaluation of poly(organo)phosphazene-based metallodrug conjugates

Hackl CM, **Schoenhacker-Alte B (contributed equally)**, Klose MHM, Henke H, Legina MS, Jakupec MA, Berger W, Keppler BK, Brüggemann O, Teasdale I, Heffeter P, Kandioller W.

Dalton Trans. 2017 Sep 28;46(36):12114-12124.

Impact Factor 4.0

doi: 10.1039/c7dt01767g. Epub 2017 Sep 1.

Prior to this study, a series of organoruthenium and -rhodium complexes had been found to be highly potent in vitro. Unfortunately, the pharmacodynamic and toxicity profile was not desirable including unselective activity and local side effects. Therefore, the aim of this study was to improve the in vivo activity by attaching the complexes to a degradable poly(organo)-phosphazene macromolecule. The respective drug–polymer conjugates were prepared by our collaboration partners at the Institute of Inorganic Chemistry as well as thoroughly studied by means of ^{31}P NMR and UV-Vis spectroscopy, ICP-MS analyses and SEC coupled to ICP-MS. Subsequently, the complexes, as well as their respective macromolecular prodrug formulations were tested again *in vitro* and *in vivo*. The latter was performed in mice bearing CT-26 colon carcinoma which were treated with the complexes, the unloaded polymer and the drug-polymer conjugates. The assessment included anticancer activity of the poly(organo)phosphazene drug conjugates, possible side effects caused by the treatment, as well as organ distribution of the complexes.

The biological part of the experimental work of this study was mainly conducted by me. The biological part of the manuscript was written by me together with P. Heffeter with revision and input from all other authors. C. Hackl was responsible for the synthesis of the organometallic complexes, the deprotection of the polyphosphazenes and the subsequent preparation and isolation of the macromolecular drug conjugates. Additionally, C. Hackl characterized the obtained conjugates *via* ^{31}P NMR measurements, UV-Vis analyses, and DLS measurements [149].

Dalton Transactions

PAPER

View Article Online
View Journal | View Issue

Cite this: *Dalton Trans.*, 2017, **46**, 12114

Synthesis and *in vivo* anticancer evaluation of poly(organo)phosphazene-based metallodrug conjugates†

Carmen M. Hackl,‡[a] Beatrix Schoenhacker-Alte,‡[a,b,d] Matthias H. M. Klose,[a] Helena Henke,[c] Maria S. Legina,[a] Michael A. Jakupec,[a,d] Walter Berger,[b,d] Bernhard K. Keppler,[a,d] Oliver Brüggemann,[c] Ian Teasdale,[c] Petra Heffeter*[b,d] and Wolfgang Kandioller*[a,d]

Within this work we aimed to improve the pharmacodynamics and toxicity profile of organoruthenium and -rhodium complexes which had previously been found to be highly potent *in vitro* but showed unselective activity *in vivo*. Different organometallic complexes were attached to a degradable poly(organo)phosphazene macromolecule, prepared *via* controlled polymerization techniques. The conjugation to hydrophilic polymers was designed to increase the aqueous solubility of the typically poorly soluble metal-based half-sandwich compounds with the aim of a controlled, pH-triggered release of the active metallodrug. The synthesized conjugates and their characteristics have been thoroughly studied by means of ^{31}P NMR and UV-Vis spectroscopy, ICP-MS analyses and SEC coupled to ICP-MS. In order to assess their potential as possible anticancer drug candidates, the complexes, as well as their respective macromolecular prodrug formulations were tested against three different cancer cell lines in cell culture. Subsequently, the anticancer activity and organ distribution of the poly(organo)phosphazene drug conjugates were explored *in vivo* in mice bearing CT-26 colon carcinoma. Our investigations revealed a beneficial influence of this macromolecular prodrug by a significant reduction of adverse effects compared to the free metallodrugs.

Received 15th May 2017,
Accepted 4th July 2017

DOI: 10.1039/c7dt01767g

rsc.li/dalton

Introduction

One of the most frequent reasons for premature discontinuation of clinical trials is the occurrence of unforeseen side effects caused by the novel drug candidates.[1–3] A promising research branch sprouting from the intention to selectively target solid tumors makes use of the enhanced permeability and retention (EPR) effect. This effect describes the accumulation of macromolecules by passive diffusion into tumor tissues which are usually characterized by an abnormal vasculature and irregular architecture of cell layers.[4–6] Leakages in the endothelial layer of capillaries permit the infiltration of the intercellular space of tumor tissues by macromolecules, where they are retained due to deficient lymphatic drainage. One of the leading and most elegant strategies to exploit this effect is based on the utilization of human serum albumin (HSA) as a natural transport vehicle.[7–9] Approval was granted to an albumin nanoformulation of the established drug paclitaxel (trade name: Abraxane®) for the treatment of different cancer types, with especially high responses in breast cancer therapy.[7] The fundamental role of HSA is also reflected in the minor side-effects of the first-in-class drug candidate IT-139 (NKP-1339; sodium *trans*-[tetrachloridobis(1*H*-indazole)ruthenate(III)]), which is attributed to its high affinity for human serum albumin. In this special case, binding occurs non-covalently at hydrophobic domains of the protein, allowing for the attachment of more than one drug unit per HSA molecule.[8] As for synthetic macromolecules, next to fulfilling certain size requirements to utilize the EPR effect (commonly 20–200 kDa),[9] a potential drug carrier has to guarantee controlled release of the active load at the biological target.[10] Hence, an exclusive trigger that can initiate drug release from

[a]*Institute of Inorganic Chemistry, University of Vienna, Waehringer Str. 42, 1090 Wien, Austria. E-mail: wolfgang.kandioller@univie.ac.at*
[b]*Institute of Cancer Research and Comprehensive Cancer Center, Department of Medicine I, Medical University of Vienna, Borschkegasse 8a, 1090 Vienna, Austria. E-mail: petra.heffeter@meduniwien.ac.at*
[c]*Institute of Polymer Chemistry, Johannes Kepler University Linz (JKU), Altenberger Straße 69, 4040 Linz, Austria*
[d]*Research Cluster "Translational Cancer Therapy Research", University of Vienna, Waehringer Str. 42, 1090 Wien, Austria*
†Electronic supplementary information (ESI) available. See DOI: 10.1039/c7dt01767g
‡These authors contributed equally.

a macromolecular prodrug under the given circumstances must be identified. In poly(organo)phosphazenes deliberate selection of building blocks grants extensive control over essential characteristics such as degradation rate and aqueous solubility.[11,12] Additionally, the degradable backbone, suitable functional groups, and the degradation into physiologically nonhazardous metabolites satisfy several of the conditions required for polymer therapeutics.[10] As previously shown for platinum-based anticancer drugs coupled to polyphosphazene structures, the cellular uptake and accumulation into tumor tissue of such macromolecular drug formulations could be significantly increased compared to the free drug. The *in vivo* evaluation of polyphosphazenes equipped with established platinum(II) drugs capable of assembling into either micelles or nanoparticles of suitable diameters revealed pronounced accumulation within the tumor, while only low platinum levels were detected in healthy tissues.[13–15] Furthermore, we recently investigated the effect of polyphosphazene conjugation with representatives of the supposedly more inert class of Pt^{IV} prodrugs. In this work we observed a 30-fold increase in cellular uptake and at the same time an increase in cytotoxic activity *in vitro*. While Pt^{II} compounds such as cisplatin or carboplatin reign supreme in cytotoxic activity, these polymer–drug conjugates were shown to accumulate as well in tested cisplatin-resistant cell lines, where they were nevertheless able to exert their cytotoxic effect.[16] The beneficial influence of macromolecular drug delivery on the pharmaceutical efficacy has been adopted likewise for the conjugation of promising organometallic anticancer agents and several interesting approaches are described in the literature.[17]

The extensive collection of organometallic half-sandwich complexes comprises many representatives that have been assessed in a variety of *in vitro* and *in vivo* studies where they exhibited great potential as cytotoxic agents.[18–20] The assumed mode of action of this compound class is associated with an aquation step wherein an aqua ligand replaces the leaving group. In a prior attempt to stabilize highly cytotoxic thiomaltolato complexes in the presence of biomolecules the N-donating ligand 1-methylimidazole was employed as leaving group.[21] Thus, the stability was significantly increased and selective activation was possible at decreased pH levels, that are frequently found in solid tumors.[22] Hence, these promising results prompted us to develop polyphosphazene conjugates *via* coordination of the free amine linker group to different organometallic compounds of known activity. The pH-sensitivity of both polyphosphazene backbone and drug–amine interaction are eligible characteristics for the application of the respective drug–polymer conjugates in targeted therapy. In our approach, four promising organometallic complexes (Fig. 1) with small molecule ligands of known biological activity were chosen in order to improve their *in vivo* activity profile, which was shown to involve local adverse effects in a previously performed test series.

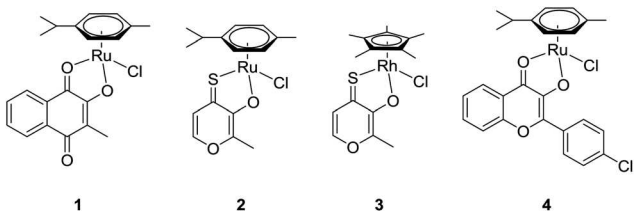

Fig. 1 Complexes **1–4** prepared for macromolecular conjugation.

Experimental

Materials

Menadione (2-methylnaphthalene-1,4-dione, 98%, Acros), sodium methoxide (*ca.* 95%, Fluka), α-terpinene (90%, Acros), $RuCl_3{\cdot}H_2O$ (Johnson Matthey), trifluoroacetic acid (99%, Sigma-Aldrich), triethylamine (99%, Acros), ammonium acetate (≥98%, Fluka), citric acid anhydrous (99.6%, Acros), trisodium citrate dihydrate (min. 99.5%, Sigma-Aldrich) were used without further purification. Other chemicals and solvents were purchased from commercial suppliers (Sigma Aldrich, Merck, Acros, Fluka and Fisher Scientific). Methanol and dichloromethane were distilled prior to use. Dialysis membranes (Spectra/Por 1, 6000–8000 Da) were purchased from SpectrumLabs. NMR spectra were recorded at 25 °C on a Bruker Avance III™ 500 MHz FT-NMR spectrometer. ^{1}H NMR spectra were measured at 500.10 MHz, ^{13}C NMR spectra at 125.75 MHz and $\{^1H\}^{31}P$ NMR spectra at 202.44 MHz from solutions in deuterated dimethyl sulfoxide, methanol, chloroform, and water. Milli-Q water (18.2 MΩ cm, Milli-Q Advantage, Darmstadt, Germany) was used for all dilutions for ICP-MS measurements. Nitric acid (≥69%, p.a., TraceSELECT®, Fluka, Buchs, Switzerland) was used without further purification. Ruthenium, rhodium and indium standards for ICP-MS measurements were derived from CPI International (Amsterdam, The Netherlands). Bovine serum albumin (BSA) (>98%, Sigma) and Uracil (99%, Fluka) for calibration of the column for SEC-ICP-MS studies were used without further purification. CHNS elemental analyses were carried out on a Eurovector EA3000 elemental analyzer in the microanalytical laboratory of the University of Vienna.

A detailed description of the synthetic procedures for the ligands, complex **1** as well as for the used polymer is given in the ESI.†

General synthetic procedures

General procedure for the synthesis of ruthenium and rhodium complexes. Syntheses of complexes **1–4** were performed according to the well-established protocol using sodium methoxide in absolute methanol to deprotonate the respective chelating ligand followed by the addition of the dimeric metal precursor complex $[(\eta^6\text{-}p\text{-cymene})Ru^{II}Cl_2]_2$ or $[(\eta^5\text{-}1,2,3,4,5\text{-pentamethylcyclopentadien})Rh^{III}Cl_2]_2$. After stirring at ambient temperature for a varying reaction time ranging from 1.5 to 24 h, the solvent was removed under

reduced pressure, the crude product was extracted with dichloromethane and insoluble by-products were removed by filtration. The mixture was then concentrated and the addition of *n*-hexane afforded the desired complexes in good to excellent yields. Detailed reaction conditions for complexes **2–4** are described elsewhere.[21,23,24]

General procedure for deprotection and loading of polyphosphazenes. For the removal of the *tert*-butyloxycarbonyl (Boc) protecting group, the poly(organo)phosphazene was dissolved in a dry CH_2Cl_2/TFA mixture (2 : 1 ratio, 2 mL per 100 mg polymer) and stirred under argon atmosphere for 1 h. After evaporation of the solvent mixture under reduced pressure, the deprotected polyphosphazene was dried *in vacuo*. In order to form drug-loaded polymer conjugates, the deprotected polyphosphazene was dissolved in dry methanol and Et_3N was added to the mixture. The methanolic solution of the respective complex was carefully added to the polymer and the coupling reaction was stirred at room temperature and under argon atmosphere for 24 h. Conjugates were then purified by dialysis against methanol for 5 days.

Conjugate **1a**: Deprotected polymer (300 mg, 0.016 mmol), complex **1** (150 mg, 0.33 mmol), Et_3N (55 μL, 0.40 mmol); yield: 187 mg; ^{1}H NMR (500.10 MHz, D_2O): δ 1.11 (m, 6H), 1.37 (m, 4H), 3.17 (s, 6H), 3.31 (bs, 6H), 3.63 (s, 154H) ppm. $\{^1H\}^{31}$P NMR (202.44 MHz, D_2O): δ 0.21 ppm. DLS (H_2O): d_h = 16.5 nm; ξ = 1.75 mV. Conjugate **2a**: Deprotected polymer (300 mg, 0.016 mmol), complex **2** (150 mg, 0.36 mmol), Et_3N (55 μL, 0.40 mmol); yield: 205 mg; ^{1}H NMR (500.10 MHz, D_2O): δ 1.02 (m, 6H), 1.12 (m, 4H), 3.19 (s, 6H), 3.23 (bs, 6H), 3.55 (s, 156 H) ppm. $\{^1H\}^{31}$P NMR (202.44 MHz, D_2O): δ 0.16 ppm. DLS (H_2O): d_h = 11.7 nm; ξ = 5.92 mV. Conjugate **3a**: Deprotected polymer (300 mg, 0.014 mmol), complex **3** (150 mg, 0.36 mmol), Et_3N (55 μL, 0.40 mmol); yield: 161 mg; ^{1}H NMR (500.10 MHz, D_2O): 1.07 (m, 6H), 1.20 (m, 4H), 3.13 (s, 6H), 3.29 (bs, 6H), 3.61 (s, 151H) ppm. $\{^1H\}^{31}$P NMR (202.44 MHz, D_2O): δ 0.86 ppm. DLS (H_2O): d_h = 11.9 nm; ξ = 2.85 mV. Conjugate **4a**: Deprotected polymer (300 mg, 0.016 mmol), complex **4** (150 mg, 0.28 mmol), Et_3N (55 μL, 0.40 mmol); yield: 216 mg; ^{1}H NMR (500.10 MHz, D_2O): 1.03 (m, 6H), 1.18 (m, 4H), 3.17 (s, 6H), 3.33 (bs, 3H), 3.57 (s, 160H) ppm. $\{^1H\}^{31}$P NMR (202.44 MHz, D_2O): δ 0.93 ppm. DLS (H_2O): d_h = 13.1 nm; ξ = 0.58 mV.

ICP-MS analyses

Quantification of metal content of conjugates **1a–4a** as well as the determination of the ruthenium/rhodium content in tissue and blood samples from *in vivo* experiments was carried out with an ICP-MS instrument Agilent 7500ce. The ICP-MS Agilent 7500ce (Agilent Technologies, Waldbronn, Germany) was equipped with a CETAC ASX-520 autosampler (Nebraska, USA) and a MicroMist nebulizer at a sample uptake rate of approx. 0.25 mL min^{-1}. The Agilent MassHunter software package (Workstation Software, version B.01.01, Build 123.11, Patch 4, 2012) was used for data processing. The experimental parameters for ICP-MS analyses are summarized in Table S1† and detailed description of sample preparation procedures can be found in the section S2.4 in the ESI.†

General procedures for biological studies

Animals and xenograft experiments. Eight-week-old Balb/c or C57/B6JRj mice were purchased from Harlan Laboratories (San Pietro al Natisone, Italy). The animals were kept in a pathogen-free environment and every procedure was done in a laminar airflow cabinet. The experiments were done according to the regulations of the Ethics Committee for the Care and Use of Laboratory Animals at the Medical University Vienna (proposal number BMWF-66.009/0084-II/3b/2013), the U.S. Public Health Service Policy on Human Care and Use of Laboratory Animals as well as the United Kingdom Coordinating Committee on Cancer Prevention Research's Guidelines for the Welfare of Animals in Experimental Neoplasia.

For the evaluation of tolerability and 24 h organ distribution, non-tumor bearing C57/B6JRj mice were treated with a single dose of the drug conjugates **1a**, **2a** or **3a** *via* intravenous administration. The doses used were 100 mg kg^{-1} for **1a**, 25, 50 and 100 mg kg^{-1} for **2a** and 50 and 100 mg kg^{-1} for **3a**. Animals were sacrificed 24 h after administration of the compounds.

For the testing of *in vivo* anticancer activity, CT-26 (5×10^5) were injected subcutaneously into the right flank of Balb/c mice. When tumor nodules reached a mean size of 25 mm^3 (day 3), animals were treated twice for five consecutive days (day 3–7 and 10–15) in groups of four with **1** (30 mg kg^{-1} in 10% DMSO in water), **2** (10 mg kg^{-1} in 10% DMSO in water) and **3** (10 mg kg^{-1} in 10% PG in water) by intraperitoneal injection. Compounds **1a–3a** were dissolved in 0.9% NaCl solution and sterile filtered afterwards. Animals were treated intravenously with compound **1a**, **3a** (both 50 mg kg^{-1}) and **2a** (25 mg kg^{-1}) on days 3, 5, 7, 10, 12 and 14 after the injection of tumor cells. The tumor size was assessed by caliper measurement and tumor volume was calculated using the formula: (length × width^2)/2. Animals were sacrificed upon tumor ulceration or when a tumor length >20 mm was reached.

Cell culture. In the presented study, the following cell lines were used: the human cell line CH1 (identified *via* STR profiling as PA-1 ovarian teratocarcinoma cells by Multiplexion; see also ref. 25) was kindly provided by Lloyd R. Kelland (CRC Centre for Cancer Therapeutics, Institute of Cancer Research, Sutton, UK), and the colon cancer cell line SW480 was purchased from American Tissue Culture Collection (ATCC). These two cell lines were grown in MEM (supplemented with 1% L-glutamine, 1% sodium pyruvate, and 1% non-essential amino acids solution (all from Sigma Aldrich, Austria, Vienna) and 10% FCS (Gibco™, ThermoFisher)). The non-small cell lung carcinoma cell line A549 was purchased from ATCC and grown in RPMI 1640 supplemented with 10% FCS. The murine colon cancer cell line CT-26 (purchased from ATCC) was grown in DMEM/F12 medium (Sigma-Aldrich) supplemented with 10% FCS. FCS was purchased from PAA (Linz, Austria). All cultures were grown in humidified air with 5% CO_2 at 37 °C and were regularly checked for mycoplasma contamination.

Cell viability assay (MTT). 96 h cytotoxicity was determined by the colorimetric MTT assay (MTT = 3-(4,5-dimethyl-2-thiazolyl)-2,5-diphenyl-2*H*-tetrazolium bromide). Briefly, cells were harvested by trypsinisation and seeded in medium (*vide supra*) into 96-well plates in 100 μL per well. The following densities were used to ensure exponential growth of untreated controls throughout the experiment: 1.0×10^3 (CH1/PA-1), 2.0×10^3 (SW480), 3.0×10^3 (A549) cells per well. For 24 h, cells were allowed to settle and resume exponential growth. Then the test compounds were dissolved and serially diluted in medium with 100 μL per well. After 96 h at 37 °C, the medium was replaced with 100 μL per well RPMI 1640 medium (supplemented with 10% FCS and 4 mM L-glutamine) and MTT solution (MTT reagent in phosphate-buffered saline, 5 mg mL^{-1}) in a ratio of 6 : 1, and plates were incubated for further 4 h. Then medium/MTT was removed, and the formed formazan was dissolved in DMSO (150 μL per well). Optical densities at 550 nm were measured (reference wavelength: 690 nm) with a microplate reader (ELX880, BioTek). The quantity of viable cells was expressed relative to untreated controls, and 50% inhibitory concentrations (IC_{50}) were interpolated. At least three independent experiments were performed, each with triplicates per concentration level.

Viability assay (EZ4U). For the 72 h viability experiments, cells were plated in 100 μL per well in 96-well plates. The number of cells per well was A549 (2×10^3), CH1/PA-1 (3×10^3), SW480 (2×10^3), and CT-26 (3×10^3). Cells were allowed to recover for 24 h, then drugs were added in another 100 μL growth medium and cells were exposed for the time indicated. Cell survival was determined by the EZ4U assay following the manufacturer's recommendations (Biomedica, Vienna, Austria). Cytotoxicity was evaluated using the Graph Pad Prism software (La Jolla, USA) (using a point-to-point function) and was expressed as IC_{50} values calculated from full dose–response curves (drug concentrations resulting in 50% reduction of viable cells compared to untreated control cells cultured in parallel).

Cellular drug uptake studies. Sample preparation from cell culture: 3×10^5 cells per well were seeded in 6-well-plates and allowed to recover for 24 h, then the cells were treated with 10 μM solution of compounds **1–4** or an equimolar amount of conjugates **1a–4a**, respectively. All compounds were added in culture medium with 10% FCS and incubated for 3 h at 37 °C. Cells were washed twice with PBS. Then, the pellet was lysed in 500 μL of 69% HNO_3 at room temperature for 1.5 h. 400 μL of the resulting lysates were diluted in 8 mL Milli-Q water and measured by ICP-MS instrument Agilent 7500ce as described above (see ref. 26).

Results and discussion

Synthesis and biological characterization of the Ru^{II} and Rh^{III} organometallic complexes

For the synthesis of complexes **1–4**, the respective ligands 2-hydroxy-3-methyl-1,4-naphthoquinone, 2-hydroxy-3-methyl-pyran-4(1*H*)-thione and 3-hydroxy-2-(4-chlorophenyl)-4*H*-chromen-4(1*H*)-one were synthesized according to established, straightforward procedures (Schemes S1–S3†). The synthesis of the naphthoquinone derivative started from the commercially available menadione (2-methyl-1,4-naphthoquinone) which was converted into the corresponding epoxide by reaction with sodium hydroxide and hydrogen peroxide in a methanol/water mixture, followed by acid catalyzed ring opening on silica.[27] Commercially available maltol represented the starting point for the synthesis of the second ligand, thiomaltol. Lawessons's reagent, a standard compound for thionation reactions, was applied to convert the carbonyl group into the respective thiocarbonyl *via* the replacement of the oxygen by sulfur.[28] Finally, in order to synthesize the desired flavone ligand, 2-hydroxyacetophenone and 4-chlorobenzaldehyde were reacted in a classic aldol condensation to give the hydroxychalcone intermediate with subsequent ring closing under Algar–Flynn–Oyamada reaction conditions to afford the flavonol ligand.[29] Complexes **1–4** (Fig. 1) were synthesized by deprotonation of the ligands' hydroxyl group by sodium methoxide in methanol followed by the addition of the respective dimeric metal precursor as has been reported previously for compounds **2**, **3**, and **4**.[21,23,24] The synthesis of the thiomaltolato-based ruthenium(II) and rhodium(III) complexes required exclusion of water and oxygen from the reaction vessel in order to circumvent side reactions. Hence, reactions were performed in dry methanol using Schlenk techniques. Standard analytical methods including ^1H and ^{13}C NMR, elemental analysis, and X-ray diffraction analysis were performed and the obtained data was compared to the respective literature data to confirm purity and formation of the desired organometallics (reaction scheme and NMR spectra of complex **1** are shown in the ESI, Scheme S4 and Fig. S1 and S2†). The compounds were then tested for their anticancer activity in an MTT assay in three human cancer cell lines with an exposure time of 96 h, where they displayed varying cytotoxic potencies depending on the cell line (Table 1). Cytotoxicity decreases in the following order: **3** ≥ **4** > **2** > **1**. Even compound **1** displaying the highest IC_{50} values can still be considered a valid candidate for *in vivo* assessment, as its IC_{50} values are lower than those of the clinically active investigational ruthenium drug IT-139.

Subsequently, complexes **1–3** were evaluated for their *in vivo* anticancer activity against murine CT-26 colon carcinoma cells. Unfortunately, the poor solubility of complex **4** precluded

Table 1 Comparison of IC_{50} values of compounds **1–4** after 96 h of incubation

IC_{50} [μM]	A549	CH1/PA-1	SW480
1	47 ± 4	31 ± 10	15 ± 3
2	12 ± 4	2.9 ± 0.7	3.7 ± 1.0
3 [a]	5.9 ± 0.8	0.97 ± 0.11	1.0 ± 0.1
4 [b]	9.5 ± 0.5	0.86 ± 0.06	3.8 ± 0.5
IT-139[c]	156 ± 11	62 ± 9	88 ± 19

IC_{50} data taken from [a] Ref. 21. [b] Ref. 24. [c] Ref. 30.

further *in vivo* investigations with this compound. For the experiments Balb/c mice bearing the syngeneic tumor cells were treated intraperitoneally with the drugs applied at their maximal tolerated dose of 30 mg kg^{-1} for compound **1** and 10 mg kg^{-1} for compound **2** and **3**. In these experiments, only compound **1** exerted significant activity ($p < 0.01$ by two-way-ANOVA and Bonferroni posttest) (Fig. 2) and lowered the tumor burden of the treated animals on the final day of the experiment (data not shown). In contrast, compound **2** and **3** were widely inactive. Remarkably, the dissection of the animals revealed strong local adverse effects at multiple organs in the abdominal cavity, *e.g.*, stiff and swollen intestine, lesions on the liver, and spleen grown together with liver and stomach (Fig. S9†) for complexes **1–3**. Consequently, we hypothesized that the compounds exerted excessive local reactivity, which prevented sufficient amounts of drug to be delivered to the malignant tissue. Thus, a nanoformulation approach using polymer conjugates to avoid local reactions and facilitate drug transport into the tumor nodules was chosen as the next step.

Synthesis and characterization of the polyphosphazene conjugates

Star-branched polyphosphazenes were utilized as macromolecular drug carriers due to their excellent aqueous solubility and highly branched architecture.[31,32] Polymers were synthesized *via* living cationic polymerization providing control over chain length and molecular weight.[33,34] In a successive two-step post-polymerization substitution the chlorine atoms of the poly(dichlorophosphazene) $[NPCl_2]_n$ were partially substituted with mono-Boc-protected 2,2′-(ethylenedioxy)-bis (ethylamine) introducing the reaction sites, which were used for coordination to the organometallic complexes after deprotection. In the next step complete substitution of the remaining chlorine atoms with Jeffamine, a mono-amine PPO-PEO random copolymer (M_n = 1000) was performed, resulting in highly branched and water-soluble polymers (Scheme S5†). The percentage of reactive sites was determined *via* ^{1}H NMR spectroscopy by calculating the ratio of the integrated Boc-group signal to the OCH_3 end group peak of the Jeffamine moieties (29% Boc-groups). ^{1}H and ^{31}P NMR spectra are shown in the ESI (Fig. S3 and S4†). The Boc-protecting group was cleaved under dry, acidic conditions yielding free amino groups which were subsequently used to form coordinative bonds with the organometallic complexes **1–4** in methanolic solution, affording the desired conjugates after purification *via* dialysis. The obtained products were dried under reduced pressure, dissolved in water and lyophilized. For subsequent investigations, conjugates were dissolved in a 0.9% sodium chloride solution and stored at −80 °C.

In order to evaluate the degradation behavior of conjugates during storage in 0.9% sodium chloride solution, ^{31}P NMR spectra were periodically measured over four weeks. The collected spectra confirmed the suitable stability of all prepared conjugates after several weeks in aqueous solution (Fig. S5†).

The rate of degradation of polyphosphazenes can be readily tailored and these polymers were chosen from previous studies to have a relatively slow degradation rate to simplify these preliminary drug conjugation studies.[35] The extent of drug loading was determined by measurement of the metal content *via* ICP-MS analyses. Sample preparation involved the microwave-assisted digestion of the poly(organo)phosphazene backbone in nitric acid (20%) to guarantee complete release of the metal. The samples were then diluted with Milli-Q water resulting in nitric acid concentrations below 4% and ruthenium or rhodium concentrations below 15 μg kg^{-1}, suitable for ICP-MS analysis. Conjugates **2a** and **3a**, both bearing thiomaltolato-based complexes, show a high drug loading with 73.68 mg g^{-1} ruthenium and 34.21 mg g^{-1} rhodium (corresponds to an amine linker conversion of 85 and 40%, respectively), while lower ruthenium levels were detected for conjugates **1a** and **4a** (15 and 7% conversion; Table 2). Conjugate **4a** was deemed not suitable for *in vivo* investigations due to its insufficient drug loading. As application of the conjugates *in vivo* requires sterile filtration through 0.2 μm cellulose acetate filters prior to the administration, the metal content was determined both before and after sterile filtration and showed no discernable effect of the filtration process on the metal contents of the samples.

Drug-release studies. One fundamental prerequisite for polymeric prodrugs is the controlled release of the active moiety in proximity to the biological target. There are several possible triggers to initiate the liberation of the drug. The hypoxic

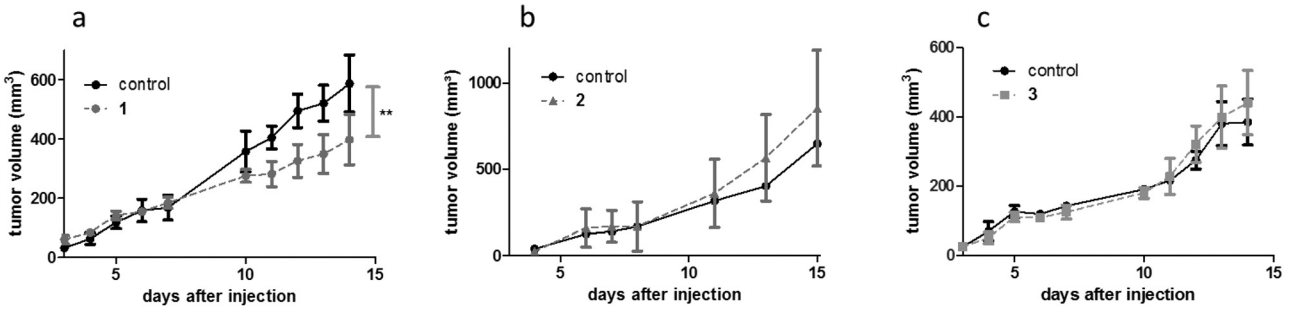

Fig. 2 Anticancer activity of compounds **1–3** *in vivo*. CT-26 allografts were grown in Balb/c mice (four animals per group) and treated with (a) **1** (30 mg kg^{-1} i.p.; male animals), (b) **2** (10 mg kg^{-1} i.p.; male animals), and (c) **3** (10 mg kg^{-1} i.p.; female animals) on days 3–7 and 10–15. **$p < 0.01$ statistically different from solvent control by two-way ANOVA and Bonferroni post test.

Table 2 Ruthenium and rhodium concentrations of analyzed aqueous polymer solutions acquired with ICP-MS measurements before and after sterile-filtration

Conjugate	Metal content [mg g^{-1}]	Metal concentration before filtration [mg mL^{-1}]	Metal concentration after filtration [mg mL^{-1}]
1a	12.08	0.23	0.24
2a	73.68	1.49	1.49
3a	34.21	0.63	0.65
4a	5.74	0.15	0.16

milieu in solid tumors induces a pH drop by up to 1 unit, which has been exploited for the development of pH sensitive macromolecules or linkers for drug-delivery systems.[36,37] Another common tactic is intracellular targeting by use of the lower pH of the endosomal and lysosomal environment.[38] The amine bond to the metal center is proposed to be sensitive to acidic cleavage (Fig. 3) as was demonstrated in our recently reported work on 1-methylimidazole substituted organometallic complexes.[30] Preliminary UV-Vis spectroscopic investigations indicated that the conjugates underwent the same transformation under acidic conditions (Fig. S6†). Complex **1** and conjugate **1a** were diluted with citric acid buffer (50 mM, pH 3, 4, 5, and 6) and measured in 1 h intervals over a period of 24 h. While spectra recorded at pH 6 and 5 remained nearly unchanged during the monitored time frame, the acidic milieu of pH 4 and 3 caused changes in the spectrum of **1a** where the absorption at 280 nm increased similar to the free complex **1**. Similar results were found for **2** and **2a** under neutral and acidic conditions (data not shown). To confirm transformations of the conjugate at lower pH levels further studies using SEC-ICP-MS were performed using conjugate **2a**. Again, the sensitivity of the conjugate to variations in the pH level became apparent in a different experimental setup using a mobile phase with 0.1 vol% formic acid. The acidic milieu (~pH 3) of the mobile phase led to the rapid decomposition of the conjugate and different ruthenium containing species were detected (Fig. S7†). The degradation process of the polymer was circumvented by use of an ammonium acetate buffered eluent (Fig. S8†). These experiments confirm that intracellular transformation of the conjugate under acidic conditions is possibly enabling the release of the attached metallodrug (free and/or attached to linker). Further investigations on the exact transformation and release processes at lowered pH levels are necessary and will be subject of further research.

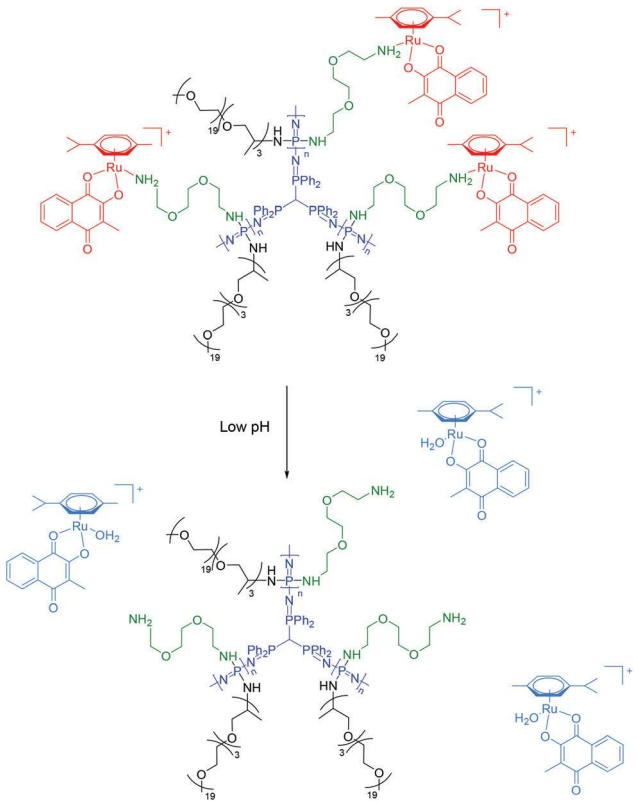

Fig. 3 Chemical structure of the macromolecular carriers and their proposed drug release mechanism at lowered pH shown for conjugate **1a**.

Recent studies have unveiled a certain affinity of albumin for ruthenium compounds. For this reason conjugate **2a** was co-incubated with a 10-fold excess of bovine serum albumin (BSA) at 37 °C and analyzed by size-exclusion chromatography coupled ICP-MS measurements to rule out possible transfer processes of the ruthenium complex. The obtained results indicate that the metallodrug remains attached to the polymer in the presence of albumin under the given conditions. The chromatogram showed an undiminished ruthenium peak at the retention time corresponding to the polymer conjugate even after 24 h of incubation (Fig. S8†). To appraise the relative retention time of the conjugate when eluted in a mobile phase containing an ammonium acetate buffer (10 mm), size-exclusion chromatography (SEC) with a UV-Vis detector (λ = 240 nm) were performed prior to SEC-coupled ICP-MS studies for the determination of the ^{101}Ru content.

Evaluation of anticancer activity and drug uptake in cell culture. Compounds **1–4** and their corresponding polymer-bound equivalents (conjugates **1a–4a**) were analyzed in cell culture after 72 h of incubation (Table 3). These experiments revealed that the polymer formulation effectively protected the cells from the reactivity of the organometallic complexes,

Table 3 Comparison of IC_{50} values for free complexes **1–4** and conjugates **1a–4a** after 72 h of incubation

IC_{50} [μM]	A549	CH1/PA-1	SW480	CT-26
1	33 ± 3.3	32 ± 6.0	15 ± 6.2	>50
1a	>50	>50	>50	>50
2	16 ± 2.0	6.2 ± 0.8	15 ± 6.6	14 ± 0.4
2a	>50	>50	>50	>50
3	14 ± 5.5	2 ± 1.5	10 ± 4.1	9 ± 2.3
3a	25 ± 8.0	11 ± 1.5	11 ± 7.1	>50
4	13 ± 1.0	2 ± 0.4	7 ± 2.0	7 ± 2.4
4a	>50	>50	>50	>50

especially in case of conjugates **1a**, **2a** and **4a**. Only conjugate **3a** still displayed some activity in the μM range.

We have previously shown that the use of polyphosphazene nanocarriers can lead to increased drug uptake of metallodrugs into cancer cells due to endocytosis.[16] Consequently, intracellular accumulation of all compounds was determined in two cell lines (Table 4). For this purpose, cells were treated with **1–4** (10 μM) or equimolar amounts of **1a–4a** for 3 h. After lysis with HNO_3 (69%), the samples were diluted and analyzed with ICP-MS for the determination of the metal content.[26] Surprisingly, the impact of the coupling to the phosphazene carrier differed between the tested compounds. Thus, in line with our previous publication on Pt^{IV}–polyphosphazene conjugates,[16] the intracellular accumulation of **2a** and **3a** was distinctly enhanced by the nanoformulation. This effect was especially pronounced with conjugate **2a**, which showed 15-fold and 11-fold higher intracellular accumulation compared to complex **2** in SW480 cells and in CT-26 cells, respectively. In contrast, the intracellular accumulation of **1a** and **4a** was significantly decreased compared to the free complexes. This observation already indicated that, despite the use of the same polyphosphazene nanocarrier, the individual polymer conjugates behaved markedly different in the performed biological assessments.

Organ distribution. In order to evaluate tolerability and organ distribution of the polymer-coupled complexes *in vivo*, studies in non-tumor bearing C57/B6JRj mice were carried out. In these experiments, the animals received a single dose of the drug conjugates **1a**, **2a** or **3a** *via* intravenous administration, while the biological investigation of **4a** was discontinued due to its insufficient metal-content as mentioned above. These experiments revealed that polymer-conjugate concentrations above 50 mg kg^{-1} were associated with severe (transient) fatigue. Consequently, for all subsequently performed *in vivo* experiments, concentrations of 50 mg kg^{-1} for **1a** and **3a**, and (due to the high drug loading) 25 mg kg^{-1} for **2a** were administered. The mice used for the tolerability tests were then sacrificed after 24 h and samples of blood, kidney, liver, lung, and, where possible, urine were collected. After microwave-assisted digestion of the tissue samples (25–50 mg) in half-concentrated nitric acid, the samples were diluted and the ruthenium or rhodium content was measured with ICP-MS. Conjugate **2a** was administered in three different concentrations (100 mg kg^{-1}, 50 mg kg^{-1} and 25 mg kg^{-1} containing 7.5 mg kg^{-1}, 3.75 mg kg^{-1} and 1.9 mg kg^{-1} ruthenium, respectively), while the conjugate **3a** was tested in two different concentrations (100 mg kg^{-1} and 50 mg kg^{-1} containing 3.25 mg kg^{-1} and 1.6 mg kg^{-1} rhodium, respectively). In case of conjugate **1a**, a concentration of 100 mg kg^{-1} containing 1.2 mg kg^{-1} of ruthenium was used. An overview of all tested schemes is given in the ESI (Table S2†). Each concentration and conjugate was tested in parallel in two mice to assess the reproducibility of the measured metal concentration in all analyzed tissues. Overall, the highest metal contents were found in the liver and kidneys, while only low concentrations were observed in the remaining samples (Fig. 4 and Table S3†). In general, the determined metal concentrations met the expected distribution profile well, since the administered conjugates prefer-

Table 4 Comparison of intracellular accumulation of ruthenium and rhodium after treatment with compounds **1–4** and **1–4a**

pg metal/10^4 cells	SW480	CT-26
1	215 ± 89	90 ± 34
1a	72 ± 12	7 ± 1
2	<LOD[a]	<LOD
2a	24 ± 6	23 ± 11
3	62 ± 13	55 ± 3
3a	932 ± 14	635 ± 13
4	302 ± 24	187 ± 10
4a	<LOD	<LOD

[a] LOD: limit of detection.

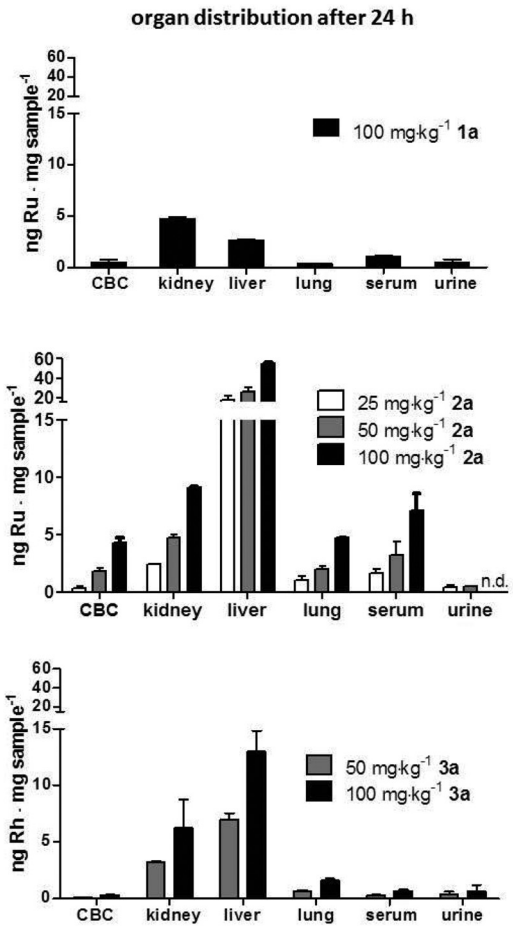

Fig. 4 Organ distribution of **1a–3a** 24 h after treatment. Female C57/B6JRj mice were intravenously injected with 100 mg kg^{-1} of **1a** (containing 1.2 mg kg^{-1} Ru), 25, 50 and 100 mg kg^{-1} **2a** (containing 1.9, 3.8 and 7.5 mg kg^{-1} Ru, respectively) and 50 and 100 mg kg^{-1} **3a** (containing1.6 and 3.2 mg kg^{-1} Rh, respectively). After 24 h, mice were anesthetized and blood as well as urine was collected by heart and bladder punctuation, respectively, and together with liver, lung and kidney samples were analyzed with ICP-MS to determine the metal content. Abbreviations: CBC, cellular blood compartment.

entially accumulate in organs responsible for clearance and excretion.

Conjugates **2a** and **3a** containing thiomaltolato-coordinated Ru^{II} and Rh^{III} metal centers, respectively, exhibited very similar distribution profiles despite their different metal centers. Both accumulated preferentially in the liver with metal concentrations more than five times higher than in kidney samples. Contrary to the distribution profile of conjugates **2a** and **3a**, mice treated with the ruthenium(II) naphthoquinone conjugate **1a** exhibited ruthenium levels twice as high in kidney tissue compared to liver samples. The obtained data suggests that the metal content in all examined organs scales linearly with the applied dose and is almost identical after normalization of the metal content in reference to the dosage (Fig. 4). Furthermore, it can be seen that organ distribution of the tested conjugates is mainly affected by the coordinated ligand systems, whereas the different metal centers appear to have no discernable effect.

Subsequently, a second drug distribution experiment was conducted on CT-26 tumor-bearing animals 3 h after intravenous drug treatment (at concentrations which were subsequently used for the anticancer activity experiments in the same tumor model). Again, each concentration and conjugate was tested in parallel in two mice. Comparable to the experiments performed 24 h after therapy, **1a**-treated animals again showed highest drug levels in the kidney, while after application of **2a** and **3a** the highest concentrations were found in the liver tissue (Fig. 5). The high drug levels in the urine (especially in case of **1a** and **3a**) compared to the animals investigated after 24 h, indicate a surprisingly high drug excretion during the first hours after treatment. As this effect cannot be explained by simple chemical reasons, it is assumed to be based on biological transformation or metabolism of the conjugates, which need to be further investigated in depth in subsequent studies. Interestingly, in case of compound **2a** the ruthenium levels in the liver (in contrast to all other tissues) were approximately twice as high in the animals investigated after 24 h as of those examined after 3 h. This fact could indicate a time-dependent (maybe metabolism-associated) accumulation of **2a** in this tissue. The effect was weaker for **1a** and **3a**, where the hepatic levels after 3 h and 24 h were very similar. With regard to the drug accumulation in the tumor, the metal content of **2a** and **3a** was higher than of conjugate **1a**, which is in line with the higher drug loading of these two polymers.

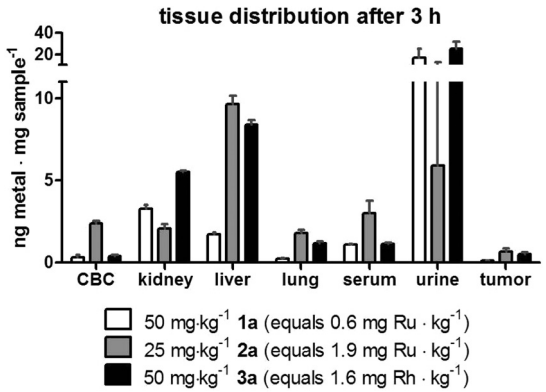

Fig. 5 Tissue distribution of **1a–3a** 3 h after treatment. Murine CT-26 cells (5×10^5) were injected subcutaneously into the right flank of female Balb/c mice (n = 2 per group). Animals were treated once intravenously with the indicated concentrations of compounds **1a**, **2a** and **3a** on day 10 after tumor inoculation, when the tumors reached a size of ~250 mm^3. After 3 h, mice were anesthetized and blood as well as urine was collected by heart and bladder punctuation, respectively, and together with liver, lung, kidney and tumor samples were analyzed with ICP-MS to determine the metal content. Abbreviations: CBC cellular blood compartment.

Anticancer activity *in vivo*. With the intriguing organ distribution profile at hand, the antineoplastic effect of conjugates **1a**, **2a**, and **3a** was next assessed by treatment of tumor-bearing Balb/c mice using the syngeneic murine tumor model CT-26 comparable to the experiments on complexes **1–3** described above. The animals were treated with the respective drugs intravenously on days 3, 5, 7, 10, 12 and 14.

The applied doses were 50 mg kg^{-1}, 25 mg kg^{-1} and 50 mg kg^{-1} (containing 2.7 mg kg^{-1}, 7.7 mg kg^{-1} and 6.5 mg kg^{-1} of the particular active metal complex, respectively) for conjugates **1a**, **2a**, and **3a**, respectively. During the first week of treatment, tumor growth curves for single mice revealed that administration of the macromolecular prodrugs induced drastic tumor shrinkage in some animals (Fig. 6 and Fig. S9†). Within the tested series, this effect was most pronounced for the naphthoquinone-based Ru^{II} conjugate **1a**. In contrast, no comparable tumor shrinkage was induced in the control group treated with 0.9% sodium chloride solution. However, this beneficial effect of our conjugates was only of a transient nature and diminished over the course of the treatment resulting in rapid tumor regrowth in most of the animals. Consequently, only in the case of conjugate **3a**, a trend towards improved overall survival was found (Fig. 6h). In addition, one of the animals treated with conjugate **1a**, experienced a long lasting tumor stabilization and thus an >100% increase in life span (Fig. 6d). With regard to the unloaded polymer, we observed (compared to the 0.9% NaCl-treated group) an increase of tumor ulceration, which necessitated an earlier sacrifice of the animals. Notably, the final dissection of the animals revealed no indications of severe organ damage comparable to the treatment with the free complexes **1–3** (Fig. S10 and S11†).

In order to get insights into the impact of repeated polymer application on the tissue distribution, samples from two mice that had to be sacrificed on day 17 (three days after the last treatment) were analyzed by ICP-MS (Fig. 7). One of these animals had been treated with compound **1a**, the other with compound **2a**. Overall, the metal content in the analyzed organs of these mice largely resembled the distribution profiles determined 3 h and 24 h after single dose administration. Interestingly, in case of **2a**, the ruthenium levels of serum and urine were 5- and 25-fold higher than in the animals investi-

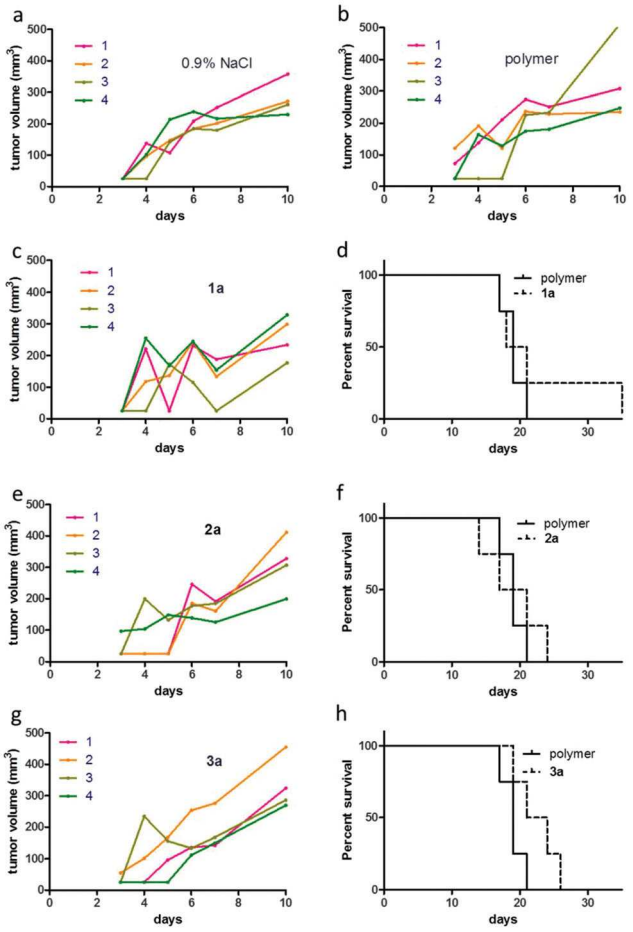

Fig. 6 Anticancer activity of **1a–3a**. Murine CT-26 cells (5×10^5) were injected subcutaneously into the right flank of female Balb/c mice ($n = 4$ per group). Animals were treated intravenously with **1a**, **2a** and **3a**. The applied doses were 50 mg kg^{-1} for **1a** and **3a**, and 25 mg kg^{-1} for **2a** on day 3, 5, 7, 10, 12, and 14. Tumor growth curves of single CT-26-bearing animals under treatment with (a) 0.9% NaCl, (b) unloaded polymer, (c) **1a**, (e) **2a** and (g) **3a** are shown. Figures (d), (f) and (h) display the overall survival of CT-26-bearing animals upon the indicated drug treatment.

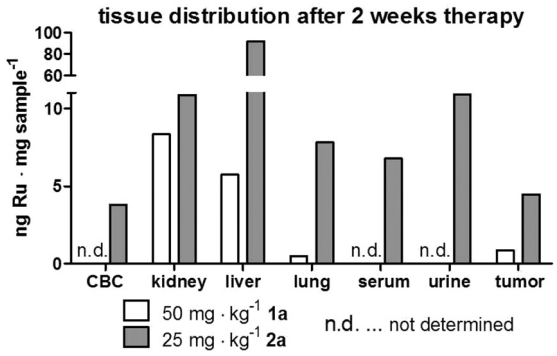

Fig. 7 Tissue distribution of conjugates in two animals after 2 weeks of drug treatment. Two animals of the experiment depicted in Fig. 6 were sacrificed on day 17 (3 days after the last application) due to tumor ulceration. Mice (one treated with **1a** and one with **2a**) were anesthetized and blood as well as urine was collected by heart and bladder punctuation, respectively, together with tissue samples for ICP-MS analyses.

gated 24 h after single dose application. Unfortunately, we did not succeed in collecting blood and urine samples of the animal treated with **1a**. The values found in blood and urine samples of **2a** indicate a distinctly prolonged plasma half-life time along with slow drug release from the macromolecule. This assumption is also supported by the observation that, although the sample collection happened 3 days after the last drug application, the ruthenium levels in kidney and liver of the repeatedly treated animals still were significantly above the ones observed 3 h after a single dose application of the two different drugs. The effect was especially pronounced for **2a**, where the liver levels were about 6-fold higher than the ones detected 24 h after a single application, which supports the hypothesis that this polymer slowly accumulates over time in the hepatic tissue with only limited elimination. Since such a strong drug accumulation in the liver could lead to drug-induced tissue damage, a histological evaluation of the collected samples was performed. For this purpose, the organs of all animals that had received therapy over a period of two weeks were embedded in paraffin, stained with hematoxylin/eosin and were microscopically investigated. Representative pictures for 0.9% NaCl, unconjugated polymer, as well as for conjugates **1a**, **2a** and **3a** are shown in the ESI (Fig. S11†).

Overall, no major organ injury was found, thus confirming the protective nature of our approach. Solely Bowman's space in kidney tissue showed some reduction upon treatment with **2a** and **3a**. Taken together, our drug distribution data indicate that despite the use of the same polymer for all three organometallic complexes, the organ distribution pattern as well as kinetics strongly differed. Moreover, the drug accumulation levels in the malignant tissue were not predictive for the *in vivo* anticancer activity, as **1a** (with the lowest tumor accumulation) was the only drug resulting in distinct life prolongation of an animal, while **2a** (with the highest tumor levels) had no visible impact on overall survival of the animals.

Conclusions

Within this work organometallic complexes have been attached to polyphosphazene macromolecules to obtain metallodrug conjugates. The extent of drug loading of the polymers was determined by measurement of the metal content *via* ICP-MS analysis after microwave-assisted digestion. Highest metal levels were detected for conjugates **2a** and **3a**, both bearing thiomaltolate as chelating ligand. The obtained macromolecular prodrugs were found to be highly stable in neutral aqueous solution as confirmed by ^{31}P NMR spectroscopy and UV-Vis kinetic studies. The free drug was observed to be released under acidic conditions potentially enabling selective intracellular lysosomal release. The antiproliferative potency of the free complexes was determined in different human cancer cell lines and compared to the respective polymer adduct. Thereby, we found that conjugation of the free organometallics to polyphosphazenes sig-

nificantly diminished the activity *in vitro* compared to the parent small molecule complexes. The potential of the developed polymer adducts as anticancer agents was elucidated *in vivo* and compared to the respective complexes. In contrast to the unconjugated drugs no morphological changes of the animals' organs were observed, confirming the stabilization of the highly active organometallics. Furthermore, pronounced tumor shrinkage after administration of the first dose of loaded polymer was observed for all tested conjugates and especially in the case of **1a**, the beneficial effect was evident as one mouse experienced increased survival time by more than 100%. However, this effect cannot be explained by increased drug accumulation, because **1a** showed both lowest polymer drug loading and cellular accumulation in CT-26 *in vitro* and *in vivo*. In addition, tissue distribution analysis revealed a totally different accumulation profile of **1a** compared to **2a** or **3a** which contrasts their respective anticancer activity. Conjugates **2a** and **3a** preferably accumulated in the liver, while **1a** caused highest metal levels in the kidneys. To preclude that the conjugates have a detrimental effect on organs with the highest accumulation level, liver and kidney tissues were evaluated histologically and microscopic images revealed no severe drug induced tissue damage. Overall **2a** and **3a** showed similar results in all biological studies and therefore an impact of the metal center (Ru and Rh) on the anticancer potential *in vivo* can be excluded. It appears more likely that the coordinated bioactive ligand scaffold is the main activity determining factor in this class of organometallics, since investigated conjugates do not show differences in size or drug release behavior. Overall, the conjugation of metallodrugs to poly(organo)phosphazenes is a promising approach for drug delivery. Stabilization of the reactive organometallics by this macromolecular drug formulation tremendously reduced the observed local adverse effects such as the deformation of organs. Based on the obtained results presented herein, the naphthoquinone-containing complex **1** is a promising candidate for further research regarding lead optimization and mode of action studies. Improvement of the poly(organo)phosphazenes concerning drug loading efficacy, and in particular the drug release kinetics, as well as an optimization of the hydrodynamic volume with the aim of extending blood retention times and exploiting the EPR effect might be promising approaches to further enhance the very positive *in vivo* effects of our conjugates.

Acknowledgements

The authors acknowledge financial support from the Austrian Science Fund (FWF) (Grant No. P24659-N28) and the Fellinger Krebsforschungsverein. We are grateful to Sushilla van Schoonhoven for the skillful handling of cell cultures, to Anita Brandstetter and the team of the Histology Core Facility of the Institute of Cancer Research for competent technical assistance and Gerhard Zeitler for devoted animal care.

Notes and references

1 K. Morrissey, T. Yuraszeck, C.-C. Li, Y. Zhang and S. Kasichayanula, *Clin. Transl. Sci.*, 2016, **9**, 89–104.
2 J. Arrowsmith and P. Miller, *Nat. Rev. Drug Discovery*, 2013, **12**, 569–569.
3 D. Cook, D. Brown, R. Alexander, R. March, P. Morgan, G. Satterthwaite and M. N. Pangalos, *Nat. Rev. Drug Discovery*, 2014, **13**, 419–431.
4 H. Maeda, *Adv. Drug Delivery Rev.*, 2015, **91**, 3–6.
5 H. Maeda, J. Wu, T. Sawa, Y. Matsumura and K. Hori, *J. Controlled Release*, 2000, **65**, 271–284.
6 Y. Matsumura and H. Maeda, *Cancer Res.*, 1986, **46**, 6387–6392.
7 E. Miele, G. P. Spinelli, E. Miele, F. Tomao and S. Tomao, *Int. J. Nanomed.*, 2009, **4**, 99–105.
8 O. Dömötör, C. G. Hartinger, A. K. Bytzek, T. Kiss, B. K. Keppler and E. A. Enyedy, *JBIC, J. Biol. Inorg. Chem.*, 2013, **18**, 9–17.
9 R. Haag and F. Kratz, *Angew. Chem., Int. Ed.*, 2006, **45**, 1198–1215.
10 E. Markovsky, H. Baabur-Cohen, A. Eldar-Boock, L. Omer, G. Tiram, S. Ferber, P. Ofek, D. Polyak, A. Scomparin and R. Satchi-Fainaro, *J. Controlled Release*, 2012, **161**, 446–460.
11 H. R. Allcock, *Soft Matter*, 2012, **8**, 7521–7532.
12 S. Rothemund and I. Teasdale, *Chem. Soc. Rev.*, 2016, **45**, 5200–5215.
13 R. Song, Y. Joo Jun, J. Ik Kim, C. Jin and Y. S. Sohn, *J. Controlled Release*, 2005, **105**, 142–150.
14 J. Y. Yu, Y. J. Jun, S. H. Jang, H. J. Lee and Y. S. Sohn, *J. Inorg. Biochem.*, 2007, **101**, 1931–1936.
15 S.-C. Song, S. B. Lee, B. H. Lee, H.-W. Ha, K.-T. Lee and Y. S. Sohn, *J. Controlled Release*, 2003, **90**, 303–311.
16 H. Henke, K. Kryeziu, J. Banfić, S. Theiner, W. Körner, O. Brüggemann, W. Berger, B. K. Keppler, P. Heffeter and I. Teasdale, *Macromol. Biosci.*, 2016, **16**, 1239–1249.
17 B. M. Blunden and M. H. Stenzel, *J. Chem. Technol. Biotechnol.*, 2015, **90**, 1177–1195.
18 B. S. Murray, M. V. Babak, C. G. Hartinger and P. J. Dyson, *Coord. Chem. Rev.*, 2016, **306**((Part 1), 86–114.
19 R. Fernández, M. Melchart, A. Habtemariam, S. Parsons and P. J. Sadler, *Chem. – Eur. J.*, 2004, **10**, 5173–5179.
20 F. Wang, A. Habtemariam, E. P. L. van der Geer, R. Fernández, M. Melchart, R. J. Deeth, R. Aird, S. Guichard, F. P. A. Fabbiani, P. Lozano-Casal, I. D. H. Oswald, D. I. Jodrell, S. Parsons and P. J. Sadler, *Proc. Natl. Acad. Sci. U. S. A.*, 2005, **102**, 18269–18274.
21 C. M. Hackl, M. S. Legina, V. Pichler, M. Schmidlehner, A. Roller, O. Dömötör, E. A. Enyedy, M. A. Jakupec, W. Kandioller and B. K. Keppler, *Chem. – Eur. J.*, 2016, **22**, 17269–17281.
22 I. F. Tannock and D. Rotin, *Cancer Res.*, 1989, **49**, 4373–4384.
23 W. Kandioller, C. G. Hartinger, A. A. Nazarov, M. L. Kuznetsov, R. O. John, C. Bartel, M. A. Jakupec, V. B. Arion and B. K. Keppler, *Organometallics*, 2009, **28**, 4249–4251.
24 A. Kurzwernhart, W. Kandioller, S. Bächler, C. Bartel, S. Martic, M. Buczkowska, G. Mühlgassner, M. A. Jakupec, H.-B. Kraatz,

P. J. Bednarski, V. B. Arion, D. Marko, B. K. Keppler and C. G. Hartinger, *J. Med. Chem.*, 2012, **55**, 10512–10522.
25 C. Korch, M. A. Spillman, T. A. Jackson, B. M. Jacobsen, S. K. Murphy, B. A. Lessey, V. C. Jordan and A. P. Bradford, *Gynecol. Oncol.*, 2012, **127**, 241–248.
26 A. E. Egger, C. Rappel, M. A. Jakupec, C. G. Hartinger, P. Heffeter and B. K. Keppler, *J. Anal. At. Spectrom.*, 2009, **24**, 51–61.
27 R. Zhu, L. Xing, X. Wang, C. Cheng, B. Liu and Y. Hu, *Synlett*, 2007, 2267–2271.
28 D. Brayton, F. E. Jacobsen, S. M. Cohen and P. J. Farmer, *Chem. Commun.*, 2006, 206–208.
29 M. Bennett, A. J. Burke and W. Ivo O'Sullivan, *Tetrahedron*, 1996, **52**, 7163–7178.
30 P.-S. Kuhn, V. Pichler, A. Roller, M. Hejl, M. A. Jakupec, W. Kandioller and B. K. Keppler, *Dalton Trans.*, 2015, **44**, 659–668.
31 H. Henke, O. Brüggemann and I. Teasdale, *Macromol. Rapid Commun.*, 2017, **38**, 1600644.
32 M. E. Fox, F. C. Szoka and J. M. J. Fréchet, *Acc. Chem. Res.*, 2009, **42**, 1141–1151.
33 H. Henke, S. Wilfert, A. Iturmendi, O. Brüggemann and I. Teasdale, *J. Polym. Sci., Part A: Polym. Chem.*, 2013, **51**, 4467–4473.
34 H. Henke, S. Posch, O. Brüggemann and I. Teasdale, *Macromol. Rapid Commun.*, 2016, **37**, 769–774.
35 S. Wilfert, A. Iturmendi, W. Schoefberger, K. Kryeziu, P. Heffeter, W. Berger, O. Brüggemann and I. Teasdale, *J. Polym. Sci., Part A: Polym. Chem.*, 2014, **52**, 287–294.
36 R. Duncan, *Nat. Rev. Drug Discovery*, 2003, **2**, 347–360.
37 R. Duncan, *Nat. Rev. Cancer*, 2006, **6**, 688–701.
38 R. Duncan and S. C. W. Richardson, *Mol. Pharm.*, 2012, **9**, 2380–2402.

Electronic Supplementary Material (ESI) for Dalton Transactions.

Supplementary Information

Synthesis and *in vivo* Anticancer Evaluation of Poly(organophosphazene)-based Metallodrug Conjugates

Carmen M. Hackl,[a]‡ Beatrix Schoenhacker-Alte,[a,b]‡ Matthias H. M. Klose,[a,c] Helena Henke,[d] Maria S. Legina,[a] Michael A. Jakupec,[a,c] Walter Berger,[b,c] Bernhard K. Keppler,[a,c] Oliver Brüggemann,[d] Ian Teasdale,[d] Petra Heffeter,*[b,c] and Wolfgang Kandioller*[a,c]

[a] Institute of Inorganic Chemistry, University of Vienna,
Waehringer Strasse 42, 1090 Vienna (Austria)

[b] Institute of Cancer Research and Comprehensive Cancer Center,
Department of Medicine I, Medical University of Vienna,
Borschkegasse 8a, 1090 Vienna (Austria)

[c] Research Platform “Translational Cancer Therapy Research,” University of Vienna,
Waehringer Strasse 42, 1090 Vienna (Austria)

[d] Institute of Polymer Chemistry, Johannes Kepler University Linz (JKU),
Altenberger Straße 69, 4040 Linz (Austria)

‡ These authors contributed equally

Contents

1 Synthetic Procedures 4

1.1 Synthesis of 2-Hydroxy-3-methyl-1,4-naphthoquinone 4

1.2 Synthesis of the Ligands for Complexes 2–4 5

1.3 Synthesis of Complex 1 Chlorido[2-methyl-3-(oxo-κO)-1,4-naphthoquinonato-κO1](η6-p-cymene)ruthenium(II) 6

1.4 Synthesis of the Poly(organo)phosphazene 7

2 Characterization 8

2.1 NMR Measurements 8

2.1.1 ^{1}H NMR Spectrum of Complex 1 8

2.1.2 ^{13}C NMR Spectrum of Complex 1 9

2.1.3 ^{1}H NMR Spectrum of the Boc-protected Polymer 10

2.1.4 {^{1}H}^{31}P NMR Spectrum of the Boc-protected Polymer 10

2.1.5 {^{1}H}^{31}P NMR Spectrum of Conjugate 2a 11

2.2 UV-Vis Investigations 12

2.3 DLS 13

2.4 ICP-MS Measurements 13

2.5 SEC-ICP-MS Analysis 14

3 Biological Investigations 16

3.1 Applied Dosages of Conjugates 1a–3a 16

3.2 Organ Distribution – Metal levels 16

3.3 Anticancer Activity in vivo 17

3.4 Morphological Changes of Organs and Tissues 18

3.5 Histological Evaluation of Tissue Samples 19

4 References 20

1 Synthetic Procedures

1.1 Synthesis of 2-Hydroxy-3-methyl-1,4-naphthoquinone

The ligand 2-hydroxy-3-methyl-1,4-naphthoquinone was synthesized starting from 2-methyl-1,4-naphthoquinone (menadione) (1.0 g, 5.8 mmol, 1 equiv.), which was dissolved in a 1:4 mixture of water/methanol and cooled to 0 °C. After the addition of NaOH (1.5 mL, 2 M, 3.0 mmol) and H_2O_2 (0.9 mL, 30%, 8 mmol, 1.3 equiv.), the solution was stirred for ten minutes at 0 °C followed by two hours of stirring at room temperature. The mixture was concentrated under reduced pressure and the remaining solution stored at 4 °C to maximize the yield of the intermediate product. The off-white intermediate (long, bright needles) was filtered, washed with water, dried in vacuo, and used without further purification (yield: 81%, 0.89 g). For the subsequent ring-opening reaction 2,3-epoxy-2-methyl-1,4-naphtoquinone (0.7 g, 3.7 mmol, 1 equiv.) and 7 g silica gel were suspended in THF. After the addition of conc. H_2SO_4 (1.4 mL, 96%, 13.7 mmol, 3.7 equiv.), the solvent was removed under reduced pressure (70 °C, 500 mbar) and the residue was extracted with CH_2Cl_2. The organic layer was then washed with a saturated solution of $NaHCO_3$. The combined aqueous layers were acidified using conc. HCl and re-extracted with CH_2Cl_2. The organic solvent was removed under reduced pressure and the yellow, fluffy product was dried in vacuo (yield: .92%, 0.69 g). ^{1}H NMR (500.10 MHz, DMSO-d_6): δ: 1.96 (s, 3H, H_{CH3}), 7.79 (ddd, ^4J(H,H) = 2 Hz, ^{3}J = 8 Hz, ^3J(H,H) = 8 Hz, 1H, H_{ar}), 7.84 (ddd, ^4J(H,H) = 2 Hz, ^3J(H,H) = 8 Hz, ^3J(H,H) = 8 Hz, 1H, H_{ar}), 7.98 (d, ^3J(H,H) = 8 Hz, 1H, H_{ar}), 8.01 (d, ^4J(H,H) = 8 Hz, 1H, H_{ar}), 10.94 ppm (s, 1H, OH).

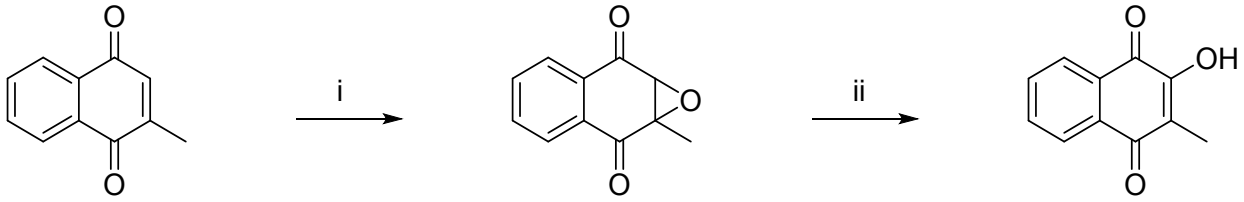

Scheme S1: Synthesis of the naphthoquinone ligand. i) NaOH, H_2O_2, methanol/H_2O 4:1, O °C; ii) H_2SO_4 conc., silica, THF, 500 mbar, 70 °C.

1.2 Synthesis of the Ligands for Complexes 2–4

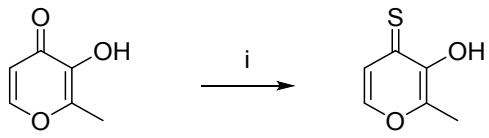

Scheme S2: Commercially available maltol was converted to thiomaltol by reaction with Lawesson's reagent. i) Lawesson's reagent (0.5 equiv.), dry THF, reflux, 4h.

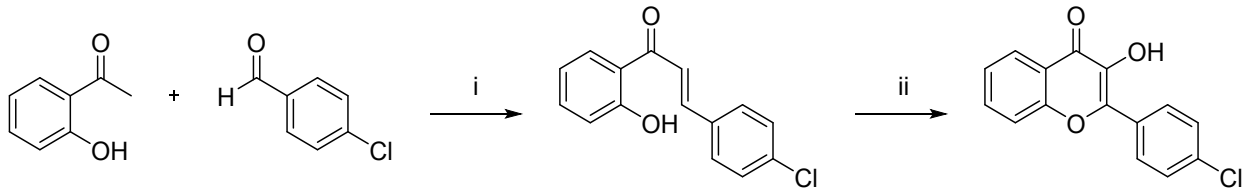

Scheme S3: 2-Hydroxyacetophenone and *p*-chlorobenzaldehyde were reacted to the corresponding hydroxychalcone intermediate in a classic aldol condensation i) NaOH (5 M), CH_3COOH, ethanol. The subsequent ring-closing reaction was performed under Algar-Flynn-Oyamada reaction conditions ii) NaOH (5 M), H_2O_2 (30%), ethanol.

1.3 Synthesis of Complex 1 Chlorido[2-methyl-3-(oxo-κO)-1,4-naphthoquinonato-κO1](η6-p-cymene)ruthenium(II)

Complex **1** was synthesized according to the general procedure using 2-hydroxy-3-methyl-1,4-naphthoquinone (302 mg, 1.61 mmol, 1 equiv.) which was deprotonated with NaOMe (95 mg, 1.76 mmol, 1.1 equiv.) and reacted with bis[dichlorido(η^6-*p*-cymene)Ru(II)] (439 mg, 0.72 mmol, 0.45 equiv.). After precipitation from dichloromethane/*n*-hexane the product was isolated as dark blue crystals (Yield: 69%, 450 mg). ^{1}H NMR (500.10 MHz, $CDCl_3$, 25 °C) δ = 1.38 (dd, ^4J(H,H) = 7 Hz, ^3J(H,H) = 13 Hz, 6H, $H_{CH3,Cym}$), 2.15 (s, 3H, H_{CH3}), 2.44 (s, 3H, $H_{CH3,Cym}$), 2.73–2.93 (m, 1H, $H_{CH,Cym}$) 5.95 (d, ^3J(H,H) = 6 Hz, 1H, $H_{ar,Cym}$), 6.24 (d, ^3J(H,H) = 6 Hz, 1H, $H_{ar,Cym}$), 7.55 (ddd, ^4J(H,H) = 2 Hz, ^3J(H,H) = 8 Hz, ^3J(H,H) = 8 Hz, 1H, H_{ar}), 7.73 (ddd, ^4J(H,H) = 2 Hz, ^3J(H,H) = 8 Hz, ^3J(H,H) = 8 Hz, 1H, H_{ar}), 8.00–8.05 ppm (m, 2H, H_{ar}); ^{13}C NMR (125.75 MHz, $CDCl_3$, 25 °C) *δ* = 9.0 (CH_3), 19.22 ($CH_{3,Cym}$), 22.9 & 23.0 ($2CH_{3,Cym}$), 32.6 (CH_{Cym}), 69.3 & 70.3 ($CH_{ar,Cym}$), 72.7 & 73.7 ($CH_{ar,Cym}$), 88.2 ($C_{ar,Cym}$), 91.3 ($C_{ar,Cym}$), 124.2 (C3), 126.8 (C5), 128.0 (C8), 131.6 (C7), 133.0 (C4a), 136.4 (C6), 170.2 (C2), 183.5 (C4), 195.5 ppm (C1). elemental analysis calcd. (%) for $C_{21}H_{21}ClO_3Ru$: C 55.08, H 4.62, O 10.48; found: C 54.73, H 4.59, O 10.84.

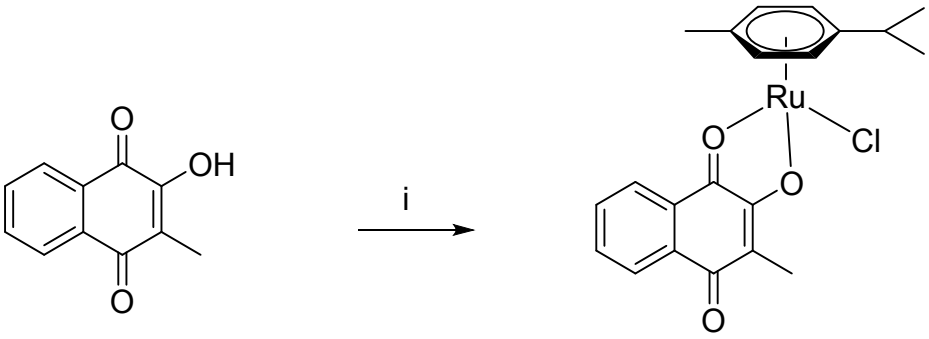

1

Scheme S4: Synthesis of complex **1**. i) NaOMe, Methanol, [dichlorido(η^6-*p*-cymene)Ru(II)]$_2$

1.4 Synthesis of the Poly(organo)phosphazene

The star branched poly(dichlorophosphazene) $[NPCl_2]_n$ was synthesized according the literature procedures.[1] Briefly: in a glove box at room temperature 1,1,1-tris(diphenylphosphino)methane (35 mg, 0.06 mmol) was chlorinated with C_2Cl_6 (48.1 mg, 0.20 mmol, 3.3 equiv.) in anhydrous CH_2Cl_2 overnight, yielding three ionic $[RPh_2PCl]^+$ species with Cl^- as counter ions. The monomer $Cl_3PNSi(CH_3)_3$[2] (2.07 g, 9.23 mmol, for n_{arm}=50) was dissolved in anhydrous CH_2Cl_2 (2 mL), the phosphine solution was then added and the mixture was stirred for 24 h.

Tertbutyl-2-(2-(2-aminoethoxy)ethoxy)ethylcarbamate (1.83 g, 7,39 mmol) was dissolved in THF and Et_3N (0.75 g, 1.1 mL, 1 equiv) was added. The poly(dichlorophosphazene) solution was slowly added to the THF solution and the mixture was stirred for 24 h. An excess amount of Jeffamine M-1000 (15.70 g, 15.70 mmol) was dissolved in THF and Et_3N (1.70 g, 2.2 mL, 1 equiv), added to the solution containing the partially substituted polyphosphazene, and stirred for 24 h. After filtration and removal of the solvent at reduced pressure, the polymer was purified by dialysis (12 kDa cutoff) in H_2O for 24 h, followed by dialysis in ethanol for 72 h. Removal of the solvent at reduced pressure gave a waxy solid. Yield: 6.71 g, 50%. ^{1}H NMR (300 MHz, $CDCl_3$) δ = 1.12 (br, 11.16H), 1.42 (s, 9H), 3.37(s, 7.4H), 3.63 (m, 167.7H) ppm; {1H}^{31}P NMR (121 MHz, $CDCl_3$, δ): 1.08 ppm. $M_{n,theo}$ = 2.16 × 10^5 g mol^{-1}, SEC (linear polystyrene (PS) standards): M_n = 1.84 × 10^4 g mol^{-1}, M_w/M_n = 1.60, DLS (H_2O): d_h = 10.3 nm.

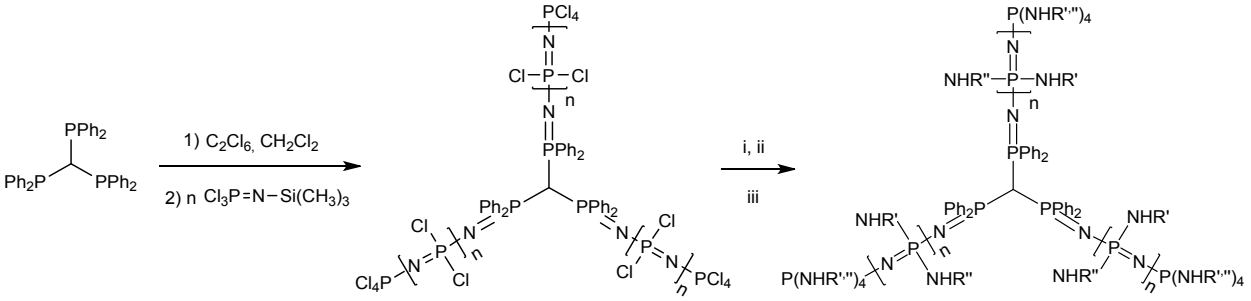

Scheme S5. i) tertbutyl-2-(2-(2-aminoethoxy)ethoxy)ethylcarbamate (R'), Et_3N, THF, 24 h; ii) Jeffamine M-1000 (R''), Et_3N, THF, 24 h; iii) CH_2Cl_2/TFA (2:1), 1h; iv) Et_3N, methanol abs., complexes **1–4**, 24 h. Ratio R':R''= 29:71.

2.1.2 ^{13}C NMR Spectrum of Complex 1

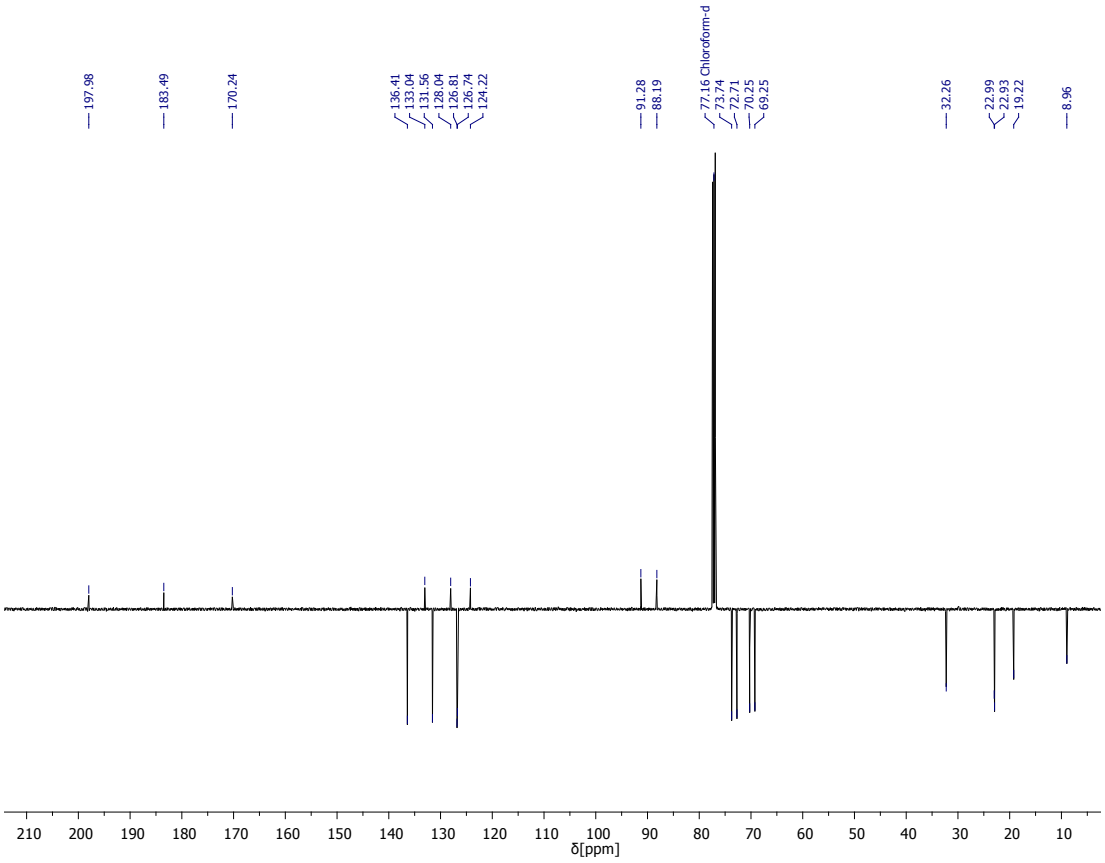

Figure S2: ^{31}C NMR spectrum of complex **1** recorded in $CDCl_3$.

2.1.3 ^{1}H NMR Spectrum of the Boc-protected Polymer

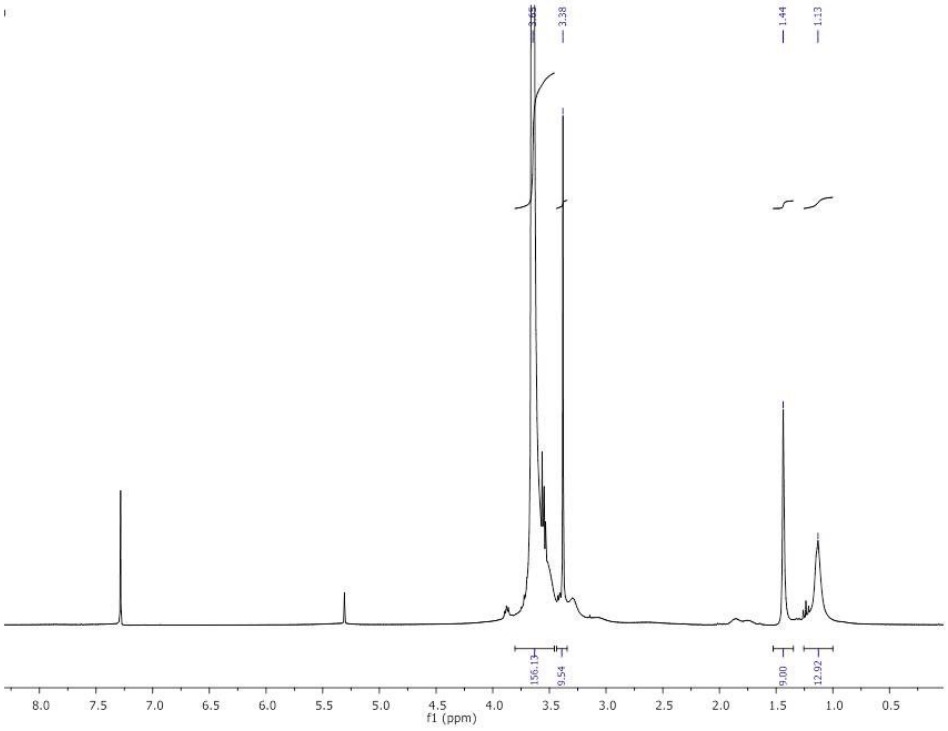

Figure S3: ^{1}H NMR spectrum of the BOC-protected polymer recorded in $CDCl_3$.

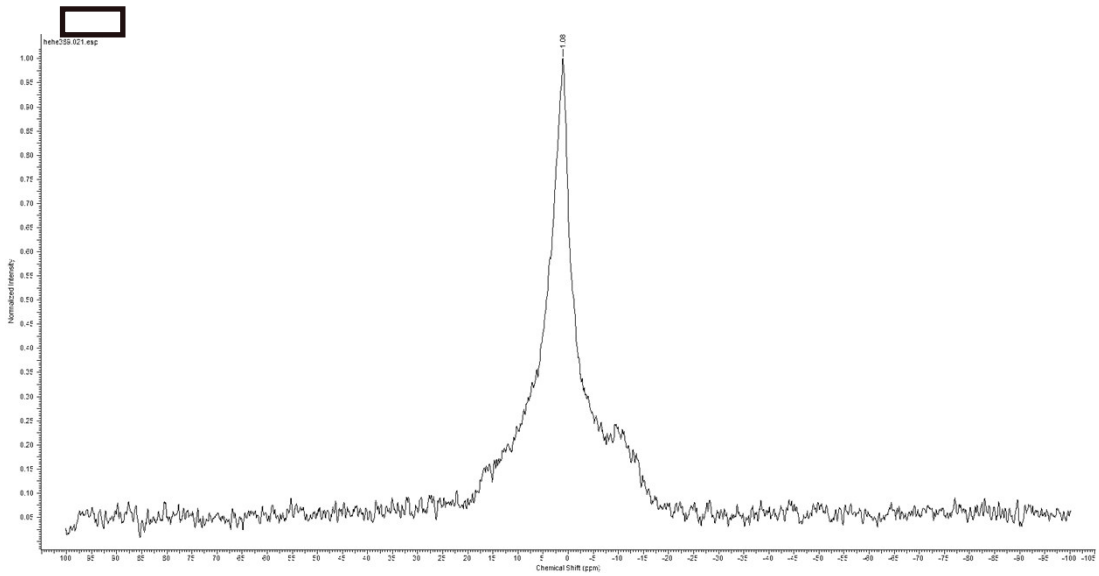

2.1.4 {^{1}H}^{31}P NMR Spectrum of the Boc-protected Polymer

Figure S4: {^{1}H}^{31}P NMR spectrum of the BOC-protected polymer recorded in $CDCl_3$.

2.1.5 {^{1}H}^{31}P NMR Spectrum of Conjugate 2a

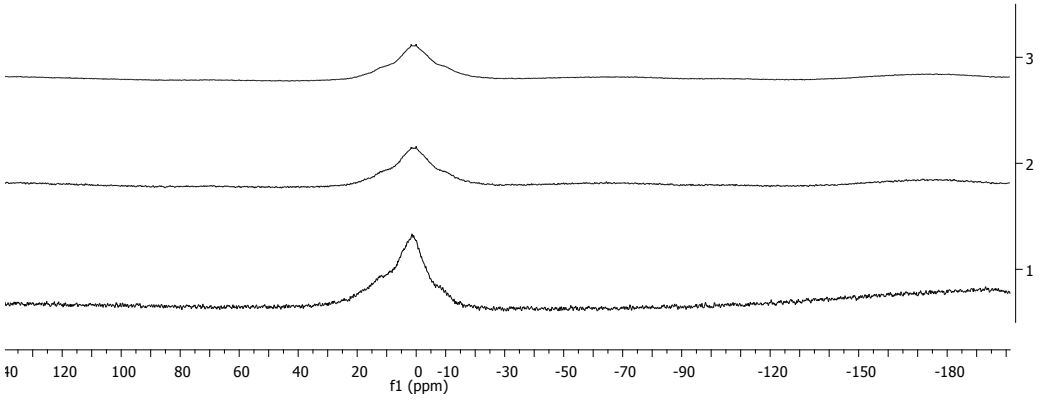

Figure S5: {^{1}H}^{31}P NMR Spectra of conjugate **2a** in aqueous solution; samples drawn and measured after one day (1), one week (2), and 4 weeks (3).

2.2 UV-Vis Investigations

A stock solution of complex **1** in DMSO (2 mM) was prepared and diluted with ammonium acetate buffer (50 mM, pH 7.0) or citric acid buffer (50 mM, pH 6.0, 5.0, 4.0, and 3.0) to a final concentration of 20 µM in 1% DMSO/buffer. An aqueous solution of conjugate **1a** (2 mM ruthenium) was diluted with ammonium acetate buffer or citric acid buffer (all 50 mM) to obtain samples of pH 7.0, 6.0, 5.0, 4.0 and 3.0. pH values were measured with an EcoScan pH 6 pH-meter equipped with a Eutech Instruments Ag/AgCl pH electrode calibrated with Alfa Aesar Specpure standard buffer solutions at pH 4.00, 7.00, and 10.00. UV−Vis spectra were recorded in 1 h intervals for 24 h at 25 °C on a PerkinElmerLambda 35 UV−Vis spectrophotometer.

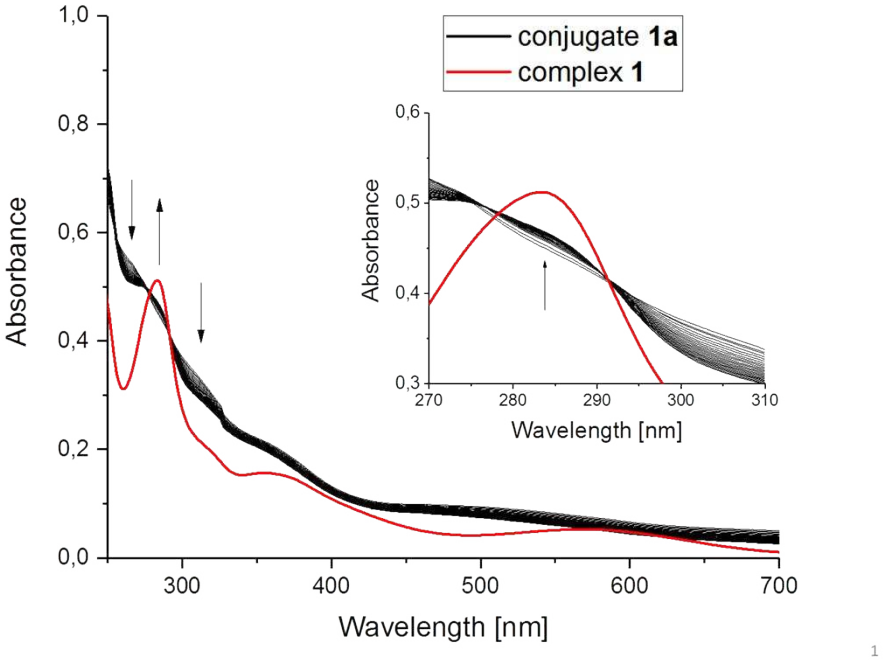

Figure S6: UV-Vis spectra of **1** and **1a** incubated at 37 °C for 24 h at pH 3.

2.3 DLS

The zeta potential measurements and the dynamic light scattering (DLS) measurements were carried out with a Malvern ZetaSizer Nano-ZS analyzer (Malvern Instruments, UK) in a disposable capillary cell and polystyrene cuvette, respectively, at 25 °C. To yield a 1 mg mL^{-1} concentration, the samples were dissolved in deionized H_2O and filtered through a 0.2 mm nylon filter. For the DLS, the 4 mW HeNe Laser was set at λ = 633 nm with the detector angle at 173° for backscattering measurements, and the volume particle size distribution was used to determine the hydrodynamic diameter.

2.4 ICP-MS Measurements

Table S1: ICP-MS parameters

ICP-MS Agilent 7500ce	
RF power (W)	1560
Cone material	Nickel
Carrier gas ($L \cdot min^{-1}$)	0.92–0.97
Make up gas ($L \cdot min^{-1}$)	0.22–0.27
Plasma gas ($L \cdot min^{-1}$)	15
Monitored isotopes	^{101}Ru, ^{102}Ru, ^{103}Rh, ^{115}In, ^{185}Re
Dwell time (s)	0.3
Number of replicates	10

The instrument was tuned on a daily basis to achieve maximum sensitivity.

Sample preparation

After the indicated drug treatment, mice were anesthetized and blood as well as urine was collected by heart and bladder punctuation, respectively. Serum was separated from the cellular blood compartment (CBC) by centrifugation at 3000 rpm for 10 min for two times and stored at -20 °C. In addition, samples of tissues (kidney, liver, lung, tumor) were collected and also stored at -20 °C for quantitative metal determination. Digestion of tissue (approx. 20 mg or 50 µL gravimetrically) was performed in nitric acid (2 mL, 20%, 4.6 M) using a microwave system (Discover SP-D, CEM Microwave Technology, Germany). The following microwave parameters were used: 200 °C, 5 min ramp time, 6 min hold time and 300 W maximal power. Digested samples were diluted with Milli-Q water resulting in nitric acid concentrations <4% and ruthenium/rhodium concentrations <15 $\mu g \cdot kg^{-1}$.

2.5 SEC-ICP-MS Analysis

Conjugate **2a** was diluted with a 10 mM ammonium acetate buffered solution to give a final ruthenium concentration of 150 µM for UV-Vis detection and 0.5 µM for ICP-MS detection. The samples were subjected to SEC-UV-Vis spectroscopy and SEC-ICP-MS, respectively. A size exclusion column (10 mm × 300 mm, 13 µm) (Superdex^{TM} 200, 10/300 GL, GE Healthcare) with an approximate bed volume of 24 mL and a linear separation range of 10–600 kDa was used. Analysis was carried out on an Agilent 1260 Infinity System (Agilent, Waldbronn, Germany) controlled by the Agilent OpenLAB CDS ChemStation Edition Rev. C.01.06[61] software. The injection volume in both experimental set-ups was 50 µL and elution was performed in isocratic mode with an aqueous solution of ammonium acetate (10 mmol·L^{-1}, pH 7.4) as mobile phase at a flow rate of 0.3 mL·min^{-1}. The column was calibrated with bovine serum albumin (66 kDa) and uracil (112.09 g·mol^{-1}) using UV–Vis detection at 240 nm. The column was coupled via a PEEK tubing directly to a MicroMist nebulizer of the ICP-MS. The ruthenium trace was recorded using the Agilent MassHunter Chromatography software package (Workstation Software, Version B.01.01, Build 123.11, Patch 4, 2012). The instrumental parameters of the ICP-MS are given in **Table S1**, in **Section 2.4**.

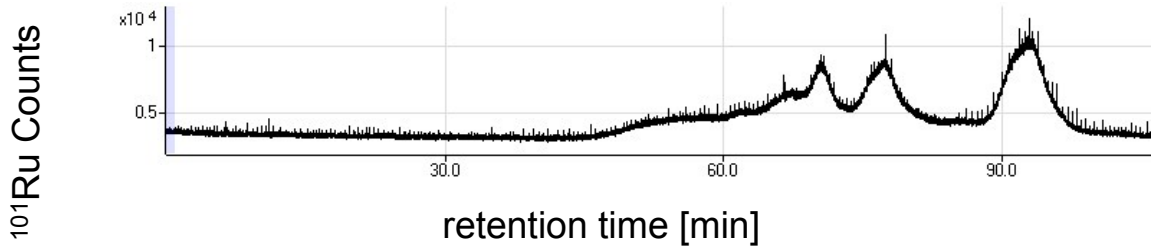

Figure S7: Degradation of conjugate **2a** due to acid-containing mobile phase (H_2O, 0.1 vol% formic acid) evaluated with SEC-ICP-MS analysis (^{101}Ru), no buffer used. The chromatogram was recorded directly without prior incubation. Different peaks might correspond to released drug, complex **2** still attached to linker sidechains or smaller fractions of the original conjugate.

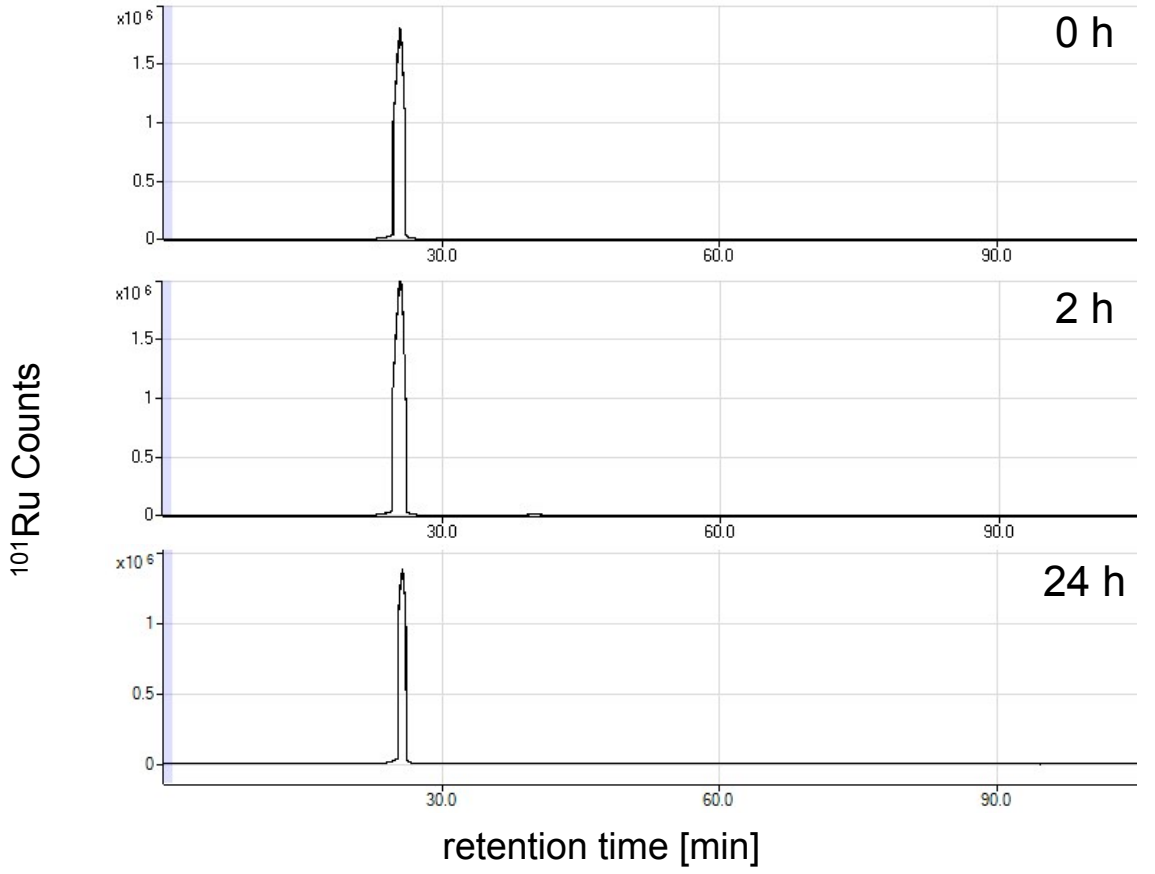

Figure S8: SEC-ICP-MS analysis of conjugate **2a**, co-incubated at 37 °C with a 10-fold excess of BSA. Sample measured after 0, 2, and 24 h of incubation (0.5 μM ruthenium, 10 mM ammonium acetate buffer). No transfer of active ruthenium-containing moiety to HSA was observed (no ruthenium traces were detected at retention times different from the signal corresponding to conjugate **2a** at 28 min even after 24 h).

3 Biological Investigations

3.1 Applied Dosages of Conjugates 1a–3a

Table S2: Overview of dosages used for animal experiments

Dosages	Conjugate 1a	Conjugate 2a	Conjugate 3a
Total amount	100 mg·kg^{-1}	100 mg·kg^{-1}	100 mg·kg^{-1}
Complex load	5.4 mg compound **1**·kg^{-1}	30 mg compound **2**·kg^{-1}	13 mg compound **3**·kg^{-1}
Metal load	1.2 mg Ru·kg^{-1}	7.5 mg Ru·kg^{-1}	3.2 mg Rh·kg^{-1}
Total amount	50 mg·kg^{-1}	50 mg·kg^{-1}	50 mg·kg^{-1}
Complex load	2.7 mg compound **1**·kg^{-1}	15 mg compound **2**·kg^{-1}	6.5 mg compound **3**·kg^{-1}
Metal load	0.6 mg Ru·kg^{-1}	3.8 mg Ru/kg	1.6 mg Rh·kg^{-1}
Total amount	-	25 mg·kg^{-1}	-
Complex load		7.7 mg compound **2**·kg^{-1}	
Metal load		1.9 mg Ru·kg^{-1}	

3.2 Organ Distribution – Metal levels

Table S3: Ruthenium und rhodium levels in [ng·mg^{-1}], data collected via ICP-MS measurements after microwave-assisted digestion of blood and tissue samples (measurement errors are within <5% RSD).

	Ruthenium levels [ng·mg^{-1}]				**Rhodium levels [ng·mg^{-1}]**	
Conjugate	**1a**		**2a**		**3a**	
Metal dose	1.2 mg·kg^{-1}	1.9 mg·kg^{-1}	3.75 mg·kg^{-1}	7.5 mg·kg^{-1}	1.6 mg·kg^{-1}	3.25 mg·kg^{-1}
Cellular blood compartment	0.70	0.19	2.05	3.97	0.09	0.34
	0.35	0.49	1.67	4.60	0.14	0.28
Kidney	4.82	2.46	4.53	9.13	3.29	4.44
	4.64	2.42	4.93	9.05	3.11	7.97
Liver	2.58	20.11	23.48	55.35	7.36	11.67
	2.74	15.02	28.67	55.70	6.53	14.30
Lung	0.35	1.27	1.87	4.74	0.57	1.46
	0.34	0.79	2.20	4.68	0.74	1.71
Serum	1.12	1.41	2.46	5.95	0.32	0.59
	1.09	1.87	4.02	8.15	0.28	0.76
Urine	0.18	0.31	0.54	-	0.54	0.26
	0.68	0.55	-	-	0.27	1.04

3.3 Anticancer Activity in vivo

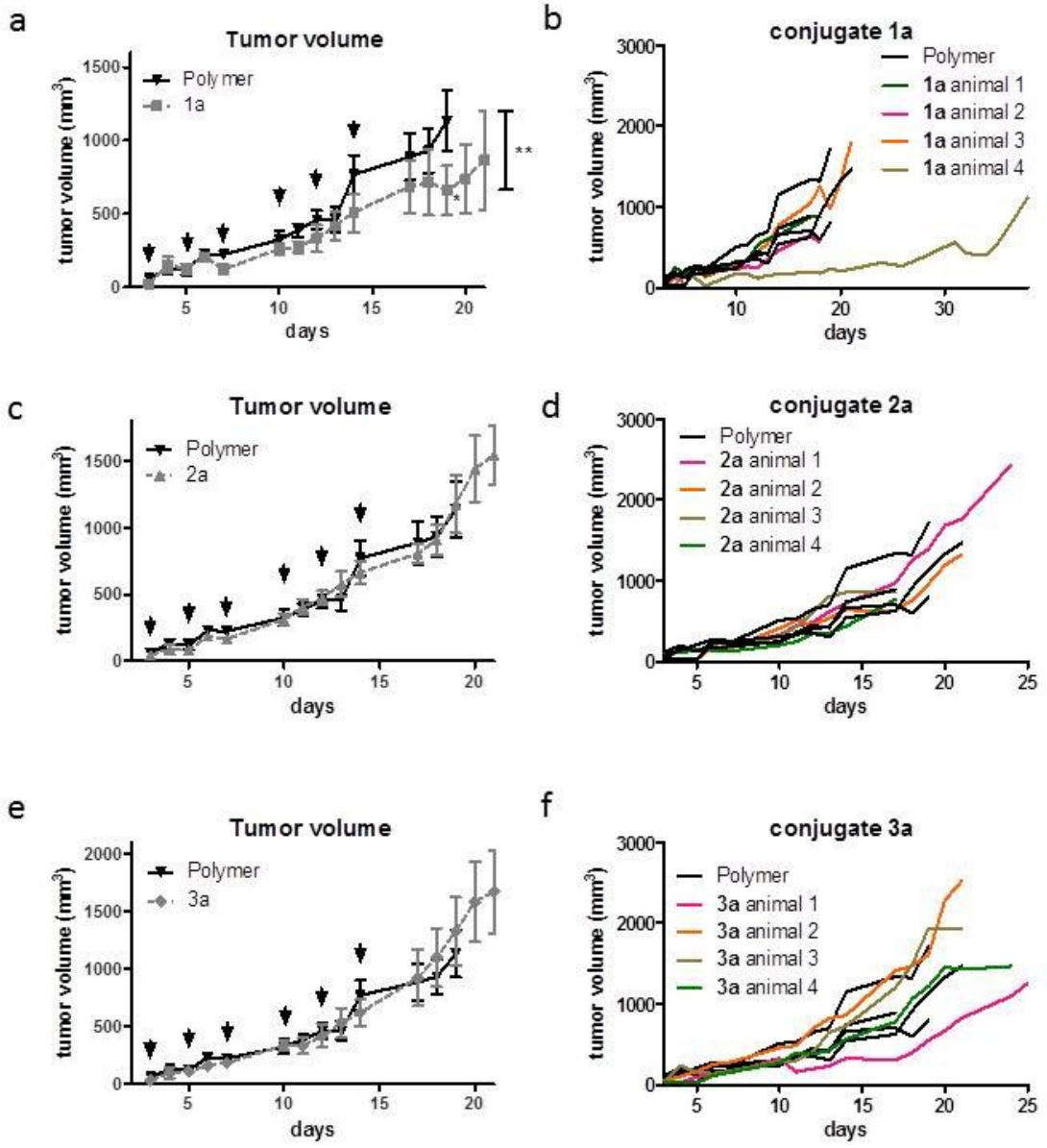

Figure S9: Anticancer activity of **1a–3a**. Murine CT-26 cells ($5x10^5$) were injected subcutaneously into the right flank of female Balb/c mice (n=4 per group). Animals were treated intravenously with **1a**, **2a** and **3a**. The applied doses were 50 $mg \cdot kg^{-1}$ for **1a** and **3**a, and 25 $mg \cdot kg^{-1}$ for 2a on day 3, 5, 7, 10, 12, and 14. Tumor volume is depicted as mean ±SD for treatment with unloaded polymer or with **1a** (a), **2a** (c) and **3a** (e). Additionally, tumor growth curves of single CT-26-bearing animals under treatment with unloaded polymer or **1a** (b), **2a** (d) and **3a** (f) are shown. **p<0.01 statistically different from unloaded polymer by two-way ANOVA (day 3-19). * p<0.05 statistically different from unloaded polymer (at day 19) by Bonferroni post test

3.4 Morphological Changes of Organs and Tissues

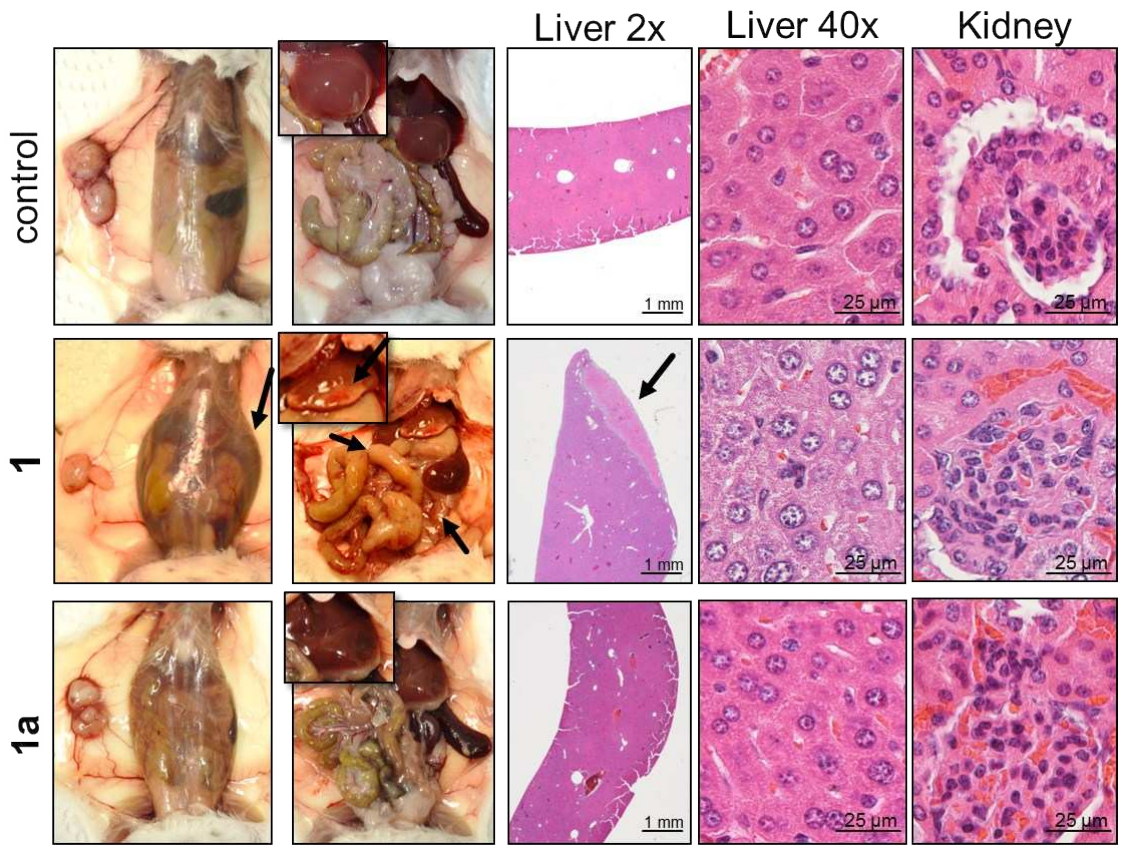

Figure S10: Representative pictures from CT-26 tumor-bearing animals treated with the indicated substances. Animals were treated with **1** (30 mg·kg^{-1} i.p.) and **1a** (50 mg·kg^{-1} i.v.) and sacrificed on day 17 and 24, respectively. Local adverse effects of treatment with **1** are indicated with arrows in pictures taken during dissection (ascites, inflated intestine, lesions on liver, growth of additional tissue) and photographs of hematoxylin/eosin-stained, paraffin-embedded liver and kidney tissue (arrow). In contrast, no macroscopic or microscopic tissue damage was found after treatment with **1a**.

3.5 Histological Evaluation of Tissue Samples

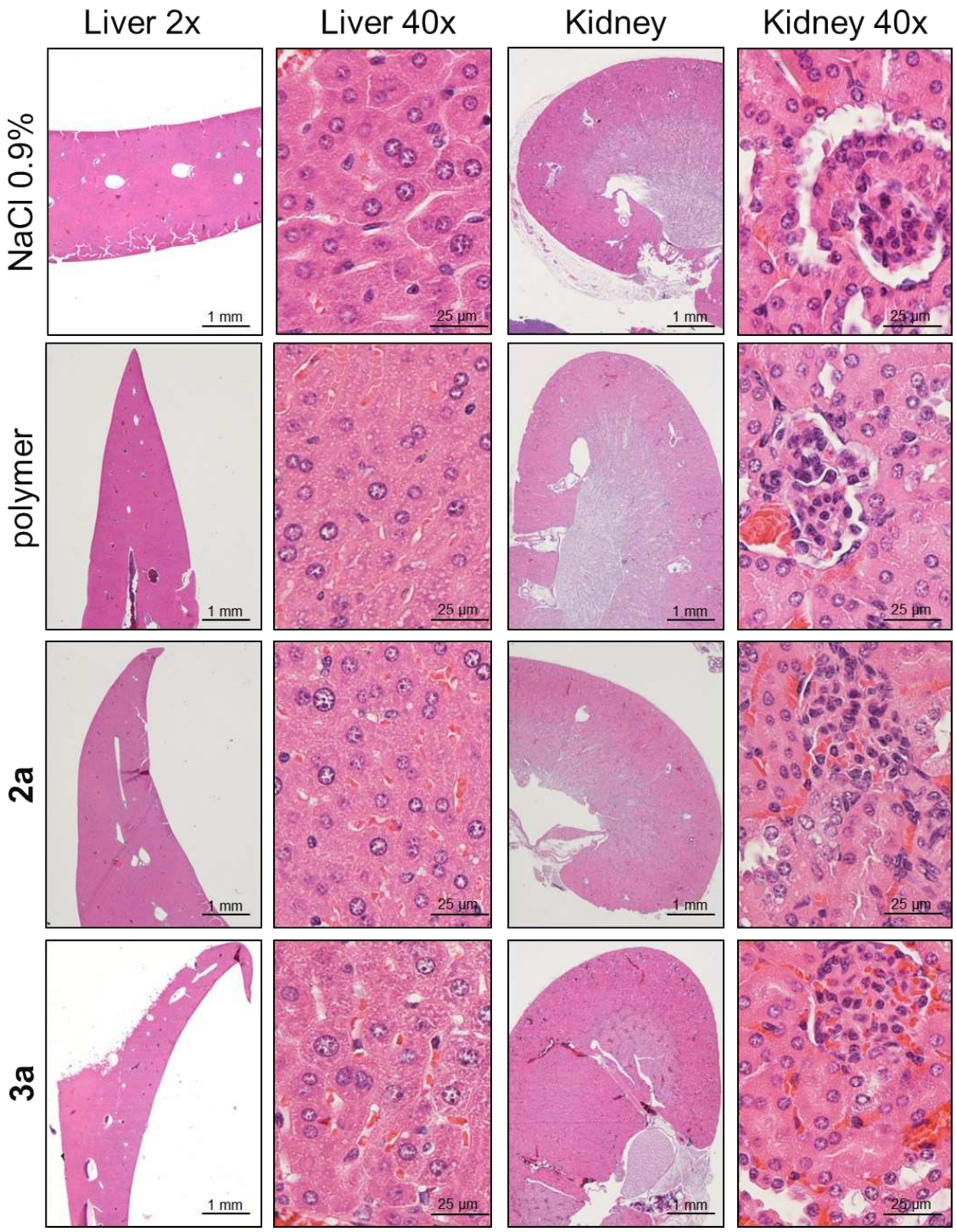

Figure S11: Histological evaluation of liver and kidney tissue after drug treatment. Animals were treated intravenously with 0.9% NaCl, unconjugated polymer, 25 mg·kg^{-1} and 50 mg·kg^{-1} of **2a** and **3a**, respectively, on day 3, 5, 7, 10, 12, and 14. Animals were sacrificed on day 24, 19, 17 and 25 and organs were formalin-fixed, paraffin-embedded and stained with hematoxylin/eosin.

4 References

[1] H. Henke, S. Posch, O. Brüggemann, I. Teasdale, *Macromol. Rapid Commun.* **2016**, *37*, 769–774.
[2] B. Wang, E. Rivard, I. Manners, *Inorg. Chem.* **2002**, *41*, 1690–1691.

Interlude: Second peer-reviewed paper

Sensitivity towards the GRP78 inhibitor KP1339/IT-139 is characterized by apoptosis induction via caspase 8 upon disruption of ER homeostasis

Schoenhacker-Alte, B., Mohr, T.; Pirker, C.; Kryeziu, K; Kuhn, P.-S.; Buck, A.; Hofmann, T.; Gerner, C.; Hermann, G., Koellensperger, G.; Keppler, B.K.; Berger, W.; Heffeter, P.

Impact Factor 6.3

https://doi.org/10.1016/j.canlet.2017.07.009

The sodium salt of trans-[tetrachlorobis(1H-indazole)ruthenate(III)], better known under the name KP1339/IT-139, had already proven distinct anticancer activity combined with exceptional good tolerability. Remarkably, KP1339 treatment caused diverse tumors to respond favorably in the phase I clinical trial. Although this response in general is considered very positive, yet, it lacks potential predictive markers for further studies. Therefore, my aim was to identify and further characterize KP1339-sensitive cancer cell models in contrast to non-responsive cell models. In more detail we could show that neither differences in ruthenium accumulation, nor sensitivity to oxidative stress or constituents of KP1339 were underlying the exceptional sensitivity. Whole genome expression arrays indicated that the biochemical response of sensitive cell lines mainly involved “response to chemical stimuli” and “regulation of cell death”. In contrast, DNA repair, metabolism and control of the cell cycle were altered in non-responsive cells. The latter was confirmed by cell culture experiments as non-responsive cells executed cell cycle arrest in G2 phase. Concurrently, sensitive cells exhibited pronounced apoptosis induction *via* activation of caspase 8 which we traced back to disruption of the ER homeostasis. The reason for the disruption was determined as depletion of key cellular chaperones including GRP78 in combination with enhanced KP1339-mediated protein damage.

The majority of practical work, writing of the manuscript, data analysis and assembly of all tables and figures was performed by myself under the supervision of W. Berger and P. Heffeter. All other authors were involved in the internal revision of the manuscript. The co-authors provided the following contributions to the practical work and data analysis: K. Kryeziu and C. Pirker performed the whole genome expression arrays. C. Pirker and T. Mohr also performed bioinformatic analysis of the data derived from the whole genome expression arrays. K. Kryeziu and A. Buck performed some of the cell viability assays. The quantification of reduced and oxidized glutathione was conducted by T. Hofmann, G. Herman and G. Koellensperger. P.-S. Kuhn was responsible for the synthesis and quality assurance of KP1339/IT-139 under the supervision of B. K. Keppler.

Cancer Letters 404 (2017) 79–88

Contents lists available at ScienceDirect

Cancer Letters

journal homepage: www.elsevier.com/locate/canlet

Original Article

Sensitivity towards the GRP78 inhibitor KP1339/IT-139 is characterized by apoptosis induction via caspase 8 upon disruption of ER homeostasis

Beatrix Schoenhacker-Alte [a, b], Thomas Mohr [b], Christine Pirker [b], Kushtrim Kryeziu [b], Paul-Steffen Kuhn [a], Alicia Buck [b], Thilo Hofmann [d], Christopher Gerner [e], Gerrit Hermann [e], Gunda Koellensperger [e], Bernhard K. Keppler [a, b], Walter Berger [b, c], Petra Heffeter [b, c, *]

[a] Institute of Inorganic Chemistry, University of Vienna, Waehringer Str. 42, A-1090, Vienna, Austria
[b] Department of Medicine I, Institute of Cancer Research, Comprehensive Cancer Center of the Medical University, Medical University of Vienna, Borschkegasse 8a, A-1090, Vienna, Austria
[c] Research Cluster "Translational Cancer Therapy Research", Vienna, Austria
[d] Department of Environmental Geosciences, University of Vienna, Althanstraße 14, A-1090, Vienna, Austria
[e] Department of Analytical Chemistry, University of Vienna, Waehringer Str. 38, A-1090, Vienna, Austria

ARTICLE INFO

Article history:
Received 12 May 2017
Received in revised form
5 July 2017
Accepted 7 July 2017

Keywords:
Sodium *trans*-[tetrachlorobis(1H-indazole) ruthenate(III)]
Ruthenium
Extrinsic pathway of programmed cell death
GRP78
Caspase 8

ABSTRACT

The ruthenium drug and GRP78 inhibitor KP1339/IT-139 has already demonstrated promising anticancer activity in a phase I clinical trial. This study aimed to identify mechanisms underlying increased sensitivity to KP1339 treatment. Based on a screen utilizing 23 cell lines, a small panel was selected to compare KP1339-sensitive and low-responsive models. KP1339 sensitivity was neither based on differences in ruthenium accumulation, nor sensitivity to oxidative stress or constituents of KP1339 (ruthenium chloride and indazole). Subsequently, the biochemical response to KP1339 was analyzed using whole genome expression arrays indicating that, while sensitive cell lines were characterized by "response to chemical stimuli" and "regulation of cell death", low-responsive cells preferentially activated pathways controlling cell cycle, DNA repair, and metabolism. Cell culture experiments confirmed that, while low-responsive cells executed cell cycle arrest in G2 phase, pronounced apoptosis induction via activation of caspase 8 was found in sensitive cells. Cell death induction is based on a unique disruption of the ER homeostasis by depletion of key cellular chaperones including GRP78 in combination with enhanced KP1339-mediated protein damage.

Introduction

Due to the major limitations (adverse effects and rapid resistance development) of systemic therapy for late stage patients, still high interest in the development of more effective and better tolerated drugs exists [1,2]. One of them is KP1339, which has already proven distinct anticancer activity, while being extraordinarily well tolerated [3]. Thus, in a clinical phase I study of KP1339,

Abbreviations: 4-PBA, 4-phenylbutyric acid; CHOP, C/EBP-homologous protein; CI, combination index; CFTR, cystic fibrosis transmembrane conductance regulator; DAPI, 4′,6-diamidine-2′-phenylindole dihydrochloride; DCF-DA, 2′,7′−dichlorofluorescin diacetate; EPR, enhanced permeability and retention; ER homeostasis, endoplasmatic reticulum homeostasis; Ero1α, endoplasmic reticulum oxidoreductase 1 alpha; FACS, fluorescence-activated cell sorting; FBS, fetal bovine calf serum; GO, gene ontology; GOrilla, gene ontology enrichment analysis and visualization tools; GRP78, 78 kDa glucose-regulated protein; GSH, glutathione; logFC, logarithmic fold change; ICP-MS, inductively coupled plasma mass spectroscopy; Ire1α, inositol-requiring enzyme 1; JC-1, 5,5′,6,6′-tetrachloro-1,1′,3,3′-tetraethylbenzimidazol-carbocyanine iodide; KP1339, sodium *trans*-[tetrachlorobis(1H-indazole)ruthenate(III)]; MTT, 3-(4,5-dimethylthiazol-2-yl)-2,5-diphenyltetrazoliumbromide; NSCLC, non-small cell lung cancer; PARP, poly(ADP-ribosyl)polymerase; PBS, phosphate-buffered saline; PERK, protein kinase-like endoplasmic reticulum kinase; ROS, reactive oxygen species; RDC, ruthenium-derived compounds; STR, short-tandem-repeat; TMAH, tetramethylammoniumhydroxide; TRAIL, tumor necrosis factor-related apoptosis-inducing ligand.

* Corresponding author. Department of Medicine I, Institute of Cancer Research, Medical University of Vienna, Borschkegasse 8a, A-1090, Vienna, Austria.
E-mail address: petra.heffeter@meduniwien.ac.at (P. Heffeter).

http://dx.doi.org/10.1016/j.canlet.2017.07.009
0304-3835/

ten cases of disease stabilization out of 38 evaluable patients were observed [3] especially for tumor entities known for very limited treatment options (e.g. NSCLC, metastasized neuroendocrine tumor, or colon cancer). One patient with a carcinoid tumor achieved a durable partial response and remained on treatment for 100 weeks. Noteworthy, dose-limiting effects (nausea, creatinine levels $\leq$ grade 2) were comparably mild [3].

The exceptional good tolerability of KP1339 is based on its dual prodrug nature: Tumor accumulation via albumin binding followed by tumor-specific activation by reduction [4–7]. This rapid binding also supports passive tumor targeting by the "enhanced permeability and retention" (EPR) effect, which describes the accumulation of larger particles but also proteins such as albumin in the intercellular space of malignant tissue due to the combination of chaotic blood vessel formation with a lack of lymph drainage [8,9]. Importantly, malignant cells frequently take up albumin by endocytosis/macropinocytosis as source of amino acids to meet the requirements of their often upregulated metabolism [10]. By this mechanism, cancer cells accumulate distinctly higher intracellular levels of protein-bound drugs compared to non-malignant tissue [9]. After uptake of albumin-bound KP1339, we propose that the second prodrug mechanism takes place: activation by reduction inside the malignant cells, which results in tumor-specific release of the reactive Ru(II) species as also seen with the indazolium salt KP1019 [11,12]. With regard to the exact mode of action, KP1339 has been recently identified as potent inhibitor of GRP78 activation [13], an ER stress-sensing chaperone [14].

For further preclinical studies, it is essential to acquire information about the intracellular mechanism of action preferably in combination with biomarkers to indicate the response of the malignant cells to treatment. As in the phase I clinical trial diverse tumors responded favorably to KP1339 treatment, the aim of this study was to identify and further characterize KP1339-sensitive cancer cell models to allow the future definition of potential markers indicative for response to KP1339 treatment.

Material and methods

Chemicals

KP1339 (Suppl. Fig. 1) was prepared as described previously [15] and dissolved in dimethyl sulfoxide (dimethyl sulfoxide concentrations in all experiments were below 1%). Tetramethylammoniumhydroxide (TMAH) was purchased from Merck (Darmstadt, Germany), TRAIL from Life Technologies (Carlsbad, California, USA), Z-VAD-FMK from Enzo Life Sciences (Lausen, Switzerland), Z-IETD-FMK (THP medical products, Vienna, Austria) and Indazole from Polivalent-95 (Chisinau, Republic of Moldova). All other substances were purchased from Sigma-Aldrich (St. Louis, MO). All solutions were freshly prepared before usage.

Cell culture

Detailed information as well as culture and MTT seeding conditions for cell lines used are provided in Supplementary Table 1. All cultures were grown under standard cell culture conditions, regularly checked for *Mycoplasma* contamination and their authentication verified either by short-tandem-repeat (STR) profiling or array comparative genomic hybridization. Fetal bovine calf serum (FBS) was purchased from PAA (Linz, Austria).

Cytotoxicity assays

Cells were plated in 96-well plates (number of used cells is given in Supplementary Table 1) and allowed to recover for 24 h before drug treatment for 72 h. Cell survival was determined by MTT assay following the manufacturer's recommendations (EZ4U, Biomedica, Vienna, Austria). Cytotoxicity was calculated using the Graph Pad Prism software (La Jolla, USA) (using a point-to-point function) and expressed as IC_{50} values calculated from full dose-response curves (drug concentrations resulting in 50% reduction of viable cells compared to untreated control cells cultured in parallel). Synergism is expressed by combination index (CI) according to Chou and Talalay [16] using CalcuSyn software (Biosoft, Ferguson, MO, USA).

Western blot analyses

Sample collection, protein separation and Western blotting were performed as described [17]. The antibodies used including source and dilutions are given in Supplementary Table 2.

Cell cycle analysis

After seeding (1×10^5 cells/well in 6-well plates) with 24 h recovery, cells were treated for 24 h and (after fixation in 70% ethanol) prepared for staining with 5 μg/ml propidium iodide as previously published [18]. Fluorescence intensity was measured by flow cytometry using a FACS Calibur (Becton Dickinson, Palo Alto, CA) and quantified by ModeFit software (Becton Dickinson and Company, New York, USA).

Preparation of DAPI-stained nuclei

Briefly, 1×10^5 cells were seeded in 6-well plates, allowed to recover for 24 h and treated for another 24 h. Subsequently, cells were collected and cytospins prepared using a cytocentrifuge (Cytospin 4, Thermo Scientific, Waltham, USA) at 400 rpm for 5 min. After fixation with ethanol/acetone (−20 °C, 1:1) cells were stained with 4′,6-diamidine-2′-phenylindole dihydrochloride (DAPI). For each slide, 200 to 300 nuclei were scored as normal, mitotic or apoptotic.

Time-lapse microscopy analyses

1×10^5 cells were seeded in a cell culture dish (3.5 cm diameter), allowed to recover for 24 h, and treated with 100 μM KP1339. Filming started immediately after treatment (a humidified incubation chamber ensured stable cell culture conditions throughout the experiment (37 °C, 5% CO_2)). Photomicrographs (20× magnification) were taken with an OLYMPUS IMT-2 inverted microscope connected to a DSLR camera (Canon 100D) every minute for 72 h.

Inductively coupled plasma mass spectroscopy (ICP-MS)

To determine cellular accumulation of KP1339, cells were incubated with 100 μM KP1339 for 3 h at 37 °C, washed twice with PBS, then lysed in 500 μl of TMAH at room temperature for 5 min. The resulting lysates were dissolved in 25 ml 0.6 M HNO_3. Ruthenium concentrations were determined using an Elan 6100 (PerkinElmerSciex Instruments, Boston, MA).

Total-RNA isolation and whole genome gene expression array

All details on RNA preparation and array analysis are given in the Supporting Information.

Results

Cytotoxicity screen for KP1339 sensitivity

In order to identify cell models with enhanced sensitivity towards KP1339, a broad panel of cell lines (n = 23) was screened (Fig. 1a). In general, responsiveness to KP1339 was not associated with a specific tumor entity, p53- or k-ras mutation status. Thus, most of the tested cell lines had IC_{50} values around 100 μM. However, five cell lines were characterized by enhanced KP1339 sensitivity ($IC_{50} \leq 50$ μM): Capan1, Capan2, HCC3, and HCT116 as well as its p53-deleted subline HCT116/p53ko. For subsequent studies, a panel of five models was chosen: sensitive Capan1 and HCT116 vs. low-responsive CCL13, SW480 and KB-3-1. First, we tested whether the sensitivity towards KP1339 was based on its constituents (ruthenium, indazole) or increased drug accumulation in sensitive cell lines. Table 1 clearly demonstrates that sensitivity to KP1339 is not linked to enhanced responsiveness to ruthenium or indazole treatment. In addition, no significant difference in drug accumulation was detected (Table 1). Also, altered sensitivity to disturbance of redox homeostasis did not offer an explanation, as neither sensitivity to H_2O_2 (Table 1) nor cellular GSH levels (Suppl. Fig. 2a) correlated with KP1339 responsiveness. In accordance, also no correlation of KP1339 sensitivity with the levels of drug-induced intracellular reactive oxygen species induction was found (Suppl. Fig. 2b).

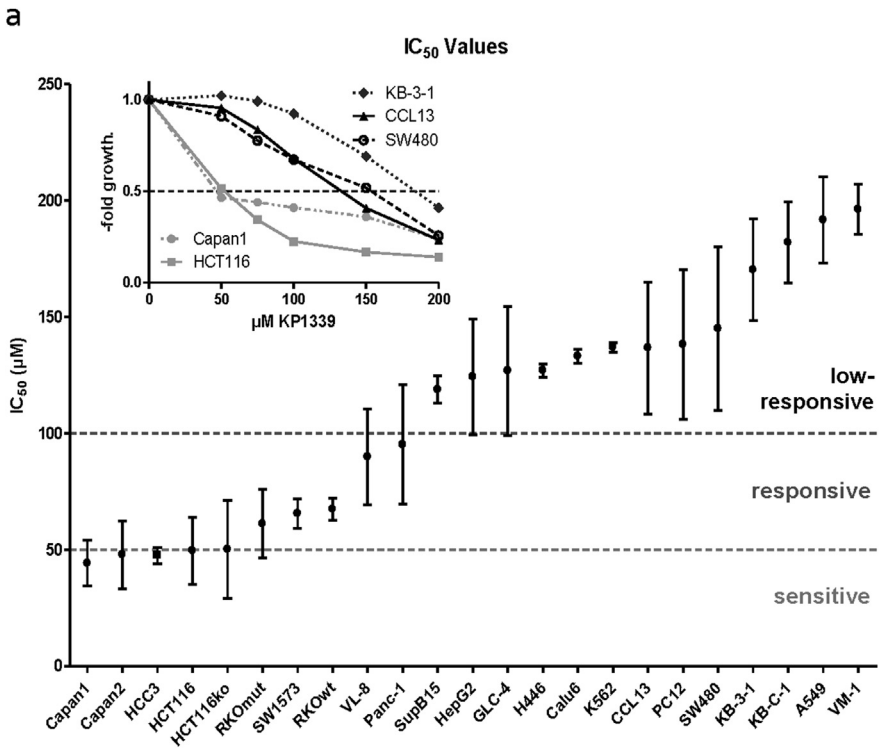

Fig. 1. KP1339 sensitivity screening in cancer cell lines and panel selection for further investigations. 23 cell lines were screened for sensitivity to KP1339 treatment and classified by their IC_{50} value as sensitive, medium or low-responsive. The IC_{50} values were calculated from MTT assays performed after 72 h KP1339 treatment. Data represent the mean and SD of the IC_{50} values of at least two independent experiments performed in triplicates. Insert: representative full dose-response curves of the 5 cell lines selected for further analyses.

Table 1
Sensitivity against KP1339, its constituents and H_2O_2-induced ROS as well as cellular ruthenium accumulation following KP1339 exposure.

Investigated factor		Capan1	HCT116	SW480	KB-3-1
IC_{50} (µM)	KP1339	44 ± 10	50 ± 14	145 ± 35	170 ± 22
	$RuCl_3$	>200	>200	>200	>200
	Indazole	>400	>400	>400	>400
	H_2O_2	22 ± 4	10 ± 2	12 ± 2	18 ± 8
Cellular accumulation of Ru [ng Ru/10^5 cells]		7 ± 1.5	1.6 ± 0.45	2.2 ± 0.37	2.1 ± 0.7

Gene expression changes induced by short-time-KP1339 treatment

To gain a deeper insight into the characteristics associated with sensitivity to KP1339, whole genome expression arrays of mRNA samples isolated from our test panel after 3 and 6 h of incubation with 100 µM KP1339 were performed and compared to untreated samples. Already after 3 h exposure, distinct changes in gene expression were observed in all four cell lines tested. Notably, sensitive cells reacted faster and more pronounced to KP1339 treatment (~10-fold more significantly changed genes after 3 h, ~3-fold after 6 h) than low-responsive cell models (Fig. 2a). Thus, the number of mRNAs changed by KP1339 exposure ($p < 0.001$) was 6386 and 5382 for Capan1, 7302 and 7621 for HCT116, 747 and 2641 for SW480 vs. 575 and 2721 for CCL13 after 3 and 6 h, respectively (Fig. 2b and c). Interestingly, the sensitive models appeared to react not only faster but also in a different mode than the low-responsive models, which was reflected by the distinctly increased number of mRNAs exclusively changed in the two sensitive as compared to the resistant models after 3 h (8385 vs. 253, proportion 30:1; Fig. 2b), while after 6 h, this proportion shifted to 5:1 (6258 vs. 1253; Fig. 2c). This shift indicated a later onset of response in low-responsive cells. Concordantly, the number of differentially expressed mRNAs shared between all four cell lines increased over time (74 after 3 h vs. 577 after 6 h) (Fig. 2b and c).

As a next step, these data were analyzed using the gene ontology enrichment analysis and visualization tools (GOrilla) of Eden et al. (2009) [19]. For easier comparison, GOrilla-derived data (Suppl. Fig. 3, 4) of GO terms of interest are presented as heat map (Fig. 2d and e). While sensitive cell lines upregulated the GO terms indicative for “response to chemical stimuli”, “regulation of cell death” and “chromatin organization” (Fig. 2d), in low-responsive models preferentially GO terms regarding regulation of “cell cycle” and “metabolism” were enriched (Fig. 2e). Furthermore, indications for protein damage were found in all cell lines (Suppl. Fig. 5).

Cell cycle distribution is affected by KP1339 treatment

To examine the dynamics of KP1339 activity, the selected cell line panel was analyzed by time-lapse microscopy. These studies revealed that, in line with the array data, sensitive cell lines were characterized by enhanced apoptosis induction, with the majority of these KP1339-induced cell deaths occurring 20–30 h after treatment (Fig. 3a, Suppl. Fig. 6a). In contrast, low-responsive cell

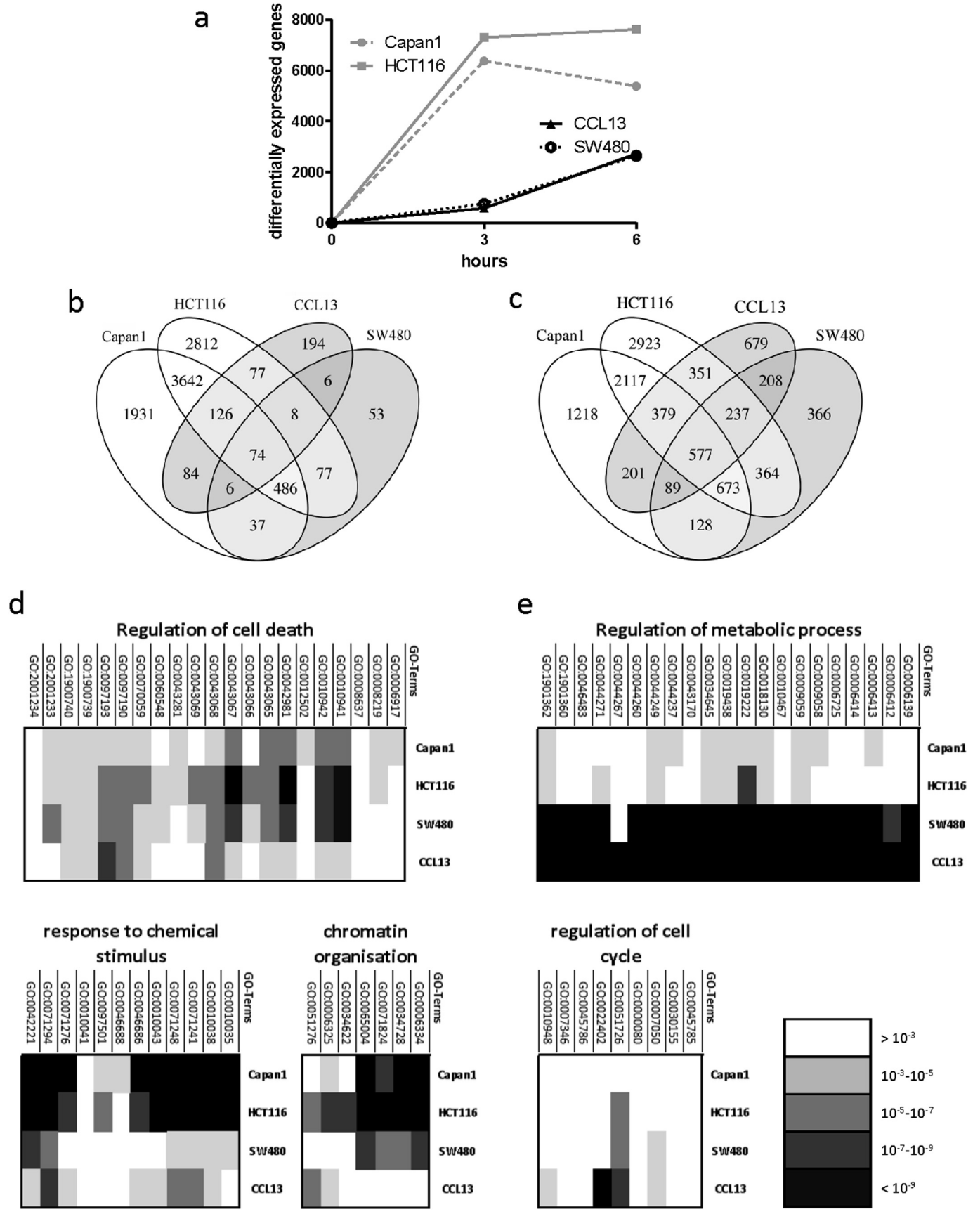

Fig. 2. Whole genome gene expression arrays after short-time KP1339 exposure. Whole genome gene expression arrays were performed with mRNA isolated from sensitive and low-responsive cells that were either untreated or treated with KP1339 for 3 h and 6 h. a) Number of differentially expressed genes (p-value < 0.001) in sensitive and low-responsive cell lines at the indicated time points. b, c) Venn diagrams of significantly altered mRNAs (p-value < 0.001) for all tested cell lines after (b) 3 h and (c) 6 h of treatment. d, e) Upregulation of selected GO-terms after 6 h treatment compared to respective control is shown as heat maps (p value is indicated by the gray scale on the right).

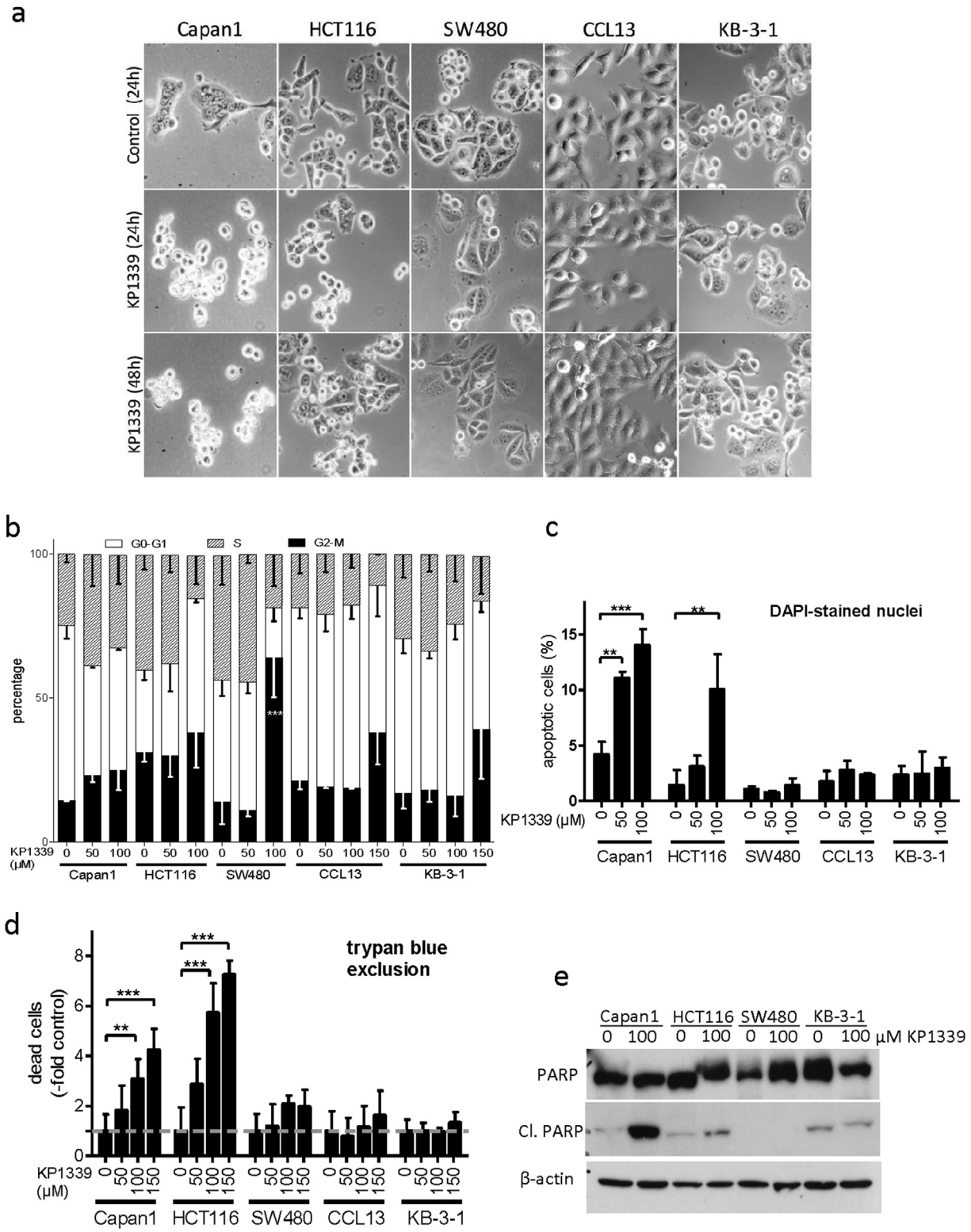

Fig. 3. Changes in cell cycle distribution upon KP1339 treatment. Impact of KP1339 treatment on Capan1, HCT116, SW480 and KB-3-1 cells at the indicated concentrations was investigated by time-lapse microscopy or FACS analyses. a) Representative phase-contrast photomicrographs to indicate morphologic changes of KP1339-treated Capan1, HCT116, SW480, CCL13 and KB-3-1 cells compared to their untreated controls, were taken after 24 h and 48 h treatment with 100 µM KP1339. b) Cell cycle analysis was done by flow cytometry determining the DNA content of the indicated ethanol-fixed, PI-stained cells after 24 h treatment with the indicated drug concentrations. Percentages of 25 000 cells in G0/G1, S and G2/M phase of cell cycle were calculated by Cell Quest Software. c) Impact of KP1339 treatment on Capan1, HCT116, SW480 and KB-3-1 cells at the indicated concentrations was investigated using DAPI-stained nuclei. Percentage of cells with visible apoptotic bodies was determined after KP1339 treatment for 24 h. Morphological features of 300–500 nuclei of at least 2 slides for each concentration were analyzed by DAPI staining. Percentages of apoptotic nuclei at the indicated concentrations are shown. d) The percentage of dead cells was evaluated counting viable cells using trypan blue exclusion test. The experiment was done in triplicates, at least 80 cells were scored per sample. e) Caspase-induced cleavage of PARP was determined via Western blotting. Antibodies used are described under Material and Methods. All p-values were calculated by one-way ANOVA with Bonferroni post test. $^{**}p < 0.01$, $^{***}p < 0.001$.

lines depicted tendencies towards cell flattening and reduced proliferation (Fig. 3a). Subsequent cell cycle analysis showed that this was based on an increased G2/M population in all three low-responsive cell lines after KP1339 treatment (Fig. 3b). Also, sensitive Capan1 and HCT116 depicted a slight (but not significant) increase of both G2/M and S fractions. Nevertheless, this was far less pronounced than in low-responsive models. Further evaluation of DAPI-stained nuclei from KP1339-treated cells led to the conclusion that cell division in low-responsive cells was blocked mainly in G2 phase, as no increase in the mitotic cell fraction was detected (Suppl. Fig. 6b). Taken together, this indicates that sensitivity towards KP1339 is associated with enhanced cell death induction.

KP1339-mediated cell death is caspase 8-dependent

To evaluate the apoptosis-inducing potential of KP1339 in sensitive models, DAPI-stained nuclei were evaluated after drug treatment, which revealed enhanced levels of dead cells exclusively in sensitive Capan1 and HCT116 models (Fig. 3c). This finding was in line with trypan blue exclusion assays (Fig. 3d) as well as the occurrence of the PARP cleavage product at 89 kD indicative for activation of the caspase-mediated cell death (Fig. 3e). Thus, activation of the caspase cascade was investigated. Remarkably, although some activation of the caspase 3/7 axis was detected (Fig. 4a), there was no correlation with KP1339 sensitivity as HCT116 responded similarly as compared to the low-responsive cell lines. Besides, neither cleavage of caspase 9 (Suppl. Fig. 7) nor strong mitochondrial membrane depolarization (measured by JC-1 stain, data not shown) was detectable after KP1339 treatment at the concentrations used. This suggests that the intrinsic pathway of apoptosis [20,21] was not the main driver for KP1339-induced cell death of sensitive cells. In contrast, cleavage of caspase 8 in a time-dependent manner was found (Fig. 4b), which is indicative for apoptosis via the extrinsic pathway [22,23]. Low-responsive KB-3-1 cells did not show increased cleavage of this protein. Interestingly, these blots also suggested that our SW480 clone has only low (to undetectable) caspase 8 expression (Suppl. Fig. 7).

To investigate the role of caspase 8 in the cell death induced by KP1339, caspase inhibitors either for pan-caspase (Z-VAD-fmk) or specific for caspase 8 (Z-IETD-fmk) were used. DAPI-stained nuclei (Fig. 4c) clearly illustrated that sensitive cells treated with KP1339 in combination with caspase inhibitors resulted in decreased cell death compared to KP1339 alone. Low-responsive CCL13 and KB-3-1 exhibited enhanced apoptosis when treated with the caspase 8 inhibitor, whereas the pan-caspase inhibition did not alter apoptosis levels in these cells.

Basal expression of death receptors DR4/5 is associated with but not underlying responsiveness to KP1339 and its synergism with TRAIL

To further evaluate players in the extrinsic pathway, the above-described mRNA expression array data were analyzed concerning death receptors and their ligands. Notably, the sensitive Capan1 and HCT116 were characterized by higher basal mRNA levels of death receptors 4 and 5, while low-responsive cells displayed stronger Fas receptor expression (Suppl. Fig. 8a). However, no mRNA increase of any death ligands or receptors was observed in all cell lines after short-term KP1339 treatment (Suppl. Fig. 8b and c). Next, we investigated the impact of TRAIL (the ligand of death receptor 4 and 5) on the activity of KP1339. These experiments revealed that combination of KP1339 with TRAIL was highly synergistic in sensitive cell lines (combination indices (CI values) around 0.3) (Fig. 4d). With regard to low-responsive cells, only KB-3-1 depicted a slight synergism. Interestingly, using higher doses of KP1339, this synergism was most pronounced in the low-responsive, caspase 8-proficient KB-3-1 and CCL13 cells (Suppl. Fig. 9). In accordance to the expectations, the low-level caspase 8-expressing SW480 did not respond to this combination treatment (Fig. 4d, Suppl. Fig. 9). Together this indicates that KP1339 activates caspase 8 signaling only to some extent and probably in a death receptor-independent manner, which can be further potentiated by combination with TRAIL. Moreover, sensitive models seem to be more susceptible to this (combined) activation of the extrinsic cell death pathway.

Caspase 8 activation after KP1339 treatment is initiated by disruption of ER homeostasis

As activation of the death receptor axis did not seem to be the main driver of KP1339-induced apoptosis, alternative mechanisms for caspase 8 activation were investigated. Noteworthy, death receptor-independent caspase 8 activation through ER stress was reported [24], which is of interest as (in line with the GRP78-inhibitory potential of KP1339) ER stress induction was also suggested for our test drug [13,25]. Therefore, ER stress marker expression was assessed in sensitive vs. low-responsive cell models after KP1339 treatment (Fig. 5a). Indeed, severe deregulations of several ER proteins were found: besides the ER-stress sensor GRP78 (BIP), also the signaling molecules PERK, Ire1α and Ero1α as well as the protein chaperon calnexin were strongly down-regulated especially in sensitive models. Only in case of CHOP, an ER stress-activated transcription factor [14], a concentration-dependent increase of protein expression was found in Capan1 and HCT116, whereas CCL13 and KB-3-1 depicted a minor or no increase in expression of this protein (Fig. 5a). Noteworthy, viability experiments using the known ER stress inducer thapsigargin revealed no correlation with KP1339 (Suppl. Fig. 10).

As a next step, we investigated the impact of the chemical chaperon 4-phenylbutyric acid (4-PBA) on KP1339 activity. This drug was shown to prevent the aggregation of misfolded and denaturated proteins in the ER lumen (e.g. caused by mutation of the cystic fibrosis transmembrane conductance regulator (CFTR) [26] or inhibition of ER-specific Ca^{2+} pumps by thapsigargin [27,28]). 4-PBA co-treatment had strong synergistic activity in all low-responsive cell lines (CI values down to 0.07), which was far less pronounced in the KP1339-sensitive models (Fig. 5b, Suppl. Fig. 11). Together, these findings indicate that there is indeed a difference between sensitive and low-responsive cell lines with regard to KP1339-induced deregulation of ER homeostasis. However, this is not based on a general enhanced sensitivity to ER stress but on different responses in the ER signaling pathways.

Discussion

KP1339 is a ruthenium(III)-based anticancer agent with promising anticancer activity [3]. With regard to its mode of action, KP1339 can be considered as double prodrug combining selective tumor targeting via albumin binding with tumor-specific activation by reduction, which results in targeted release of a reactive Ru(II) species [12]. In addition, KP1339 has been recently identified as potent inhibitor of GRP78 [13], an ER stress-sensing chaperone [14]. In order to support the further clinical development of KP1339, the presented study was performed to find factors associated with enhanced cellular KP1339 sensitivity. Our investigations revealed that unlike many other compounds (e.g. cisplatin) [30], KP1339 responsiveness is not associated with drug uptake or mutation of p53 and k-ras. This independence of KP1339 from p53 suggests, that in contrast to some reports regarding its indazolium analogue KP1019 (e.g. in yeast [31]), DNA damage is not a major mediator of its activity. In addition, KP1339 sensitivity neither correlated with

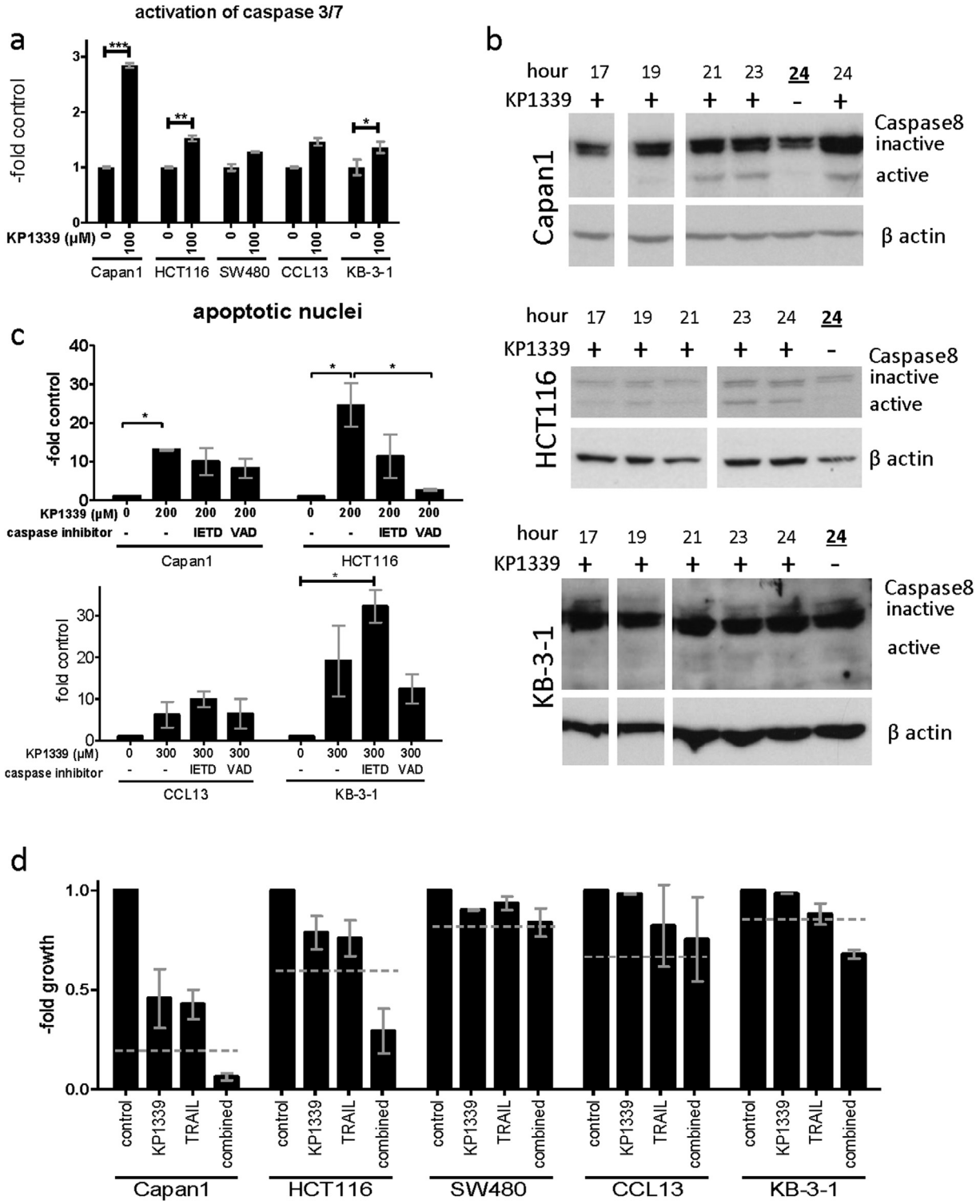

Fig. 4. Involvement of caspases in KP1339-induced cell death. Induction of apoptosis in the indicated cell models was determined after treatment with KP1339 for 24 h. a) To further investigate the caspases involved in the execution of KP1339-mediated cell death CaspaseGlo® assay was performed according to the manufacturer's protocol. b) Time-dependent activation of caspase 8 was tested by Western blotting. c) The relevance of caspase activation was assessed by DAPI stain of cells that were treated with a combination of KP1339 with 20 µM of caspase 8 inhibitor Z-IEDT-fmk (IETD) or pan-caspase inhibitor Z-VAD-fmk (VAD) as indicated. All p-values were calculated by one-way ANOVA with Bonferroni post test. *$p < 0.05$, **$p < 0.01$, ***$p < 0.001$; d) Cells were treated with 50 µM KP1339 and 25 ng/ml TRAIL, which is a known activator of caspase 8, both as single agents and as combination. Cell viability was assessed by MTT assays performed after 72 h treatment. Data represent the mean and SD of at least two independent experiments performed in triplicates. Inserted lines represent the expected values for additivity.

cellular GSH levels nor KP1339-induced ROS production. For in depth investigations, sensitive as well as low-responsive models were evaluated by mRNA expression arrays after short-term treatment. Concerning the reaction to KP1339, it became evident that sensitive cell lines distinctly differ from low-responsive ones regarding number as well as onset of gene expression alterations. Similar observations were reported for other metal compounds such as e.g. cadmium in barley [32] and mercury derivatives in

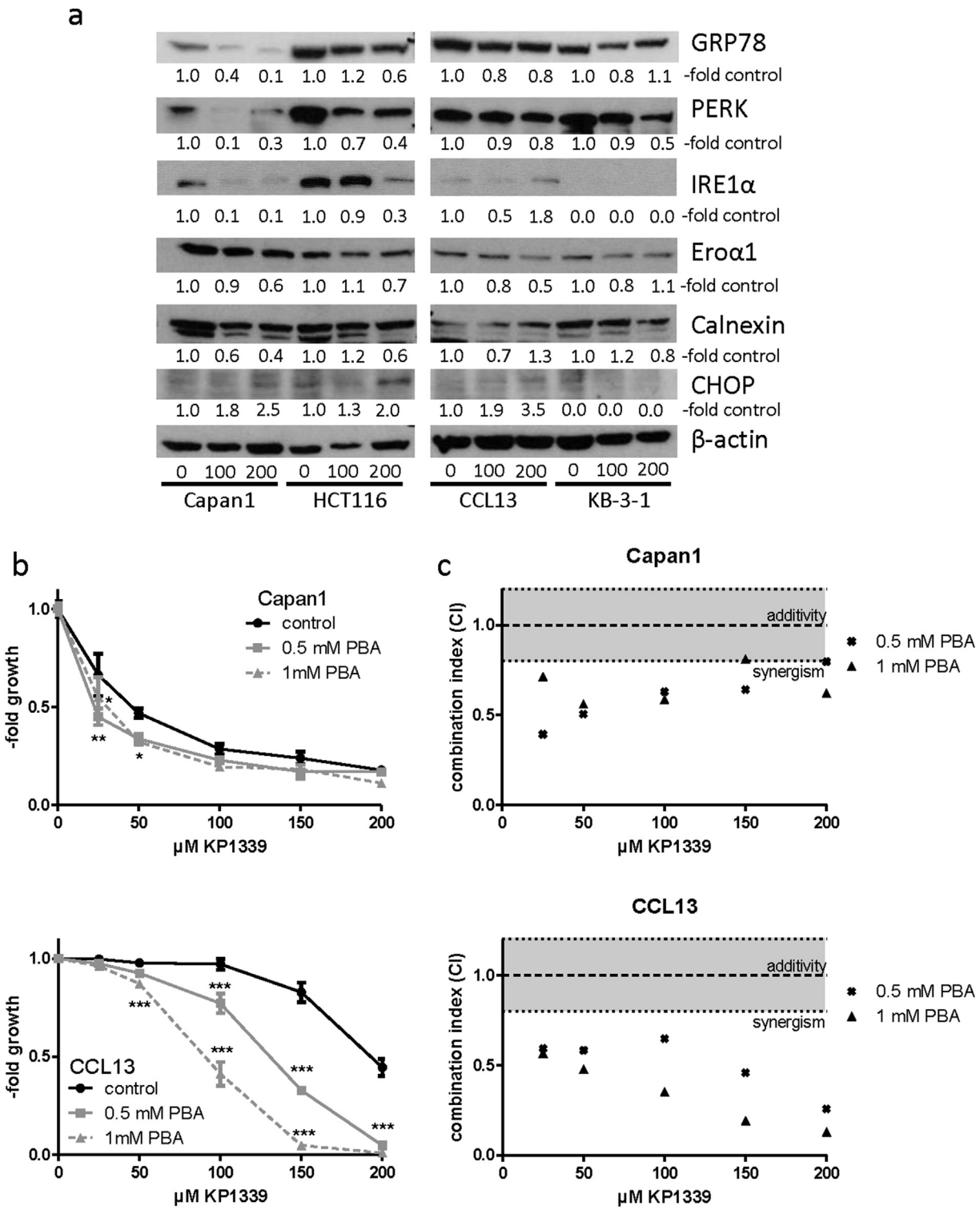

Fig. 5. Deregulation of the ER homeostasis by KP1339. a) Expression levels of diverse proteins involved in ER stress detection and signaling were determined in the indicated cell models after treatment with KP1339 for 24 h. Band intensity was quantified using ImageJ, first normalized to β-actin and then normalized to the respective control. b) Representative full dose-response curves of KP1339 combined with the chemical chaperone 4-PBA are exemplarily shown for Capan1 and CCL13. Cells were pre-incubated with the indicated concentrations of 4-PBA for 4 h prior to application of KP1339. Cell viability was assessed by MTT assays performed after 72 h treatment. p-values were calculated by two-way ANOVA with Bonferroni post test. *$p < 0.05$, **$p < 0.01$, ***$p < 0.001$. c) Combination indices (CI) were calculated using CalcuSyn software.

Caenorhabditis elegans [33], where resistance was comparably associated with a more specific and narrowed gene response. This indicates that resistance to treatment is a controlled process, while sensitivity is connected to a rather unspecific response. With regard to the specific biological processes, sensitive cell lines upregulated "response to chemical stimuli", "cell death" and "chromatin organization", while in low-responsive ones preferentially "cell cycle" and "metabolism" but also "protein damage" as well as some DNA

damage terms were preferentially enriched. This again supports the hypothesis that KP1339 is not a DNA-damaging agent [12,15], but has also other (probably protein) targets [34].

Subsequent wet lab analyses confirmed that indeed KP1339 treatment leads to increased cell death in sensitive cells, while low-responsive cells were characterized mainly by cell cycle arrest in G2 phase. Unexpectedly (contrary to reports on KP1019 [35,36]), we found neither mitochondrial membrane depolarization nor cleavage of caspase 9 at cytotoxic KP1339 concentrations in the sensitive cell models. In contrast, time-dependent cleavage of the initiator caspase 8 was detected together with activation of the down-stream effector caspases 3/7. Moreover, inhibition of this caspase pathway rescued sensitive cells from KP1339-induced cell death. These data are in good agreement with a report on activation of caspase 8 (however, in combination with caspase 9) by a panel of ruthenium (II) compounds (RDC) in HCT116 cells [37].

Regarding the underlying mechanisms leading to caspase 8 induction, the binding of death ligands like FASL or TRAIL to their respective receptors is the best-described process [22,23]. Notably, KP1339-sensitive Capan1 and HCT116 were characterized by higher basal levels of death receptors 4 and 5, while low-responsive cells displayed higher Fas receptor expression. Yet, despite a certain synergism of KP1339 with TRAIL, neither the expression of the death receptors nor of the respective ligands was altered upon KP1339 treatment. Whether transcription-independent release of death ligand proteins is induced by KP1339 is a matter of ongoing investigations. Alternatively, ligand-independent death receptor activation by the ruthenium compound could be involved (comparable to other compounds [24,38,39]).

Besides this commonly accepted mechanism, several initiators for death receptor-independent activation of caspase 8 are reported: In anoikis, a special form of cell death that is induced by cell detachment from extracellular matrix [40–42], several publications indicate integrins and caspase 8 as key players [43,44]. However, the exact mechanism of caspase 8 activation in integrin-dependent cell death is not clarified yet. With regard to ruthenium, a recent publication showed that the ruthenium(III) drug NAMI-A inhibited invasion of HCT116 cells via integrin $\alpha5\beta1$ [45]. Interestingly, preliminary data indicate that development of acquired KP1339 resistance could be associated with changes of the integrin pattern (data not shown). However, there are so far no indications that the intrinsic sensitivity of certain cell lines (like HCT116 and Capan1) is associated with differences in integrin expression (data not shown).

On the other hand, activation of caspase 8 through ER stress via interaction of CHOP has recently been shown [24]. This is of interest, as we detected (in line with earlier publications [13,25]) upregulation of CHOP in sensitive cells after KP1339 treatment. Furthermore, KP1339-induced deregulation of proteins involved in detection and signaling of ER stress were found. As we hypothesized that sensitive cells could be characterized by general ER stress vulnerability [13,25,34], the known ER stress inducer thapsigargin was tested [27,28]. However, no correlation between sensitivity to KP1339 and thapsigargin was found. In contrast, all low responsive models were characterized by a very strong synergistic activity of KP1339 with 4-PBA. This is of interest, as 4-PBA is a compound known as “chemical chaperon”, shown to prevent the aggregation of misfolded and de-naturated proteins in the ER lumen. Thus, the synergism indicates that KP1339 is not solely an ER stress-inducing drug. In contrast, the combination of ruthenium-protein adducts with the GRP78-inhibitory potential of this drug seems to induce a complex and unique deregulation of the ER homeostasis, which needs to be further elaborated in subsequent in-depth studies.

Taken together, this study reports that cell death induction upon KP1339 treatment is based on a unique disruption of the ER homeostasis by depletion of key cellular chaperones including GRP78 in combination with enhanced KP1339-mediated protein damage.

Funding

This work was performed within the Research Cluster Translational Cancer Therapy Research Vienna and supported by the Fellinger Krebsforschung. The funding sources had no involvement in collection, analysis and interpretation of data as well as in the decision to submit the article for publication.

Acknowledgements

We are indebted to Sushilla van Schoonhoven and Mirjana Stojanovic for competent technical assistance as well as skillful handling of cell cultures. Furthermore, we are grateful to Irene Herbacek for fluorescence-activated cell sorting analysis. Many thanks go to Rita Dornetshuber, Diana Groza and Carina Dinhof for inspiring discussions.

Appendix A. Supplementary data

Supplementary data related to this article can be found at http://dx.doi.org/10.1016/j.canlet.2017.07.009.

Conflicts of interest

None.

References

[1] F.M. Muggia, A. Bonetti, J.D. Hoeschele, M. Rozencweig, S.B. Howell, Platinum antitumor complexes: 50 Years since Barnett Rosenberg's discovery, J. Clin. Oncol. Off. J. Am. Soc. Clin. Oncol. 33 (2015) 4219–4226.
[2] J.T. Hartmann, H.-P. Lipp, Toxicity of platinum compounds, Expert Opin. Pharmacother. 4 (2003) 889–901.
[3] H.A. Burris, S. Bakewell, J. Bendell, J. Infante, S. Jones, D. Spigel, et al., Safety and activity ot IT-139, a ruthenium-based compound, in patients with advanced solid tumors: a first-in-human, open label, dose escalation phase 1 study with expansion cohort, ESMO Open 1 (2016) e000154, http://dx.doi.org/10.1136/esmoopen-2016-000154.
[4] A.K. Bytzek, G. Koellensperger, B.K. Keppler, G.H. C, Biodistribution of the novel anticancer drug sodium trans-[tetrachloridobis(1H-indazole) ruthenate(III)] KP-1339/IT139 in nude BALB/c mice and implications on its mode of action, J. Inorg. Biochem. 160 (2016) 250–255.
[5] S.W. Chang, A.R. Lewis, K.E. Prosser, J.R. Thompson, M. Gladkikh, M.B. Bally, et al., CF3 derivatives of the anticancer Ru(III) complexes KP1019, NKP-1339, and their imidazole and pyridine analogues show enhanced lipophilicity, albumin interactions, and cytotoxicity, Inorg. Chem. 55 (2016) 4850–4863.
[6] O. Domotor, C.G. Hartinger, A.K. Bytzek, T. Kiss, B.K. Keppler, E.A. Enyedy, Characterization of the binding sites of the anticancer ruthenium(III) complexes KP1019 and KP1339 on human serum albumin via competition studies, J. Biol. Inorg. Chem. JBIC Publ. Soc. Biol. Inorg. Chem. 18 (2013) 9–17.
[7] F. Lentz, A. Drescher, A. Lindauer, M. Henke, R.A. Hilger, C.G. Hartinger, et al., Pharmacokinetics of a novel anticancer ruthenium complex (KP1019, FFC14A) in a phase I dose-escalation study, Anti-cancer Drugs 20 (2009) 97–103.
[8] H. Maeda, K. Tsukigawa, J. Fang, A retrospective 30 Years after discovery of the enhanced permeability and retention effect of solid tumors: next-generation chemotherapeutics and photodynamic therapy—problems, solutions, and prospects, Microcirculation 23 (2016) 173–182.
[9] A.D. Wong, M. Ye, M.B. Ulmschneider, P.C. Searson, Quantitative analysis of the enhanced permeation and retention (EPR) effect, PloS One 10 (2015) e0123461.
[10] F. Kratz, M. Hartmann, B. Keppler, L. Messori, The binding properties of two antitumor ruthenium(III) complexes to apotransferrin, J. Biol. Chem. 269 (1994) 2581–2588.
[11] C.G. Hartinger, S. Zorbas-Seifried, M.A. Jakupec, B. Kynast, H. Zorbas, B.K. Keppler, From bench to bedside—preclinical and early clinical development of the anticancer agent indazolium trans-[tetrachlorobis(1H-indazole) ruthenate(III)] (KP1019 or FFC14A), J. Inorg. Biochem. 100 (2006) 891–904.
[12] R. Trondl, P. Heffeter, C.R. Kowol, M.A. Jakupec, W. Berger, B.K. Keppler, NKP-1339, the first ruthenium-based anticancer drug on the edge to clinical application, Chem. Sci. 5 (2014) 2925–2932.

[13] J.B. Gifford, W. Huang, A.E. Zeleniak, A. Hindoyan, H. Wu, T.R. Donahue, et al., Expression of GRP78, master regulator of the unfolded protein response, increases chemoresistance in pancreatic ductal adenocarcinoma, Mol. Cancer Ther. 15 (2016) 1043.
[14] C. Xu, B. Bailly-Maitre, J.C. Reed, Endoplasmic reticulum stress: cell life and death decisions, J. Clin. Investig. 115 (2005) 2656–2664.
[15] P. Heffeter, K. Bock, B. Atil, M.A. Reza Hoda, W. Korner, C. Bartel, et al., Intracellular protein binding patterns of the anticancer ruthenium drugs KP1019 and KP1339, J. Biol. Inorg. Chem. JBIC Publ. Soc. Biol. Inorg. Chem. 15 (2010) 737–748.
[16] T.C. Chou, P. Talalay, Quantitative analysis of dose-effect relationships: the combined effects of multiple drugs or enzyme inhibitors, Adv. Enzyme Regul. 22 (1984) 27–55.
[17] P. Heffeter, M. Pongratz, E. Steiner, P. Chiba, M.A. Jakupec, L. Elbling, et al., Intrinsic and acquired forms of resistance against the anticancer ruthenium compound KP1019 [indazolium trans-[tetrachlorobis(1H-indazole)ruthenate (III)] (FFC14A), J. Pharmacol. Exp. Ther. 312 (2005) 281–289.
[18] P. Heffeter, B. Atil, K. Kryeziu, D. Groza, G. Koellensperger, W. Korner, et al., The ruthenium compound KP1339 potentiates the anticancer activity of sorafenib in vitro and in vivo, Eur. J. Cancer 49 (2013) 3366–3375.
[19] E. Eden, R. Navon, I. Steinfeld, D. Lipson, Z. Yakhini, GOrilla: a tool for discovery and visualization of enriched GO terms in ranked gene lists, BMC Bioinforma. 10 (2009) 48.
[20] S. Shalini, L. Dorstyn, S. Dawar, S. Kumar, Old, new and emerging functions of caspases, Cell Death Differ. 22 (2015) 526–539.
[21] P.D. Mace, S.J. Riedl, Molecular cell death platforms and assemblies, Curr. Opin. Cell Biol. 22 (2010) 828–836.
[22] G.S. Salvesen, C.M. Walsh, Functions of caspase 8: the identified and the mysterious, Semin. Immunol. 26 (2014) 246–252.
[23] B.K. Sun, J.H. Kim, H.N. Nguyen, S. Oh, S.Y. Kim, S. Choi, et al., MEKK1/MEKK4 are responsible for TRAIL-induced JNK/p38 phosphorylation, Oncol. Rep. 25 (2011) 537–544.
[24] Y. Estornes, M.A. Aguileta, C. Dubuisson, J. De Keyser, V. Goossens, K. Kersse, et al., RIPK1 promotes death receptor-independent caspase-8-mediated apoptosis under unresolved ER stress conditions, Cell Death Dis. 5 (2014) e1555.
[25] L.S. Flocke, R. Trondl, M.A. Jakupec, B.K. Keppler, Molecular mode of action of NKP-1339 – a clinically investigated ruthenium-based drug – involves ER- and ROS-related effects in colon carcinoma cell lines, Investig. New Drugs (2016) 1–8.
[26] K. Kubota, Y. Niinuma, M. Kaneko, Y. Okuma, M. Sugai, T. Omura, et al., Suppressive effects of 4-phenylbutyrate on the aggregation of Pael receptors and endoplasmic reticulum stress, J. Neurochem. 97 (2006) 1259–1268.
[27] T. Andersen, C. López, T. Manczak, K. Martinez, H. Simonsen, Thapsigargin—from Thapsia L. to mipsagargin, Molecules 20 (2015) 6113.
[28] C. Cui, R. Merritt, L. Fu, Z. Pan, Targeting calcium signaling in cancer therapy, Acta Pharm. Sin. B 7 (2017) 3–17.
[30] W.-J. Shi, J.-B. Gao, Molecular mechanisms of chemoresistance in gastric cancer, World J. Gastrointest. Oncol. 8 (2016) 673–681.
[31] V. Singh, G.K. Azad, P. Mandal, M.A. Reddy, R.S. Tomar, Anti-cancer drug KP1019 modulates epigenetics and induces DNA damage response in Saccharomyces cerevisiae, FEBS Lett. 588 (2014) 1044–1052.
[32] F. Cao, F. Chen, H. Sun, G. Zhang, Z.-H. Chen, F. Wu, Genome-wide transcriptome and functional analysis of two contrasting genotypes reveals key genes for cadmium tolerance in barley, BMC Genom. 15 (2014) 611.
[33] M.K. McElwee, L.A. Ho, J.W. Chou, M.V. Smith, J.H. Freedman, Comparative toxicogenomic responses of mercuric and methyl-mercury, BMC Genom. 14 (2013), 698–698.
[34] M.R. Jones, C. Mu, M.C. Wang, M.I. Webb, C.J. Walsby, T. Storr, Modulation of the Abeta peptide aggregation pathway by KP1019 limits Abeta-associated neurotoxicity, Metallomics Integr. Biometal Sci. 7 (2015) 129–135.
[35] S. Kapitza, M.A. Jakupec, M. Uhl, B.K. Keppler, B. Marian, The heterocyclic ruthenium(III) complex KP1019 (FFC14A) causes DNA damage and oxidative stress in colorectal tumor cells, Cancer Lett. 226 (2005) 115–121.
[36] S. Kapitza, M. Pongratz, M.A. Jakupec, P. Heffeter, W. Berger, L. Lackinger, et al., Heterocyclic complexes of ruthenium(III) induce apoptosis in colorectal carcinoma cells, J. Cancer Res. Clin. Oncol. 131 (2005) 101–110.
[37] V. Vidimar, X. Meng, M. Klajner, C. Licona, L. Fetzer, S. Harlepp, et al., Induction of caspase 8 and reactive oxygen species by ruthenium-derived anticancer compounds with improved water solubility and cytotoxicity, Biochem. Pharmacol. 84 (2012) 1428–1436.
[38] T. Das, G. Sa, E. Paszkiewicz-Kozik, C. Hilston, L. Molto, P. Rayman, et al., Renal cell carcinoma tumors induce T cell apoptosis through receptor-dependent and receptor-independent pathways, J. Immunol. 180 (2008) 4687–4696.
[39] C. von Haefen, J. Wendt, G. Semini, M. Sifringer, C. Belka, S. Radetzki, et al., Synthetic glycosidated phospholipids induce apoptosis through activation of FADD, caspase-8 and the mitochondrial death pathway, Apoptosis Int. J. Program. Cell Death 16 (2011) 636.
[40] P. Chiarugi, E. Giannoni, Anoikis: a necessary death program for anchorage-dependent cells, Biochem. Pharmacol. 76 (2008) 1352–1364.
[41] S.M. Frisch, R.A. Screaton, Anoikis mechanisms, Curr. Opin. Cell Biol. 13 (2001) 555–562.
[42] P. Paoli, E. Giannoni, P. Chiarugi, Anoikis molecular pathways and its role in cancer progression, Biochim. Biophys. Acta (BBA) – Mol. Cell Res. 1833 (2013) 3481–3498.
[43] R. Lotti, A. Marconi, F. Truzzi, K. Dallaglio, C. Gemelli, R.G. Borroni, et al., A previously unreported function of beta(1)B integrin isoform in caspase-8-dependent integrin-mediated keratinocyte death, J. Investig. Dermatol. 130 (2010) 2569–2577.
[44] A. Marconi, P. Atzei, C. Panza, C. Fila, R. Tiberio, F. Truzzi, et al., FLICE/caspase-8 activation triggers anoikis induced by β1-integrin blockade in human keratinocytes, J. Cell Sci. 117 (2004) 5815–5823.
[45] C. Pelillo, H. Mollica, J.A. Eble, J. Grosche, L. Herzog, B. Codan, et al., Inhibition of adhesion, migration and of alpha5beta1 integrin in the HCT-116 colorectal cancer cells treated with the ruthenium drug NAMI-A, J. Inorg. Biochem. 160 (2016) 225–235.

Schoenhacker-Alte et al. Supplementary Figure 1

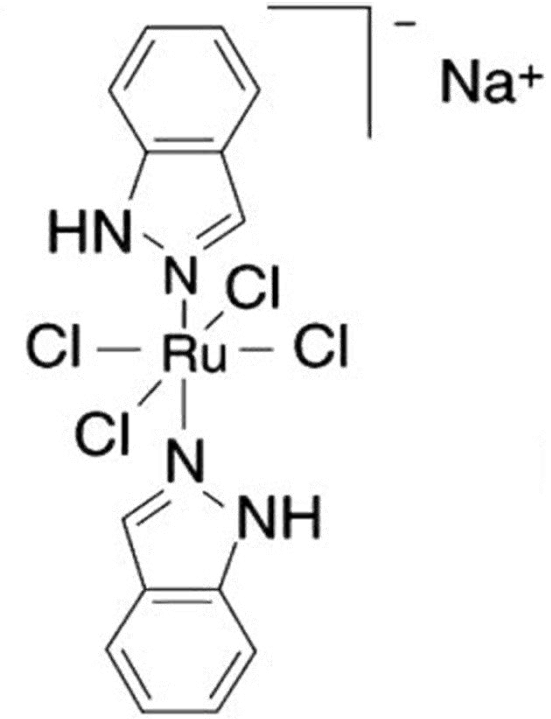

Schoenhacker-Alte et al. Supplementary Figure 2

a

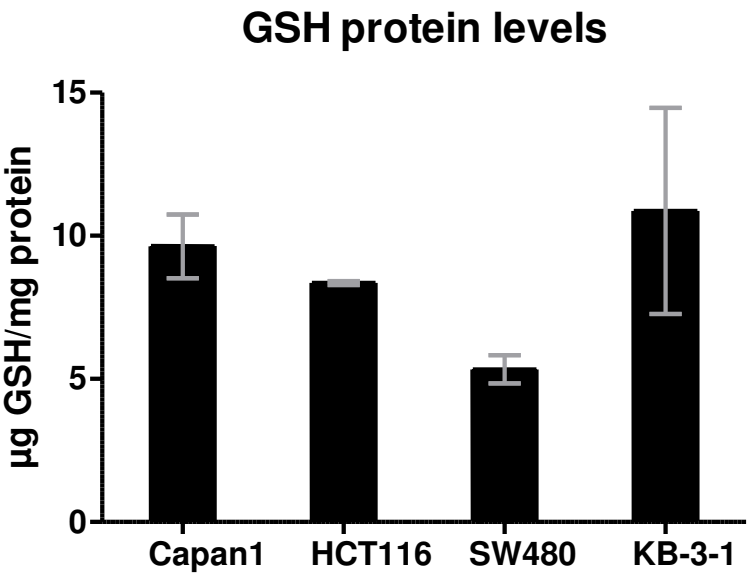

b

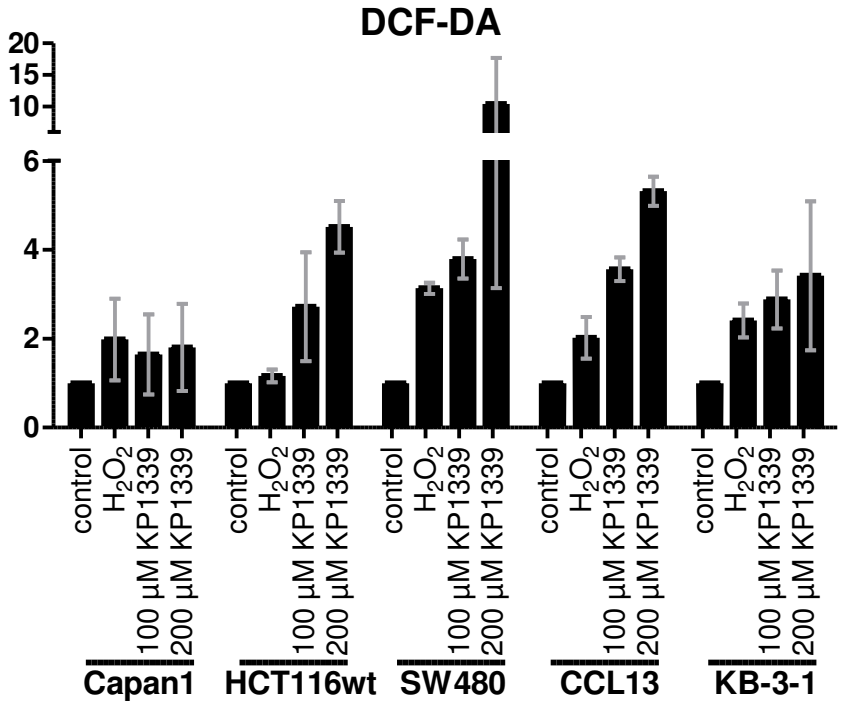

Schoenhacker-Alte et al. Supplementary Figure 3

GO terms highly regulated
in sensitive cells

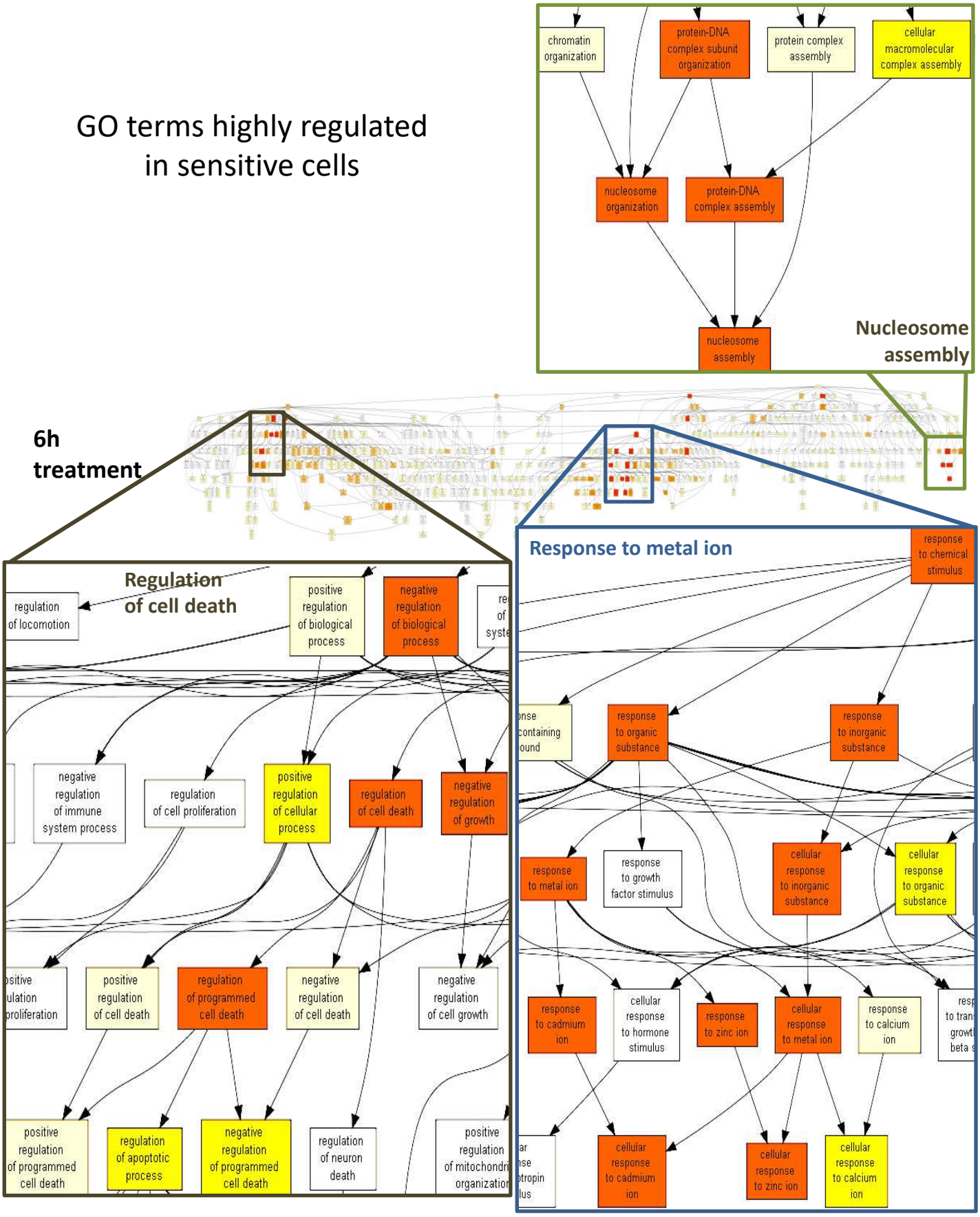

Schoenhacker-Alte et al. Supplementary Figure 4

GO Terms highly regulated in low-responsive cells

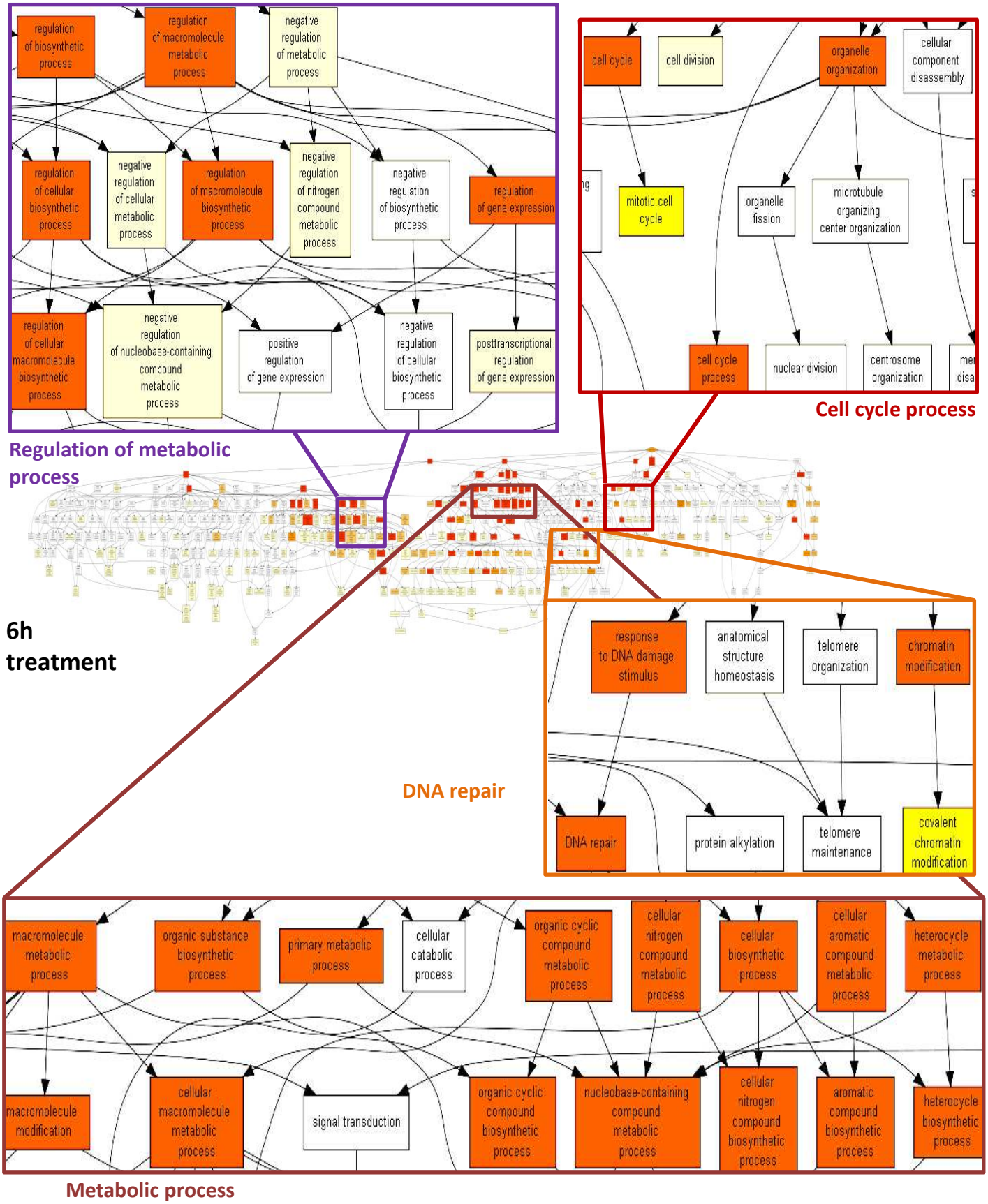

Schoenhacker-Alte et al. Supplementary Figure 5

Protein Damage

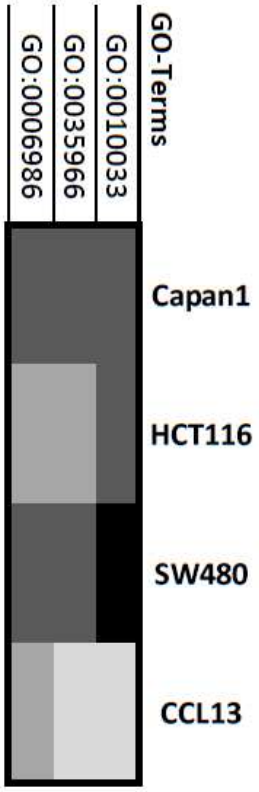

Schoenhacker-Alte et al. Supplementary Figure 6

a

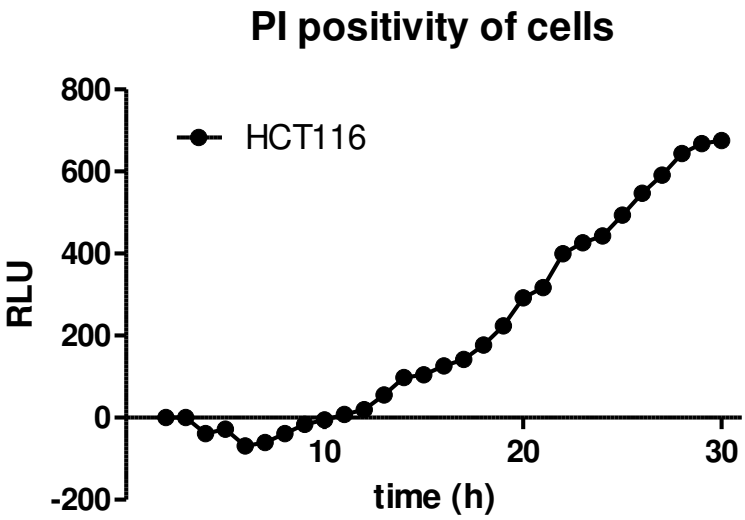

b

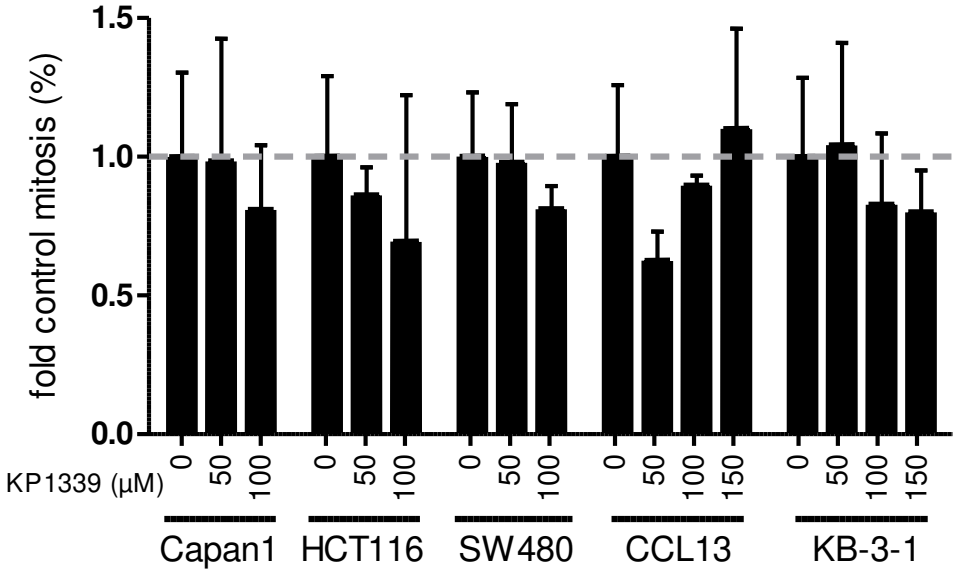

Schoenhacker-Alte et al. Supplementary Figure 7

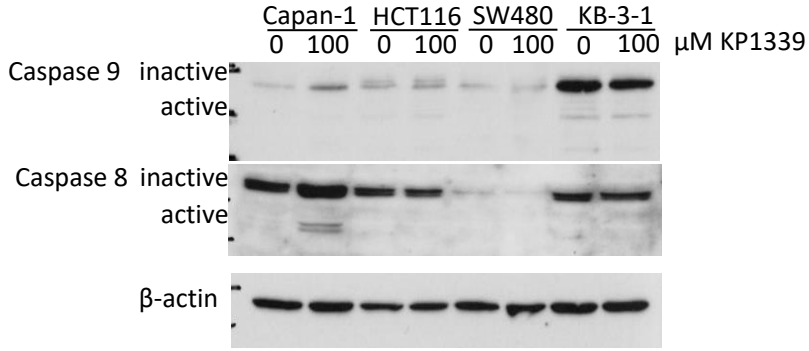

Schoenhacker-Alte et al. Supplementary Figure 8

a

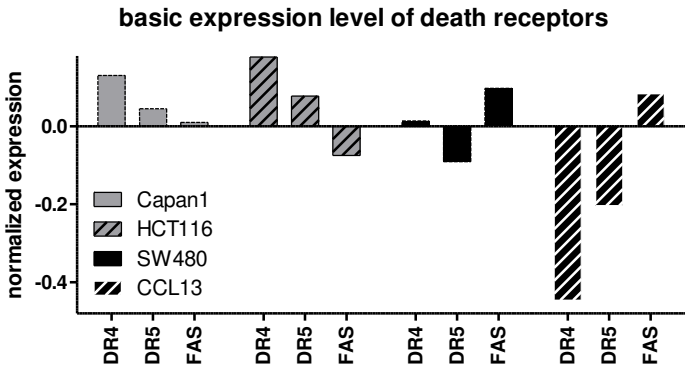

b

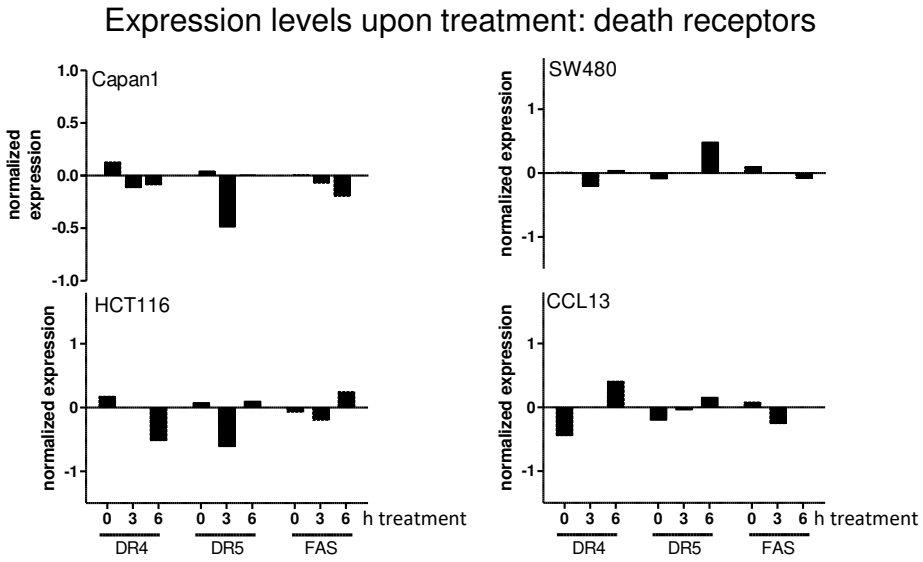

c

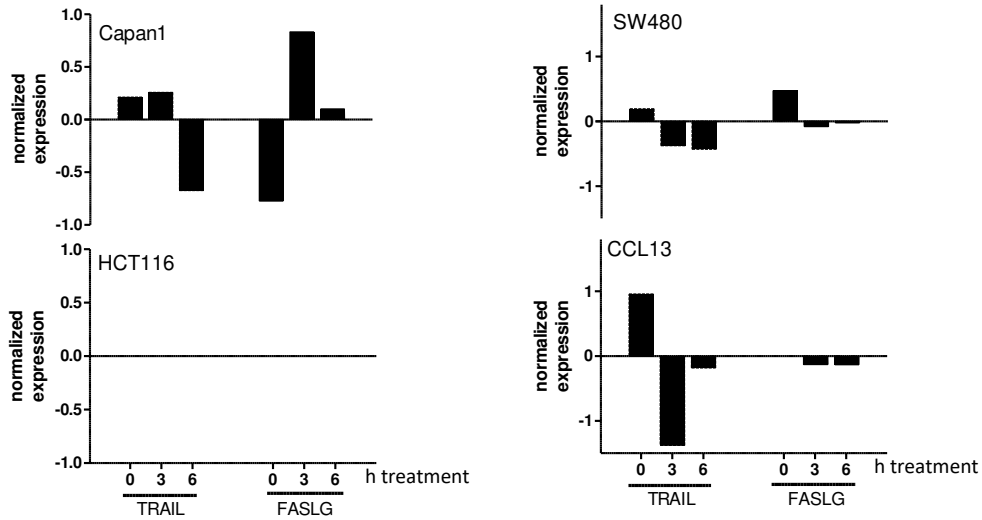

Schoenhacker-Alte et al. Supplementary Figure 9

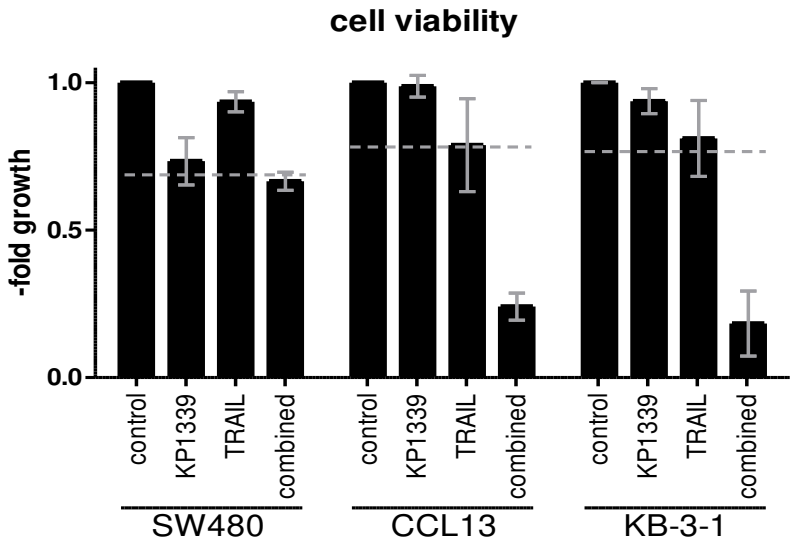

Schoenhacker-Alte et al. Supplementary Figure 10

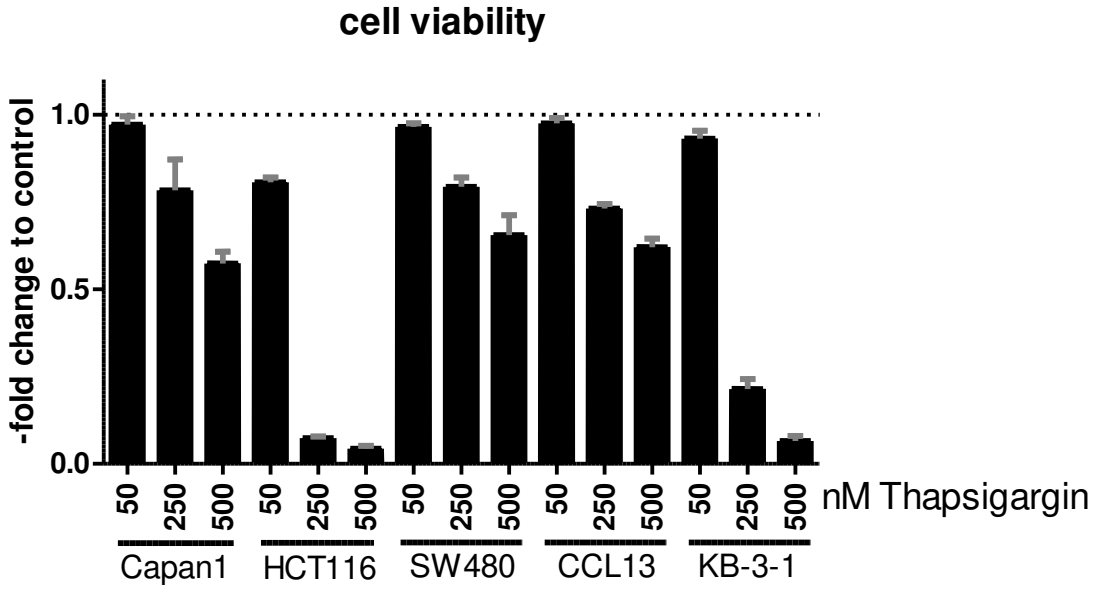

Schoenhacker-Alte et al. Supplementary Figure 11

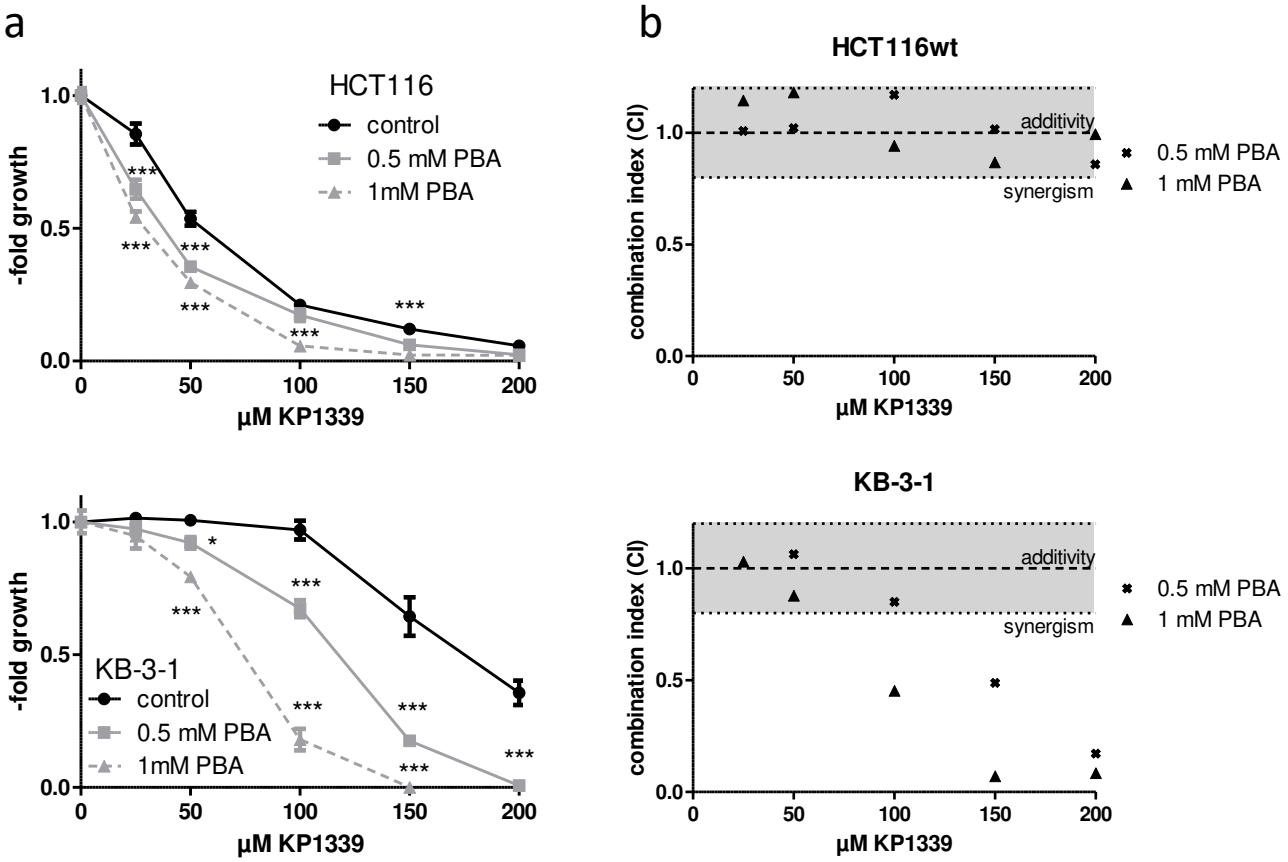

Sensitivity towards the GRP78 inhibitor KP1339/IT-139 is characterized by apoptosis induction via caspase 8 upon disruption of ER homeostasis

Beatrix Schoenhacker-Alte, Thomas Mohr, Christine Pirker, Kushtrim Kryeziu, Paul-Steffen Kuhn, Alicia Buck, Thilo Hofmann, Christopher Gerner, Gerrit Hermann, Gunda Koellensperger, Bernhard K. Keppler, Walter Berger, Petra Heffeter*

Supporting Information

Contents:

Materials and Methods……3-5

Supplementary Tables…….....6-8

References…..…….....9

Supplementary Materials and Methods

Measurement of Reactive Oxygen Species

DCF-DA (2′,7′-dichlorofluorescein diacetate) was used to detect the production of ROS [1]. DCF-DA stock solutions (33.4 mM, DMSO) were stored at –20°C. 2.5×10^5 cells per sample in phenol-free Hanks' balanced salt solution were incubated with DCF-DA (1 µM) for 30 minutes. Subsequently, the compounds were added in the indicated concentrations. After incubation for another 30 minutes, mean fluorescence intensity was measured by flow cytometry using a fluorescence-activated cell sorter (FACSCalibur; Becton Dickinson, Schwechat, Austria). A concentration of 1 mM H_2O_2 was used as a positive control. The resulting histograms were quantified by using ModeFit software (Becton Dickinson).

Quantification of Reduced and Oxidized Glutathione

The sample preparation was conducted according to Hermann et al. [2]. Following the preparation, the samples were separated using an LC system consisting of a Thermo Scientific CTC PAL autosampler, a Thermo Scientific Accela 1250 pump and an Atlantis T3® reversed phase column (150 x 2.1 mm, 3 µm particle size) equipped with an Atlantis T3® guard column (20 x 2.1 mm, 3 µm particle size) from Waters (Milford, USA). Tandem mass spectrometric analysis was carried out with a Thermo Scientific TSQ Vantage.

Total-RNA Isolation and Whole Genome Expression Array

Cell cultures that were either untreated or treated with 100 µM KP1339 for 3 and 6 hours were collected in Trizol (Life Technologies, Carlsbad, CA, USA) for total RNA extraction. Quantity and integrity of RNA was analyzed on an Agilent 2100 Bioanalyzer (Agilent Technologies, Santa Clara, CA, USA). Gene expression arrays were performed using 4x44K whole genome oligonucleotide-based gene expression microarrays (Agilent). Labeling and hybridization procedures were performed according to the instructions provided by Agilent

using the Quick Amp Labeling Kit. Slides were scanned on a G2505B Micro Array Scanner (Agilent). Feature extraction and data analysis were carried out using the Feature Extraction version 10.7.3.1 and Gene Spring version 11.5.1 software, respectively. Statistical analysis was performed to identify significantly differentially expressed genes (differences were considered significant if the p-value was less than 0.05). Only probes with annotated array results were considered.

GOrilla

To estimate the biological impact of treatment with KP1339, data were analyzed using the gene ontology enrichment analysis and visualization tools (GOrilla) by Eden et al. (2009) [3]. Contrary to GO-Enrichment analysis, this algorithm takes the GO-tree into account. Expression data were ranked by logFC and tested against the gene ontology "biological process" with the ranked dataset as test set and the entirety of genes annotated by any term of the gene-ontology "biological process" as reference set. Significantly enriched GO-terms were visualized as an acyclic tree with GO-terms as nodes colored according to their respective p-values.

PI positivity of cells

$1x10^5$ cells were seeded in a cell culture dish (3.5 cm diameter), allowed to recover for 24 h, treated with 100 µM KP1339 and co-incubated with 1µg/ml Höchst33258 and 2.5 µg/ml propidium iodide. Filming started immediately after treatment (a humidified incubation chamber ensured stable cell culture conditions throughout the experiment (37 °C, 5% CO_2)). Photomicrographs (20x magnification) were taken with an NIKON Ti fully automatic inverted microscope from Visitron Systems (Puchheim, Germany) every hour for 48 h. Subsequently, the pictures showing PI accumulation were analyzed in ImageJ for integrated

density of the whole picture, which is indicative for cell membrane permeabilisation and cell death. This value is referred to as “PI positivity” of cells.

Supplementary Table 1. Overview on the Used Cell Lines

Cell line	Tissue	Culture medium	Cell number 96-well plate	Source
A549	NSCLC	RPMI 1640	$2x10^3$	ATCC
Calu6	NSCLC	MEME	$3x10^3$	ATCC
Capan1	Pancreatic adenocarcinoma	RMPI 1640	$5x10^3$	ATCC
Capan2	Pancreatic adenocarcinoma	RPMI 1640	$5x10^3$	ATCC
GLC-4	Small cell lung cancer	RPMI 1640	$2x10^3$	E.G.E. de Vries (Univ. of Groningen)
H446	Small cell lung cancer	RPMI 1640	$2x10^3$	ATCC
HCC3	Hepatoma	RPMI 1640	$4x10^3$	Established at ICR
HCT116	Colon carcinoma (p53/wt)	McCoy's	$2x10^3$	B. Vogelstein (JHU, USA)
HCT116 p53/ko	Colon carcinoma (p53/ko)	McCoy's	$2x10^3$	B. Vogelstein (JHU, USA)
CCL13	Hepatoma	RPMI 1640	$2x10^3$	ATCC
HepG2	Hepatoma	RPMI 1640	$2x10^3$	ATCC
K562	CML	RPMI 1640	$2x10^3$	ATCC
KB-3-1	Hela-derivative (cervix)	RPMI 1640	$2x10^3$	D.W. Shen (Bethesda, USA)
KB-C-1	Colchicine-resistant subline of KB-3-1	RPMI 1640	$2x10^3$	D.W. Shen (Bethesda, USA)
Panc-1	Pancreas carcinoma	RPMI 1640	$2x10^3$	ATCC
PC12	Pheochromocytoma (adrenal gland, rat)	RPMI 1640 15 % FBS	$5x10^3$	ATCC
RKO wt	Colon carcinoma (p53/wt)	McCoy's	$2x10^3$	ATCC
RKO mut	Colon carcinoma (p53/mut)	McCoy's	$2x10^3$	ATCC
SupB15	Acute lymphoblastic leukemia	RPMI 1640	$2x10^3$	ATCC
SW1573	NSCLC	DMEM	$2x10^3$	ATCC

SW480	Colon carcinoma	MEME	$2x10^3$	ATCC
VM-1	Melanoma	RPMI 1640	$2x10^3$	Establish at ICR
VL-8	Squamous cell carcinoma of the lung	RPMI 1640	$2x10^3$	Establish at ICR

Abbreviations: ATCC, American Type Culture Collection Manassas VA; CML, Chronic myelogenous leukemia; DMEM, Dulbecco's Modified Eagle's Medium; ICR, Institute for Cancer Research Vienna; JHU, John Hopkins University; NSCLC, Non-small cell lung carcinoma; MEM, Minimal Essential Medium;

Supplementary Table 2. Used Antibodies

Detected protein	Species	Dilution	Purchased from:
Caspase 8	rabbit	1:1000	Cell Signalling Technology
Caspase 9	rabbit	1:1000	Cell Signalling Technology
PARP	rabbit	1:1000	Cell Signalling Technology
cleaved PARP	rabbit	1:1000	Cell Signalling Technology
Calnexin	rabbit	1:1000	Cell Signalling Technology
PERK	rabbit	1:1000	Cell Signalling Technology
IRE1α	rabbit	1:1000	Cell Signalling Technology
Ero1α	rabbit	1:1000	Cell Signalling Technology
GRP78	rabbit	1:1000	Cell Signalling Technology
CHOP	rabbit	1:1000	Cell Signalling Technology
β-actin	rabbit	1:1000	Sigma
Secondary anti-rabbit	goat	1:10000	Pierce by Thermo Scientific

References

[1]A. Gomes, E. Fernandes, J.L. Lima, Fluorescence probes used for detection of reactive oxygen species. Journal of biochemical and biophysical methods 65 (2005) 45-80.

[2]G. Hermann, P. Heffeter, K. Kryeziu, W. Berger, S. Hann, G. Koellensperger, The study of reduced versus oxidized glutathione in cancer cell models employing isotopically labelled standards. Anal Methods-Uk 6 (2014) 3086-3094.

[3]E. Eden, R. Navon, I. Steinfeld, D. Lipson, Z. Yakhini, GOrilla: a tool for discovery and visualization of enriched GO terms in ranked gene lists. BMC bioinformatics 10 (2009) 48.

Interlude: Third peer reviewed paper

The Anticancer Ruthenium Compound BOLD-100 Targets Glycolysis and Generates a Metabolic Vulnerability towards Glucose Deprivation

Baier, D.; **Schoenhacker-Alte, B**.; Rusz, M.; Pirker, C.; Mohr, T.; Mendrina, T.; Kirchhofer, D.; Meier-Menches, S.M.; Hohenwallner, K.; Schaier, M.; Sgarioto, N.; Raynal, N. J.-M.; Nowikovsky, K.; Schmidt, W.M.; Heffeter, P.; Meier-Menches, S. M.; Koellensperger, G.; Keppler, B.K.; Berger, W.

Pharmaceutics 2022, *14*, 238.

Impact Factor: 5.4 (2022)

https://doi.org/10.3390/pharmaceutics14020238

Prior to the study, I conducted the selection of resistant cell models derived from cell lines which were originally sensitive to KP1339 treatment. Furthermore, I characterized the resulting resistant cell lines in cross resistance screens by cell viability assays and for their respective ruthenium uptake levels upon treatment with KP1339. The mRNA expression data presented in Figure 1 and Supplementary Figure 1 constitute the practical work performed by me. The pictures of cancer cell models with and without BOLD-100 in Supplementary Figure 1 were taken and composed by me. All other biological experiments were conducted by D. Baier with the help of T. Mendrina under the supervision of W. Berger.

pharmaceutics

MDPI

Article

The Anticancer Ruthenium Compound BOLD-100 Targets Glycolysis and Generates a Metabolic Vulnerability towards Glucose Deprivation

Dina Baier [1,2,3], Beatrix Schoenhacker-Alte [1,2,3], Mate Rusz [1,4], Christine Pirker [2,3], Thomas Mohr [2], Theresa Mendrina [1,2,3], Dominik Kirchhofer [2], Samuel M. Meier-Menches [4], Katharina Hohenwallner [1,4], Martin Schaier [1,4], Evelyn Rampler [1,4], Gunda Koellensperger [4], Petra Heffeter [2,3], Bernhard Keppler [1,3] and Walter Berger [2,3,*]

1 Institute of Inorganic Chemistry, University of Vienna, 1090 Vienna, Austria; dina.baier@univie.ac.at (D.B.); beatrix.schoenhacker-alte@gmx.at (B.S.-A.); mate.rusz@univie.ac.at (M.R.); theresa.mendrina@univie.ac.at (T.M.); katharina.hohenwallner@univie.ac.at (K.H.); martin.schaier@univie.ac.at (M.S.); evelyn.rampler@univie.ac.at (E.R.); bernhard.keppler@univie.ac.at (B.K.)
2 Center for Cancer Research and Comprehensive Cancer Center, Department of Medicine I, Medical University Vienna, 1090 Vienna, Austria; christine.pirker@meduniwien.ac.at (C.P.); thomas.mohr@mohrkeg.co.at (T.M.); dominik.kirchhofer@meduniwien.ac.at (D.K.); petra.heffeter@meduniwien.ac.at (P.H.)
3 Research Cluster "Translational Cancer Therapy Research", 1090 Vienna, Austria
4 Department of Analytical Chemistry, Faculty of Chemistry, University of Vienna, 1090 Vienna, Austria; samuel.meier@univie.ac.at (S.M.M.-M.); gunda.koellensperger@univie.ac.at (G.K.)
* Correspondence: walter.berger@meduniwien.ac.at; Tel.: +43-(0)-1-40160-57555

Abstract: Cellular energy metabolism is reprogrammed in cancer to fuel proliferation. In oncological therapy, treatment resistance remains an obstacle and is frequently linked to metabolic perturbations. Identifying metabolic changes as vulnerabilities opens up novel approaches for the prevention or targeting of acquired therapy resistance. Insights into metabolic alterations underlying ruthenium-based chemotherapy resistance remain widely elusive. In this study, colon cancer HCT116 and pancreatic cancer Capan-1 cells were selected for resistance against the clinically evaluated ruthenium complex sodium trans-[tetrachlorobis(1H-indazole)ruthenate(III)] (BOLD-100). Gene expression profiling identified transcriptional deregulation of carbohydrate metabolism as a response to BOLD-100 and in resistance against the drug. Mechanistically, acquired BOLD-100 resistance is linked to elevated glucose uptake and an increased lysosomal compartment, based on a defect in downstream autophagy execution. Congruently, metabolomics suggested stronger glycolytic activity, in agreement with the distinct hypersensitivity of BOLD-100-resistant cells to 2-deoxy-D-glucose (2-DG). In resistant cells, 2-DG induced stronger metabolic perturbations associated with ER stress induction and cytoplasmic lysosome deregulation. The combination with 2-DG enhanced BOLD-100 activity against HCT116 and Capan-1 cells and reverted acquired BOLD-100 resistance by synergistic cell death induction and autophagy disturbance. This newly identified enhanced glycolytic activity as a metabolic vulnerability in BOLD-100 resistance suggests the targeting of glycolysis as a promising strategy to support BOLD-100 anticancer activity.

Keywords: BOLD-100/KP1339; ruthenium; chemotherapy resistance; 2-deoxy-D-glucose; glycolysis; ER stress; autophagy; lysosome; colon cancer; pancreatic cancer

check for updates

Citation: Baier, D.; Schoenhacker-Alte, B.; Rusz, M.; Pirker, C.; Mohr, T.; Mendrina, T.; Kirchhofer, D.; Meier-Menches, S.M.; Hohenwallner, K.; Schaier, M.; et al. The Anticancer Ruthenium Compound BOLD-100 Targets Glycolysis and Generates a Metabolic Vulnerability towards Glucose Deprivation. *Pharmaceutics* **2022**, *14*, 238. https://doi.org/10.3390/pharmaceutics14020238

Academic Editors: Elena Cerrada and Vanesa Fernández-Moreira

Received: 23 December 2021
Accepted: 13 January 2022
Published: 20 January 2022

1. Introduction

The reprogramming of cellular energy metabolism characterizes a hallmark of diverse types of cancer to efficiently fuel biomass production and sustain cell proliferation [1]. The mechanisms underlying a metabolic reprogramming are manifold and highly complex. Besides other metabolic changes, including alterations in oxidative phosphorylation or

glutaminolysis [2], diverse types of solid cancers show enhanced glycolysis to convert glucose to lactate, even under aerobic conditions, a phenomenon termed the "Warburg effect" [3,4]. In the development of anticancer therapy resistance, cellular metabolism, for example, glycolytic activity, is often further enhanced [5]. In this regard, several combined or independently emerging mechanisms have been identified, including (1) the upregulated expression of (rate-limiting) enzymes of the glycolytic pathway [2,6], such as hexokinase 2 (HK2) and phosphofructokinases (PFK), (2) enhanced expression of glucose transporters (GLUT) [7–9], (3) aberrant activity of signaling pathways sensing the metabolic state [10,11], and (4) Myc-induced metabolic reprogramming [12,13]. Accordingly, enhanced cellular glycolytic activity confers a poor prognosis in patients suffering from diverse types of solid tumors [5,7,8]. This increased and vital glycolytic activity in (therapy-resistant) cancer cells translates into an exploitable vulnerability [14] and, hence, provides a rational therapy target.

The glucose analogue 2-deoxy-D-glucose (2-DG) (Figure S1a, right) is irreversibly converted to 2-DG-6-phosphate by HK in the first step of glycolysis and cannot be further metabolized, thereby halting glycolysis [15] and culminating, depending on glycolysis dependency, in growth inhibition and cell death by diverse mechanisms of action [16–18]. Kurtoglu et al. showed that glycolysis inhibition by 2-DG affected protein *N*-glycosylation, causing unfolded protein response (UPR) induction via upregulation of the endoplasmic reticulum (ER) chaperone glucose-regulated protein of 78 kDa (GRP78), and finally resulting in apoptosis [19]. Hence, glucose deprivation upregulates GRP78 expression at the transcriptional [20] and translational [21] levels. Furthermore, 2-DG-induced ER stress and ATP-depletion can prompt autophagy [22,23], a cellular catabolic organelle recycling program. Under basal conditions, autophagy ensures cellular survival by the removal of damaged proteins or organelles. If hyperactivated, autophagy can lead to a widely caspase-independent form of programmed cell death [24,25]. Other described modes of action concerning 2-DG were associated with perturbations of cell cycle progression and antiproliferative activity [19]. 2-DG was investigated in clinical trials as a single agent [26,27] or combined with the chemotherapeutic docetaxel for the treatment of advanced solid tumors [28]. Overall, 2-DG therapy was well-tolerated and patients experienced mild side effects, including nausea and fatigue. Concerning the clinical combination approach, the authors emphasized that 2-DG should be combined with chemotherapeutic agents to yield a more significant therapeutic success. This is also supported by several in vitro experiments that demonstrated an enhanced anticancer activity of chemotherapy upon combination with 2-DG [29]. Moreover, glucose deprivation with 2-DG combined with platinum-based chemotherapy was shown to overcome acquired metal drug resistance [11,30].

Insights into the mechanisms in response to ruthenium-based anticancer therapy and underlying an acquired resistance against this approach, especially concerning metabolic alterations, remain widely enigmatic. In a recent publication, we demonstrated that metabolite abundances and metabolic flux alterations underlying acquired platinum- and ruthenium-based chemotherapy differ distinctly [31]. The aim of the present study was to investigate the molecular mechanisms characterizing acquired resistance against the clinically evaluated ruthenium complex BOLD-100 (sodium trans-[tetrachlorobis(1H-indazole)ruthenate(III)] with cesium as an intermediate salt form (Figure S1a left); predecessor molecules: IT-139/NKP-1339/KP1339). BOLD-100 is an inhibitor of stress-induced GRP78 upregulation, thus disrupting ER homeostasis and inducing ER stress and UPR. This is reflected by the phosphorylation of eukaryotic translation initiation factor 2A (eIF2A) [32] and caspase-8-dependent cell death [33]. After the successful completion of a phase I safety and activity study [34], BOLD-100 is currently in phase Ib clinical investigation, in combination with folinic acid, fluorouracil, and oxaliplatin (FOLFOX regimen), for the treatment of colorectal, pancreatic, and gastric cancers, as well as cholangiocarcinoma (NCT04421820). Besides BOLD-100, imidazolium [trans-tetrachloro(1H-imidazole)(S-dimethylsulfoxide)ruthenate(III)] (NAMI-A) was clinically investigated as the first ruthenium compound reaching phase II study stage but failed, due to an insufficient

activity, a low response rate, and the development of painful blisters at higher doses [35,36]. The BOLD-100 progenitor indazolium [trans-tetrachlorobis(1H-indazole)ruthenate(III)] (KP1019) followed NAMI-A into clinical investigation [36]. Due to an insufficient solubility that prevented the identification of a maximum tolerated dose and also based on the low toxicity profile, KP1019 was replaced by the more soluble sodium salt analogue BOLD-100 [37,38].

The development of (chemo)therapy resistance presents a major obstacle in anticancer therapy. Therefore, it is essential to dissect the mechanisms underlying acquired BOLD-100 resistance concomitantly to early clinical development. Hence, in the present study, colon cancer HCT116 and pancreatic cancer Capan-1 cells were selected for acquired BOLD-100 resistance and investigated for the underlying molecular mechanisms by multi-omics approaches and cell/molecular biological and analytical chemistry methods. Summarizing, we identified specific metabolic changes upon short- and long-term BOLD-100 treatment associated with altered glycolytic activities. Accordingly, we show that these metabolic adaptations contribute to acquired BOLD-100 resistance and open novel approaches for synergistic pharmacological interventions.

2. Materials and Methods

2.1. Chemicals and Drugs

BOLD-100 was obtained from Bold Therapeutics Inc. (Vancouver, Canada) and dissolved in dimethyl sulfoxide (DMSO) to generate a 20 mM stock. 2-DG was purchased from Sigma-Aldrich Inc. (St. Louis, MO, USA) and freshly dissolved in cell culture medium prior to use. Bis-2-[5-(phenylacetamido)-1,3,4-thiadiazol-2-yl]ethyl sulfide (BPTES) and chloroquine (CQ) were obtained from Selleckchem (EUBIO, ANDREAS KOCK e.U., Vienna, Austria).

2.2. Cell Culture

The human colorectal carcinoma cell line HCT116 was kindly provided by Dr. Vogelstein from Johns Hopkins University, Baltimore. The pancreatic adenocarcinoma cell line Capan-1 was purchased from the American Type Culture Collection (ATCC, Manassas, VA, USA). HCT116 cells were cultured in McCoy's 5A Modified Media (Sigma-Aldrich, St. Louis, MO, USA) supplemented with 10% heat-inactivated fetal calf serum (FCS, PAA, Linz, Austria) and 2 mM glutamine (Sigma-Aldrich, St. Louis, MO, USA). Capan-1 cells were grown in RPMI-1640 (Sigma-Aldrich, St. Louis, MO, USA) supplemented with 10% FCS. BOLD-100-resistant HCT116 and Capan-1 sublines were generated over several months by regular exposure to increasing concentrations of BOLD-100, followed by a drug-free recovery phase. Finally, BOLD-100-resistant HCT116 (HCTR) and Capan-1 (CapanR) cells were selected with 200 µM BOLD-100 in two-week-intervals. Resistance was maintained for >1 month without selection pressure. All cell cultures were grown in 5% CO_2 at 37 °C and regularly checked for *Mycoplasma* contamination.

2.3. Cell Viability Assay

HCT116 and HCTR cells were seeded at a density of 3.5×10^3 cells/100 µL and Capan-1 and CapanR cells were seeded at a density of 6×10^3 cells/100 µM in 96-well microtiter plates and allowed to adhere overnight. Cells were exposed to BOLD-100, 2-DG, CQ, or their combination in the indicated concentrations for 72 h. Cell viability was determined using the 3-(4,5-dimethylthiazol-2-yl)-2,5-diphenyltetrazolium bromide (MTT) assay (EZ4U, Biomedica, Vienna, Austria), following the manufacturer's recommendations. The colorimetric signal was measured spectrophotometrically at 450 nm and a reference wavelength of 620 nm, using the Asys Expert Plus micro plate reader (v1.4, Asys Hitech GmbH Hitech, Eugendorf, Austria). Data were analyzed using the GraphPad Prism software (La Jolla, CA, USA). IC_{50} values, indicating the drug concentration resulting in a 50% reduction of cell viability as compared to untreated control cells, were calculated from full dose-response curves by non-linear regression curve fitting (sigmoidal dose-response

with a variable slope). For the evaluation of the synergistic effects of drug combinations, the CalcuSyn software (Biosoft, Ferguson, MO, USA) was used [39]. The respective effects are expressed as combination indices (CI). CI values indicate drug activity as follows: CI < 0.9, synergism; CI = 0.9–1.2, additive effects; or CI > 1.2, antagonism.

2.4. Clonogenicity (Clone Formation) Assay

To determine the clone formation capacity, HCT116 and HCTR cells were seeded at a density of 2000 cells/mL in 250 µL of medium in 24-well microtiter plates and allowed to adhere overnight. The cells were treated with the indicated concentrations of the BOLD-100, 2-DG, or their combination for 7 days. Cells were washed with ice-cold phosphate-buffered saline (PBS, pH 7.4 Sigma-Aldrich Inc., St. Louis, MO, USA), fixed with acetone and methanol in a ratio of 1:1 for 30 min., washed twice, and stained with 0.01% (*w*/*v*) crystal violet dissolved in ethanol for 5 min. Next, the plates were washed with ddH_2O, dried, and the fluorescent signal (610/30 nm BP emission filter, 633 laser) of the stained cell clones was scanned with a Typhoon TRIO Variable Mode Manager Imager System (Amersham Bioscienes, UK) using the Typhoon Scanner Control software (V5.0). From the derived images, pixel intensities per well were quantified by Image J 1.50i (NIH, Bethesda, MD, USA).

2.5. Cellular Ruthenium Uptake Measurements

HCT116 and HCTR or Capan-1 and CapanR cells were seeded at a density of 1×10^5 cells/mL in 1 mL of respective cell culture medium in 6-well plates in a total volume of 2 mL and left to recover overnight. Cells were treated in triplicates with 100 µM BOLD-100 for 24 h. BOLD-100 was additionally added to cell-free blank wells to determine the absorption of the compound to the plastic well. Sample processing, measurement of cellular ruthenium content, and data evaluation were performed as described previously [40]. In short, ^{102}Ru standards were derived from Labkings (Hilversum, The Netherlands). Total ruthenium content was determined using a quadrupole-based inductively coupled plasmon mass spectrometry (ICP-MS) instrument Agilent 7800 (Agilent Technologies, Tokyo, Japan) equipped with the Agilent SPS 4 autosampler (Agilent Technologies, Tokyo, Japan) and a MicroMist nebulizer at a sample uptake rate of approximately 0.2 mL min^{-1}. Argon was used as the plasma gas (15 L min^{-1}) and carrier gas (1.06 L min^{-1}). The integration time was set to 0.3 s with 10 replicates and 100 sweeps/replicate. ^{115}In served as the internal standard for ruthenium. The Agilent MassHunter software package (Workstation Software, Version C.01.04, 2018) was used for data evaluation.

2.6. Total-RNA Isolation and Whole Genome Gene Expression Array

Whole genome gene expression arrays were performed as described previously [41]. Briefly, mRNA was isolated with the RNeasy Mini Kit (QIAGEN GmbH, Hilden, Germany) from HCT116, HCTR, Capan-1, and CapanR cells that were either left untreated or treated with 100 µM BOLD-100 for 6 h. Whole genome gene expression analyses were performed on 4 × 44 K oligonucleotide microarrays (G4845A, Agilent Technologies, Santa Clara, CA, USA) according to manufacturer's recommendations. Feature extraction was carried out using the Feature Extraction software (version 11.5.1.1). Differentially expressed genes in BOLD-100-treated vs. untreated cells were analyzed using the GeneSpring software (version 13.0). Gene Set Enrichment Analysis (GSEA) on the loess (within arrays) and quantile (between arrays) normalized gene expression matrix was conducted on the C2 dataset of the molecular signature database (version 7.4) using the GSEA software (version 4.0.3) with default parameters and the log2FC as ranking metric [42,43].

2.7. Metabolomics

HCT116 and HCTR cells were seeded at a density of 0.25×10^6 cells/mL in 1 mL medium in 12-well plates and left to recover overnight. The medium was replaced and the cells were treated with 100 µM BOLD-100 or the corresponding concentration of DMSO for

24 h. The cells were washed 3 times with PBS (pH 7.4), quenched with liquid nitrogen, and stored at −80 °C until further processing. The metabolomics experiments were carried out as described before [31]. In short, liquid chromatography high-resolution mass spectrometry (LC-MS) measurement with a Thermo Scientific Q Exactive HF quadrupole-Orbitrap mass spectrometer was utilized in full mass scan mode (both positive and negative ionization-mode) at a resolution of 120,000. External calibration with fully labelled ^{13}C internal standards ISOtopic solutions (Vienna, Austria) was used for quantification. The obtained absolute metabolite amounts (pmol) were normalized to the total protein content in their respective well (µg) with the Thermo BCA kit, according to manufacturer's instructions.

2.8. Gene-Metabolite Network Analysis

A pathway-based compound-gene network was constructed with the Cytoscape [44] plugin MetScape [45,46] based on annotated data from the Kyoto Encyclopedia of Genes and Genomes (KEGG) database [47–49] and significantly regulated compounds and genes (raw p-value < 0.05) were mapped on it. The metabolomics data were provided with raw p-values and fold-changes, based on pmol absolute amounts normalized to µg of protein content in the respective sample. While 5-methyluridine, *N*-acetyl-serine, methionine sulfone, and N4-acetylcytidine were not retrieved from KEGG, otherwise 46 unique compounds could be mapped on the network. The respective KEGG pathways were extracted as subnetworks for further analysis.

2.9. Western Blot Analyses

Groups of 1–2 × 10^6 cells were seeded in 1 mL medium in 6-well plates in a total volume of 2 mL and allowed to adhere overnight. The cells were treated for 24 h with 100 µM BOLD-100, 1 or 10 mM 2-DG, 50 µM CQ, or their combination. Two solvent controls, medium without or with DMSO, were included. Cells were harvested by scratching into the supernatant, centrifugation, and washing with ice-cold PBS (pH 7.4). Sample collection, protein separation, and Western blotting were performed as described in detail previously [50]. The protein concentration was determined using the Micro BCA™ Protein Assay Kit (Thermo Fisher Scientific, Waltham, MA, USA). Sodium dodecyl sulfate polyacrylamide gel electrophoresis (SDS-PAGE) was performed to separate protein extracts. Subsequently, the proteins were transferred onto polyvinylidene difluoride membranes (PVDF, Thermo Fisher Scientific, Waltham, MA, USA). The primary antibodies Anti-GRP78 (C50B12) (#3177, dilution 1:1000), p-eIF2A (Ser51) (#9721S, 1:1000), eIF2A (L57A5) (#2103, 1:1000), HSP70 (#4872, 1:1000), PARP (46D11) (#9532, 1:1000), beclin-1 (#3495, 1:1000), p62/SQSTM1 (#8025, 1:500), and LC3 B I/II (#12741, 1:1000) were purchased from Cell Signaling Technology (Danvers, MA, USA). To obtain the horseradish-peroxidase-linked secondary antibodies, anti-Mouse IgG (Fc specific) antibody (A0168) was purchased from Merck KGaA (Darmstadt, Germany), and anti-rabbit IgG antibody (7074S) was purchased from Cell Signaling Technology (Danvers, MA, USA). Anti-ß-actin (AC-15) (A5441, 1:2000) was obtained from Sigma-Aldrich (St. Louis, MO, USA).

2.10. Flow Cytometry Analysis of Cellular 2-NBDG Uptake

HCT116 and HCTR cells were seeded at a density of 1 × 10^5 cells/mL and Capan-1 and CapanR cells at a density of 2 × 10^5 cells/mL in 1 mL medium 12-well plates and allowed to adhere overnight. The next day, the cells were washed with pre-warmed PBS (pH 7.4) and the medium was replaced with glucose-free RPMI-1640 medium containing L-glutamine (Sigma-Aldrich, St. Louis, MO, USA) supplemented with 10% FCS. The cells were treated with 100 µM BOLD-100 or the corresponding amount of DMSO (control) for 24 h. The medium with or without drug or solvent was replaced by serum-free medium containing 25 µM fluorescent D-glucose analog 2-[*N*-(7-nitrobenz-2-oxa-1,3-diazol-4-yl) amino]-2-deoxy-D-glucose (2-NBDG) (ab146200, Abcam, Cambridge, UK) and incubated in the dark for 1 h at 37 °C with 5% CO_2 before flow cytometry analysis. 2-NBDG incubation was stopped by the removal of the incubation medium and careful washing of the cell layer

with cold PBS (pH 7.4). The cells were detached by trypsinization, washed two times, and resuspended with FACS-PBS (7.81 mM $Na_2HPO_4 \times 2H_2O$, 1.47 mM KH_2PO_4, 2.68 mM KCl, and 0.137 M NaCl) and transferred into FACS tubes. The fluorescence intensity was measured on a LSRFortessa flow cytometer (BD Biosciences, East Rutherford, NJ, USA) with the FITC (530/30 nm) bandpass emission filter. The data were analyzed using the Flowing Software (University of Turku, Finland) and are depicted as fluorescence intensities (arbitrary units, a.u.).

2.11. Cell Cycle Analysis

For analysis of the cell cycle state, HCT116 and HCTR cells were seeded in triplicates at a density of 1.5×10^5 cells/mL in 1 mL medium in 12-well plates and allowed to adhere overnight. Cells were treated with DMSO corresponding to BOLD-100 treatment, 100 µM BOLD-100, 10 mM 2-DG, or their combination for 24 h. Cells were trypsinized, washed with PBS (pH 7.4), and the resulting pellet was resuspended in 0.9% NaCl and fixed in ice-cold 70% ethanol by slow, drop-wise addition. Ethanol-fixed cells were stored at −20 °C until further use. Cells were centrifuged, the pellet was resuspended in FACS-PBS (7.81 mM $Na_2HPO_4 \times 2H_2O$, 1.47 mM KH_2PO_4, 2.68 mM KCl, and 0.137 M NaCl) containing RNAse (50 mg/mL, heat-inactivated) and 1 mg/mL propidium iodide (PI) (Sigma-Aldrich, St. Louis, MO, USA), and incubated for 30 min at 37 °C in the dark. The cells were measured by flow cytometry with a LSRFortessa flow cytometer (BD Biosciences, East Rutherford, NJ, USA) with the 610/20 nm bandpass emission filter. The percentages of 50.000 cells in G0/G1, S, G2/M, and <G1 or >G2 phase of the cell cycle were calculated by FlowJo software (v10.06) using the Watson Pragmatic algorithm.

2.12. Cell Proliferation Assay

HCT116 and HCTR cells were seeded in triplicates at a density of 3×10^3 cells/100 µL medium in 96-well plates and allowed to adhere overnight. The cells were exposed to DMSO, BOLD-100, 2-DG, or their combination in the indicated concentrations for 24 h. 5-ethynyl-2′-deoxyuridine (EdU) incorporation into de novo synthesized DNA was determined using the Click-iTTM EdU proliferation assay for microplates (C10499, Invitrogen, Waltham, MA, USA) according to manufacturer's recommendations. The fluorescence was measured on a Tecan infinite 200Pro (Zurich, Switzerland) micro plate reader at 520/585 nm. The data were analyzed using the GraphPad Prism software (La Jolla, CA, USA). Antiproliferative IC_{50} values indicated the drug concentration resulting in a 50% reduction of EdU incorporation, reflecting the proliferation rate as compared to untreated control cells.

2.13. Hoechst 33258/PI Staining

HCT116 and HCTR cells were seeded in triplicates at a density of 4×10^4 cells/mL in 1 mL medium in 24-well plates and allowed to adhere overnight. The cells were exposed to DMSO, BOLD-100, 2-DG, or their combination in the indicated concentrations for 72 h. After the drug incubation period, the cells were stained with 2 µL/mL of a 1:1 mixture of Hoechst 33258 (1 mg/mL in PBS (pH 7.4); termed Hoechst in this manuscript) and PI (2.5 mg/mL in PBS pH 7.4) for 1 h at 37 °C. Microscopic images were taken using a Nikon Eclipse Ti inverted microscope (Visitron Systems, Puchheim, Germany) with the DAPI (Hoechst) and Cy3 (PI) filters. Light and evenly distributed blue fluorescence on PI-negative cells indicated living cells. A bright blue fluorescent signal of condensed chromatin on PI-negative cells indicated mitotic nuclei together with mitosis-characteristic features. Bright blue fluorescence of condensed nuclei associated with the formation of apoptotic bodies in the absence of a PI signal was considered indicative for early apoptotic cells. PI-positive cells were considered to be dead cells with late apoptotic nuclei.

2.14. High-Resolution Live-Cell Spinning-Disc Imaging of Lysotracker Red and Hoechst 33258-Stained Cells

HCT116 and HCTR cells were seeded at a density of 0.5×10^5 cells/mL in 200 µL medium in 8-well ibiTreat 1.5 polymer µ-slides (80826, ibidi GmbH, Gräfelfing, Germany) and allowed to adhere overnight. The cells were exposed to DMSO, BOLD-100, 2-DG, or their combination in the indicated concentrations for 24 or 72 h. After the drug incubation period, the cells were stained with 0.5 µM Lysotracker Red (L7528, Life Technologies, CA, USA) and Hoechst 33258 (blue) (1 mg/mL in PBS pH 7.4, Sigma-Aldrich). High-resolution live-cell spinning-disc images were taken using an IX83 P2ZF microscope (Olympus Austria GmbH, Vienna, Austria) with a UPLXAPO O 60 oil-immersion objective at 192× magnification. Image acquisition was performed using the OLMYPUS cellSens Dimension 3.1 imaging software (OLYMPUS CORPORATION, Tokio, Japan).

2.15. High-Resolution Live-Cell Spinning-Disc Imaging of LC3B II Foci

HCT116 and HCTR cells were seeded at a density of 0.5×10^5 cells/mL in 200 µL medium in 8-well ibiTreat 1.5 polymer µ-slides (80826, ibidi GmbH, Gräfelfing, Germany) and allowed to adhere overnight. The cells were exposed to DMSO, BOLD-100, 2-DG, or their combination in the indicated concentrations for 24 h. The cells were fixed with 4% paraformaldehyde (PFA)/PBS (pH 7.4) for 30 min. and permeabilized in PBS/0.5% *v*/*v* Triton X-100 (pH 7.4) for 20 min at room temperature. The cells were blocked in PBS (pH 7.4) containing 20% *w*/*v* BSA for 20 min and stained with primary anti-LC3B rabbit monoclonal antibody (1:400, #12741 from Cell Signaling Technology, Danvers, MA, USA) in PBS (pH 7.4) containing 2% *w*/*v* BSA at 4 °C overnight. The cells were washed in PBS (pH 7.4), incubated with Alexa Fluor 488-labeled goat anti-rabbit IgG, (1:500; Invitrogen, Thermo Fisher, USA) for 1 h at room temperature in the dark, and nuclei were counterstained with Hoechst 33258 (blue) (1 mg/mL in PBS pH 7.4, Sigma-Aldrich). After a final washing step, high-resolution live-cell spinning-disc images were taken, as described above.

2.16. Flow Cytometry Analysis of Lysotracker-Red-Stained Cells

HCT116 and HCTR cells were seeded at a density of 0.5×10^5 cells/mL in 1 mL medium in 12-well plates and allowed to adhere overnight. The cells were treated with DMSO, BOLD-100, 2-DG, or their combination in the indicated concentrations for 72 h. The cells were stained with 0.5 µM Lysotracker Red (L7528, Life Technologies, CA, USA) for 30 min at 37 °C. The cells were prepared and measured, as described above for flow cytometry analysis, and measured with the 610/20 nm bandpass emission filter. The data were analyzed using the Flowing Software (University of Turku, Finland) and are depicted as fluorescence intensities.

2.17. Mass Spectrometry Analysis

Stock solutions of 20 mM D-glucose in H_2O and 20 mM BOLD-100 in DMSO were prepared and diluted with H_2O for coincubation of 100 µM BOLD-100 and 400 µM D-glucose. The reaction mixture was incubated at 37 °C in the dark under constant shaking. Reaction aliquots were taken after 30 min and 2, 4, and 24 h and immediately snap frozen with liquid nitrogen and stored at −20 °C. The data were acquired on a maXis QTOF mass spectrometer (Bruker Daltonics, Bremen, Germany) by the direct infusion of analytes diluted to 5 µM with an aqueous solution (LC-MS grade water, Fluca). The infusion rate was 3 µL min^{-1}. The instrument parameters were as follows: 4.5 kV capillary voltage, 500 V end plate offset, 3 bar nebulizer, 5 L min^{-1} dry gas, 180 °C dry temperature, and m/z 50–1200 scan range. The mass spectra were recorded in the negative ion mode over 0.4 min and averaged.

2.18. Lipidomics

HCT116 and HCTR cells were seeded at a density of 0.5×10^6 cells/mL in 1 mL medium in 6-well plates in a total volume of 2 mL and allowed to adhere overnight. Cells were treated for 24 h with 100 µM BOLD-100 or DMSO as solvent control (n = 3 per

condition). The medium was removed, and the samples were washed three times with PBS (pH 7.4). All samples were quenched with liquid nitrogen and stored at −80 °C prior to extraction. ^{13}C-labeled LILY lipids were added for internal standardization [51]. A two-phase extraction with MTBE was used to collect (1) the upper lipid-containing phase and (2) the protein pellet for protein normalization [52]. The supernatant was dried and dissolved in 100 µL of isopropanol prior to LC-MS analysis. Lipidomics measurements were performed with reversed-phase (RP) chromatography (C18 column) and a 27 min isopropanol gradient coupled to a high-resolution mass spectrometer (HRMS) (Orbitrap ID-X, Thermo Fisher Scientific, Waltham, MA, USA). A resolution of 120,000 was used for MS1 followed by a data-dependent MS2 acquisition and deep scans (Acquire X) at a resolution of 30,000 in positive and negative ionization mode. Targeted and non-targeted data evaluation was based on LipidSearch 5.0 (Lipid Search 5.0.63, Thermo Fisher Scientific, Waltham, MA, USA), Skyline (21.1.0.278, https://skyline.ms/project/home/begin.view, accessed on 2 January 2022), and R Studio (R version 4.1.2, Boston, MA, USA).

2.19. Statistical Analysis

Data were analyzed using GraphPad Prism software (version 8.0.1, La Jolla, CA, USA). If not stated otherwise in the figure legends, one out of at least three independent experiments in triplicates is displayed. Each data point represents the mean ± SD of triplicate values. The statistical evaluation of significance was performed using an unpaired Student's *t*-test, as well as a one- or two-way analysis of variance (ANOVA) with Bonferroni's or Tukey's multiple comparisons post-tests. *p*-values below 0.05 were considered statistically significant: * $p < 0.05$, ** $p < 0.01$, *** $p < 0.001$, **** $p < 0.0001$.

3. Results

3.1. Impact of BOLD-100 Exposure and Acquired Resistance on Cellular Carbohydrate Metabolism

Since BOLD-100 is currently being investigated clinically (NCT04421820) and the development of chemotherapy resistance remains a major hurdle in cancer treatment [53,54], this study aimed to characterize the mechanisms underlying acquired BOLD-100 resistance. Therefore, the intrinsically BOLD-100-sensitive colon cancer HCT116 cell line and pancreatic Capan-1 cancer cell line [33] were selected for acquired drug resistance via continuous exposure to increasing concentrations of BOLD-100 up to 200 µM. Representative phase contrast images depict the changes of cell morphology induced by treatment with 100 µM BOLD-100 in acquired -resistant (HCTR or CapanR) as compared to parental cells (Figure S1b). While the pronounced appearance of shirked and fragmented cells, indicative for apoptosis induction, was recorded in both parental cell lines, these effects were distinctly reduced or even absent in the resistant sublines. This corresponded well with a significantly decreased sensitivity of the BOLD-100-resistant sublines in the MTT assay, reflected by increased IC_{50} values (Figure 1a). Overall, the selection resulted in 2.2-fold increased BOLD-100 resistance in HCTR (IC_{50} of HCTR vs. HCT116 cells) and a 4.1-fold increased resistance in CapanR cells. Whole genome gene expression analyses of drug transporter expression in BOLD-100-resistant as compared to parental cells (Figure S1c) revealed a slight but significant increase in ABCB1, a decrease in ABCC1, and no change in the case of ABCG2 in HCTR vs. HCT116 cells. In CapanR as compared to Capan-1 cells, no significant drug transporter regulation was detected. Accordingly, the measurement of intracellular ruthenium accumulation by ICP-MS demonstrated that acquired BOLD-100 resistance was not based on a decreased drug uptake (Figure 1b). The data of whole genome gene expression analyses of acquired BOLD-100-resistant vs. respective parental HCT116 or Capan-1 cells were processed by GSEA. Of the top 20 gene sets enriched in the acquired BOLD-100-resistant vs. sensitive HCT116 cells, seven gene sets were associated with carbohydrate metabolism. From the KEGG database, "GALACTOSE_METABOLISM" (nominal *p*-value < E^{-7}; FDR 0.010) and "FRUCTOSE_AND_MANNOSE_METABOLISM" (nominal *p*-value < E^{-7}; FDR 0.084) were identified as the third and fourth most significantly enriched gene sets, respectively, in HCTR vs. HCT116 cells (Figure 1c). Exemplarily, both heat maps show an upregulated

expression of the mRNA of hexokinase genes, translating into enzymes catalyzing the first and rate-limiting step in glycolysis. Accordingly, upon BOLD-100 treatment in HCT116 cells "GLYCOSAMINOGLYCAN_METABOLISM" (nominal *p*-value < E^{-7}; FDR 0.003) was identified as the fourth most down-regulated gene set in the REACTOME database and "O_GLYCAN_BIOSYNTHESIS" (nominal *p*-value < E^{-7}; FDR 0.003) as the seventh most down regulated in the KEGG database (Figure S1d). The GSEA of the acquired CapanR vs. Capan-1 cells identified "KEGG_PYRUVATE_METABOLISM" (nominal *p*-value 0.147; FDR 0.596) as the eighth and "KEGG_N_GLYCAN_BIOSYNTHESIS" (nominal *p*-value 0.193; FDR 0.703) as the tenth most significantly enriched gene set (Figure 1d). Screening of the mRNA data identified a higher expression of the solute carrier family 2 and facilitated glucose transporter SLC2A4 and SLC2A9 genes in HCTR, as well as a higher expression of SLC2A9 and SLC2A12 genes in CapanR as compared to their respective parental cell lines (Figure 1e). Taken together, these data show the transcriptional changes associated with cellular carbohydrate metabolism in response to acute treatment with and acquired resistance against BOLD-100. This suggests a possible role of carbohydrate metabolism as a defense/resistance mechanism against the ruthenium compound.

3.2. Enhanced Glucose Uptake and Glycolytic Activity in Acquired BOLD-100-Resistant Cells Translate into a Metabolic Vulnerability Targetable by 2-DG

Consequently, we hypothesized that the changes in glycolysis-associated gene expression should translate into an altered metabolic phenotype. Hence, BOLD-100-sensitive and –resistant cells were exposed to the fluorescent glucose analog 2-NBDG to measure and quantify glucose uptake with or without treatment with BOLD-100. Indeed, 2-NBDG uptake was significantly increased in HCTR cells as compared to parental cells (Figure 2a). In HCT116 cells, BOLD-100 treatment significantly increased intracellular 2-NBDG levels, while it was decreased in HCTR cells (Figure 2b). These results indicate both an enhanced glucose uptake as a consequence of acquired BOLD-100 resistance and a different response state to BOLD-100 treatment concerning glucose uptake as a consequence of resistance development. Concerning the pancreatic cancer cell models, CapanR cells showed, again, a significantly higher uptake of 2-NBDG as compared to Capan-1 cells and a distinct increase in glucose uptake induced by BOLD-100 treatment in the sensitive parental but not in the resistant subline (Figure S2a,b). Based on these results, extracellular formation of a potential glucose-BOLD-100 adduct with different transport characteristics than free glucose might be postulated. However, MS analysis demonstrated that under cell-free conditions BOLD-100 did not form any adduct with glucose (Figure S2c), arguing against this hypothesis. For further in-depth investigation, gene-metabolite networks were established by a combined computational analysis of the whole genome gene expression and metabolomics data from HCTR as compared to HCT116 cells. Based on these network data, a clear-cut activation of glycolysis with acquired BOLD-100 resistance was suggested (Figure 2c). Besides the above-mentioned HK genes (compare Figure 1c), phosphofructokinase genes PFKP and PFKFB4, coding for the most important rate-limiting enzymes in glycolysis, were significantly upregulated together with clearly enhanced levels of ß-D-fructose-1,6-bisphosphate, an activator of pyruvate kinase [55]. Consequently, the level of the downstream glycolysis product pyruvate was massively increased in HCTR vs. HCT116 cells, together with a decrease in cellular lactate contents (Figure 2d). Treatment with BOLD-100 distinctly reduced pyruvate and lactate levels in HCT116 cells, while this effect was clearly reduced for pyruvate and completely lost in case of lactate in HCTR cells. The above-described stimulation of glucose uptake upon BOLD-100 treatment in HCT116 cells which, however, was paralleled by decreased pyruvate and lactate levels, indicates an interference of BOLD-100 with glycolysis. This hypothesis was supported by downregulated HK2 mRNA expression upon BOLD-100 treatment in HCT116 and Capan-1 cells (Figure S2d).

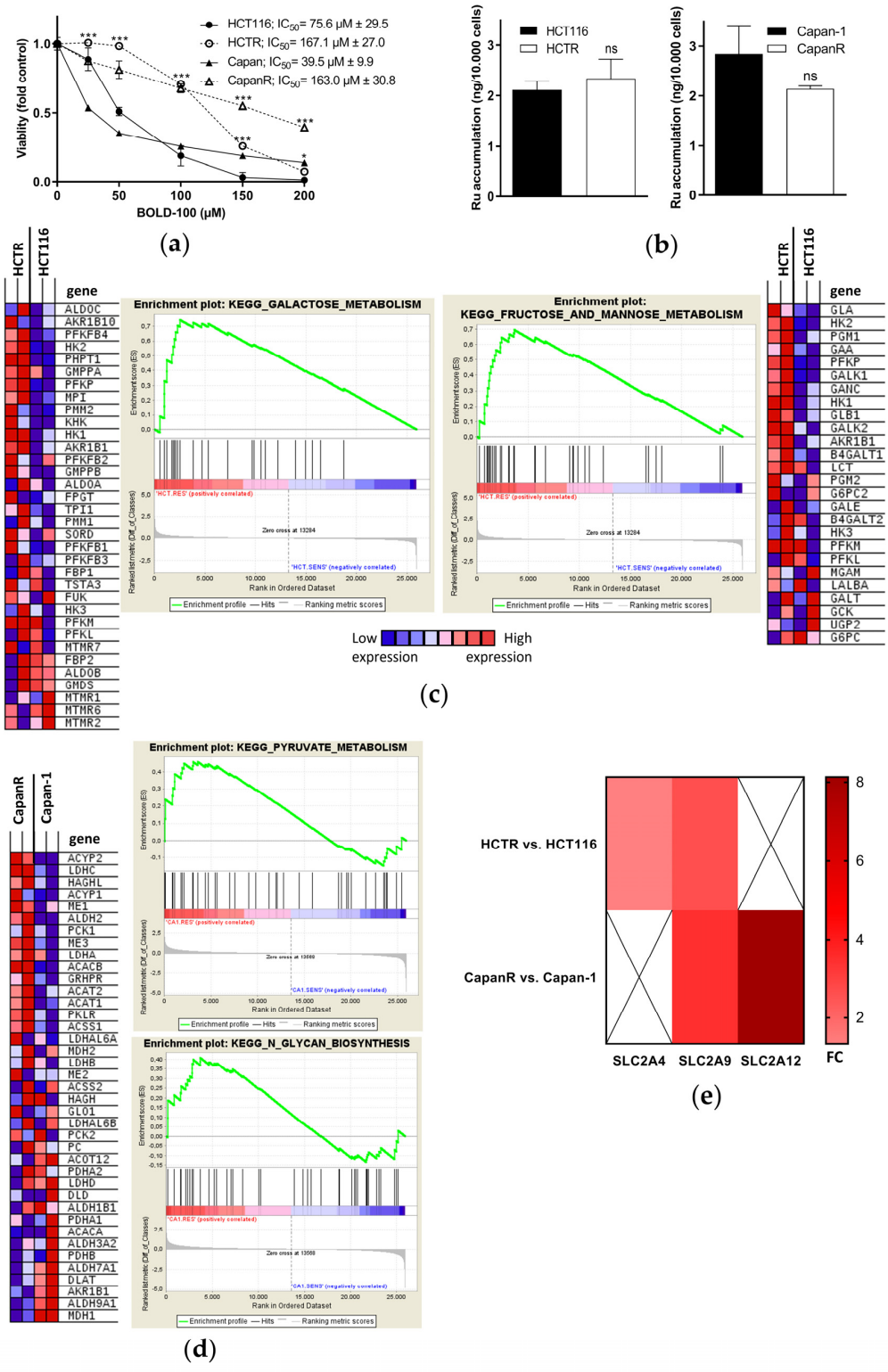

Figure 1. Whole genome gene expression profiling identifies transcriptional deregulations of cellular carbohydrate metabolism as a response to BOLD-100 and in acquired resistance against BOLD-100 in HCT116 and Capan-1 cells. (**a**) Cell viability of acquired BOLD100-resistant HCTR and CapanR cells as compared to their respective parental HCT116 and Capan-1 cells upon 72 h of treatment with increasing BOLD-100 concentrations, as determined by MTT assay. The statistical significance of the

differences was determined using a two-way ANOVA with a Bonferroni post-test: * $p < 0.05$, *** $p < 0.001$. Asterisks are given above BOLD-100-resistant cells at the indicated concentrations and indicate the level of significance of a difference in comparison to parental cells. (**b**) ICP-MS analysis of whole cell lysates of indicated cells after 24 h of treatment with 100 µM BOLD-100. Statistical significance of differences was determined using a two-tailed unpaired Student´s *t*-test: no significant (ns) difference was detected. (**c**) GSEA of HCTR vs. HCT116 cells identifies "GALACTOSE_METABOLISM" (nominal *p*-value < E^{-7}; FDR 0.010) and "FRUCTOSE_AND_MANNOSE_METABOLISM" (nominal *p*-value < E^{-7}; FDR 0.084) as the third and fourth most significantly enriched gene sets in the KEGG database. Heat maps display the differentially regulated genes of the respective gene sets. (**d**) GSEA of CapanR vs. Capan-1 cells identifies "KEGG_PYRUVATE_METABOLISM" (nominal *p*-value 0.147; FDR 0.596) as the eighth and "KEGG_N_GLYCAN_BIOSYNTHESIS" (nominal *p*-value 0.193; FDR 0.703) as the tenth most significantly upregulated gene set. The heat map displays differentially regulated genes of the "KEGG_PYRUVATE_METABOLISM" gene sets. (**e**) mRNA regulation of SLC2A4, SLC2A9, and SLC2A12 of HCTR and CapanR as compared to respective parental counterparts. The bar on the right indicates fold-change (FC) values.

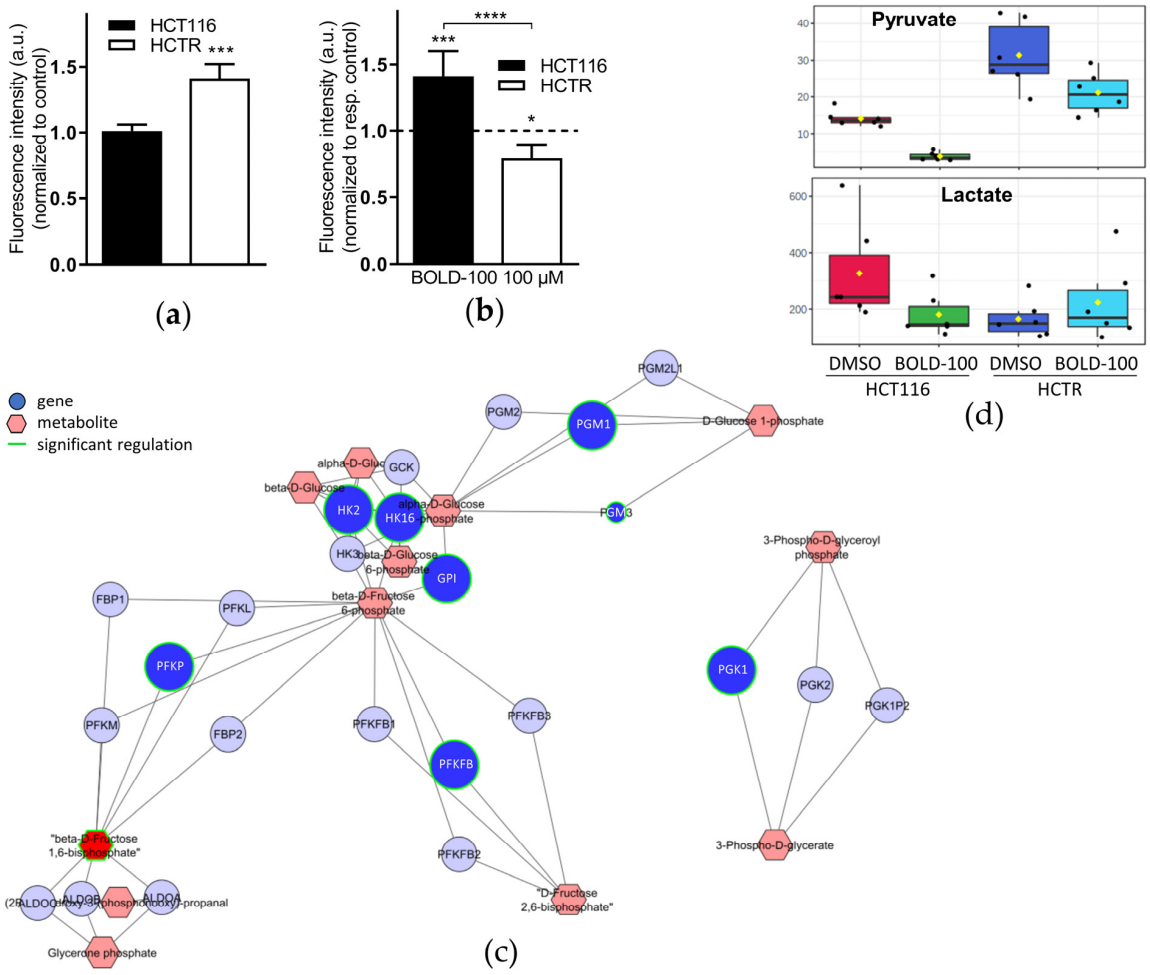

Figure 2. Acquired BOLD-100-resistant HCTR cells are characterized by enhanced glucose uptake and glycolytic activity, leading to increased intracellular pyruvate and decreased lactate levels. Flow cytometry analysis of fluorescence intensity of glucose-starved HCT116 and HCTR cells after 1 h of incubation with 25 µM 2-NBDG following treatment with solvent control (**a**) or 100 µM BOLD-100 (**b**) for 24 h. The results are the means of triplicates ± SD of two independent experiments. In (**b**) data

are normalized to the respective control (dashed line). The statistical significance of differences was calculated with a two-tailed unpaired Student's *t*-test (**a**) or a two-way ANOVA with Tukey's multiple comparisons test (**b**): * $p < 0.05$, *** $p < 0.001$, **** $p < 0.0001$. (**c**) Gene-metabolite network of whole genome gene expression data computed together with metabolomics data of HCTR vs. HCT116 cells. Dots and hexagons indicate regulated genes or metabolites, respectively. Differences in the color intensity correspond to the strength of gene expression change and the green fringe indicates significant regulation. (**d**) Metabolomics of HCTR vs. HCT116 cells with 24 h of treatment with DMSO or 100 µM BOLD-100; all metabolites in pmol/µg protein, $n = 6$ biological replicates.

Together, the identified metabolic perturbations in cells with acquired BOLD-100 resistance led us to the hypothesis that the resistance phenotype might be characterized by novel metabolic vulnerabilities. Hence, glycolysis was inhibited pharmacologically with 2-DG and the effects on cell viability were assessed. Indeed, HCTR (Figure 3a) and CapanR (Figure S3a) cells were distinctly hypersensitive to 2-DG, while inhibition of glutaminolysis with BPTES [56] did not lead to any differences (Figure 3b). This suggests that HCTR cell survival depends on a functional glucose metabolization but not on glutamate utilization. These data clearly show that increased cellular glycolysis plays a key role in acquired resistance against BOLD-100 in HCT116 as well as Capan-1 cells.

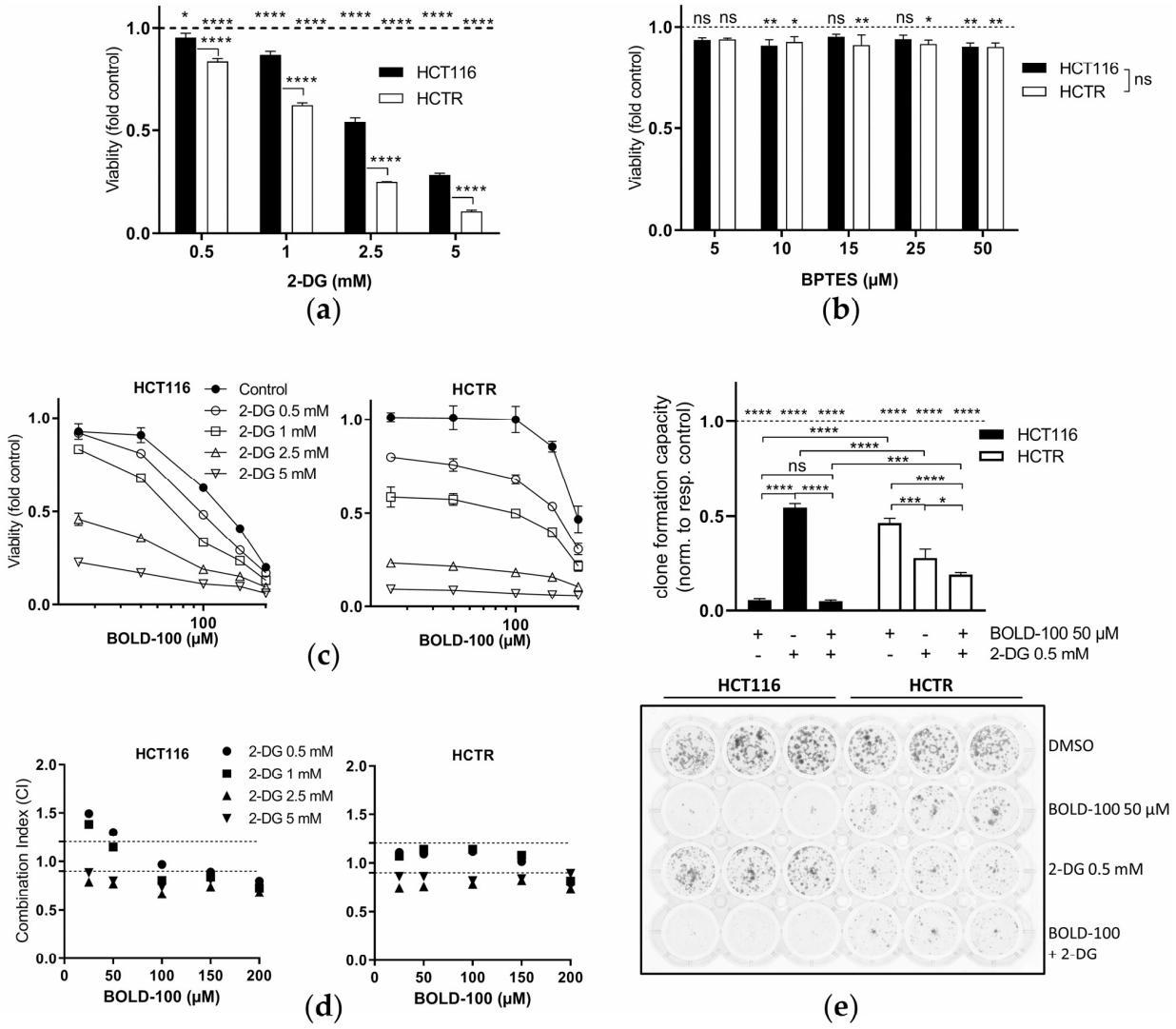

Figure 3. 2-DG targets enhanced glycolytic activity in HCTR cells and synergizes with BOLD-100. (**a**) Cell viability assay of HCT116 and HCTR cells after 72 h of treatment with 2-DG relative to their

respective controls (dashed line). Respective significance levels relative to the controls are indicated above the dashed line. The statistical significance of differences was determined using a two-way ANOVA with Tukey´s multiple comparisons test: * $p < 0.05$, **** $p < 0.0001$. The significance between respective treatment groups is given between the cell lines. (**b**) Cell viability assay of HCT116 vs. HCTR cells after 72 h of treatment with the glutaminase inhibitor BPTES relative to their respective controls (dashed line). The statistical significance of differences was determined using a two-way ANOVA with Tukey´s multiple comparisons test: * $p < 0.05$, ** $p < 0.01$; ns: non-significant. (**c**) Cell viability of indicated cells upon 72 h of treatment with BOLD-100 in combination with 2-DG at the indicated concentrations, as determined by MTT assay. One representative of three independent experiments is shown. (**d**) Combination indices (CI) based on the cell viability data from HCT116 and HCTR cells treated with BOLD-100 in combination with 2-DG at the indicated concentrations for 72 h. CI < 0.9, synergism; CI = 0.9–1.2, additive effects; or CI > 1.2, antagonism. (**e**) Crystal violet-stained clone formation assay showing clonogenic cell growth of HCT116 and HCTR cells treated with 50 µM BOLD-100, 0.5 mM 2-DG, or the combination of both compounds for seven days. For the solvent control, cells were treated with the amount of DMSO equivalent to the respective BOLD-100 samples. Quantification is shown in the lower panel. Results are normalized to the respective control (dashed line). The statistical significance of differences was determined with a two-way ANOVA with Tukey's multiple comparisons test: * $p < 0.05$, *** $p < 0.001$, **** $p < 0.0001$.

3.3. Glucose Deprivation by 2-DG Presents a Novel Strategy to Boost BOLD-100 Anticancer Activity and Overcome Acquired Resistance

Accordingly, we hypothesized that the inhibition of glycolysis might present a potential strategy to revert acquired BOLD-100 resistance. In this regard, cells were concomitantly treated with 2-DG and BOLD-100. Morphologically, BOLD-100-treated HCT116 cells appeared to be massively fragmented, indicative of apoptosis induction, while this effect was strongly reduced in HCTR cells (Figure S3a). Conversely, 2-DG treatment for only 24 h reduced the cell layer density, especially of HCTR cells and to a lesser extent of HCT116 cells. The combination of both compounds led to cell detachment, especially of the parental cells, and further reduced cell density in both sublines. Concerning the cell viability assay results, low concentrations of 2-DG antagonized low-dose cytotoxicity of BOLD-100 in HCT116 cells. Higher concentrations enhanced the cytotoxic activity (Figure 3c). In HCTR cells, already low doses of 2-DG amplified the anticancer activity of BOLD-100. This was verified by the calculation of CI values according to the method published by Chou and Talalay [57]. CI values depicted additive to synergistic activity of the two compounds in both cell models (Figure 3d). Additionally, the clone formation capacity under long-term treatment with 2-DG/BOLD-100 was tested (Figure 3e). As expected, BOLD-100 alone was highly effective in HCT116 cells, while HCTR cells were more resistant to the ruthenium drug. In line with the cell viability assays, 2-DG was more active against clone formation in HCTR cells than in HCT116 cells. The combination of 2-DG and BOLD-100 reduced the clone formation ability of HCTR cells by 31% and 53% as compared to treatment with 2-DG or BOLD-100 alone, respectively. In HCT116 cells, the effects against clone formation were mainly attributed to the already high activity of BOLD-100. Accordingly, an additive to synergistic cytotoxic activity of 2-DG with BOLD-100 was also observed in Capan-1 and CapanR cells (Figure S3c,d).

Consequently, we wondered which mechanisms underlie the hypersensitivity of HCTR cells against 2-DG and the synergistic activity of the combination with BOLD-100 in both cell lines. Previously described cellular responses to 2-DG include cell cycle arrest or reduction of the proliferation rate, both with or without apoptosis induction [16], as well as enhanced autophagy [58]. Thus, we tested the impact of BOLD-100, 2-DG, or their combination on cell cycle distribution (Figure S4a) and cellular proliferative potential via EdU incorporation during DNA synthesis (Figure S4b). Generally, HCTR cells contained a higher percentage of cells in G2/M phase. Fitting to observations from cell survival assays (compare Figure 3a,c,e), BOLD-100 decreased S and increased G0/G1 phase fractions. In line with this, the proliferation rate of HCT116 cells was dose-dependently reduced by

BOLD-100 treatment, in agreement with previous observations [33]. These effects were less pronounced in HCTR cells with a proliferation rate reduction by a factor of 2 (antiproliferative IC_{50} in HCTR: 90.74 µM vs. HCT116 cells: 47.95 µM, Figure S4b). In both cell models, 2-DG increased G0/G1 and reduced S phase, fitting to DNA synthesis rate reduction (antiproliferative IC_{50} in HCTR: 6.20 µM vs. HCT116 cells: 5.76 µM). Unexpectedly, in HCT116 cells the combination treatment counteracted the single drug-induced G0/G1 arrest and increased the G2/M phase fraction. Conversely, in HCTR cells the combination treatment induced a G0/G1 phase increase and reduced the S fraction. While in both cell models the combination treatment synergistically and dose-dependently reduced proliferation, no differences in the single drug activity of 2-DG were found. This rules out an altered impact on DNA synthesis as a factor underlying HCTR cell hypersensitivity to 2-DG.

Next, we performed apoptosis assays via Hoechst/PI co-staining of HCT116 and HCTR cells after 72 h of treatment with BOLD-100, 2-DG, or their combination (Figure 4a, quantification of early or late apoptotic cells in Figure 4b). In the solvent controls of HCT116 and HCTR, the vast majority of cells with condensed chromatin (intensified blue Hoechst staining) were PI-negative and exhibited a mitotic morphology. Conversely, only a few cells contained compacted apoptotic chromatin and were generally PI-positive (red signals; late-apoptotic and dead cells). Upon treatment with BOLD-100, HCT116 cell viability was massively reduced and multiple cells displayed compacted apoptotic nuclei with subpopulations being PI-negative (early apoptotic) or -positive. In HCTR cells, these effects were also observed but to a much lesser extent. 2-DG treatment strongly decreased HCTR cell growth as compared to DMSO-treated controls, however with only minor apoptosis induction. It is noteworthy that it dramatically affected cell morphology. Surviving HCTR cells displayed cell swelling, multinucleation, and massive cytoplasmic vacuolization (black arrows in Figure S5). In contrast, HCT116 cell morphology under 2-DG treatment appeared widely unchanged with only minor cytoplasmic vacuole formation. Concomitant 2-DG and BOLD-100 treatment in both cell lines significantly induced cell death induction by apoptosis. While surviving HCT116 cells in the combination treatment were bigger with enlarged nuclei, surviving HCTR cells again exhibited distinct morphological changes and massive vacuolization (Figure S5, black arrows).

3.4. HCT116 and HCTR Cells Differ in ER Stress Response to 2-DG and BOLD-100 Treatment

2-DG, based on glucose deprivation, is known to induce ER stress via the prevention of *N*-glycosylation of proteins, leading to improper folding and trafficking and, finally, induction of the UPR [19,59,60]. Likewise, BOLD-100 causes enhanced ER stress, at least in part by interfering with ER chaperone GRP78 expression [32,33,61]. Hence, we investigated the interplay of these two agents at the level of the UPR and ER stress signaling by detecting chaperone expression and phosphorylation of eIF2A. The latter process halts protein translation to repair improperly folded proteins and, hence, restore protein homeostasis [62]. Respective Western blot analyses from single and combination treatment samples are shown in Figure 4c. Two different solvent control groups were included: (1) the medium control representing the background of 2-DG treatment and (2) the DMSO-containing control for the BOLD-100 matrix. BOLD-100 enhanced the phosphorylation of eIF2A at serine 51 but reduced basal ER chaperone GRP78 expression in HCT116 cells. In accordance with the literature [61,63], these data prove uncoupling of ER stress induction and chaperone upregulation as a consequence of BOLD-100 treatment. The ER stress response was accompanied by a cleavage of the apoptosis marker PARP [64]. In contrast, the expression of GRP78 was unchanged by BOLD-100 treatment in HCTR cells, while the increase of eIF2A (Ser51) phosphorylation level was comparable to the parental cell line. Consistent with cell viability (compare Figure 1a), the resistant subline lacked BOLD-100-induced PARP cleavage. As expected [21], 2-DG treatment increased glucose-sensing GRP78 protein levels in the BOLD-100-sensitive as well as the BOLD-100-resistant cell model. While in HCT116 cells peIF2A levels were even reduced in response to 2-DG, in HCTR cells peIF2A levels distinctly increased. This indicates a hyperactivation of the glucose restriction-mediated

ER stress response as a consequence of acquired BOLD-100 resistance. In HCTR cells, no enhanced cleavage of PARP was detected upon 2-DG treatment. This suggested that the hypersensitivity of HCTR cells against 2-DG (compare Figure 3a) was based on other mechanisms than apoptosis induction. Concerning the drug combination experiments, BOLD-100 treatment counteracted 2-DG-induced GRP78 upregulation in HCT116 cells. Additionally, 2-DG treatment reduced BOLD-100-induced eIF2A phosphorylation. In sharp contrast to the parental cells, combined BOLD-100 and 2-DG treatment further enhanced GRP78 expression with steady peIF2A levels in HCTR cells but without the cleavage of PARP. To further evaluate the cellular response to the tested cellular stressors, HSP70 protein expression was investigated (Figure 4c). HSP70, like GRP78, belongs to the family of stress-responsive HSP70 proteins and is implicated in the maintenance of cellular protein homeostasis in an ATP-dependent manner [65]. While in HCT116 cells HSP70 levels remained widely unchanged, even under drug exposure, 2-DG treatment efficiently reduced HSP70 levels in HCTR cells. Interestingly, the combination with BOLD-100 even potentiated this effect. The loss of HSP70 expression under 2-DG treatment specifically in HCTR cells might be related to the observed hypersensitivity to glucose deprivation (compare Figure 3a).

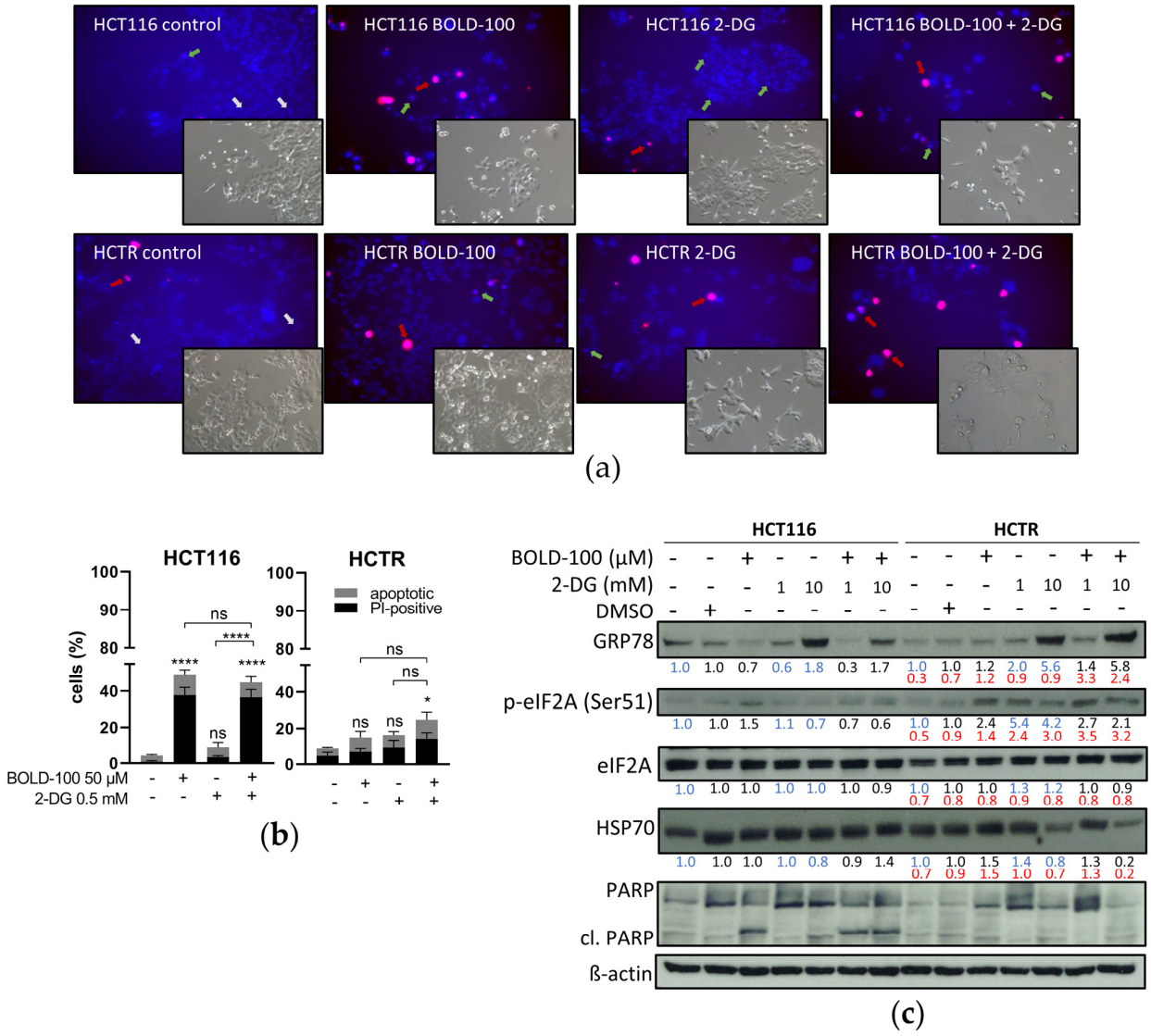

Figure 4. Glucose deprivation by 2-DG differentially regulates ER stress and leads to apoptotic cell death upon combination with BOLD-100. (**a**) Representative composite images show morphological

changes of HCT116 or HCTR cells detected with dual staining of Hoechst 33342/PI. Cells were treated for 72 h with DMSO (control, equivalent to BOLD-100), 2.5 mM 2-DG, 100 μM BOLD-100 or their combination and imaged by fluorescence microscopy (magnification 20×). Grey arrows indicate examples of mitotic nuclei. Green arrows indicate live cells with apoptotic nuclei. Red arrows indicate dead cells with late apoptotic nuclei. (**b**) Quantification of treatment-respective early and late apoptotic nuclei depicted in (**a**). Statistical significance of differences was calculated using a two-way ANOVA with Tukey´s multiple comparisons test: * $p < 0.05$, **** $p < 0.0001$; ns: non-significant. (**c**) Expression levels of GRP78, peIF2A (Ser51), eIF2A, HSP70, and PARP after 24 h of treatment of HCT116 and HCTR cells with the indicated concentrations of BOLD-100, 2-DG, or their combination, analyzed by Western blotting. Two different control states were included, i.e., medium control without DMSO for 2-DG and with DMSO as a solvent control for BOLD-100. β-actin served as the loading control. The numbers below indicate quantified Western blot signal intensities normalized to their respective controls: blue, medium; black, DMSO; and red, HCTR vs. HCT116 cells.

3.5. Cytoplasmic Lysosome HyperAccumulation Presents a Survival Mechanism against Glucose Deprivation by 2-DG

Since ER stress induction via phosphorylation of eIF2A at serine 51 is a central event in autophagy initiation [66], we hypothesized that the observed 2-DG-induced vesicle formation might be related to a deregulation of the autophagic machinery [58]. In general, autophagy is a ubiquitously executed catabolic process ensuring cellular homeostasis via the sequestration of damaged proteins and organelles into autophagosomes and their degradation upon fusion with lysosomes [67]. From the KEGG database, "Lysosome" (nominal *p*-value < E^{-7}; FDR 0.01) was the fifth most enriched gene set in HCTR cells as compared to HCT116 cells (Figure 5a, right). Exemplarily, lysosome-associated membrane protein (LAMP) family mRNA expression was strongly increased in HCTR cells (heat map in Figure 5a, left). Consequently, the impact of time-dependent single and combination treatments on lysosomal dynamics was investigated by Lysotracker (red) staining via flow cytometry (Figure 5b, left) and high-resolution live-cell spinning-disc imaging (Figure 5c). In agreement with the GSEA results, an increased lysosome content of HCTR cells as compared to HCT116 cells was suggested by both methods. Survivor HCT116 cells of acute treatment with BOLD-100 (especially at 72 h exposure) increased the number of lysosomes, while in already lysosome-enriched HCTR cells Lysotracker accumulation remained widely unchanged, indicating a vital role of regulation of lysosome dynamics in the mode of action of BOLD-100. Surviving cells of glucose deprivation by 2-DG for 72 h strongly increased the lysosomal compartment in both cell lines as compared to the respective controls, with the highest lysosomal contents, by far, achieved in the HCTR cells. In the combination setting, BOLD-100 counteracted the 2-DG-induced increase of lysosomes in the case of HCT116 cells but not in HCTR cells. In addition to the altered lysosomal compartment, the massive differences in the impact on cell morphology and vacuolization (compare Figure 4a) were confirmed. Hence, survivors of 2-DG treatment induced a switch to a more mesenchymal, fibroblastoid appearance in HCT116 cells, while HCTR cells displayed a massive retraction of cell extensions and distinct cell clustering. Moreover, Lysotracker-positive lysosomes appeared to encircle as a layer the 2-DG-induced smaller Lysotracker-negative vacuoles, especially in HCTR cells (Figure 5c, white arrows).

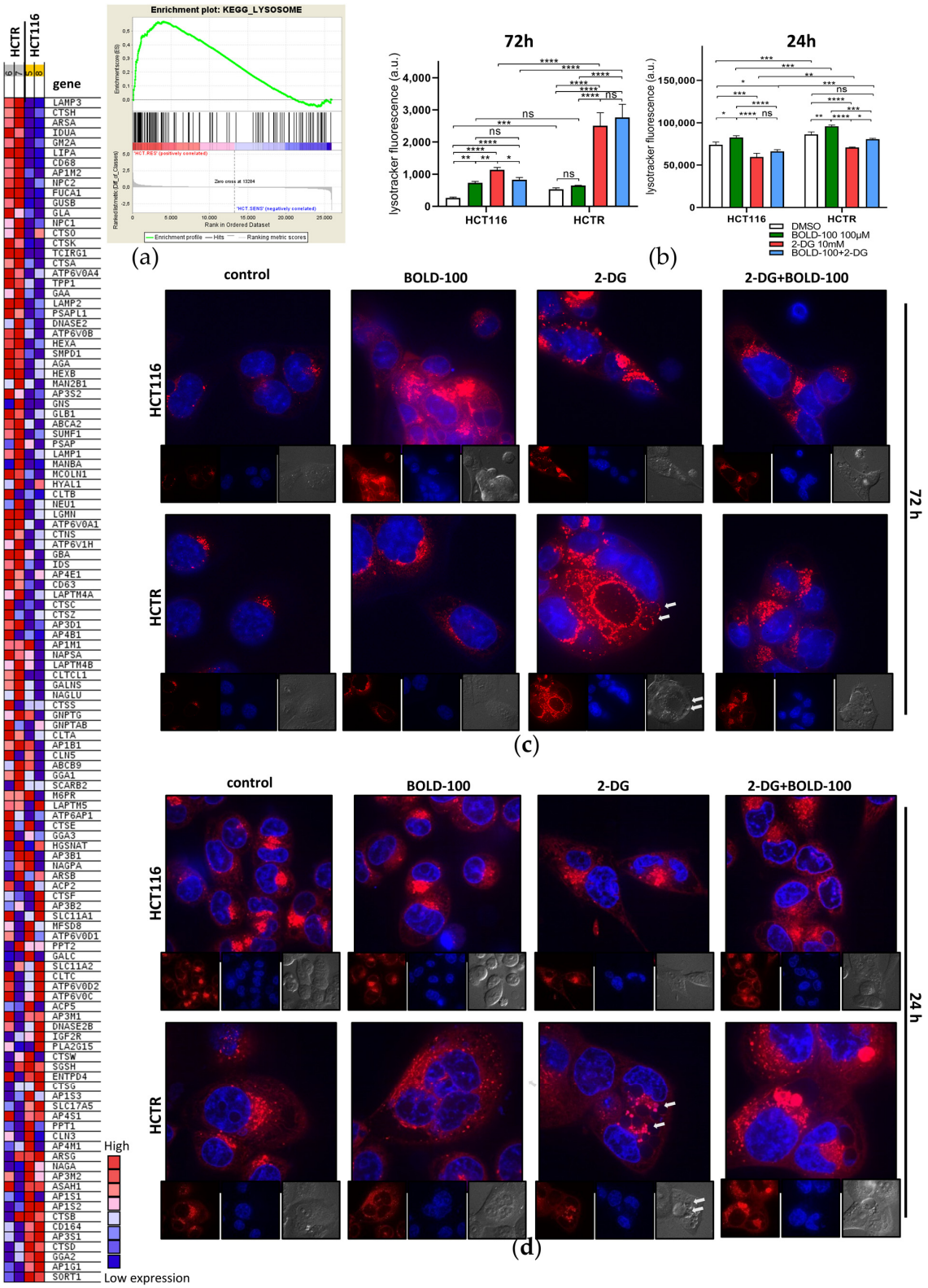

Figure 5. Survival and death from glucose deprivation by 2-DG is associated with differential regulation of the lysosomal compartment. (**a**) GSEA of HCTR vs. HCT116 cells identifies the "LYSOSOME" (nominal *p*-value < E^{-7}; FDR 0.010) as the fifth most significantly enriched gene set in the KEGG database. The heat map displays differentially regulated genes of the respective gene set. (**b**) Flow cytometry analysis of fluorescence intensity of HCT116 and HCTR cells after 72 h or 24 h of

treatment with DMSO, 100 µM BOLD-100, 10 mM 2-DG, or their combination, stained for 30 min with 0.5 µM Lysotracker red. The statistical significance of differences was calculated with a two-way ANOVA with Tukey´s multiple comparisons test: * $p < 0.05$, ** $p < 0.01$, *** $p < 0.001$, **** $p < 0.0001$; ns: non-significant. (**c**) Representative spinning-disc live cell fluorescence images (magnification 192×) of Lysotracker (red) and Hoechst 33342 (blue)-stained HCT116 and HCTR cells after 72 h or (**d**) 24 h of treatment with 100 µM BOLD-100, 10 mM 2-DG, or their combination.

3.6. 2-DG Reduces Cytoplasmic Lysosome Accumulation and Deregulates Autophagic Processing

Considering the massive induction of the lysosomal compartment observed after 72 h as potential survival mechanism against 2-DG, we treated cells for only 24 h with the aim to capture the cell population before cell death induction. Again, the impact of these short-time single and combination treatments on lysosomal dynamics was investigated by Lysotracker (red) staining evaluated by flow cytometry (Figure 5b, right) as compared to high-resolution live-cell spinning-disc imaging (Figure 5d). BOLD-100 increased the number of lysosomes in both cell models, with HCT116 cells already starting to detach from the surface (Figure 5d, inset; compare Figure 4). Supporting our hypothesis on the enrichment of the lysosomal compartment as a survival mechanism against 2-DG, glucose deprivation for 24 h decreased the number of lysosomes in HCT116 and HCTR cells. Morphologically, HCTR cells displayed the massive vacuolization already at this earlier time point (white arrows in Figure 5d), again, distinctly clustering with lysosomes. In the combination setting, BOLD-100 counteracted the 2-DG-induced decrease of lysosomes, especially in the resistant cell model. This antagonism was accompanied by a pronounced accumulation of larger lysosomes. Consequently, the regulation of the autophagic machinery in response to the investigated treatments was assessed on the marker protein level (Figure 6a). Beclin-1 binds to several co-factors forming core complexes that have a key role in the initiation of autophagosome formation [68]. p62/SQSTM1 is implicated in the formation of ubiquitinated protein aggregates that are degraded in the autophagic process [69,70]. LC3B II is the phosphatidylethanolamine (PE)-conjugated form of LC3B I that is incorporated in the membrane during autophagosome formation [71]. LC3B II foci formation, as a marker for the number of autophagosomes, was tested under respective treatment conditions and visualized using high-resolution live-cell spinning-disc imaging (Figure 6b). The ratio of LC3B II/I was calculated (Figure 6d) to monitor the autophagic flux. A reduction of both p62 and beclin-1 levels by BOLD-100 indicates either promotion of the autophagic flux or complete downregulation of the autophagic cascade in HCT116 cells (Figure 6a). Unexpectedly, BOLD-100 led to a distinct increase of both forms of LC3 B, however, with a reduced ratio of LC3B II/I. Together, these observations suggest the upregulation of autophagic flux by BOLD-100, however, paralleled by impaired execution of LC3B processing. Lipidomics analysis (Figure S6) revealed a trend towards a reduction of cellular PE levels by BOLD-100 treatment, delivering a potential mechanistic explanation for the defective LC3B processing in HCT116 cells. In HCTR cells, LC3B II remained widely unchanged and beclin-1 and p62 levels accumulated, the latter by a factor of 1.8 (black numbers in Figure 6a). Accordingly, lipidomics showed that PE levels were enriched in HCTR as compared to HCT116 cells. This suggests an adaptation of the autophagic machinery as a resistance mechanism against BOLD-100. To confirm the impact of BOLD-100 on autophagic flux, combination experiments under downstream blockade by 50 µM CQ, an inhibitor of lysosome-autophagosome fusion [72], were performed (Figure S7a, p62 quantification S7b, LC3B II/I ratio S7c). As expected, CQ treatment alone blocked autophagy comparably in both cell models, as indicated by a p62 increase and an accumulation of LC3B II. BOLD-100 potentiated p62 accumulation in response to CQ in HCT116, supporting an enhancement of the autophagic flux. Again, LC3B delivered contradictory data with an increase at the level of unprocessed LC3B I but not LC3B II, in accordance with the supposed BOLD-100 impact on LC3B lipidation in HCT116 cells. In the case of HCTR cells, BOLD-100 in combination with CQ did not induce further p62 upregulation, while the impact on LC3B conversion, absent without CQ, was recovered in the combination setting. Glucose deprivation by 2-DG increased beclin-1 and p62 as well as LC3B levels in both models (Figures 6a,c and S7) together with the formation of LC3B II

foci (Figure 6b), all indicative of stimulation of the autophagic process [73]. These effects were more distinct in HCTR cells, especially concerning the LC3B II increase, e.g., by a factor 1.5 at 10 µM 2-DG. Accordingly, only in HCTR cells 2-DG dramatically increased the LC3B II/I ratio. The combination with CQ enhanced the effects of 2-DG alone regarding p62 accumulation and increased LC3B II in HCT116 cells (Figure S7a,b). In HCTR cells, the combination with 2-DG did not further enhance CQ-induced LC3B II but, resembling the parental cell line under BOLD-100 treatment, increased LC3B I levels. The combination with BOLD-100 counteracted the 2-DG-induced accumulation of beclin-1 and p62, suggesting a more rapid processing of 2-DG-induced autophagy. Together this led to a massively induced presence of both LC3 forms in HCT116 cells, however, at a reduced LC3 B II/I ratio. Likewise, in HCTR cells, BOLD-100 combined with 2-DG increased both LC3B isoforms and decreased the LC3B II/I ratio. This suggests restored BOLD-100 autophagy inhibition at the level of LC3 conversion under glucose starvation. Concerning the hypersensitivity of HCTR cells against 2-DG, the combination with CQ delivered antagonizing effects on cell viability in HCTR cells but not in HCT116 cells (Figure 6e). This indicates that deregulated autophagy is responsible for the enhanced sensitivity of HCTR cells against glucose starvation, based on the accumulation of deglycosylated, misfolded proteins.

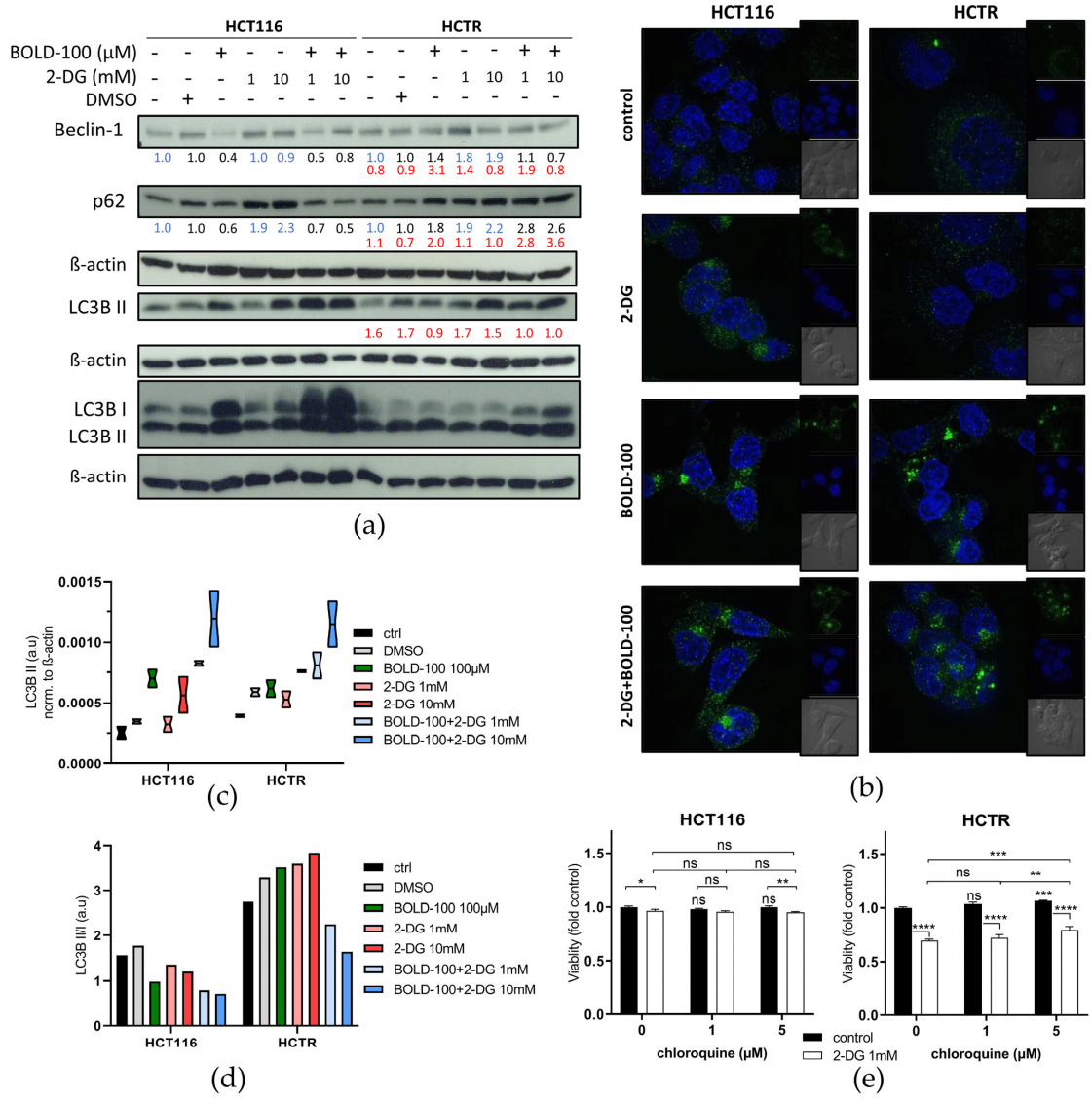

Figure 6. 2-DG differentially regulates autophagy depending on BOLD-100 sensitivity or resistance, and the combination synergistically disturbs the autophagic flux. (**a**) Expression levels of beclin-1,

p62, LC3B, and LC3B I/II in HCT116 and HCTR cells treated with the indicated concentrations of BOLD-100, 2-DG, or their combination for 24 h, analyzed by Western blotting. Two different control states were included, i.e., without DMSO for 2-DG and with DMSO as a solvent control for BOLD-100. β-actin served as the loading control. The numbers below indicate the quantified Western blot signal intensities normalized to their respective controls: blue, medium; black, DMSO; and red, HCTR vs. HCT116 cells. (**b**) Representative spinning-disc live cell fluorescence images (magnification 192×) of Lysotracker (red) and Hoechst 33342 (blue)-stained HCT116 and HCTR cells after 24 h of treatment with 100 μM BOLD-100, 10 mM 2-DG, or their combination. (**c**) Quantification of LC3B signal of two independent Western blot experiments. (**d**) Calculation of the treatment-respective LC3B II/I ratio from protein expression detected in (**a**). (**e**) Cell viability of HCT116 and HCTR cells upon 72 h of treatment with CQ in combination with 2-DG at the indicated concentrations, determined by MTT assay. The statistical significance of differences was calculated with a two-way ANOVA with Tukey´s multiple comparisons test: * $p < 0.05$, ** $p < 0.01$, *** $p < 0.001$, **** $p < 0.0001$; ns: non-significant.

Together our data suggest that BOLD-100 interferes with the complex interplay between ER-stress response, lysosome dynamics, and autophagy execution. Acquired BOLD-100 resistance is accompanied by defective autophagy execution and hypersensitivity to 2-DG by disturbing lysosome-autophagosome fusion and hindering autophagic processing. Hence, the combination of both compounds represents an interesting strategy to synergistically enhance the activity of both therapeutic approaches.

4. Discussion

Glucose is an essential fuel for cellular survival and a factor driving malignant transformation [9,74]. Enhanced cellular glycolytic activity denotes poor prognosis in several solid tumor types and is often implicated in the development of intrinsic and acquired therapy resistance [5,7,8]. Hence, new strategies to specifically target malignant tissue and disable glycolytic activity are urgently needed. Insights into the metabolic alterations in response to ruthenium-based anticancer drugs and acquired resistance against this therapy remain sparse. Recently, we demonstrated that the metabolite abundances and metabolic flux alterations underlying acquired platinum- and ruthenium-based chemotherapy are severe and differ distinctly [31]. The dissection of such specific metabolic changes and their role in the resistance phenotype might open up approaches for resistance circumvention or even allow identification of novel therapeutic vulnerabilities.

In the present study, we have identified specific mechanisms associated with acquired BOLD-100 resistance in colon (HCT116) and pancreatic (Capan-1) cancer cells. In line with previous reports suggesting that BOLD-100 is not a drug transporter substrate [75,76], BOLD-100 resistance was not associated with altered intracellular drug accumulation. These data implicate that the acquisition of BOLD-100 resistance, at least in the two cell models tested, is not primarily based on altered influx or efflux mechanisms. Accordingly, whole genome gene expression analyses revealed no dramatic upregulation in drug transporter gene expression in response to BOLD-100 selection. A significant enrichment of carbohydrate-metabolism-associated genes was identified consistently in both BOLD-100-selected cell models. These mRNA expression changes corresponded with a distinctly enforced glycolytic activity, associated with an enhanced uptake of 2-NBDG, a fluorescent glucose mimic. 2-NBDG, as a substrate for glucose transporters, is used for direct glucose uptake measurement [77]. BOLD-100 treatment in HCT116 cells distinctly stimulated 2-NBDG uptake but, unexpectedly, markedly reduced intracellular pyruvate and lactate levels. As BOLD-100 was not interacting directly with glucose under cell-free conditions, these data strongly suggest a direct interference of the ruthenium compound with glycolysis. The underlying molecular mechanisms are enigmatic so far. Future experiments will address the question of whether the above mentioned rapid downregulation of HK2 mRNA expression in HCT116 and Capan-1 cells upon BOLD-100 treatment is one key factor underlying the observed glycolysis interference. Recent findings in T cells question

if measurement of cellular 2-NBDG accumulation is, indeed, sufficient to assess cellular glucose uptake [78]. Hence, we decided to confirm the enhanced glucose metabolization in BOLD-100 resistance by combining metabolomics with the genome-wide expression data in a gene-metabolite network. This in silico approach again strongly supported an enhanced glycolytic activity in HCTR as compared to the sensitive parental cells, thus confirming the 2-NBDG uptake data.

Several studies have demonstrated an important role of altered glucose metabolism in the development of (chemo)therapy resistance [5]. Metabolic reprogramming in different platinum-, molecular targeted therapy-, or 5-fluorouracil-resistant tumor models translated into a metabolic vulnerability targetable by glycolysis inhibitors, such as 2-DG [11,30]. Accordingly, glycolysis interference by 2-DG was tested in our acquired BOLD-100-resistant cell models and, indeed, the enhanced glycolytic activity conferred hypersensitivity to 2-DG. The modes of action of 2-DG are manifold and vary distinctly in different cell models. In vitro responses to 2-DG include, amongst others, cell cycle arrest, reduction of the proliferation rate, both with or without apoptosis induction [16], regulation of epithelial-to-mesenchymal transition [30], energy stress, and growth inhibition due to ER stress [14], as well as regulation of autophagy [58]. Consequently, the question arose which factors drive HCTR cell hypersensitivity against glucose depletion by 2-DG. Together our data show that 2-DG treatment in sensitive and acquired BOLD-100-resistant HCT116 cells perturbs cell cycle progression and has antiproliferative activity at a widely comparable level, excluding general uptake/accumulation differences, as major contributing factors. One potential explanation lies in the above-mentioned rapid loss of HK2 mRNA expression under acute BOLD-100 treatment and its distinct overexpression after resistance development in HCTR cells as compared to parental cells. This suggests the induction of a stable glucose dependency by the ruthenium compound, which is present even in the absence of BOLD-100. Consequently, 2-DG-induced glucose deficiency led to distinctly higher cell death rates in HCTR as compared to parental cells. This cell-death-inducing effect was further enhanced upon the combination of 2-DG with BOLD-100 in both cell models. Together these data suggest a massive interaction of BOLD-100 with glycolysis and a stably enhanced glucose metabolization as a targetable resistance mechanism. The feasibility of this approach needs, for sure, confirmation in the in vivo situation. Animal experiments are planned in the near future.

Based on the synergy between BOLD-100 and glucose deprivation, we focused on additional molecular mechanisms known to be affected by both the ruthenium compound and 2-DG. GRP78 belongs to the HSP70 family and plays a major role as a chaperone for proper protein refolding due to the UPR and ER stress induction [79]. While GRP78 inhibition plays an important role in the mode of action of BOLD-100 [32,33,61], the ER stress-inducing activity of 2-DG is based on the prevention of the *N*-glycosylation of proteins, causing their improper folding and trafficking and leading to UPR induction [19,21,59,60]. We identified that HCTR cells display an overall decreased GRP78 expression as compared to parental cells, reflecting the GRP78 downregulating activity of BOLD-100, especially in response to protein damage stress [33]. As expected, 2-DG distinctly upregulated GRP78, based on the massive accumulation of proteins lacking proper *N*-glycosylation. In the parental cell line, BOLD-100 distinctly reduced GRP78 upregulation by 2-DG, suggesting that improper chaperone function and enhanced protein damage would be another factor underlying the synergism between the two compounds. However, GRP78 protein levels remained unchanged or even tended to be enhanced in HCTR cells under acute BOLD-100 treatment despite persisting ER stress activation, as proven by the phosphorylation of eIF2a. This suggests that acquired resistance is able to prevent GRP78-targeting by BOLD-100 despite persisting ER-stress induction.

The stronger ER stress-related response to the reduction of protein glycosylation in HCTR cells prompted us to investigate, in addition to the ER chaperone GRP78, also the cytosolic chaperone HSP70. Consistent with previous reports about a widely absent regulation of HSP70 expression upon BOLD-100 treatment [61], HSP70 levels remained

comparably unchanged in HCT116 and HCTR cells in response to BOLD-100 treatment. However, unexpectedly, HSP70 levels were markedly reduced by 2-DG treatment in the resistant HCTR cells only. This selective decrease of HSP70 in cells with acquired BOLD-100 resistance indicates a generally disturbed proteostasis [65,80] induced by BOLD-100 selection and, thus, provides another explanation for the observed hypersensitivity of resistant cells towards 2-DG treatment. HSP70, as a central protein fate hub, is known to be implicated in several protein degradation pathways, including, amongst others, micro-, macro-, or chaperone-mediated autophagy [81]. Hence, the 2-DG-induced decrease of HSP70 expression in HCTR cells, together with the enhanced phosphorylation of eIF2A and the prominent cytoplasmic vacuole formation, links 2-DG treatment with a deregulation of autophagy [66].

Indeed, single agent 2-DG treatment in HCT116 and HCTR cells caused increased p62 and beclin-1 levels, suggesting enhanced autophagic activity, in accordance with the decreased lysosomal compartment. Importantly, the combination with CQ as an inhibitor of autophagosome-lysosome fusion potentiated the 2-DG-associated increase of LC3B I, indicating a buffering role of glucose in the induction of autophagy. In sharp contrast to 2-DG, treatment with BOLD-100 resulted in decreased p62 and beclin-1 levels, pointing to an autophagy-promoting activity of the compound. These results are supported by previous studies reporting the induction of autophagy by ruthenium-based chemotherapy in different cancer types [82–84]. However, the strong increase, not only in LC3B II but also LC3B I levels especially in combination with 2-DG, raises doubts about whether BOLD-100-induced autophagy is indeed functional. The increase in LC3B I, together with the reduction of cellular PE levels, suggests a defect in LC3B processing, potentially related to a defective lipidation by PE-conjugation. Interestingly, the accumulation of LC3B isoforms in response to BOLD-100 was absent in HCTR cells. However, in the combination setting with 2-DG, this effect was at least partly restored. These data strongly suggest that the enhanced glycolysis in HCTR cells plays a central role in the prevention of autophagy defects induced by BOLD-100. Additionally, the blockade of downstream autophagy by CQ also recovered, at least partly, the BOLD-100-induced increase of unprocessed LC3B I observed in parental cells. This suggests that lipid processing by acidic lysosomes might be essential for the resistance of HCTR cells against BOLD-100-induced LC3B conversion defects. The massive increase of both forms of LC3B in the combination of BOLD-100 with 2-DG in HCT116 cells, exceeding the effect of the ruthenium compound alone, indicates that glucose deprivation further promotes the BOLD-100-associated LC3 processing defect, hindering a functional autophagic processing. We conclude that HCTR cells survive treatment with the ruthenium compound via adaptation to BOLD-100-induced autophagy defects by re-established functional ER stress signaling. 2-DG interferes with this adaptation mechanism of HCTR cells, as seen by a distinct increase in eIF2a phosphorylation that leads to autophagy deregulation at the level of autophagosome-lysosome fusion. Targeting of this autophagy adaptation by 2-DG-induced glucose starvation re-sensitizes acquired resistant cells for BOLD-100 anticancer activity.

5. Conclusions

To summarize, this study reveals a significant glycolysis-blocking anti-Warburg effect as novel mechanism of action of BOLD-100. Metabolic rewiring contributes to acquired resistance development, translating into a targetable glucose dependency as a metabolic vulnerability. This metabolic deregulation in response to the ruthenium compound cross-talks with distinct proteostasis and autophagy defects. Whether these different but closely linked activities of BOLD-100 are the consequence of the interaction with one or several molecular targets is matter of ongoing investigations. In any case, inhibition of glycolysis represents a promising strategy to overcome acquired BOLD-100 resistance and enhance BOLD-100 anticancer activity. Finally, the detection of an upregulated glucose uptake associated with BOLD-100 exposure and acquired therapy resistance might be utilized clinically using ^{18}F-fluoro-deoxy-glucose positron emission tomography (FDG-PET) [85].

Hence, we propose clinical studies on the use of ^{18}F-FDG-PET to monitor both BOLD-100 anticancer response and resistance development.

Supplementary Materials: The following supporting information can be downloaded at https://www.mdpi.com/article/10.3390/pharmaceutics14020238/s1, Figure S1: BOLD-100 treatment affects cellular carbohydrate metabolism and acquired resistance is independent from drug transporter expression changes, Figure S2: Acquired BOLD-100 resistance is characterized by enhanced glucose uptake and BOLD-100 treatment reduces HK2 expression, independent from drug-glucose adduct formation, Figure S3: Acquired BOLD-100-resistant Capan-1 and HCT116 cells are hypersensitive to 2-DG, and the anticancer effect can be boosted in combination with BOLD-100, Figure S4: Regulation of cell cycle distribution and proliferation by 2-DG and BOLD-100, Figure S5: Morphological assessment of apoptosis induction under 2-DG and BOLD-100 treatment by Hoechst 33342/PI dual-staining, Figure S6: Regulation of cellular phosphatidylethanolamine levels by BOLD-100, Figure S7: Autophagy regulation by BOLD-100 and 2-DG under autophagic flux blockade by CQ.

Author Contributions: Conceptualization, W.B. and D.B.; methodology, W.B., D.B., M.R., C.P., T.M. (Thomas Mohr), E.R., D.K., S.M.M.-M. and G.K.; software, D.B., M.R., C.P., T.M. (Thomas Mohr), D.K. and K.H.; validation, W.B., T.M. (Thomas Mohr), C.P., E.R., S.M.M.-M. and G.K.; formal analysis, D.B., B.S.-A., M.R. and K.H.; investigation, D.B., B.S.-A., M.R., K.H., S.M.M.-M., M.S., T.M. (Theresa Mendrina) and C.P.; resources, W.B., B.K., P.H., S.M.M.-M., G.K. and E.R.; data curation, W.B., G.K., S.M.M.-M., E.R. and C.P.; writing—original draft preparation, D.B.; writing—review and editing, W.B.; visualization, D.B., M.R., D.K., K.H. and S.M.M.-M.; supervision, W.B.; project administration, W.B. and B.K.; funding acquisition, B.K., W.B. and P.H. All authors have read and agreed to the published version of the manuscript.

Funding: Part of this work was funded by the AUSTRIAN SCIENCE FUND (FWF) within the project "Development of novel anticancer platinum drugs" of the TRANSLATIONAL-RESEARCH-PROGRAMM L 568 of the Research Cluster Translational Cancer Therapy Research Vienna dedicated to W.B. Additionally, part of this research was funded by the FELLINGER CANCER RESEARCH FONDS dedicated to P.H.

Institutional Review Board Statement: Not applicable.

Informed Consent Statement: Not applicable.

Data Availability Statement: Not applicable.

Acknowledgments: We would like to thank Petra Vician and Mirjana Stojanovic for their technical assistance.

Conflicts of Interest: The authors declare no conflict of interest.

References

1. Bui, T.; Thompson, C.B. Cancer's sweet tooth. *Cancer Cell* **2006**, *9*, 419–420. [CrossRef]
2. Jang, M.; Kim, S.S.; Lee, J. Cancer cell metabolism: Implications for therapeutic targets. *Exp. Mol. Med.* **2013**, *45*, e45. [CrossRef]
3. Warburg, O. On the origin of cancer cells. *Science* **1956**, *123*, 309–314. [CrossRef] [PubMed]
4. Liberti, M.V.; Locasale, J.W. The Warburg Effect: How Does it Benefit Cancer Cells? *Trends Biochem. Sci.* **2016**, *41*, 211–218. [CrossRef]
5. Lin, J.; Xia, L.; Liang, J.; Han, Y.; Wang, H.; Oyang, L.; Tan, S.; Tian, Y.; Rao, S.; Chen, X.; et al. The roles of glucose metabolic reprogramming in chemo- and radio-resistance. *J. Exp. Clin. Cancer Res.* **2019**, *38*, 218. [CrossRef]
6. Vidal, R.S.; Quarti, J.; Rodrigues, M.F.; Rumjanek, F.D.; Rumjanek, V.M. Metabolic Reprogramming During Multidrug Resistance in Leukemias. *Front. Oncol.* **2018**, *8*, 90. [CrossRef]
7. Huang, X.Q.; Chen, X.; Xie, X.X.; Zhou, Q.; Li, K.; Li, S.; Shen, L.F.; Su, J. Co-expression of CD147 and GLUT-1 indicates radiation resistance and poor prognosis in cervical squamous cell carcinoma. *Int. J. Clin. Exp. Pathol.* **2014**, *7*, 1651–1666. [PubMed]
8. Evans, A.; Bates, V.; Troy, H.; Hewitt, S.; Holbeck, S.; Chung, Y.L.; Phillips, R.; Stubbs, M.; Griffiths, J.; Airley, R. Glut-1 as a therapeutic target: Increased chemoresistance and HIF-1-independent link with cell turnover is revealed through COMPARE analysis and metabolomic studies. *Cancer Chemother. Pharmacol.* **2008**, *61*, 377–393. [CrossRef]
9. White, M.; McCubrey, J. Changes in glucose-transport associated with malignant transformation (review). *Int. J. Oncol.* **1995**, *7*, 701–712. [CrossRef]

10. Faubert, B.; Boily, G.; Izreig, S.; Griss, T.; Samborska, B.; Dong, Z.; Dupuy, F.; Chambers, C.; Fuerth, B.J.; Viollet, B.; et al. AMPK is a negative regulator of the Warburg effect and suppresses tumor growth in vivo. *Cell Metab.* **2013**, *17*, 113–124. [CrossRef] [PubMed]
11. Gremke, N.; Polo, P.; Dort, A.; Schneikert, J.; Elmshauser, S.; Brehm, C.; Klingmuller, U.; Schmitt, A.; Reinhardt, H.C.; Timofeev, O.; et al. mTOR-mediated cancer drug resistance suppresses autophagy and generates a druggable metabolic vulnerability. *Nat. Commun.* **2020**, *11*, 4684. [CrossRef]
12. Satoh, K.; Yachida, S.; Sugimoto, M.; Oshima, M.; Nakagawa, T.; Akamoto, S.; Tabata, S.; Saitoh, K.; Kato, K.; Sato, S.; et al. Global metabolic reprogramming of colorectal cancer occurs at adenoma stage and is induced by MYC. *Proc. Natl. Acad. Sci. USA* **2017**, *114*, E7697–E7706. [CrossRef]
13. Dang, C.V.; Le, A.; Gao, P. MYC-induced cancer cell energy metabolism and therapeutic opportunities. *Clin. Cancer Res.* **2009**, *15*, 6479–6483. [CrossRef]
14. Liu, H.; Kurtoglu, M.; Leon-Annicchiarico, C.L.; Munoz-Pinedo, C.; Barredo, J.; Leclerc, G.; Merchan, J.; Liu, X.; Lampidis, T.J. Combining 2-deoxy-D-glucose with fenofibrate leads to tumor cell death mediated by simultaneous induction of energy and ER stress. *Oncotarget* **2016**, *7*, 36461–36473. [CrossRef]
15. Barban, S.; Schulze, H.O. The effects of 2-deoxyglucose on the growth and metabolism of cultured human cells. *J. Biol. Chem.* **1961**, *236*, 1887–1890. [CrossRef]
16. Zhang, X.D.; Deslandes, E.; Villedieu, M.; Poulain, L.; Duval, M.; Gauduchon, P.; Schwartz, L.; Icard, P. Effect of 2-deoxy-D-glucose on various malignant cell lines in vitro. *Anticancer Res.* **2006**, *26 (5A)*, 3561–3566.
17. Aft, R.L.; Zhang, F.W.; Gius, D. Evaluation of 2-deoxy-D-glucose as a chemotherapeutic agent: Mechanism of cell death. *Br. J. Cancer* **2002**, *87*, 805–812. [CrossRef]
18. Wang, L.; Yang, Q.; Peng, S.; Liu, X. The combination of the glycolysis inhibitor 2-DG and sorafenib can be effective against sorafenib-tolerant persister cancer cells. *Onco. Targets Ther.* **2019**, *12*, 5359–5373. [CrossRef]
19. Kurtoglu, M.; Gao, N.; Shang, J.; Maher, J.C.; Lehrman, M.A.; Wangpaichitr, M.; Savaraj, N.; Lane, A.N.; Lampidis, T.J. Under normoxia, 2-deoxy-D-glucose elicits cell death in select tumor types not by inhibition of glycolysis but by interfering with *N*-linked glycosylation. *Mol. Cancer Ther.* **2007**, *6*, 3049–3058. [CrossRef]
20. Mote, P.L.; Tillman, J.B.; Spindler, S.R. Glucose regulation of GRP78 gene expression. *Mech. Ageing Dev.* **1998**, *104*, 149–158. [CrossRef]
21. Maximchik, P.; Abdrakhmanov, A.; Inozemtseva, E.; Tyurin-Kuzmin, P.A.; Zhivotovsky, B.; Gogvadze, V. 2-Deoxy-D-glucose has distinct and cell line-specific effects on the survival of different cancer cells upon antitumor drug treatment. *FEBS J.* **2018**, *285*, 4590–4601. [CrossRef]
22. Wu, H.; Zhu, H.; Liu, D.X.; Niu, T.K.; Ren, X.; Patel, R.; Hait, W.N.; Yang, J.M. Silencing of elongation factor-2 kinase potentiates the effect of 2-deoxy-D-glucose against human glioma cells through blunting of autophagy. *Cancer Res.* **2009**, *69*, 2453–2460. [CrossRef]
23. Sahra, I.B.; Laurent, K.; Giuliano, S.; Larbret, F.; Ponzio, G.; Gounon, P.; Le Marchand-Brustel, Y.; Giorgetti-Peraldi, S.; Cormont, M.; Bertolotto, C.; et al. Targeting cancer cell metabolism: The combination of metformin and 2-deoxyglucose induces p53-dependent apoptosis in prostate cancer cells. *Cancer Res.* **2010**, *70*, 2465–2475. [CrossRef]
24. Melendez, A.; Neufeld, T.P. The cell biology of autophagy in metazoans: A developing story. *Development* **2008**, *135*, 2347–2360. [CrossRef]
25. Zhang, D.; Li, J.; Wang, F.; Hu, J.; Wang, S.; Sun, Y. 2-Deoxy-D-glucose targeting of glucose metabolism in cancer cells as a potential therapy. *Cancer Lett.* **2014**, *355*, 176–183. [CrossRef] [PubMed]
26. Stein, M.; Lin, H.; Jeyamohan, C.; Dvorzhinski, D.; Gounder, M.; Bray, K.; Eddy, S.; Goodin, S.; White, E.; Dipaola, R.S. Targeting tumor metabolism with 2-deoxyglucose in patients with castrate-resistant prostate cancer and advanced malignancies. *Prostate* **2010**, *70*, 1388–1394. [CrossRef]
27. Landau, B.R.; Laszlo, J.; Stengle, J.; Burk, D. Certain metabolic and pharmacologic effects in cancer patients given infusions of 2-deoxy-D-glucose. *J. Natl. Cancer Inst.* **1958**, *21*, 485–494.
28. Raez, L.E.; Papadopoulos, K.; Ricart, A.D.; Chiorean, E.G.; Dipaola, R.S.; Stein, M.N.; Rocha Lima, C.M.; Schlesselman, J.J.; Tolba, K.; Langmuir, V.K.; et al. A phase I dose-escalation trial of 2-deoxy-D-glucose alone or combined with docetaxel in patients with advanced solid tumors. *Cancer Chemother. Pharmacol.* **2013**, *71*, 523–530. [CrossRef] [PubMed]
29. Hernlund, E.; Ihrlund, L.S.; Khan, O.; Ates, Y.O.; Linder, S.; Panaretakis, T.; Shoshan, M.C. Potentiation of chemotherapeutic drugs by energy metabolism inhibitors 2-deoxyglucose and etomoxir. *Int. J. Cancer* **2008**, *123*, 476–483. [CrossRef] [PubMed]
30. Park, G.B.; Chung, Y.H.; Kim, D. 2-Deoxy-D-glucose suppresses the migration and reverses the drug resistance of colon cancer cells through ADAM expression regulation. *Anticancer Drugs* **2017**, *28*, 410–420. [CrossRef]
31. Herrmann, H.A.; Rusz, M.; Baier, D.; Jakupec, M.A.; Keppler, B.K.; Berger, W.; Koellensperger, G.; Zanghellini, J. Thermodynamic Genome-Scale Metabolic Modeling of Metallodrug Resistance in Colorectal Cancer. *Cancers* **2021**, *13*, 4130. [CrossRef]
32. Flocke, L.S.; Trondl, R.; Jakupec, M.A.; Keppler, B.K. Molecular mode of action of NKP-1339—a clinically investigated ruthenium-based drug - involves ER- and ROS-related effects in colon carcinoma cell lines. *Investig. New Drugs* **2016**, *34*, 261–268. [CrossRef]
33. Schoenhacker-Alte, B.; Mohr, T.; Pirker, C.; Kryeziu, K.; Kuhn, P.S.; Buck, A.; Hofmann, T.; Gerner, C.; Hermann, G.; Koellensperger, G.; et al. Sensitivity towards the GRP78 inhibitor KP1339/IT-139 is characterized by apoptosis induction via caspase 8 upon disruption of ER homeostasis. *Cancer Lett.* **2017**, *404*, 79–88. [CrossRef] [PubMed]

34. Burris, H.A.; Bakewell, S.; Bendell, J.C.; Infante, J.; Jones, S.F.; Spigel, D.R.; Weiss, G.J.; Ramanathan, R.K.; Ogden, A.; Von Hoff, D. Safety and activity of IT-139, a ruthenium-based compound, in patients with advanced solid tumours: A first-in-human, open-label, dose-escalation phase I study with expansion cohort. *ESMO Open* **2016**, *1*, e000154. [CrossRef] [PubMed]
35. Leijen, S.; Burgers, S.A.; Baas, P.; Pluim, D.; Tibben, M.; van Werkhoven, E.; Alessio, E.; Sava, G.; Beijnen, J.H.; Schellens, J.H. Phase I/II study with ruthenium compound NAMI-A and gemcitabine in patients with non-small cell lung cancer after first line therapy. *Investig. New Drugs* **2015**, *33*, 201–214. [CrossRef]
36. Alessio, E.; Messori, L. NAMI-A and KP1019/1339, Two Iconic Ruthenium Anticancer Drug Candidates Face-to-Face: A Case Story in Medicinal Inorganic Chemistry. *Molecules* **2019**, *24*, 1995. [CrossRef]
37. Peti, W.; Pieper, T.; Sommer, M.; Keppler, B.K.; Giester, G. Synthesis of tumor-inhibiting complex salts containing the anion trans-tetrachlorobis(indazole)ruthenate(III) and crystal structure of the tetraphenylphosphonium salt. *Eur. J. Inorg. Chem.* **1999**, *1999*, 1551–1555. [CrossRef]
38. Trondl, R.; Heffeter, P.; Kowol, C.R.; Jakupec, M.A.; Berger, W.; Keppler, B.K. NKP-1339, the first ruthenium-based anticancer drug on the edge to clinical application. *Chem. Sci.* **2014**, *5*, 2925–2932. [CrossRef]
39. Chou, T.C.; Talalay, P. Quantitative analysis of dose-effect relationships: The combined effects of multiple drugs or enzyme inhibitors. *Adv. Enzyme Regul.* **1984**, *22*, 27–55. [CrossRef]
40. Egger, A.E.; Rappel, C.; Jakupec, M.A.; Hartinger, C.G.; Heffeter, P.; Keppler, B.K. Development of an experimental protocol for uptake studies of metal compounds in adherent tumor cells. *J. Anal. At. Spectrom.* **2009**, *24*, 51–61. [CrossRef] [PubMed]
41. Mathieu, V.; Pirker, C.; Schmidt, W.M.; Spiegl-Kreinecker, S.; Lotsch, D.; Heffeter, P.; Hegedus, B.; Grusch, M.; Kiss, R.; Berger, W. Aggressiveness of human melanoma xenograft models is promoted by aneuploidy-driven gene expression deregulation. *Oncotarget* **2012**, *3*, 399–413. [CrossRef] [PubMed]
42. Subramanian, A.; Tamayo, P.; Mootha, V.K.; Mukherjee, S.; Ebert, B.L.; Gillette, M.A.; Paulovich, A.; Pomeroy, S.L.; Golub, T.R.; Lander, E.S.; et al. Gene set enrichment analysis: A knowledge-based approach for interpreting genome-wide expression profiles. *Proc. Natl. Acad. Sci. USA* **2005**, *102*, 15545–15550. [CrossRef]
43. Mootha, V.K.; Lindgren, C.M.; Eriksson, K.F.; Subramanian, A.; Sihag, S.; Lehar, J.; Puigserver, P.; Carlsson, E.; Ridderstrale, M.; Laurila, E.; et al. PGC-1alpha-responsive genes involved in oxidative phosphorylation are coordinately downregulated in human diabetes. *Nat. Genet* **2003**, *34*, 267–273. [CrossRef] [PubMed]
44. Shannon, P.; Markiel, A.; Ozier, O.; Baliga, N.S.; Wang, J.T.; Ramage, D.; Amin, N.; Schwikowski, B.; Ideker, T. Cytoscape: A software environment for integrated models of biomolecular interaction networks. *Genome Res.* **2003**, *13*, 2498–2504. [CrossRef]
45. Gao, J.; Tarcea, V.G.; Karnovsky, A.; Mirel, B.R.; Weymouth, T.E.; Beecher, C.W.; Cavalcoli, J.D.; Athey, B.D.; Omenn, G.S.; Burant, C.F.; et al. Metscape: A Cytoscape plug-in for visualizing and interpreting metabolomic data in the context of human metabolic networks. *Bioinformatics* **2010**, *26*, 971–973. [CrossRef]
46. Karnovsky, A.; Weymouth, T.; Hull, T.; Tarcea, V.G.; Scardoni, G.; Laudanna, C.; Sartor, M.A.; Stringer, K.A.; Jagadish, H.V.; Burant, C.; et al. Metscape 2 bioinformatics tool for the analysis and visualization of metabolomics and gene expression data. *Bioinformatics* **2012**, *28*, 373–380. [CrossRef]
47. Kanehisa, M.; Goto, S. KEGG: Kyoto Encyclopedia of Genes and Genomes. *Nucleic Acids Res.* **2000**, *28*, 27–30. [CrossRef] [PubMed]
48. Kanehisa, M.; Goto, S.; Sato, Y.; Kawashima, M.; Furumichi, M.; Tanabe, M. Data, information, knowledge and principle: Back to metabolism in KEGG. *Nucleic Acids Res* **2014**, *42*, D199–D205. [CrossRef]
49. Kanehisa, M.; Furumichi, M.; Tanabe, M.; Sato, Y.; Morishima, K. KEGG: New perspectives on genomes, pathways, diseases and drugs. *Nucleic Acids Res.* **2017**, *45*, D353–D361. [CrossRef]
50. Berger, W.; Elbling, L.; Micksche, M. Expression of the major vault protein LRP in human non-small-cell lung cancer cells: Activation by short-term exposure to antineoplastic drugs. *Int. J. Cancer* **2000**, *88*, 293–300. [CrossRef]
51. Rampler, E.; Coman, C.; Hermann, G.; Sickmann, A.; Ahrends, R.; Koellensperger, G. LILY-lipidome isotope labeling of yeast: In vivo synthesis of (13)C labeled reference lipids for quantification by mass spectrometry. *Analyst* **2017**, *142*, 1891–1899. [CrossRef] [PubMed]
52. Rampler, E.; Egger, D.; Schoeny, H.; Rusz, M.; Pacheco, M.P.; Marino, G.; Kasper, C.; Naegele, T.; Koellensperger, G. The Power of LC-MS Based Multiomics: Exploring Adipogenic Differentiation of Human Mesenchymal Stem/Stromal Cells. *Molecules* **2019**, *24*, 3615. [CrossRef]
53. Lohitesh, K.; Chowdhury, R.; Mukherjee, S. Resistance a major hindrance to chemotherapy in hepatocellular carcinoma: An insight. *Cancer Cell Int.* **2018**, *18*, 44. [CrossRef]
54. Alfarouk, K.O.; Stock, C.M.; Taylor, S.; Walsh, M.; Muddathir, A.K.; Verduzco, D.; Bashir, A.H.; Mohammed, O.Y.; Elhassan, G.O.; Harguindey, S.; et al. Resistance to cancer chemotherapy: Failure in drug response from ADME to P-gp. *Cancer Cell Int.* **2015**, *15*, 71. [CrossRef]
55. Ishwar, A.; Tang, Q.; Fenton, A.W. Distinguishing the interactions in the fructose 1,6-bisphosphate binding site of human liver pyruvate kinase that contribute to allostery. *Biochemistry* **2015**, *54*, 1516–1524. [CrossRef]
56. Robinson, M.M.; McBryant, S.J.; Tsukamoto, T.; Rojas, C.; Ferraris, D.V.; Hamilton, S.K.; Hansen, J.C.; Curthoys, N.P. Novel mechanism of inhibition of rat kidney-type glutaminase by bis-2-(5-phenylacetamido-1,2,4-thiadiazol-2-yl)ethyl sulfide (BPTES). *Biochem. J.* **2007**, *406*, 407–414. [CrossRef]
57. Chou, T.C. Drug Combination Studies and Their Synergy Quantification Using the Chou-Talalay Method. *Cancer Res.* **2010**, *70*, 440–446. [CrossRef]

58. Gonzalez-Polo, R.A.; Boya, P.; Pauleau, A.L.; Jalil, A.; Larochette, N.; Souquere, S.; Eskelinen, E.L.; Pierron, G.; Saftig, P.; Kroemer, G. The apoptosis/autophagy paradox: Autophagic vacuolization before apoptotic death. *J. Cell Sci.* **2005**, *118 (Pt 14)*, 3091–3102. [CrossRef]
59. Karki, R.; Rimal, S.; Rieth, M.D. Predicted *N*-terminal *N*-linked glycosylation sites may underlie membrane protein expression patterns in Saccharomyces cerevisiae. *Yeast* **2021**, *38*, 497–506. [CrossRef] [PubMed]
60. Cherepanova, N.; Shrimal, S.; Gilmore, R. *N*-linked glycosylation and homeostasis of the endoplasmic reticulum. *Curr. Opin. Cell Biol.* **2016**, *41*, 57–65. [CrossRef] [PubMed]
61. Bakewell, S.J.; Rangel, D.F.; Ha, D.P.; Sethuraman, J.; Crouse, R.; Hadley, E.; Costich, T.L.; Zhou, X.; Nichols, P.; Lee, A.S. Suppression of stress induction of the 78-kilodalton glucose regulated protein (GRP78) in cancer by IT-139, an anti-tumor ruthenium small molecule inhibitor. *Oncotarget* **2018**, *9*, 29698–29714. [CrossRef] [PubMed]
62. Wek, R.C. Role of eIF2alpha Kinases in Translational Control and Adaptation to Cellular Stress. *Cold Spring Harb. Perspect Biol.* **2018**, *10*, a032870. [CrossRef]
63. Gifford, J.B.; Huang, W.; Zeleniak, A.E.; Hindoyan, A.; Wu, H.; Donahue, T.R.; Hill, R. Expression of GRP78, Master Regulator of the Unfolded Protein Response, Increases Chemoresistance in Pancreatic Ductal Adenocarcinoma. *Mol. Cancer Ther.* **2016**, *15*, 1043–1052. [CrossRef]
64. Kaufmann, S.H.; Desnoyers, S.; Ottaviano, Y.; Davidson, N.E.; Poirier, G.G. Specific proteolytic cleavage of poly(ADP-ribose) polymerase: An early marker of chemotherapy-induced apoptosis. *Cancer Res.* **1993**, *53*, 3976–3985.
65. Mallouk, Y.; Vayssier-Taussat, M.; Bonventre, J.V.; Polla, B.S. Heat shock protein 70 and ATP as partners in cell homeostasis (Review). *Int. J. Mol. Med.* **1999**, *4*, 463–474. [CrossRef]
66. Humeau, J.; Leduc, M.; Cerrato, G.; Loos, F.; Kepp, O.; Kroemer, G. Phosphorylation of eukaryotic initiation factor-2alpha (eIF2alpha) in autophagy. *Cell Death Dis.* **2020**, *11*, 433. [CrossRef] [PubMed]
67. Klionsky, D.J.; Emr, S.D. Autophagy as a regulated pathway of cellular degradation. *Science* **2000**, *290*, 1717–1721. [CrossRef] [PubMed]
68. Kang, R.; Zeh, H.J.; Lotze, M.T.; Tang, D. The Beclin 1 network regulates autophagy and apoptosis. *Cell Death Differ.* **2011**, *18*, 571–580. [CrossRef]
69. Pankiv, S.; Clausen, T.H.; Lamark, T.; Brech, A.; Bruun, J.A.; Outzen, H.; Overvatn, A.; Bjorkoy, G.; Johansen, T. p62/SQSTM1 binds directly to Atg8/LC3 to facilitate degradation of ubiquitinated protein aggregates by autophagy. *J. Biol. Chem.* **2007**, *282*, 24131–24145. [CrossRef] [PubMed]
70. Mathew, R.; Karp, C.M.; Beaudoin, B.; Vuong, N.; Chen, G.; Chen, H.Y.; Bray, K.; Reddy, A.; Bhanot, G.; Gelinas, C.; et al. Autophagy suppresses tumorigenesis through elimination of p62. *Cell* **2009**, *137*, 1062–1075. [CrossRef] [PubMed]
71. Tanida, I.; Ueno, T.; Kominami, E. LC3 and Autophagy. *Methods Mol. Biol.* **2008**, *445*, 77–88.
72. Jia, B.; Xue, Y.; Yan, X.; Li, J.; Wu, Y.; Guo, R.; Zhang, J.; Zhang, L.; Li, Y.; Liu, Y.; et al. Autophagy inhibitor chloroquine induces apoptosis of cholangiocarcinoma cells via endoplasmic reticulum stress. *Oncol. Lett.* **2018**, *16*, 3509–3516. [CrossRef]
73. Jeon, J.Y.; Kim, S.W.; Park, K.C.; Yun, M. The bifunctional autophagic flux by 2-deoxyglucose to control survival or growth of prostate cancer cells. *BMC Cancer* **2015**, *15*, 623. [CrossRef] [PubMed]
74. Swamy, M.; Pathak, S.; Grzes, K.M.; Damerow, S.; Sinclair, L.V.; van Aalten, D.M.; Cantrell, D.A. Glucose and glutamine fuel protein O-GlcNAcylation to control T cell self-renewal and malignancy. *Nat. Immunol.* **2016**, *17*, 712–720. [CrossRef]
75. Heffeter, P.; Pongratz, M.; Steiner, E.; Chiba, P.; Jakupec, M.A.; Elbling, L.; Marian, B.; Korner, W.; Sevelda, F.; Micksche, M.; et al. Intrinsic and acquired forms of resistance against the anticancer ruthenium compound KP1019 [indazolium trans-[tetrachlorobis(1H-indazole)ruthenate(III)] (FFC14A). *J. Pharmacol. Exp. Ther.* **2005**, *312*, 281–289. [CrossRef] [PubMed]
76. Heffeter, P.; Atil, B.; Kryeziu, K.; Groza, D.; Koellensperger, G.; Korner, W.; Jungwirth, U.; Mohr, T.; Keppler, B.K.; Berger, W. The ruthenium compound KP1339 potentiates the anticancer activity of sorafenib in vitro and in vivo. *Eur. J. Cancer* **2013**, *49*, 3366–3375. [CrossRef]
77. Zou, C.; Wang, Y.; Shen, Z. 2-NBDG as a fluorescent indicator for direct glucose uptake measurement. *J. Biochem. Biophys. Methods* **2005**, *64*, 207–215. [CrossRef] [PubMed]
78. Sinclair, L.V.; Barthelemy, C.; Cantrell, D.A. Single Cell Glucose Uptake Assays: A Cautionary Tale. *Immunometabolism* **2020**, *2*, e200029.
79. Moradi-Marjaneh, R.; Paseban, M.; Moradi Marjaneh, M. Hsp70 inhibitors: Implications for the treatment of colorectal cancer. *IUBMB Life* **2019**, *71*, 1834–1845. [CrossRef]
80. Sannino, S.; Yates, M.E.; Schurdak, M.E.; Oesterreich, S.; Lee, A.V.; Wipf, P.; Brodsky, J.L. Unique integrated stress response sensors regulate cancer cell susceptibility when Hsp70 activity is compromised. *Elife* **2021**, *10*, e64977. [CrossRef]
81. Fernandez-Fernandez, M.R.; Gragera, M.; Ochoa-Ibarrola, L.; Quintana-Gallardo, L.; Valpuesta, J.M. Hsp70—A master regulator in protein degradation. *FEBS Lett.* **2017**, *591*, 2648–2660. [CrossRef] [PubMed]
82. Piccolo, M.; Misso, G.; Ferraro, M.G.; Riccardi, C.; Capuozzo, A.; Zarone, M.R.; Maione, F.; Trifuoggi, M.; Stiuso, P.; D'Errico, G.; et al. Exploring cellular uptake, accumulation and mechanism of action of a cationic Ru-based nanosystem in human preclinical models of breast cancer. *Sci. Rep.* **2019**, *9*, 7006. [CrossRef]
83. Chen, L.; Li, G.; Peng, F.; Jie, X.; Dongye, G.; Cai, K.; Feng, R.; Li, B.; Zeng, Q.; Lun, K.; et al. The induction of autophagy against mitochondria-mediated apoptosis in lung cancer cells by a ruthenium(II) imidazole complex. *Oncotarget* **2016**, *7*, 80716–80734. [CrossRef] [PubMed]

84. Sun, Q.; Li, Y.; Shi, H.; Wang, Y.; Zhang, J.; Zhang, Q. Ruthenium Complexes as Promising Candidates against Lung Cancer. *Molecules* **2021**, *26*, 4389. [CrossRef]
85. Kawada, K.; Iwamoto, M.; Sakai, Y. Mechanisms underlying (18)F-fluorodeoxyglucose accumulation in colorectal cancer. *World J. Radiol.* **2016**, *8*, 880–886. [CrossRef] [PubMed]

pharmaceutics

Supplementary Materials: The Anticancer Ruthenium Compound BOLD-100 Targets Glycolysis and Generates a Metabolic Vulnerability towards Glucose Deprivation

Dina Baier, Beatrix Schoenhacker-Alte, Mate Rusz, Christine Pirker, Thomas Mohr, Theresa Mendrina, Dominik Kirchhofer, Samuel M. Meier-Menches, Katharina Hohenwallner, Martin Schaier, Evelyn Rampler, Gunda Koellensperger, Petra Heffeter, Bernhard Keppler and Walter Berger

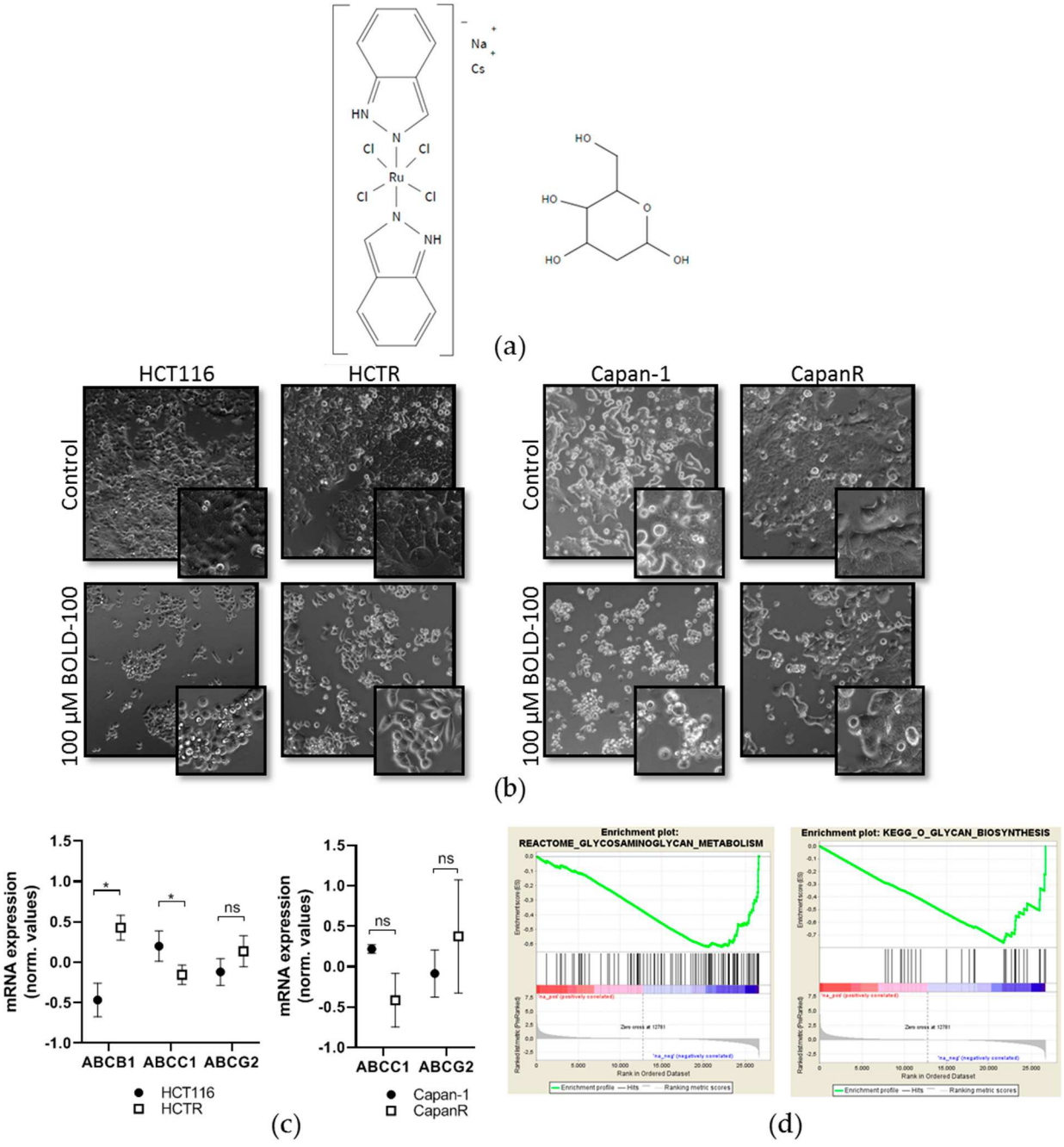

Figure S1 BOLD-100 treatment affects the cellular carbohydrate metabolism and acquired resistance is independent from drug transporter expression changes (**a**) Chemical structures of BOLD-100 (left) with cesium as an intermediate salt form and 2-DG (right)

created with SciFinder (Copyright © 2022 American Chemical Society). (**b**) Representative phase-contrast photomicrographs (4x magnification) after 24 h of treatment with 100 µM of BOLD-100 to indicate morphologic changes of parental and acquired BOLD-100-resistant HCT116 cells. Enlargements are 10x magnified. (**c**) Normalized mRNA expression of ABC drug transporters ABCB1, ABCC1, and ABCG2 in HCT116 and HCTR or Capan-1 and CapanR cells. In Capan cell models, ABCB1 mRNA expression was below the detection limit. The statistical significance of differences was calculated with an unpaired two-tailed Student´s t-test: *p<0.05; ns: non-significant. (**d**) GSEA identified "GLYCOSAMINOGLYCAN_METABOLISM" (nominal p-value < E^{-7}, FDR q-value = 0.003, and normalized enrichment score (NES) = -1.861) as top fourth downregulated gene set according to the REACTOME database and "O_GLYCAN_BIOSYNTHESIS" (nominal p-value < E^{-7}, FDR q-value = 0.003, and normalized enrichment score (NES) = -1.847) as top seventh downregulated gene set according to the KEGG database upon 100 µM BOLD-100 treatment for 6 h in HCT116 cells.

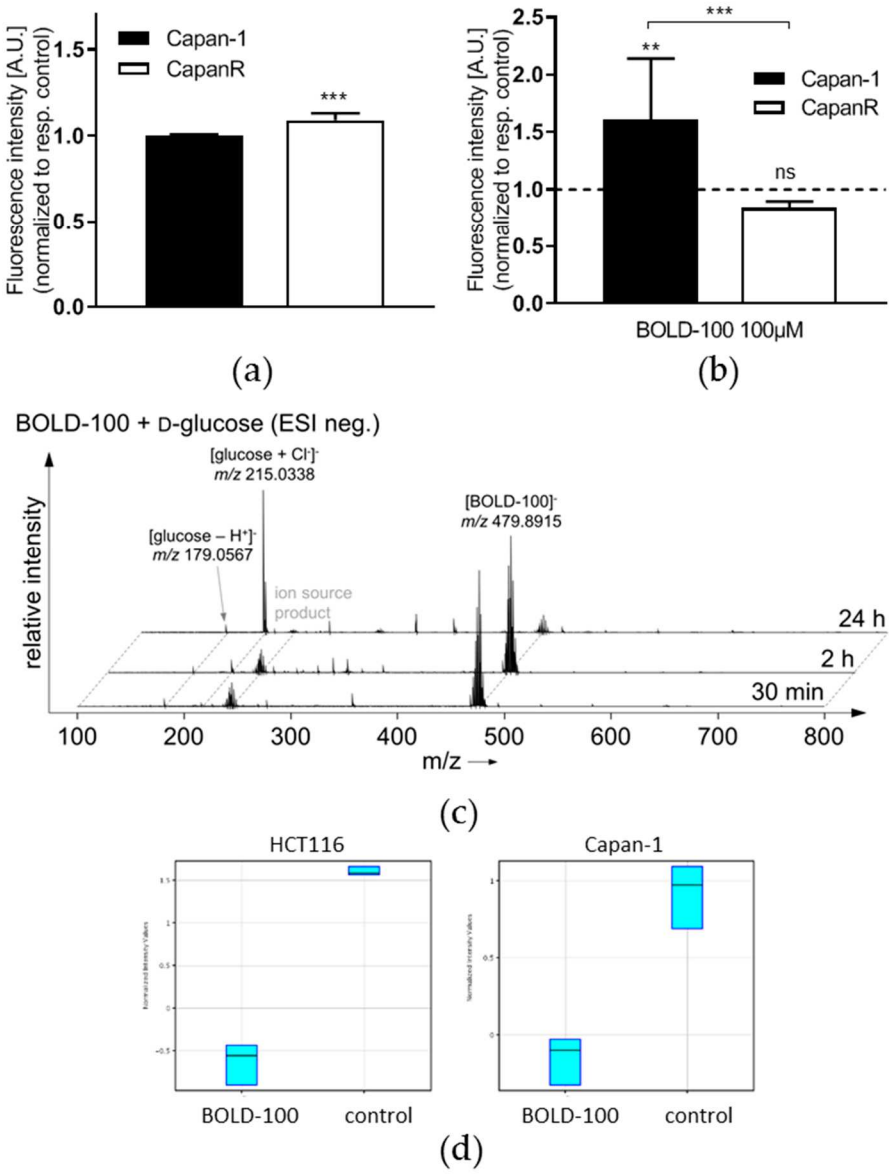

Figure S2 Acquired BOLD-100-resistance is characterized by enhanced glucose uptake and BOLD-100 treatment reduces HK2 expression independent from drug-glucose adduct formation. FACS analysis of fluorescence intensity (arbitrary units, a.u.) of glucose-starved Capan-1 and CapanR cells after 1 h incubation with 25 µM of 2-NBDG following treatment with solvent control (**a**) or 100 µM of BOLD-100 (**b**) for 24 h. Results are mean of triplicates ± SD of two independent experiments. In (**b**) data are normalized

to the respective control (dashed line). Statistical significance of differences was calculated with a two-tailed unpaired student´s t-test (**a**) or two-way ANOVA with Tukey´s multiple comparisons test (**b**): ***p<0.001; ns: non-significant**.** (**c**) Mass spectra of the interaction between BOLD-100 and D-glucose (1 : 4 molar ratio) acquired in the negative ion mode after the indicated incubation times. (**d**) Relative mRNA expression of HK2 in HCT116 and Capan-1 cells with or without 6 h treatment with 100 μM of BOLD-100.

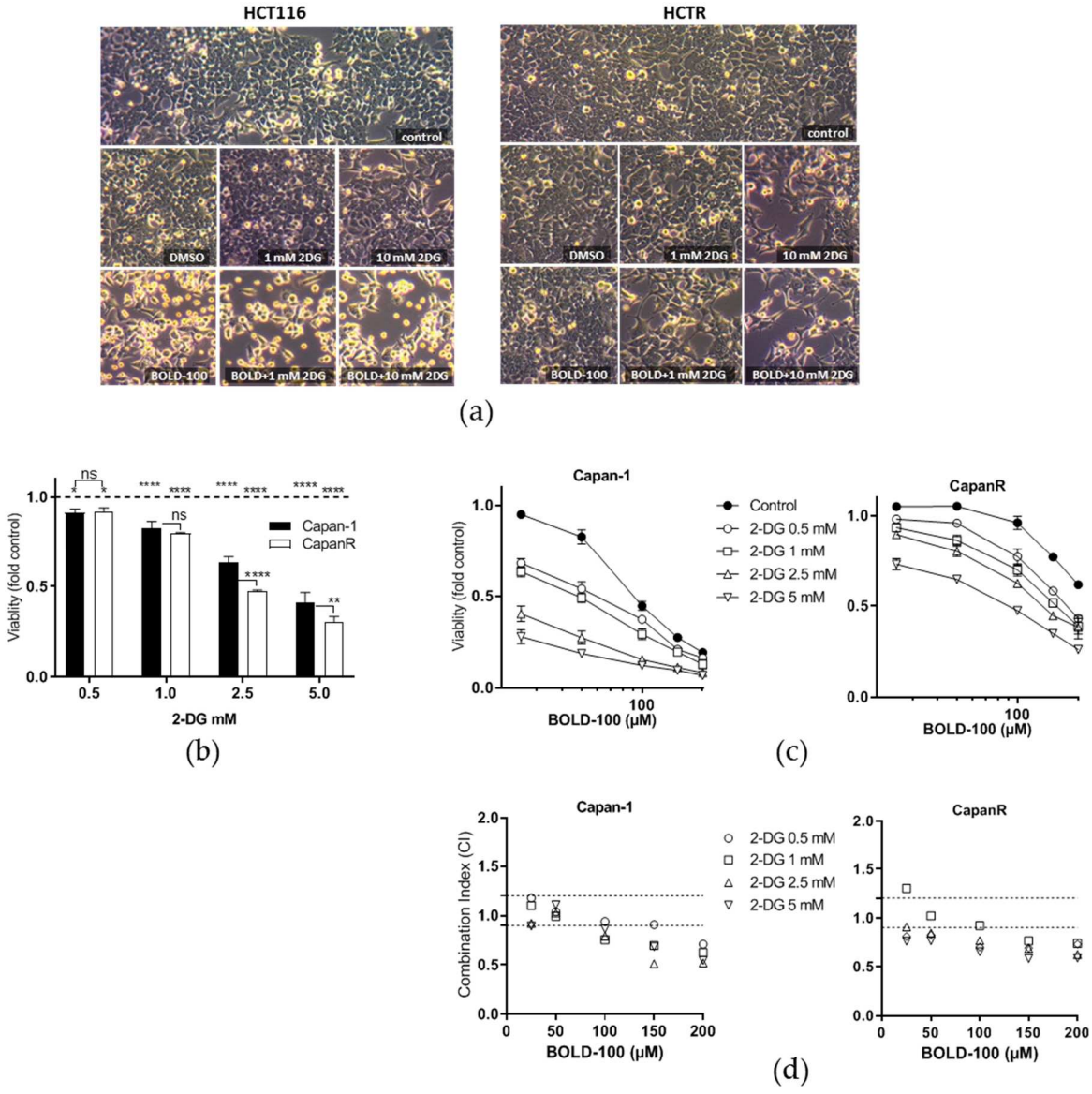

Figure S3 Acquired BOLD-100-resistant Capan-1 and HCT116 cells are hypersensitive to 2-DG and the anticancer effect can be boosted in combination with BOLD-100. (**a**) Respective phase-contrast photomicrographs (10x magnification) of HCT116 and HCTR cells after 24 h of treatment with 100 μM of BOLD-100 or the indicated concentrations of 2-DG, or the combination of both compounds to indicate morphologic changes. Two different control states were included, i.e. the medium control without and with DMSO. (**b**) Cell viability assay of Capan-1 vs. CapanR cells after 72 h of treatment with 2-DG relative to respective controls (dashed line). The statistical significance of differences was determined using a two-way ANOVA with Tukey´s multiple comparisons test: **p<0.01, ****p<0.0001 (**c**) Cell viability of Capan-1 and CapanR cells upon 72 h treatment with BOLD-100 in combination with 2-DG at the indicated concentrations determined by MTT assay. Data are mean of triplicates ± SD. One representative of three independent experiments is shown. (**d**) Combination indices (CI) based on cell viability data from Capan-1 and CapanR cells treated with BOLD-100 in combination with 2-DG at the indicated concentrations for 72 h. CI < 0.9, synergism; CI = 0.9-1.2, additive effects; or CI > 1.2 antagonism.

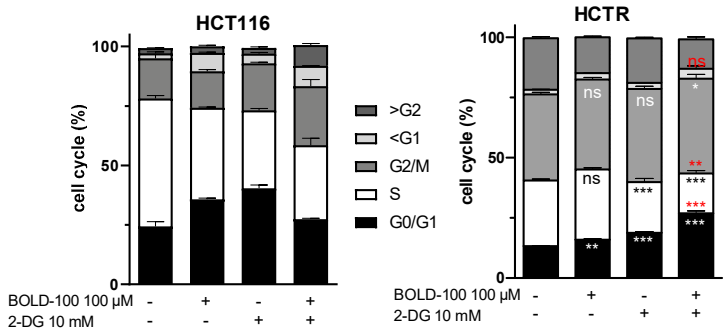

(a)

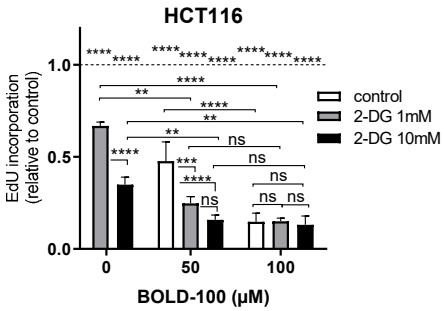

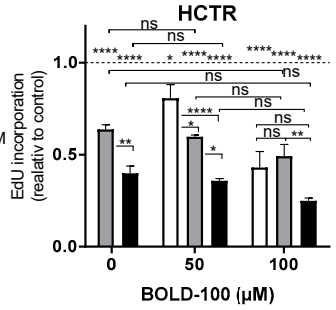

	antiproliferative IC_{50}:	
	HCT116	HCTR
BOLD-100 (µM)	47.95	90.74
2-DG (mM)	5.76	6.20

(b)

Figure S4 Regulation of cell cycle distribution and proliferation by 2-DG and BOLD-100. (**a**) Cell cycle analysis determining the DNA content of the indicated ethanol-fixed, PI-stained cells after 24 h of treatment with the indicated drug concentrations by flow cytometry. Controls contained the amount of DMSO corresponding to 100 µM of BOLD-100. Percentages of 50.000 cells in G0/G1, S, G2/M, and <G1 or >G2 phase of cell cycle were calculated by FlowJo software. The statistical significance of differences was determined using a one-way ANOVA with Tukey´s multiple comparisons test: *p<0.05, **p<0.01, ***p<0.001; ns: non-significant. Black and white asterisks indicate significant difference as compared to the control and red asterisks show significant differences compared to the single treatments. (**b**) EdU incorporation assay of HCT116 and HCTR cells after 24 h of treatment with either 2-DG or BOLD-100 or their combination at the indicated concentrations relative to respective controls (dashed line). Controls contained the amount of DMSO corresponding to 100 µM of BOLD-100. Data are mean of triplicates ± SD of one representative experiment. The statistical significance of differences was determined using a two-way ANOVA with Tukey´s multiple comparisons test: *p<0.05, **p<0.01, ***p<0.001, ****p<0.0001; ns: non-significant. Respective significance levels relative to the controls are indicated above the dashed lines. Significance between respective treatment groups is given beneath the dashed line. The table gives IC_{50} values of the drug-respective antiproliferative activity.

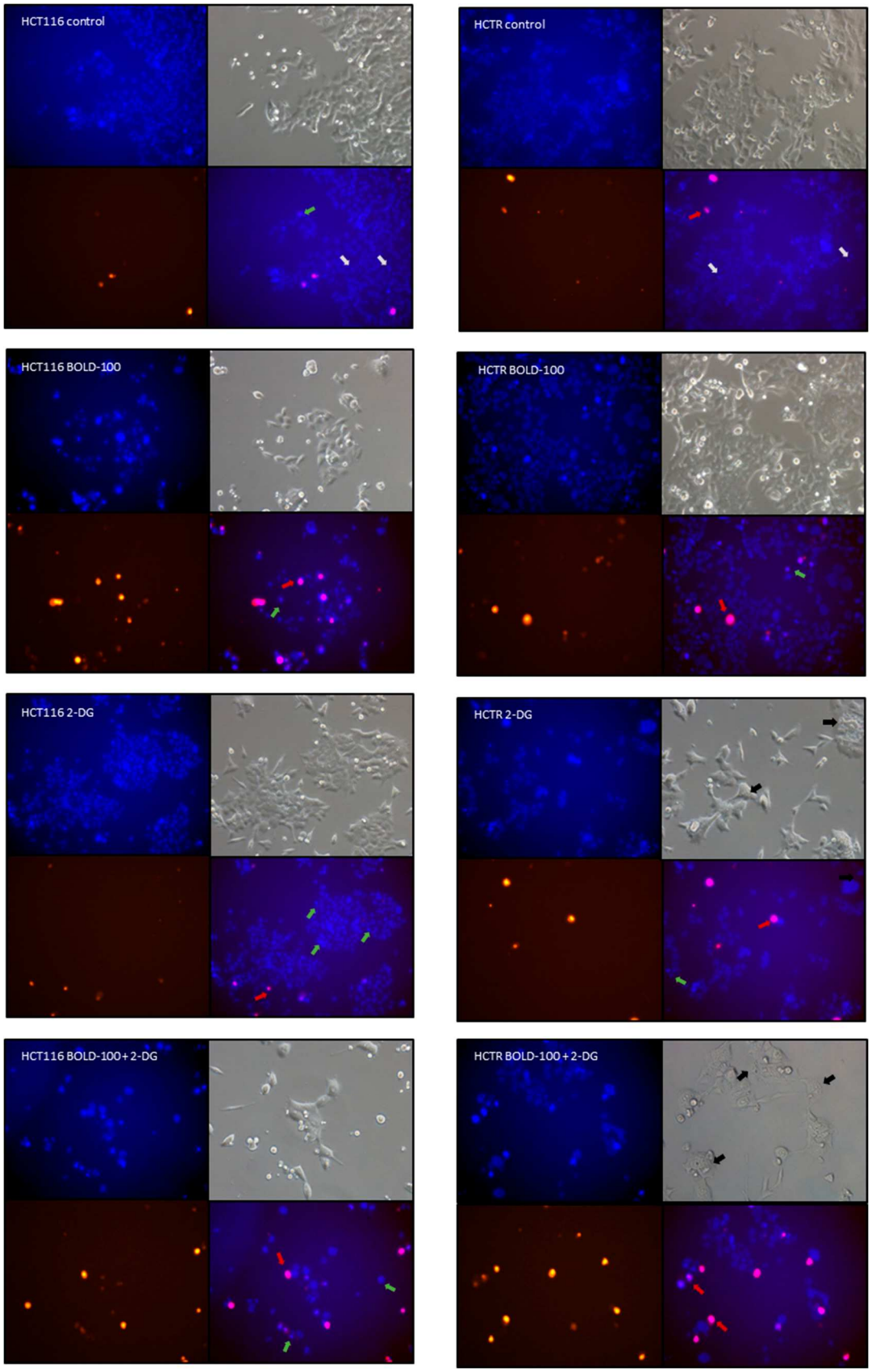

Figure S5 Morphological assessment of apoptosis induction under 2-DG and BOLD-100 treatment by Hoechst 33342/PI dual-staining. Representative images of Hoechst 33342 (blue)/PI (red)-stained HCT116 or HCTR cells after treatment for 72 h with DMSO (control, equivalent to BOLD-100), 2.5 mM of 2-DG or 100 µM of BOLD-100 or their combination. Images were taken by fluorescence microscopy (magnification 20x). Phase contrast images display corresponding cellular morphological changes. Black arrows exemplarily indicate distinct morphological changes induced by 2-DG treatment.

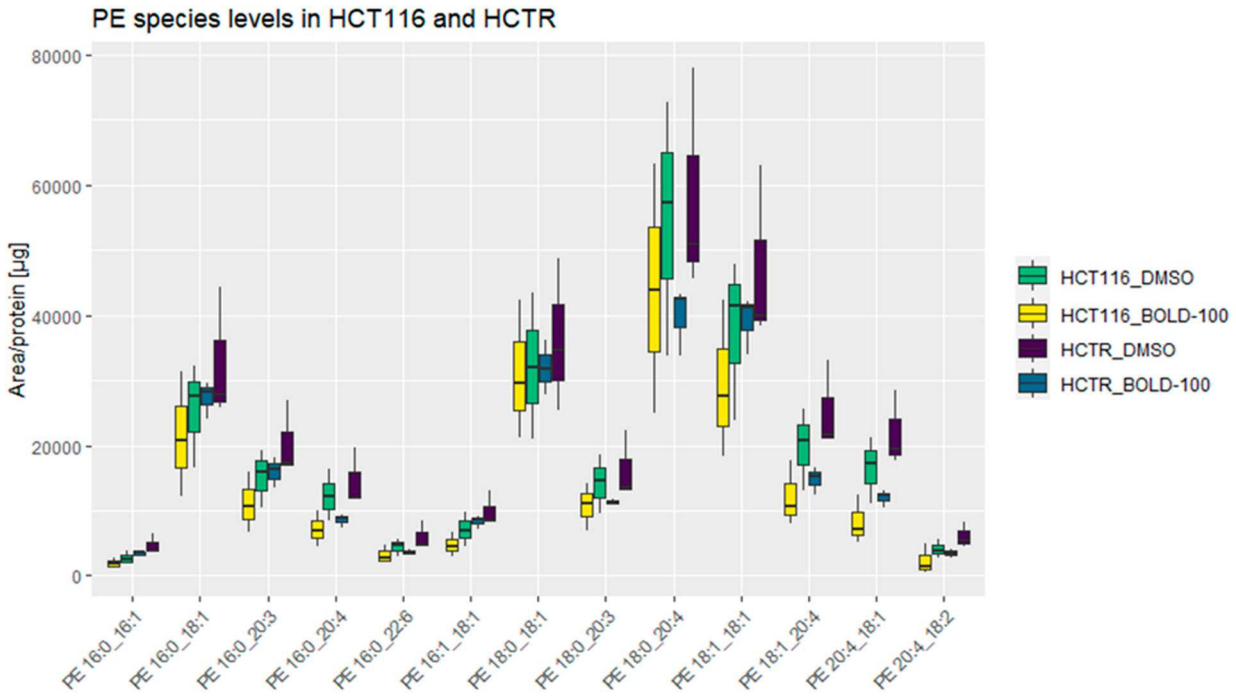

Figure S6 Regulation of cellular phosphatidylethanolamine levels by BOLD-100. Lipidomics analysis of HCT116 and HCTR cells treated with 100 µM of BOLD-100 or the corresponding amount of DMSO for 24 h. Samples were analyzed with RP-UHPLC-HRMS followed by data evaluation in LipidSearch 5.0 and R Studio. All groups were measured in triplicates, integrated areas were normalized to the protein content [µg].

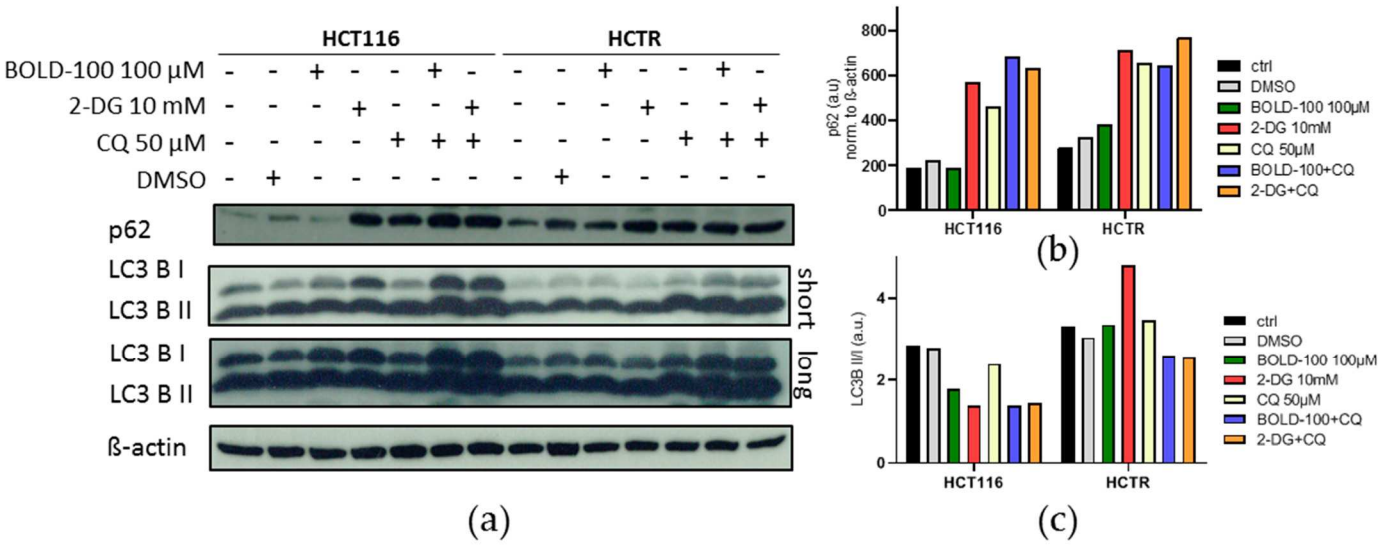

Figure S7 Autophagy regulation by BOLD-100 and 2-DG under autophagic flux blockade by CQ. (**a**) Expression levels of p62, and LC3B I/II in HCT116 and HCTR cells treated with 100 µM of BOLD-100, 10 mM of 2-DG, 50 µM of CQ, or their combination for 24 h analyzed by Western blotting. Two different control states were included, i.e. medium control for 2-DG and CQ or DMSO as solvent control for BOLD-100. β-actin served as loading control. LC3B signals are depicted with shorter (upper) and longer (lower) exposure times. (**b**) Quantification of treatment-respective p62 intensities of Western blot signals depicted in (a). (**c**) Calculation of treatment-respective LC3B II/I ratio from protein expression detected in (a).

Additional data

The novel resistant cell lines were established as described in the third peer-reviewed paper presented in this thesis. Additionally, several investigations were conducted to characterize the resulting cell lines. With this regard, Figure 22 depicts direct comparison between the originally sensitive Capan-1 and HCT116 cell lines and the established resistant sublines CapanR and HCTR, respectively. Distinct differences are documented in their response especially at treatment with 100 µM KP1339, indicating the gained resistance. Notably, while only a minor amount of cleaved PARP was detected in HCTR upon treatment with concentrations above 200 µM KP1339 (Figure 23) CapanR exhibited elevated amounts of cleaved PARP at all concentrations, even without treatment. Besides this, proteins indicative for ER-stress were examined (Figure 23). Basic levels of GRP78 and Ero1α were increased in CapanR and HCTR compared to their parental sublines.

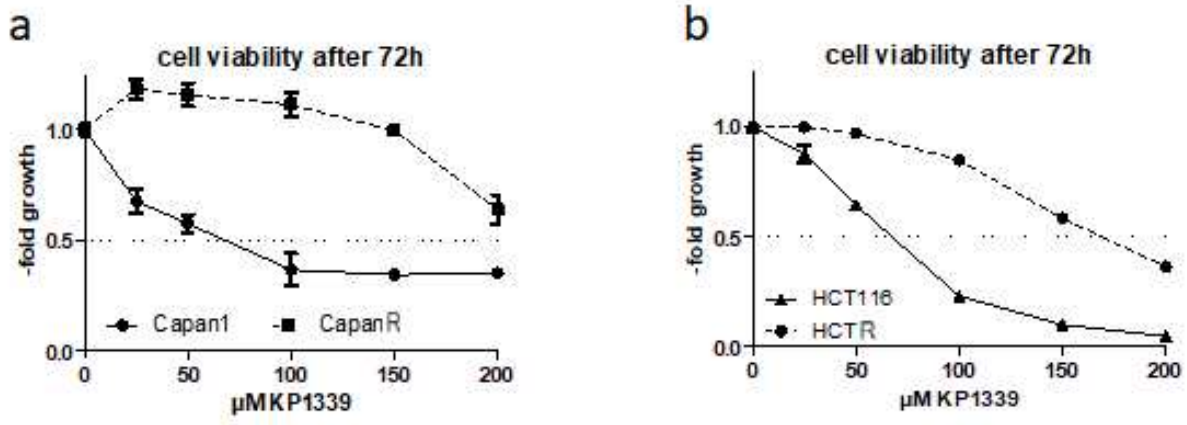

Figure 22: Full dose response curves in sensitive and resistant cell lines
Representative full dose-response curves of KP1339 are exemplarily shown for Capan1 and the resistant cell line CapanR (a) as well as for HCT116 and HCTR (b). Cell viability was assessed by MTT assays performed after 72 h treatment.

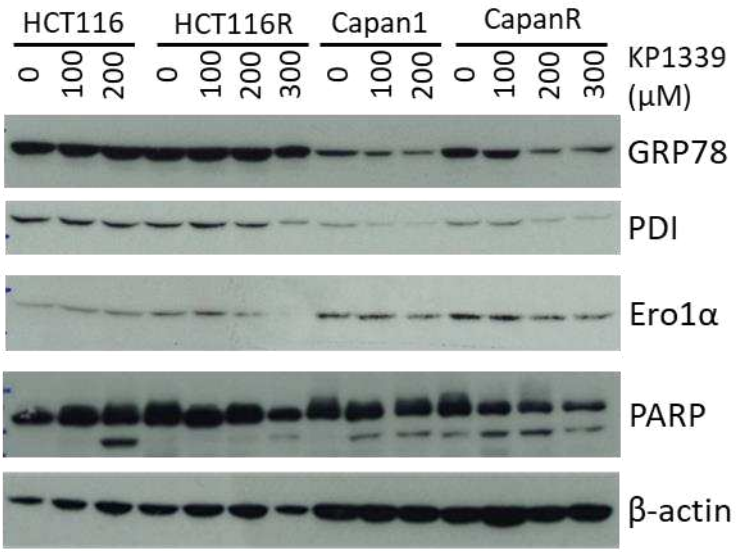

Figure 23: Western Blot of selected proteins relevant for ER homeostasis and apoptosis induction
Expression levels of proteins were determined in the indicated cell models after treatment with KP1339 for 24 h.

Subsequently to the establishment of the resistant cell lines and the first experiments regarding cytotoxicity and induction of cell death, CapanR and HCTR were investigated for changes in the behaviour *in vivo*. Thus, the same number of cells from the corresponding cell lines was injected subcutaneously in the right flank of BALB/c-mice and measured daily. As depicted in Figure 24, the growth characteristics of Capan cell lines (a) differed from those of HCT cell lines (b) regarding final tumor size and the increase over time. However, both CapanR and HCTR exhibited similar growth characteristics as their parental cell lines.

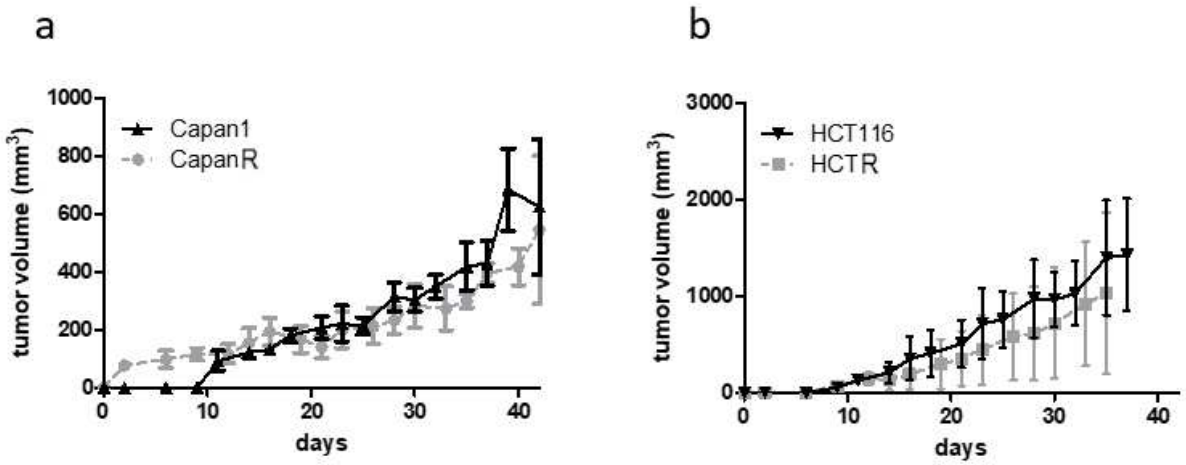

Figure 24: Xenograft growth curves of Capan-1 compared to CapanR (a) and HCT116 compared to HCTR (b)

In addition, the genetics of CapanR and HCTR were compared to their parental cell lines using Array CGH techniques. For both parental cell lines, in the upper panels of

Figure 25, their gains and losses compared to normal genomes are depicted. In this comparison, Capan1 reveals a multitude of changes (both gains and losses) scattered over all chromosomes. However, both CapanR and HCTR exhibited only minor changes compared to their parental cell lines.

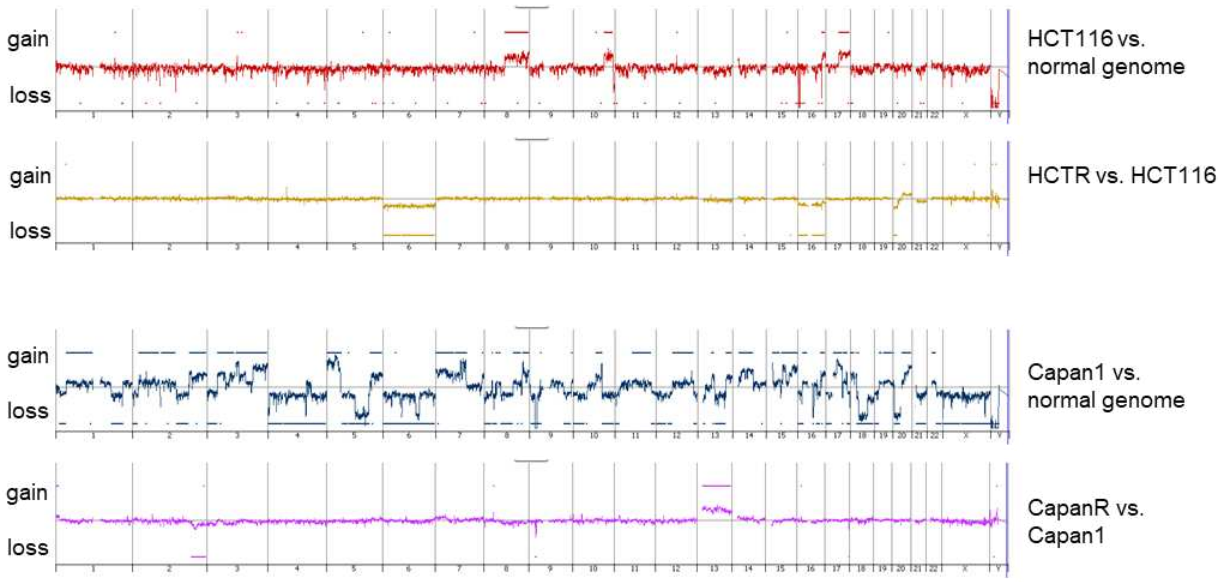

Figure 25: Comparative genomic hybridisation of HCT116, HCTR, Capan-1 and CapanR

As a next step, we aimed to establish a cross-resistance pattern of the selected resistant cell lines CapanR and HCTR. Therefore, a panel of eight compounds used in cancer therapy was selected, comprising other metal drugs (Cisplatin, AuPhen and Arsenic Trioxide), tyrosine kinase inhibitors (Sorafenib and Imatinib) as well as chemotherapeutics (Doxorubicin, Vinchristine, BCNU). Additionally, H_2O_2 was added to the panel as marker for resistance to disturbance of redox homeostasis. The results are presented in Table 1. The novel resistant cell lines did not depict distinct cross resistance which indicates a unique mode of action, not shared with the compounds selected as test panel.

Table 1: results of cytotoxicity test to establish a cross-resistance pattern

IC50	***Capan1***	***CapanR (fold resistance)***	***HCT116***	***HCTR (fold resistance)***
KP1339 (µM)	44 ± 10	227 ± 32 (5.05)	50 ± 14	137 ± 24 (2.75)
AuPhen (µM)	5.9 ± 1.7	5.3 ± 0.7 (0.9)	3.6 ± 0.2	4.1 ± 0.1 (1.18)
Cisplatin (µM)	5.4 ± 0.8	7.06 ± 2.6 (1.38)	2.8 ± 0.3	2.0 ± 0.4 (0.7)
ATO (µM)	28 ± 8	39 ± 6 (1.38)	17 ± 5	21 ± 1 (1.22)
Sorafenib (µM)	> 10	> 10	6 ± 1.9	6.0 ± 2 (1.07)
Imatinib (µM)	> 25	> 25	17 ± 1.7	16 ± 0.5 (0.91)
Doxorubicin (nM)	> 250	> 250	98 ± 16	82 ± 7 (0.83)
Vinchristine (nM)	> 25	> 25	8 ± 0.5	10 ± 2 (1.24)
BCNU (nM)	> 400	> 400	186 ± 8	175 ± 71 (0.94)
H_2O_2 (µM)	> 30	> 30	10 ± 2.9	12 ± 4.4 (1.19)

As described in the second peer-reviewed paper [150], we investigated the impact of TRAIL (the ligand of death receptor 4 and 5) on the activity of KP1339. These experiments revealed that combination of KP1339 with TRAIL was highly synergistic in sensitive cell lines (combination indices (CI values) around 0.3). In Figure 4d of this publication [150], the results for five cell lines (Capan-1, HCT116, SW480, CCL13 and KB-3-1) were shown. During the original experiments, the novel resistant cell lines CapanR and HCTR were treated and analysed together with the selected cell line panel. Therefore, in Figure 26, the data of a representative experiment is shown for the cell line panel and the novel resistant cell lines. For the original cell line panel, it was deduced that KP1339 activates caspase 8 signaling only to some extent and probably in a death receptor-independent manner, which can be further potentiated by combination with TRAIL [150]. For the single treatment with TRAIL, the sensitivity of HCTR did not differ from HCT116. Yet, the effect of the combination treatment on this cell line was decreased compared to its parental cell line. In contrast, Figure 26 demonstrated that CapanR was even more sensitive to TRAIL than

the parental Capan-1. This was also confirmed with full dose response curves (Figure 27) in combination with two different concentrations of TRAIL.

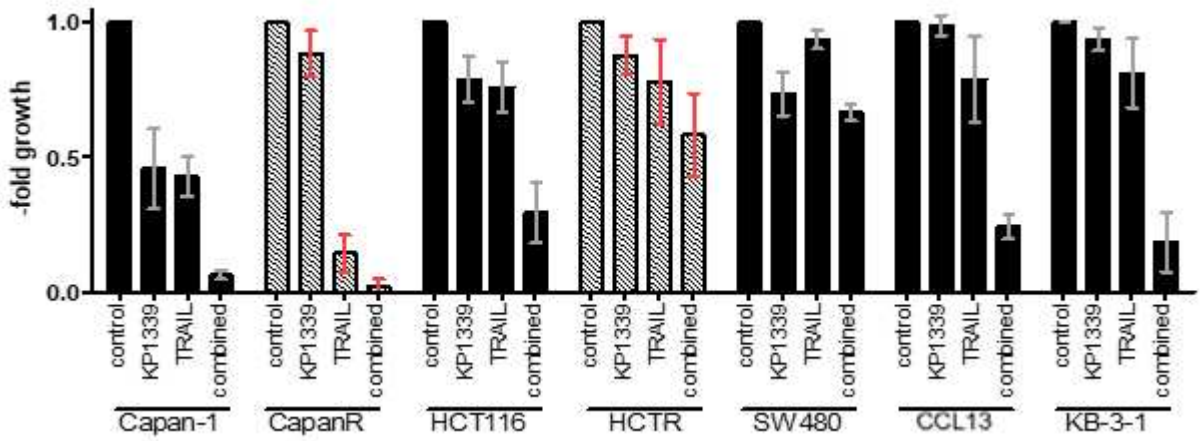

Figure 26: Cytotoxicity of KP1339, TRAIL and the combination thereof in sensitive and resistant cell lines
Cells were treated with 50 mM KP1339 and 25 ng/ml TRAIL, both as single agents and as combination. Cell viability was assessed by MTT assays performed after 72 h treatment. Data represent one representative experiment performed in triplicates.

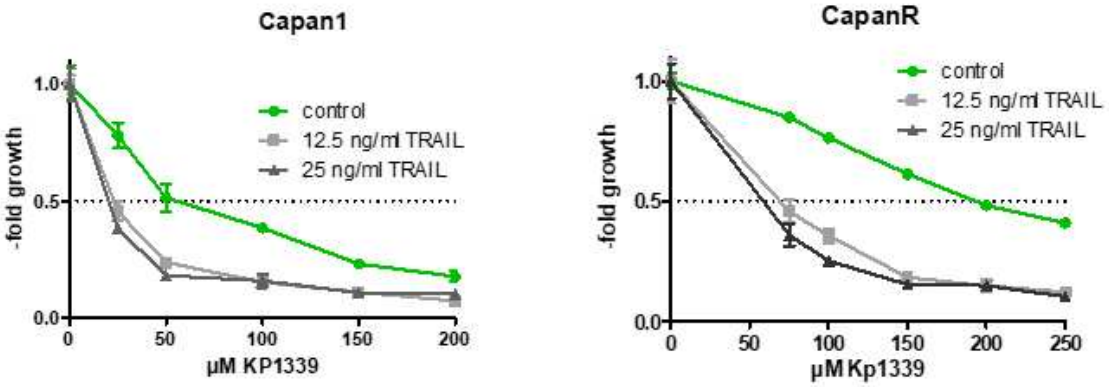

Figure 27: full range cytotoxicity assays on BOLD-100 with two concentrations of TRAIL
Representative full dose-response curves of KP1339 combined with TRAIL are exemplarily shown for Capan1 and the resistant cell line Capan-KP1339. Cell viability was assessed by MTT assays performed after 72 h treatment.

Discussion

General discussion

Given the ever-increasing incidence of various types of cancer, it is extremely important to continually expand and improve the treatment options for patients. In this context, improvement includes not only the efficiency and effectiveness of the treatment but also its tolerability. Great progress increasing tolerability has been made in recent years, especially in the subject area of metal drugs and related pro-drug systems. This is not surprising, as metal complexes provide versatile opportunities for chemical modifications to realize the improvements listed before [110]. In particular, complexes using ruthenium as central atom have proven to be very successful. Several of these compounds have already yielded promising results not only in preclinical studies, but also in clinical trials [128, 132, 151]. Although success in clinical trials is essential for the progress of development as a medicinal agent, this is not enough in the long term. The mode of action has to be deciphered and predictive markers of response to therapy have to be identified. If this is not successfully addressed, further development risks selecting ineligible patients, which might cause the discontinuation of a promising agent for seeming ineffective. In clinical practice, the selection of ineligible patient could harm them.

To support the overall goal to expand and improve the treatment options for cancer patients, this thesis aimed to gain novel insights into the biological activity of ruthenium-based prodrug systems. First, in order to foster the development of novel active compounds to be used in the clinic, metal arene complexes were coupled to poly(organo)phosphazene-based nanocarriers and characterized *in vivo* regarding their pharmacodynamic and toxicity profile [152]. Second, the ruthenium compound BOLD-100, which had already been successfully evaluated in early clinical trials, was investigated regarding its underlying mode of action. To achieve this, differences between intrinsically sensitive and resistant cell lines were identified and analysed to find novel markers indicative for either sensitivity or resistance [150]. In addition, preexisting knowledge of the effects of BOLD-100 on the cell cycle distribution was deepened and expanded. Moreover, the establishment of novel BOLD-100-resistant sublines of HCT-116 and Capan1 with their subsequent characterization regarding cross resistance profile, drug uptake and genetic changes further promoted the understanding of the mode of action of BOLD-100.

Regarding the development of novel active compounds, organoruthenium and organorhodium complexes were selected, which already showed promising results *in vitro* but had an undesirable toxicity profile *in vivo* [152]. The treatment resulted in adverse effects such as organ deformation, which not only poses a problem for the organism being treated, but also suggests that not enough of the drug may reach the tumor. Thus, a rational design utilizing poly(organo)phosphazenes was developed to ensure precise delivery to the target and prevent the compounds from premature reaction. As described in the introduction, the biodegradability of the carrier and suitable functional groups for chemical engineering are necessities in this kind of design [91, 93, 95]. Since the

selected polymer offered extensive control *via* the selection of building blocks and its degradation would yield physiologically non-hazardous metabolites, several of the conditions required for polymer therapeutics were satisfied. The advantages of this approach were manifold. First, the chosen design of the carrier macromolecule was able to compensate the aqueous solubility of the active compound, which was quite poor but typical for metal-based half-sandwich compound. Second, the approach in parallel aimed to keep the compound inactive and release the active species in a controlled, pH-triggered manner upon uptake in the tumor [152].

The designed conjugates were synthesized and their characteristics analysed thoroughly using NMR and UV-Vis spectroscopy, ICP-MS analyses and SEC coupled to ICP-MS. The focus was particularly on the question of loading of the polymer as well as release/activation in acidic environments [152]. The former was crucial because differences in drug loading of polymers were reported to influence characteristics of the conjugate such as solubility and targeting [95]. In addition, the information was needed for the practical aspects of the study because we had to ensure that equal amounts of active substance would be used. In this regard, unequal loading of the polymer macromolecule would have skewed the results. Thus, the polymer conjugates were analyzed using ICP-MS to determine the metal content to adjust the amount used in further experiments. Simultaneously, the results thereof revealed uneven yields between the complexes ranging from 5 wt% to 30 wt%. Although the optimal proportion of loaded weight to carrier is not known for the currently used polymeric carrier, the achieved loading is in the same order of magnitude as described for other carrier systems. For example, the optimal proportion for polymer–drug loading of (HPMA)-co-polymers [153] was reported to be ~10 wt%, while polyglutamic acid conjugates (PGA) were successfully used with up to 37 wt% [95].

Following the chemical analyses, the original, uncoupled complexes compared to their prodrug formulation and the unloaded polymer were evaluated *in vitro* and *in vivo*. Taking a closer look at the results, the activity of the polymer-drug-conjugates presented decreased activity *in vitro* compared to the unbound complexes [152]. Since the conjugates were designed to passively accumulate in the tumor due to the EPR effect and to be activated in the local hypoxic environment of the solid tumor, neither of which is effective under cell culture conditions, the decreased activity *in vitro* was in agreement with our expectations. In line with this, similar observations have been reported repeatedly for prodrug formulations [90, 95, 125, 154, 155]. Regarding the activity *in vivo*, pronounced tumor shrinkage was observed after administration of the first dose of all tested conjugate formulations. In addition, during dissection of the treated animals, it became evident that the internal organs were affected by treatment with the unbound complexes 1, 2 and 3 whereas no effect was visible for conjugates 1a, 2a and 3a [152]. For further investigations with regard to the safety of the application, the tissue distribution was determined. Interestingly, the tissue distribution also revealed distinct differences between conjugates 1a and 2a/3a: Conjugates 2a and 3a preferably accumulated in the liver, while 1a caused highest metal levels

in the kidneys [152]. Although our histological and microscopic evaluation of the respective organs did not detect severe adverse effects, it should be noted that this finding is not sufficient to exclude functional impairment. Overall, the conjugation of metallodrugs to poly(organo)phosphazenes has proven to be a promising approach for drug delivery.

Regarding the ruthenium compound BOLD-100, the identification of the underlying mode of action as well as of factors indicative for sensitivity or resistance were approached by screening 23 cell lines from diverse backgrounds [150]. Within these cell lines, a small panel comprising two sensitive and three low-responsive models was selected for further studies. As a first step, expression array analysis after short-term treatment for three and six hours, revealed distinct differences between sensitive and low-responsive cell lines. In low-responsive cell lines, expression of gene sets termed “cell cycle”, “metabolism”, “protein damage” and “DNA damage” were enriched, the reaction of the sensitive cell lines was more pronounced already at three hours. In addition, sensitive cell lines upregulated other and significantly more gene sets, including “response to chemical stimuli”, “cell death” and “chromatin organization” [150]. Notably, when evaluated after 24 h of treatment with BOLD-100, low-responsive cells indeed exhibited cell cycle arrest in G2-phase, whereas sensitive cell lines showed significant induction of cell death, both reflecting their initial response. Consequently, we aimed to investigate which molecular switches and signaling pathways initiated the programmed cell death observed in sensitive cell lines [150]. Although depolarization of mitochondria had previously been reported for KP1019 [156], neither this nor cleavage of caspase 9 were detected at cytotoxic BOLD-100 concentrations within our studies. Surprisingly, time-dependent cleavage of caspase 8 was detected. The theory of cell death activation *via* the “extrinsic pathway” was further backed by the ability to rescue sensitive cells through inhibition of caspase 8. However, cell death *via* caspase 8 may not solely be activated by extrinsic signal [32, 157]. At the time the research for this publication was conducted, ligand-independent activation of caspase 8 had been described, but a lot of mechanistic questions remained to be deciphered. Among these mechanism, the activation *via* integrins comparable to a special form of cell death called Anoikis [158] as well as *via* ROS-activated ASK1 [159] were researched in the literature. Because ruthenium(III) compounds are known for their redox activity [123, 144], the involvement of ROS in the BOLD-100-mediated caspase 8 activation seemed likely. However, at least in our hands, the induction of ROS did not correlate with sensitivity towards BOLD-100. Together this argues against ROS as the relevant factor underlying the observed sensitivity. Independently from this discussion, activation of caspase 8 through ER stress *via* interaction of CHOP had been reported shortly before our publication [157]. Since upregulation of CHOP was detected in sensitive cells after BOLD-100 treatment by other groups [144] as well as in ours, vulnerability to ER stress was investigated in more detail. Although BOLD-100-induced deregulation of proteins involved in detection and signalling of ER stress were found, sensitivity did not correlate with sensitivity to the ER stress inducer thapsigargin. In contrast, all low responsive models were characterized by a very strong synergistic activity of

BOLD-100 with the “chemical chaperon” 4-phenylbutyric acid (4-PBA). In summary, we speculated that a unique depletion of key cellular chaperones including GRP78 in combination with enhanced protein damage exhibits the triggering event for the apoptosis induction *via* caspase 8 [150]. Concordantly, recent publications reported the crucial role of the autophagosomal membranes for the intracellular activation of caspase 8 upon ER stress [160]. In addition, ligand-independent activity of death receptor 5 was demonstrated to be both sensor and effector for protein folding stress [161].

In addition to these published results, we aimed to deepen the understanding of the underlying mechanisms of sensitivity and resistance by establishing and then examining resistant cell lines. For this purpose, both sensitive cell lines of the panel were exposed to increasing concentrations of BOLD-100 resulting in the resistant sublines CapanR and HCTR. The results of the comparative studies between these two sublindes and the original cell lines confirmed that the resistance is not caused by reduced ruthenium uptake. A sensitivity screen with eight other active substances also showed no noticeable cross-resistance, indicating that the mode of action of the resistance against BOLD-100 does not overlap with one of the tested agents. Regardless, the new sublines behaved similarly to the intrinsically resistant cell lines with regard to combination therapy with TRAIL. Taken together, these results indicated a unique mode of action for BOLD-100 and thus also for the resistance mechanism which were investigated and deciphered in detail in subsequent studies [146, 147, 162].

Summary and outlook

Contributing to the development of novel compounds and the improvement of existing agents for effective and safe cancer therapy is a fascinating field of research the complexity of which is growing constantly. Burning questions are being answered and, at the same time, new ones arise for future scientists to decipher and marvel about the results. In course of this doctoral thesis, some answers were provided which – conjointly with the questions that arose in parallel – offered starting points for the work of subsequent colleagues. Especially the work of D. Baier who gathered, gained and integrated enormous amounts of information regarding the mode of action of BOLD-100 and the acquired resistance against the compound, should be mentioned in this context [146, 147, 162].

Despite these extraordinary achievements, additional questions remained without answers. With respect to the novel poly(organo)phosphazene conjugates, which are in a very early phase of development, further studies are needed. The safety of the potential new agents is of utmost importance. Since the tissue with the highest accumulation of metal were the liver and kidneys, investigations about possible impairments of these organs are needed. This is interconnected with the question of plasma half-life after intravenous administration of the conjugates, which has not been evaluated in detail yet. On the one hand, this information might be important for the investigations of the impact on the kidney. The underlying reason for this are reports from the field

of organ toxicology for other substances that peak concentrations have the potential to cause damage. On the other hand, a prolonged plasma half-life is usually regarded as beneficial, because it might facilitate continuous drug delivery and uptake in the tumor which is thought to yield superior treatment efficacy. Furthermore, the kinetics of the plasma concentration might be related to the polymer-drug-ratio in the conjugate. As mentioned before, differences in the behaviour of loaded polymers were reported depending on the wt%. Thus, this feature could also assist in fine tuning of the treatment options and could therefore be evaluated.

The understanding of the mode of action of BOLD-100 has grown immensely over the past years, resulting in more detailed questions than those addressed in this thesis. In the current clinical trial, BOLD-100 is used in combination with folinic acid, fluorouracil and oxaliplatin, which represents the clinically approved “FOLFOX” regime. So far the results of this study are promising, even causing BOLD-100 to be expected to receive a breakthrough therapy designation in colorectal cancer and potentially other gastrointestinal cancer indications in the near future [119]. In concordance, it was suggest that BOLD-100 could enhance the effectiveness of a wide range of existing cancer therapies and significantly improve patient outcomes [119]. Taken together with the finding that cell death caused by BOLD-100 exhibits immunogenic characteristics [147], the combination of BOLD-100 with immunotherapy might be suggested as a promising candidate to be evaluated. Additionally, a completely different type of combination could be considered at least on the theoretical level: the central atom of BOLD-100 is ruthenium, whose radioactive isotopes happen to be one of the fission products in nuclear reactors. Moreover, they accrue in the reprocessing process of the spent nuclear fuel [122]. Remarkably, the radioisotope of ruthenium, ^{106}Ru, is already successfully applied in brachytherapy [122]. Since the physical half-life of this isotope is approximately one year, the handling of it including the synthesis of BOLD-100 should not represent limiting obstacles. Recently, the use of BOLD-100 featuring a ^{103}Ru center was suggested as a probe for SPECT imaging [163]. Similarly, BOLD-100 featuring a ^{106}Ru center could be evaluated if further benefits might arise combining the effects of the compound with those of ionizing radiation.

Material and methods

Regarding the original publications, all materials and methods used are described in the original publications in CHAPTER TWO: RESULTS. Regarding the additional data also presented in Chapter two: Results are described in this part.

Chemicals. KP1339 was prepared as described previously [143] and dissolved in DMSO. DMSO concentrations in all experiments were below 1%. TRAIL was from Life Technologies (Carlsbad, California, USA). All other substances were purchased from Sigma-Aldrich (St. Louis, MO). All solutions were freshly prepared before usage.

Cell culture. Detailed information as well as culture and MTT seeding conditions for cell lines used are provided in Table 2. All cultures were grown under standard cell culture conditions, regularly checked for *Mycoplasma* contamination and their authentication verified either by short-tandem-repeat (STR) profiling or array comparative genomic hybridization. Fetal bovine calf serum (FBS) was purchased from PAA (Linz, Austria).

Cytotoxicity Assays: Cells were plated in 96-well plates (number of used cells is given in Table 2 and allowed to recover for 24 h before drug treatment for 72 h. Cell survival was determined by MTT assay following the manufacturer's recommendations (EZ4U, Biomedica, Vienna, Austria). Cytotoxicity was calculated using the Graph Pad Prism software (La Jolla, USA) (using a point-to-point function) and expressed as IC50 values calculated from full dose-response curves (drug concentrations resulting in 50% reduction of viable cells compared to untreated control cells cultured in parallel).

Table 2: Detailed Information about cell lines used for generation of additional data

Cell line	Tissue	Culture medium	Cell number 96-well plate	Source
Capan1	Pancreatic adenocarcinoma,	RMPI 1640	$5x10^3$	ATCC
HCT116	Colon carcinoma (p53/wt)	McCoy's	$2x10^3$	B. Vogelstein (JHU, USA)
CCL13	Hepatoma	RPMI 1640	$2x10^3$	ATCC
KB-3-1	Hela-derivative (cervix)	RPMI 1640	$2x10^3$	D.W. Shen (Bethesda, USA)
SW480	Colon carcinoma	MEME	$2x10^3$	ATCC

Abbreviations: ATCC, American Type Culture Collection Manassas VA; JHU, John Hopkins University; MEME, Minimal Essential Medium;

Western Blot Analyses: Sample collection, protein separation and Western blotting were performed as described [164]. The antibodies used including source and dilutions are given in Table 3.

Table 3: used antibodies

Detected protein	Species	Dilution	Purchased from:
PARP	rabbit	1:1000	Cell Signalling Technology
cleaved PARP	rabbit	1:1000	Cell Signalling Technology
β-actin	rabbit	1:1000	Sigma
Secondary anti-rabbit	goat	1:10000	Pierce by Thermo Scientific

Xenografts: Eight-week-old Balb/c mice were were purchased from Harlan Laboratories (San Pietro al Natisone, Italy) and kept in a pathogen-free environment and every procedure was done in a laminar airflow cabinet. The experiments were done according to the regulations of the Ethics Committee for the Care and Use of Laboratory Animals at the Medical University Vienna (proposal number BMWF-66.009/0084-II/3b/2013), the U.S. Public Health Service Policy on Human Care and Use of Laboratory Animals as well as the United Kingdom Coordinating Committee on Cancer Prevention Research's Guidelines for the Welfare of Animals in Experimental Neoplasia. For the testing of tumor growth, 5×10^5 cells of Capan-1, CapanR, HCT116 and HCTR were injected subcutaneously into the right flank of Balb/c mice. The tumor size was assessed by caliper measurement and tumor volume was calculated using the formula: (length × width^2)/2. Animals were sacrificed upon tumor ulceration or when a tumor length >20 mm was reached.

ArrayCGH (aCGH) analyses: aCGH was performed using 4x44K human whole genome oligonucleotide-based arrays (Agilent Technologies Österreich GmbH, Austria) as published [165]. Labeling and hybridization procedures were done according to the instructions provided by Agilent. Briefly, 500 ng of tumor DNA and reference DNA (human male genomic DNA, Promega Corporation, Madison, USA) were digested with AluI and RsaI (both from Promega), then differentially labeled by random priming with cyanine 5- and cyanine 3-dUTP (Perkin-Elmer, Massachusetts, USA), respectively, using the BioPrime Array CGH Genomic Labeling Kit (Life Technologies Corporation, Invitrogen, Paisley, UK). After purification with Amicon Ultra Centrifugal Filters (MILLIPORE GmbH, Vienna, Austria) the two labeled products together with blocking agents, Hybridization Buffer (both included in the Oligo aCGH/Chip-on-Chip Hybridization Kit, Agilent Technologies), and human cot-DNA (Roche Austria GmbH, Vienna, Austria) were combined and hybridized onto 4x44K oligonucleotide arrays. Hybridization was carried out for 48 h at 65 °C in a hybridization oven. Afterwards, slides were washed according to the protocol and scanned with a G2505B Micro Array Scanner (Agilent Technologies). Feature extraction and data analyses were carried out using the Feature Extraction (version 10.7.3.1) and DNA Analytics software (version 4.0.81), respectively.

Abbreviations

2-DG	2-deoxy-D-glucose
4-PBA	4-phenylbutyric acid
aCGH	Array comparative genomic hybridization
AD	Anno Domini
ADME	Administration – Distribution – Metabolism - Excretion
ATCC	American Type Culture Collection
ATO	Arsenic Trioxide
BC	Befor Christ
BCNU	1,3-bis-(2-chlorethyl)-l-nitroso-urea
CDK	Cyclin dependent kinase
CKI	Cyclin dependent kinase inhibitor
CML	chronic myelogenous leukemia
DcR3	decoy receptor 3
DMSO	Dimethylsulfoxide
EGF	epidermal growth factor
EGFR	epidermal growth factor receptor
EPR	enhanced permeability and retention
ER	Endoplasmatic Reticulum
FasL	Fas Ligand
FBS	Fetal bovine calf serum
FGF	Fibroblast growth factor
FGFR	fibroblast growth factor receptor
FOLFOX	combination therapy regime of folinic acid, fluorouracil and oxaliplatin
GRP78	glucose related protein 78
HPMA	*N*-(2-hydroxypropyl)methacrylamide
ICD-O-3	International Classification of Diseases for Oncology
IGF	Insulin-like growth factor
ICI	Immune checkpoint inhibitors
ICP-MS	inductively coupled plasma mass spectrometry
JHU	John Hopkins University
MEF	mouse embryonic fibroblasts
MTT	3-(4,5-Dimethylthiazol-2-yl)-2,5-diphenyltetrazoliumbromid

2 Characterization

2.1 NMR Measurements

NMR spectra of the monomer, poly(dichlorophosphazene) and substituted polymer(organo)phosphazene were measured on a Bruker 300 MHz spectrometer. The signal of $CDCl_3$ was used as internal reference for the ^1H NMR measurements. The $\{^1H\}^{31}P$ NMR measurements were carried out at 121 MHz and 85% phosphoric acid was used as external standard. NMR spectra of the final compounds and organometallic precursors were recorded on a Bruker FT-NMR Avance III™ 500 MHz instrument at 500.10 MHZ for ^1H NMR and 202.44 MHz for $\{^1H\}^{31}P$ NMR measurements.

2.1.1 ^1H NMR Spectrum of Complex 1

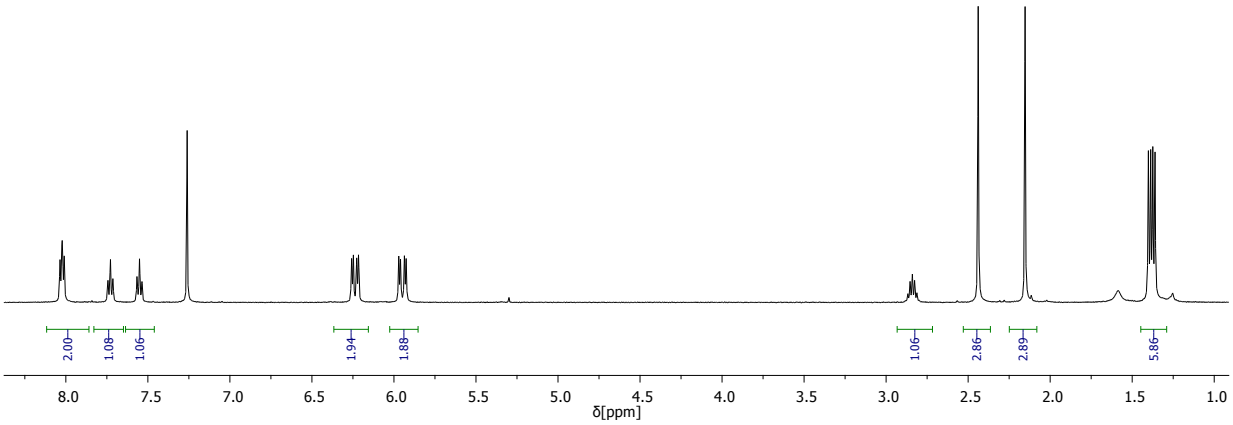

Figure S1: ^1H NMR spectrum of complex **1** recorded in $CDCl_3$.

NMR	nuclear magnetic resonance
PARP	Poly (ADP-ribose) polymerase
PCT	photochemotherapy
PDGF	platelet-derived growth factor
PDT	photodynamic therapy
PEG	polyethylene glycol
SEC	Size exclusion chromatography
SOD	Superoxide dismutase
STR	short-tandem-repeat
Rb	retinoblastoma protein
ROS	reactive oxygen species
TCA	tricarboxylic acid
TGFα	tumor growth factor alpha
TRAIL	TNF-related apoptosis-inducing ligand
UPR	unfolded protein response
VEGF	vascular endothelial growth factor

References

1. Hajdu, S.I., *Greco-Roman thought about cancer.* Cancer, 2004. **100**(10): p. 2048-51.
2. Hajdu, S.I., *A note from history: landmarks in history of cancer, part 1.* Cancer, 2011. **117**(5): p. 1097-102.
3. Hajdu, S.I., *Pathfinders in oncology from the end of the Middle Ages to the beginning of the 19th century.* Cancer, 2017. **123**(11): p. 1888-1897.
4. Fritz, A., et al., *International classification of diseases for oncology*. 2000, World Health Organization: Geneva.
5. Institute, N.C. *Types of Cancer*. 2024 21.02.2024]; Available from: https://training.seer.cancer.gov/disease/categories/classification.html.
6. [cited 2024 18.02.2024]; Available from: https://www.cancer.gov/about-cancer/treatment/types.
7. Institute, N.C. *What is Cancer?* 2021 11.10.2021 [cited 2024 06.03.2024]; Available from: https://www.cancer.gov/about-cancer/understanding/what-is-cancer#types.
8. Sung, H., et al., *Global Cancer Statistics 2020: GLOBOCAN Estimates of Incidence and Mortality Worldwide for 36 Cancers in 185 Countries.* CA: A Cancer Journal for Clinicians, 2021. **71**(3): p. 209-249.
9. Kufe, D.W., et al., *Cancer medicine 6*. 6th ed. 2003, Hamilton, Ont. ; Lewiston, NY: BC Decker.
10. Pitot, H.C., T. Goldsworthy, and S. Moran, *The natural history of carcinogenesis: implications of experimental carcinogenesis in the genesis of human cancer.* J Supramol Struct Cell Biochem, 1981. **17**(2): p. 133-46.
11. Troll, W. and R. Wiesner, *The role of oxygen radicals as a possible mechanism of tumor promotion.* Annu Rev Pharmacol Toxicol, 1985. **25**: p. 509-28.
12. Yuspa, S.H. and M.C. Poirier, *Chemical carcinogenesis: from animal models to molecular models in one decade.* Adv Cancer Res, 1988. **50**: p. 25-70.
13. Nik-Zainal, S., et al., *The life history of 21 breast cancers.* Cell, 2012. **149**(5): p. 994-1007.
14. Lengauer, C., K.W. Kinzler, and B. Vogelstein, *Genetic instabilities in human cancers.* Nature, 1998. **396**(6712): p. 643-9.
15. Hanahan, D. and R.A. Weinberg, *The hallmarks of cancer.* Cell, 2000. **100**(1): p. 57-70.
16. Hanahan, D., *Hallmarks of Cancer: New Dimensions.* Cancer Discov, 2022. **12**(1): p. 31-46.
17. Hanahan, D. and R.A. Weinberg, *Hallmarks of cancer: the next generation.* Cell, 2011. **144**(5): p. 646-74.
18. Duronio, R.J. and Y. Xiong, *Signaling pathways that control cell proliferation.* Cold Spring Harb Perspect Biol, 2013. **5**(3): p. a008904.
19. Tzavlaki, K. and A. Moustakas, *TGF-beta Signaling.* Biomolecules, 2020. **10**(3).
20. Hu, Q. and T. Huang, *Regulation of the Cell Cycle by ncRNAs Affects the Efficiency of CDK4/6 Inhibition.* Int J Mol Sci, 2023. **24**(10).
21. Fedi, P., S. Tronick, and S. Aaronson, *Growth factors.* Cancer medicine, 1997: p. 41-64.
22. Han, C.W., M.S. Jeong, and S.B. Jang, *Structure, signaling and the drug discovery of the Ras oncogene protein.* BMB Rep, 2017. **50**(7): p. 355-360.
23. Weinberg, R.A., *The retinoblastoma protein and cell cycle control.* Cell, 1995. **81**(3): p. 323-30.
24. Mittnacht, S., *The retinoblastoma protein--from bench to bedside.* Eur J Cell Biol, 2005. **84**(2-3): p. 97-107.
25. Counter, C.M., et al., *Dissociation among in vitro telomerase activity, telomere maintenance, and cellular immortalization.* Proc Natl Acad Sci U S A, 1998. **95**(25): p. 14723-8.
26. Bryan, T.M., et al., *Telomere elongation in immortal human cells without detectable telomerase activity.* EMBO J, 1995. **14**(17): p. 4240-8.
27. Bryan, T.M. and T.R. Cech, *Telomerase and the maintenance of chromosome ends.* Curr Opin Cell Biol, 1999. **11**(3): p. 318-24.
28. Bertheloot, D., E. Latz, and B.S. Franklin, *Necroptosis, pyroptosis and apoptosis: an intricate game of cell death.* Cell Mol Immunol, 2021. **18**(5): p. 1106-1121.
29. McConkey, D.J., S. Orrenius, and M. Jondal, *Cellular signalling in programmed cell death (apoptosis).* Immunol Today, 1990. **11**(4): p. 120-1.
30. Frisch, S.M. and E. Ruoslahti, *Integrins and anoikis.* Curr Opin Cell Biol, 1997. **9**(5): p. 701-6.
31. Abou-Ghali, M. and J. Stiban, *Regulation of ceramide channel formation and disassembly: Insights on the initiation of apoptosis.* Saudi J Biol Sci, 2015. **22**(6): p. 760-72.
32. Kowalski, S., et al., *An overview of programmed cell death: Apoptosis and pyroptosis-Mechanisms, differences, and significance in organism physiology and pathophysiology.* J Cell Biochem, 2023. **124**(6): p. 765-784.
33. Searle, J., J.F. Kerr, and C.J. Bishop, *Necrosis and apoptosis: distinct modes of cell death with fundamentally different significance.* Pathol Annu, 1982. **17 Pt 2**: p. 229-59.
34. Wyllie, A.H., J.F. Kerr, and A.R. Currie, *Cell death: the significance of apoptosis.* Int Rev Cytol,

1980. **68**: p. 251-306.
35. Paus, R., et al., *Patterns of cell death: the significance of apoptosis for dermatology.* Exp Dermatol, 1993. **2**(1): p. 3-11.
36. Kesavardhana, S., R.K.S. Malireddi, and T.-D. Kanneganti, *Caspases in Cell Death, Inflammation, and Pyroptosis.* Annual Review of Immunology, 2020. **38**(1): p. 567-595.
37. Werner, H. and D. Le Roith, *The insulin-like growth factor-I receptor signaling pathways are important for tumorigenesis and inhibition of apoptosis.* Crit Rev Oncog, 1997. **8**(1): p. 71-92.
38. Kulik, G., A. Klippel, and M.J. Weber, *Antiapoptotic signalling by the insulin-like growth factor I receptor, phosphatidylinositol 3-kinase, and Akt.* Mol Cell Biol, 1997. **17**(3): p. 1595-606.
39. Pitti, R.M., et al., *Genomic amplification of a decoy receptor for Fas ligand in lung and colon cancer.* Nature, 1998. **396**(6712): p. 699-703.
40. Harris, C.C., *p53 tumor suppressor gene: from the basic research laboratory to the clinic--an abridged historical perspective.* Carcinogenesis, 1996. **17**(6): p. 1187-98.
41. Levine, A.J., *p53, the cellular gatekeeper for growth and division.* Cell, 1997. **88**(3): p. 323-31.
42. Harrington, E.A., A. Fanidi, and G.I. Evan, *Oncogenes and cell death.* Curr Opin Genet Dev, 1994. **4**(1): p. 120-9.
43. Korsmeyer, S.J., *Bcl-2 initiates a new category of oncogenes: regulators of cell death.* Blood, 1992. **80**(4): p. 879-86.
44. Carpenter, R. and M.F. Brady, *BAX Gene*, in *StatPearls*. 2024: Treasure Island (FL).
45. Brown, J.M. and A.J. Giaccia, *The unique physiology of solid tumors: opportunities (and problems) for cancer therapy.* Cancer Res, 1998. **58**(7): p. 1408-16.
46. Palm, W. and C.B. Thompson, *Nutrient acquisition strategies of mammalian cells.* Nature, 2017. **546**(7657): p. 234-242.
47. Pavlova, N.N. and C.B. Thompson, *The Emerging Hallmarks of Cancer Metabolism.* Cell Metab, 2016. **23**(1): p. 27-47.
48. Warburg, O., F. Wind, and E. Negelein, *The Metabolism of Tumors in the Body.* J Gen Physiol, 1927. **8**(6): p. 519-30.
49. Lindsten, T., et al., *The proapoptotic activities of Bax and Bak limit the size of the neural stem cell pool.* J Neurosci, 2003. **23**(35): p. 11112-9.
50. Rathmell, J.C., et al., *In the absence of extrinsic signals, nutrient utilization by lymphocytes is insufficient to maintain either cell size or viability.* Mol Cell, 2000. **6**(3): p. 683-92.
51. Pavlova, N.N., J. Zhu, and C.B. Thompson, *The hallmarks of cancer metabolism: Still emerging.* Cell Metab, 2022. **34**(3): p. 355-377.
52. Kerr, M.C. and R.D. Teasdale, *Defining macropinocytosis.* Traffic, 2009. **10**(4): p. 364-71.
53. Commisso, C., et al., *Macropinocytosis of protein is an amino acid supply route in Ras-transformed cells.* Nature, 2013. **497**(7451): p. 633-7.
54. Palm, W., et al., *The Utilization of Extracellular Proteins as Nutrients Is Suppressed by mTORC1.* Cell, 2015. **162**(2): p. 259-270.
55. Schworer, S., et al., *Proline biosynthesis is a vent for TGFbeta-induced mitochondrial redox stress.* EMBO J, 2020. **39**(8): p. e103334.
56. Sullivan, L.B., et al., *Supporting Aspartate Biosynthesis Is an Essential Function of Respiration in Proliferating Cells.* Cell, 2015. **162**(3): p. 552-63.
57. Meiers, P., et al., *Sentinel lymph node biopsy in early-stage breast cancer patients: improved survival through better staging?* Langenbecks Arch Surg, 2013. **398**(5): p. 687-90.
58. Veronesi, U., et al., *A randomized comparison of sentinel-node biopsy with routine axillary dissection in breast cancer.* N Engl J Med, 2003. **349**(6): p. 546-53.
59. Wolff, J., *Die Lehre von der Krebskrankheit von den ältesten Zeiten bis zur Gegenwart*. 1907, Jena: G. Fischer.
60. Hajdu, S.I., *2000 years of chemotherapy of tumors.* Cancer, 2005. **103**(6): p. 1097-102.
61. DeVita, V.T., Jr. and S.A. Rosenberg, *Two hundred years of cancer research.* N Engl J Med, 2012. **366**(23): p. 2207-14.
62. Druker, B.J., et al., *Effects of a selective inhibitor of the Abl tyrosine kinase on the growth of Bcr-Abl positive cells.* Nat Med, 1996. **2**(5): p. 561-6.
63. Evans, S.T., et al., *Understanding and overcoming resistance to immunotherapy in genitourinary cancers.* Cancer Biol Ther, 2024. **25**(1): p. 2342599.
64. Majernikova, S.M., *Risk and safety profile in checkpoint inhibitors on non-small-cel lung cancer: A systematic review.* Hum Vaccin Immunother, 2024. **20**(1): p. 2365771.
65. Grant, M., et al., *Unlocking cancer vaccine potential: What are the key factors?* Hum Vaccin Immunother, 2024. **20**(1): p. 2331486.
66. Gold, J.M. and A. Raja, *Cisplatin*, in *StatPearls*. 2024: Treasure Island (FL).
67. Gandin, V., J.D. Hoeschele, and N. Margiotta, *Special Issue "Cisplatin in Cancer Therapy: Molecular Mechanisms of Action 3.0".* Int J Mol Sci, 2023. **24**(9).
68. Smith, L.A., et al., *Cardiotoxicity of anthracycline agents for the treatment of cancer: systematic*

review and meta-analysis of randomised controlled trials. BMC Cancer, 2010. **10**: p. 337.
69. Kciuk, M., et al., *Doxorubicin-An Agent with Multiple Mechanisms of Anticancer Activity.* Cells, 2023. **12**(4).
70. Sant, M., et al., *EUROCARE-4. Survival of cancer patients diagnosed in 1995-1999. Results and commentary.* Eur J Cancer, 2009. **45**(6): p. 931-91.
71. Raber, I. and A. Asnani, *Cardioprotection in cancer therapy: novel insights with anthracyclines.* Cardiovasc Res, 2019. **115**(5): p. 915-921.
72. Rivankar, S., *An overview of doxorubicin formulations in cancer therapy.* J Cancer Res Ther, 2014. **10**(4): p. 853-8.
73. Marupudi, N.I., et al., *Paclitaxel: a review of adverse toxicities and novel delivery strategies.* Expert Opin Drug Saf, 2007. **6**(5): p. 609-21.
74. Alani, A.W., et al., *Polymeric micelles for the pH-dependent controlled, continuous low dose release of paclitaxel.* Biomaterials, 2010. **31**(7): p. 1765-72.
75. Markman, M., *Taxol: an important new drug in the management of epithelial ovarian cancer.* Yale J Biol Med, 1991. **64**(6): p. 583-90.
76. Gallego-Jara, J., et al., *A Compressive Review about Taxol((R)): History and Future Challenges.* Molecules, 2020. **25**(24).
77. *Albumin-bound paclitaxel (Abraxane) for advanced breast cancer.* Med Lett Drugs Ther, 2005. **47**(1208): p. 39-40.
78. Buergy, D., et al., *Unfinished business: Terminated cancer trials and the relevance of treatment intent, sponsors and intervention types.* Int J Cancer, 2021. **148**(7): p. 1676-1684.
79. Zhang, E. and S.G. DuBois, *Early Termination of Oncology Clinical Trials in the United States.* Cancer Med, 2023. **12**(5): p. 5517-5525.
80. Rudmann, D.G., *On-target and off-target-based toxicologic effects.* Toxicol Pathol, 2013. **41**(2): p. 310-4.
81. Doogue, M.P. and T.M. Polasek, *The ABCD of clinical pharmacokinetics.* Ther Adv Drug Saf, 2013. **4**(1): p. 5-7.
82. Stella, V.J. and K.J. Himmelstein, *Prodrugs and site-specific drug delivery.* J Med Chem, 1980. **23**(12): p. 1275-82.
83. Aghebati-Maleki, A., et al., *Nanoparticles and cancer therapy: Perspectives for application of nanoparticles in the treatment of cancers.* J Cell Physiol, 2020. **235**(3): p. 1962-1972.
84. Nichols, J.W., et al., *Nano-sized drug carriers: Extravasation, intratumoral distribution, and their modeling.* J Control Release, 2017. **267**: p. 31-46.
85. Attia, M.F., et al., *An overview of active and passive targeting strategies to improve the nanocarriers efficiency to tumour sites.* J Pharm Pharmacol, 2019. **71**(8): p. 1185-1198.
86. Maeda, H., et al., *Tumor vascular permeability and the EPR effect in macromolecular therapeutics: a review.* J Control Release, 2000. **65**(1-2): p. 271-84.
87. Maeda, H., *Polymer therapeutics and the EPR effect.* J Drug Target, 2017. **25**(9-10): p. 781-785.
88. Davis, M.E., Z.G. Chen, and D.M. Shin, *Nanoparticle therapeutics: an emerging treatment modality for cancer.* Nat Rev Drug Discov, 2008. **7**(9): p. 771-82.
89. Lakkireddy, H.R. and D.V. Bazile, *Nano-carriers for drug routeing - towards a new era.* J Drug Target, 2019. **27**(5-6): p. 525-541.
90. Jain, A.K. and S. Thareja, *In vitro and in vivo characterization of pharmaceutical nanocarriers used for drug delivery.* Artif Cells Nanomed Biotechnol, 2019. **47**(1): p. 524-539.
91. Duncan, R., H. Ringsdorf, and R. Satchi-Fainaro, *Polymer therapeutics--polymers as drugs, drug and protein conjugates and gene delivery systems: past, present and future opportunities.* J Drug Target, 2006. **14**(6): p. 337-41.
92. Ringsdorf, H., *Structure and properties of pharmacologically active polymers.* Journal of Polymer Science: Polymer Symposia, 1975. **51**(1): p. 135-153.
93. Kaur, H., et al., *Polymer Particulates in Drug Delivery.* Curr Pharm Des, 2016. **22**(19): p. 2761-87.
94. Wen, R., et al., *Polymer-Based Drug Delivery Systems for Cancer.* Crit Rev Ther Drug Carrier Syst, 2018. **35**(6): p. 521-553.
95. Duncan, R., *Polymer conjugates as anticancer nanomedicines.* Nat Rev Cancer, 2006. **6**(9): p. 688-701.
96. Lieleg, O., R.M. Baumgartel, and A.R. Bausch, *Selective filtering of particles by the extracellular matrix: an electrostatic bandpass.* Biophys J, 2009. **97**(6): p. 1569-77.
97. Mishra, V. and R.J. Heath, *Structural and Biochemical Features of Human Serum Albumin Essential for Eukaryotic Cell Culture.* Int J Mol Sci, 2021. **22**(16).
98. Kratz, F., *Albumin as a drug carrier: Design of prodrugs, drug conjugates and nanoparticles.* Journal of Controlled Release, 2008. **132**(3): p. 171-183.
99. Ullah, A., G. Shin, and S.I. Lim, *Human serum albumin binders: A piggyback ride for long-acting therapeutics.* Drug Discov Today, 2023. **28**(10): p. 103738.
100. Spada, A., et al., *The Uniqueness of Albumin as a Carrier in Nanodrug Delivery.* Mol Pharm,

2021. **18**(5): p. 1862-1894.
101. Hornok, V., *Serum Albumin Nanoparticles: Problems and Prospects.* Polymers (Basel), 2021. **13**(21).
102. Wagner, A.J., et al., *Phase II Trial of nab-Sirolimus in Patients With Advanced Malignant Perivascular Epithelioid Cell Tumors (AMPECT): Long-Term Efficacy and Safety Update.* J Clin Oncol, 2024. **42**(13): p. 1472-1476.
103. Kratz, F., et al., *Probing the cysteine-34 position of endogenous serum albumin with thiol-binding doxorubicin derivatives. Improved efficacy of an acid-sensitive doxorubicin derivative with specific albumin-binding properties compared to that of the parent compound.* J Med Chem, 2002. **45**(25): p. 5523-33.
104. Mita, M.M., et al., *Pharmacokinetic study of aldoxorubicin in patients with solid tumors.* Invest New Drugs, 2015. **33**(2): p. 341-8.
105. Chamberlain, F.E., R.L. Jones, and S.P. Chawla, *Aldoxorubicin in soft tissue sarcomas.* Future Oncol, 2019. **15**(13): p. 1429-1435.
106. Schueffl, H., et al., *Albumin-targeting of an oxaliplatin-releasing platinum(iv) prodrug results in pronounced anticancer activity due to endocytotic drug uptake in vivo.* Chem Sci, 2021. **12**(38): p. 12587-12599.
107. Yao, H. and G. Zhu, *Blood Components as Carriers for Small-Molecule Platinum Anticancer Drugs.* ChemMedChem, 2022. **17**(23): p. e202200482.
108. Kratz, F. and B. Elsadek, *Clinical impact of serum proteins on drug delivery.* J Control Release, 2012. **161**(2): p. 429-45.
109. Kauffmann, G.B. and J. Halpern. *coordination compound*. 2018 03.08.20218 [cited 2024 05.07.2024]; Available from: https://www.britannica.com/science/coordination-compound.
110. Valente, A., et al., *Metal- and metalloid-based compounds to target and reverse cancer multidrug resistance.* Drug Resist Updat, 2021. **58**: p. 100778.
111. Dasmahapatra, U., et al., *Anti-cancer property and DNA binding interaction of first row transition metal complexes: A decade update.* Eur J Med Chem, 2024. **275**: p. 116603.
112. Gianferrara, T., I. Bratsos, and E. Alessio, *A categorization of metal anticancer compounds based on their mode of action.* Dalton Transactions, 2009(37): p. 7588-7598.
113. Boros, E., P.J. Dyson, and G. Gasser, *Classification of Metal-based Drugs According to Their Mechanisms of Action.* Chem, 2020. **6**(1): p. 41-60.
114. Gasser, G. and N. Metzler-Nolte, *Metal Compounds as Enzyme Inhibitors*, in *Bioinorganic Medicinal Chemistry*. 2011. p. 351-382.
115. Skoczynska, A., et al., *An Overview of the Potential Medicinal and Pharmaceutical Properties of Ru(II)/(III) Complexes.* Int J Mol Sci, 2023. **24**(11).
116. Franz, K.J. and N. Metzler-Nolte, *Introduction: Metals in Medicine.* Chem Rev, 2019. **119**(2): p. 727-729.
117. Englinger, B., et al., *Metal Drugs and the Anticancer Immune Response.* Chemical Reviews, 2019. **119**(2): p. 1519-1624.
118. Szefler, B., et al., *The assessment of physicochemical properties of Cisplatin complexes with purines and vitamins B group.* J Mol Graph Model, 2022. **113**: p. 108144.
119. Casini, A. and A. Pothig, *Metals in Cancer Research: Beyond Platinum Metallodrugs.* ACS Cent Sci, 2024. **10**(2): p. 242-250.
120. Adhikari, S., et al., *A review on metal complexes and its anti-cancer activities: Recent updates from in vivo studies.* Biomed Pharmacother, 2024. **171**: p. 116211.
121. Mjos, K.D. and C. Orvig, *Metallodrugs in medicinal inorganic chemistry.* Chem Rev, 2014. **114**(8): p. 4540-63.
122. Zuba, I., et al., *Ruthenium as an important element in nuclear energy and cancer treatment.* Applied Radiation and Isotopes, 2020. **162**: p. 109176.
123. Jungwirth, U., et al., *Anticancer activity of metal complexes: involvement of redox processes.* Antioxid Redox Signal, 2011. **15**(4): p. 1085-127.
124. Swaminathan, S. and R. Karvembu, *Dichloro Ru(II)-p-cymene-1,3,5-triaza-7-phosphaadamantane (RAPTA-C): A Case Study.* ACS Pharmacology & Translational Science, 2023. **6**(7): p. 982-996.
125. Rausch, M., P.J. Dyson, and P. Nowak-Sliwinska, *Recent Considerations in the Application of RAPTA-C for Cancer Treatment and Perspectives for Its Combination with Immunotherapies.* Advanced Therapeutics, 2019. **2**(9): p. 1900042.
126. Murray, B.S., et al., *The development of RAPTA compounds for the treatment of tumors.* Coordination Chemistry Reviews, 2016. **306**: p. 86-114.
127. Babak, M.V., et al., *Target profiling of an antimetastatic RAPTA agent by chemical proteomics: relevance to the mode of action.* Chem Sci, 2015. **6**(4): p. 2449-2456.
128. Monro, S., et al., *Transition Metal Complexes and Photodynamic Therapy from a Tumor-Centered Approach: Challenges, Opportunities, and Highlights from the Development of TLD1433.*

Chemical Reviews, 2019. **119**(2): p. 797-828.
129. Bonnett, R., *Chemical Aspects of Photodynamic Therapy*. 2000: Taylor & Francis.
130. Medicine, N.L.o. 2019 21.07.2024]; Available from: https://clinicaltrials.gov/study/NCT03945162.
131. Alessio, E. and L. Messori, *NAMI-A and KP1019/1339, Two Iconic Ruthenium Anticancer Drug Candidates Face-to-Face: A Case Story in Medicinal Inorganic Chemistry.* Molecules, 2019. **24**(10).
132. Srividya, S. and R. Karvembu, *Bold 100: A Ruthenium-based Anticancer Therapeutic.* Resonance, 2023. **28**(12): p. 1827-1844.
133. Hartinger, C.G., et al., *From bench to bedside--preclinical and early clinical development of the anticancer agent indazolium trans-[tetrachlorobis(1H-indazole)ruthenate(III)] (KP1019 or FFC14A).* J Inorg Biochem, 2006. **100**(5-6): p. 891-904.
134. Kersten, L., et al., *Comparative nephrotoxicity of some antitumour-active platinum and ruthenium complexes in rats.* J Appl Toxicol, 1998. **18**(2): p. 93-101.
135. Bergamo, A., et al., *Ruthenium-based NAMI-A type complexes with in vivo selective metastasis reduction and in vitro invasion inhibition unrelated to cell cytotoxicity.* Int J Oncol, 2002. **21**(6): p. 1331-1338.
136. Sava, G., et al., *Dual Action of NAMI-A in inhibition of solid tumor metastasis: selective targeting of metastatic cells and binding to collagen.* Clin Cancer Res, 2003. **9**(5): p. 1898-905.
137. Coverdale, J.P.C., T. Laroiya-McCarron, and I. Romero-Canelón, *Designing Ruthenium Anticancer Drugs: What Have We Learnt from the Key Drug Candidates?* Inorganics, 2019. **7**(3): p. 31.
138. Leijen, S., et al., *Phase I/II study with ruthenium compound NAMI-A and gemcitabine in patients with non-small cell lung cancer after first line therapy.* Investigational New Drugs, 2015. **33**(1): p. 201-214.
139. Trondl, R., et al., *NKP-1339, the first ruthenium-based anticancer drug on the edge to clinical application.* Chemical Science, 2014. **5**(8): p. 2925-2932.
140. Dittrich, C., et al. *Phase I and Pharmacokinetic Study of Sodium trans-[tetrachlorobis (1H-indazole) Ruthenate (III)]/Indazole-hydrochloride (1: 1.1)(FFC14A, KP1019) in Patients with Solid Tumors-A Study of the CESAR Central European Society for Anticancer Drug Research-EWIV in: Proceedings of the 96th Annual Meeting of the American Association for Cancer Research, Anaheim, 46, 110*. 2005. Abstr.
141. Happl, B., et al., *Synthesis and preclinical evaluation of BOLD-100 radiolabeled with ruthenium-97 and ruthenium-103.* Dalton Trans, 2024. **53**(13): p. 6031-6040.
142. Pötsch, I., et al., *Challenges and Chances in the Preclinical to Clinical Translation of Anticancer Metallodrugs*, in *Metal-based Anticancer Agents*, A. Casini, A. Vessières, and S.M. Meier-Menches, Editors. 2019, The Royal Society of Chemistry. p. 0.
143. Heffeter, P., et al., *Intracellular protein binding patterns of the anticancer ruthenium drugs KP1019 and KP1339.* J Biol Inorg Chem, 2010. **15**(5): p. 737-48.
144. Flocke, L.S., et al., *Molecular mode of action of NKP-1339 - a clinically investigated ruthenium-based drug - involves ER- and ROS-related effects in colon carcinoma cell lines.* Invest New Drugs, 2016. **34**(3): p. 261-8.
145. Ranzato, E., G. Bonsignore, and S. Martinotti, *ER Stress Response and Induction of Apoptosis in Malignant Pleural Mesothelioma: The Achilles Heel Targeted by the Anticancer Ruthenium Drug BOLD-100.* Cancers (Basel), 2022. **14**(17).
146. Baier, D., et al., *The Anticancer Ruthenium Compound BOLD-100 Targets Glycolysis and Generates a Metabolic Vulnerability towards Glucose Deprivation.* Pharmaceutics, 2022. **14**(2).
147. Baier, D., et al., *The Lipid Metabolism as Target and Modulator of BOLD-100 Anticancer Activity: Crosstalk with Histone Acetylation.* Adv Sci (Weinh), 2023. **10**(32): p. e2301939.
148. Medicine, N.L.o. *BOLD-100 in Combination With FOLFOX for the Treatment of Advanced Solid Tumours*. 2020 [cited 2024 24.07.2024]; Available from: https://clinicaltrials.gov/study/NCT04421820?cond=NCT04421820&rank=1.
149. Hackl, C., *Leaving group variation of "piano-stool" complexes for the development of novel organometallic anticancer drugs with targeting properties*, in *Department of Inorganic Chemistry*. 2017, University of Vienna: Vienna.
150. Schoenhacker-Alte, B., et al., *Sensitivity towards the GRP78 inhibitor KP1339/IT-139 is characterized by apoptosis induction via caspase 8 upon disruption of ER homeostasis.* Cancer Lett, 2017. **404**: p. 79-88.
151. Murray, B.S. and P.J. Dyson, *Recent progress in the development of organometallics for the treatment of cancer.* Curr Opin Chem Biol, 2020. **56**: p. 28-34.
152. Hackl, C.M., et al., *Synthesis and in vivo anticancer evaluation of poly(organo)phosphazene-based metallodrug conjugates.* Dalton Trans, 2017. **46**(36): p. 12114-12124.
153. Chytil, P., L. Kostka, and T. Etrych, *HPMA Copolymer-Based Nanomedicines in Controlled Drug Delivery.* J Pers Med, 2021. **11**(2).

154. Salari, N., et al., *Polymer-based drug delivery systems for anticancer drugs: A systematic review.* Cancer Treat Res Commun, 2022. **32**: p. 100605.
155. Wilding, J.L. and W.F. Bodmer, *Cancer cell lines for drug discovery and development.* Cancer Res, 2014. **74**(9): p. 2377-84.
156. Kapitza, S., et al., *Heterocyclic complexes of ruthenium(III) induce apoptosis in colorectal carcinoma cells.* J Cancer Res Clin Oncol, 2005. **131**(2): p. 101-10.
157. Estornes, Y., et al., *RIPK1 promotes death receptor-independent caspase-8-mediated apoptosis under unresolved ER stress conditions.* Cell Death Dis, 2014. **5**(12): p. e1555.
158. Lotti, R., et al., *A previously unreported function of beta(1)B integrin isoform in caspase-8-dependent integrin-mediated keratinocyte death.* J Invest Dermatol, 2010. **130**(11): p. 2569-77.
159. Chen, L., et al., *The marine fungal metabolite, dicitrinone B, induces A375 cell apoptosis through the ROS-related caspase pathway.* Mar Drugs, 2014. **12**(4): p. 1939-58.
160. Hattori, T., et al., *ER stress elicits non-canonical CASP8 (caspase 8) activation on autophagosomal membranes to induce apoptosis.* Autophagy, 2024. **20**(2): p. 349-364.
161. Law, M.E., et al., *DR5 disulfide bonding as a sensor and effector of protein folding stress.* bioRxiv, 2024.
162. Baier, D.S., *Mechanisms underlying the anticancer activity of novel metal compounds : focus on BOLD-100/KP1339*. 2024: Wien. p. 200 Seiten, Seite 9-10 : Illustrationen.
163. Happl, B., et al., *Synthesis and Preclinical Evaluation of Radiolabeled [(103)Ru]BOLD-100.* Pharmaceutics, 2023. **15**(11).
164. Heffeter, P., et al., *Intrinsic and acquired forms of resistance against the anticancer ruthenium compound KP1019 [indazolium trans-[tetrachlorobis(1H-indazole)ruthenate (III)] (FFC14A).* J Pharmacol Exp Ther, 2005. **312**(1): p. 281-9.
165. Pirker, C., et al., *Response of experimental malignant melanoma models to the pan-Aurora kinase inhibitor VE-465.* Exp Dermatol, 2010. **19**(12): p. 1040-7.